The Use of the Lattice Boltzmann Method in Thrombosis Modelling

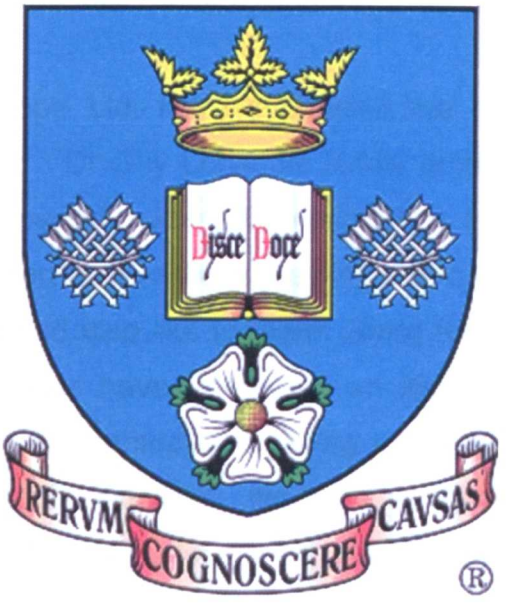

Sarah Elinor Harrison

School of Medicine and Biomedical Sciences

Academic Unit of Medical Physics

Submitted for the degree of PhD

Submission Date

March 2007

University of Sheffield, UK

Acknowledgements

I must thank my supervisors Dr Rod Hose and Dr Pat Lawford, not only for their continued academic support but also for ensuring that everything went smoothly on the numerous overseas trips made during this project.

The staff at NEC Europe Ltd. have supported me in many ways and are gratefully acknowledged. Dr Guy Lonsdale kindly arranged the funding of the project and writing-up period. Joerg Bernsdorf has answered my numerous lattice Boltzmann and Fortran questions, helping me to further the project to the best of my ability. I would also like to thank Joerg for helping me, above and beyond what I could ever have imagined, on each of my visits to Sankt Augustin; arranging my accommodation, taking me to and from the airport and involving me in many social activities. He is a true friend. I would also like to thank the remaining staff at NEC for making me feel so welcome and helping me in so many ways, mainly in ordering my Bier in the Brauhaus!

I would like to thank Aaron Fogelson for his inspiration during a discussion in Nottingham; his encouragement was invaluable in the final stages of my work.

The PhD and Postdoc colleagues in the department of Medical Physics helped me settle in the early stages of the project and provided much help and guidance along the way. I would also like to thank Margaret Beckett for all her help, from organising my overseas travel to cheering me on in my 10K run.

I am extremely grateful to all those who came to visit me in Germany whilst I was studying; Mum, Dad, Lorna, Phil, Steve, Chris, Denise, Kerry, Claire, Siobhan and Jules. My Mum and Dad have always been at the end of the phone, supporting me, encouraging me and listening to my many whinging episodes. I really couldn't have come this far without you both.

Finally, thank you Steve, not only for providing such a challenging set of experiments for me to model, but just for being you, keeping me sane.

Table of Figures

Abstract

The effects of thrombosis greatly contribute to the incidence of mortality in the Western World. Understanding thrombosis is therefore crucial in providing the correct treatment for the underlying pathologies. Numerical methods have previously been used to investigate various factors associated with thrombosis, usually starting from solutions of the Navier-Stokes equations.

This thesis presents the development and implementation of models of thrombosis using the lattice Boltzmann method, which is a relatively new technique for simulating fluid dynamics. The advantages and disadvantages of this methodology are critically reviewed and two major pathologies, atherosclerosis and deep vein thrombosis have been chosen to demonstrate principles of the application.

The first part of the work concentrates on the simulation of flow and clotting in idealised stenotic occlusions representative of the geometry and flow conditions in a diseased human femoral artery. Simulations of unsteady flow are reported and comparisons are made to previous flow visualisation studies. Stability issues regarding the diffusion algorithm are investigated in detail. In the first instance, clotting is simulated with the use of an aging model with extensions including proximity and shear stress. Comparisons are made with experimental results obtained using milk as a blood analogue.

The second part of the work focuses on increasing the complexity of the models to incorporate the representations of the actions and distribution of the platelets, proteins and enzymes involved in the coagulation cascade. The models are tested in 2D geometries to demonstrate their functionality. As an example of this work, a model of deep vein thrombosis was developed, based on a hypothesis supported by the clinical literature.

The foundations laid in this project allow for future developments, which will incorporate further details of thrombotic processes, in the hope that a valuable predictor of thrombosis can be developed.

Chapter One: Introduction

1.1 Simulation in Medicine

Computer simulation techniques can help improve understanding of normal physiology and pathological conditions and have been applied to a wide spectrum of biomechanical applications from the structural properties of bones and tissues to fluid dynamic processes such as air or blood flow.

There are many groups all over the world, working in isolation on computational simulations of medical and biological processes. These tend to focus on small aspects of the overall physiological system on a single joint or vessel for example. The Physiome project [1, 2] is an international initiative which seeks to stimulate collaboration between modelling groups. One of the aims of this is to establish common methodologies to enable integration of such models in order to provide a quantitative description of complete systems.

A more recent initiative, the Virtual Physiological Human project [3, 4] sets out to develop a framework to enable the integration of models of diverse types representing the mechanical, physical and biochemical functions of the human body in order to describe and predict behaviour in both physiological and pathological conditions. The complete range of length scales is considered, from the whole body down to cells or individual molecules. Anatomical descriptors may consider generic or patient specific geometries. The vision is that patient data coupled with simulations can ultimately be used to predict the response to various treatments.

One example of an initiative encompassing the vision of the Virtual Physiological Human is @neurIST [5], a large European project with the aim of improving rupture-risk assessment for cerebral aneurysms. Since the interventional procedures currently used to treat aneurysms are not in themselves without risk, it might be beneficial to simply monitor the aneurysm over time, without treatment. @neurIST will gather a large body of patient data and use simulated flow fields in order to analyse the stresses placed on the aneurysm wall, in order to more effectively assess risk of rupture for individual aneurysms.

A further example is the Complex Automata Simulation Technique project (COAST) [6], which is developing a multi-scale, multi-science framework to be used for modelling complex systems. The test case being employed to demonstrate this framework is in-stent restenosis. This is a significant complication of the treatment of coronary artery disease, whereby after placement of the stent, tissues within the vessel wall grow and may re-occlude the lumen and restrict blood flow to the heart muscle.

The popularity of developing computer models of physiological processes is no doubt increased because of such projects and each development contributes to the unveiling of the complexity of the human body.

The work described in this thesis could be developed further and integrated into projects such as these. The topic of interest is thrombosis and, in essence, computer models of thrombotic processes have been developed with a variety of levels of complexity.

1.2 Clinical Pathologies

Human whole blood consists predominantly of plasma (55% by volume) with a suspension of formed elements, comprised of erythrocytes (45%), leucocytes and platelets (<1%) [7]. Erythrocytes are biconcave in shape with a diameter of $7.5-8.5\mu m$ [8]. There are between 4,000 and 11,000 leucocytes per cubic millimetre of blood [7] and between 180,000 and 350,000 platelets [9]. Homeostatic mechanisms act constantly to maintain the normal circulation of blood within the body, ensuring the efficient delivery of oxygen to all cells [7]. However, complications can arise, causing the conversion of fluid blood to a solid mass, known colloquially as a blood clot or, more correctly, as thrombus. Formation of thrombus within a blood vessel can potentially have fatal consequences. The thrombus may occlude the vessel or dislodge (embolise) to lodge elsewhere in the circulation. Emboli occluding the coronary arteries can result in myocardial infarction. Those lodging in the brain may cause ischaemic stroke [10].

A common vascular disease is atherosclerosis. This pathology, which is one focus of the current work, leads to the formation of plaques, consisting of fat and fibrous tissue [7] within the artery walls. Rupture of the plaque exposes highly thrombogenic material. Clinically, of secondary concern are the flow-related effects of the physical obstacles presented by plaques, which project into the lumen of the vessel and provide ideal conditions for the formation of thrombus. Berger and Jou [11] present a detailed review of flow in stenotic vessels where the effects of important factors, such as flow pulsatility, Reynolds number and vessel geometry are described. Over 17 million people worldwide are estimated to have died of cardiovascular disease in 2005 [12] and this figure is expected to rise to 20 million by the year 2020 [13]. However, 80% of heart attacks and strokes are preventable [12], the major risk factors being physical inactivity and obesity [8]. Figure 1.1 shows an angiogram of a stenosed coronary artery.

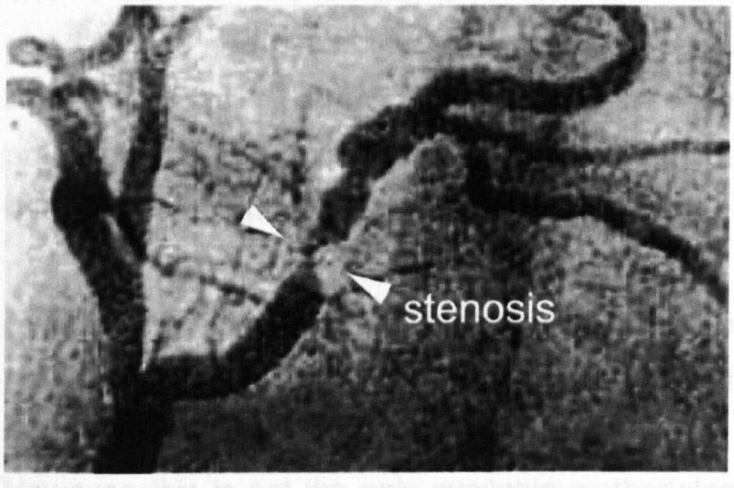

Figure 1.1: Angiographic image of stenosed coronary artery. Diameter of parent vessel is approximately 3mm. Image courtesy of Dr Julian Gunn.

The second pathology of interest is deep vein thrombosis (DVT) whereby thrombus forms in the deep veins of the legs due to prolonged immobility. The dangers of DVT are similar to those described above in that the thrombus can dislodge and occlude an artery. In the case of DVT, this commonly occurs in the lungs, leading to pulmonary embolism. DVT has recently received significant publicity because of its increased incidence in passengers on long-haul flights, which have become more popular as the costs have decreased and the availability increased. However, DVT is also common in patients following surgery.

1.3 Modelling Thrombosis

The changes that take place as blood is transformed from fluid to solid are not fully understood. However, it is certain that the location and magnitude of thrombosis are governed by factors such as the geometry of the vessel and the flow field. The understanding of the interrelationship between these factors can be aided by computer models which, given appropriate boundary conditions, can solve the flow field within a given geometry. This geometry may be idealised or a more accurate representation, taken from patient scans. Steinman presents an excellent review of this type of work and considers the imaging modalities, the accuracy and methods used [14]. The flow of blood in arteries, even without consideration of the mechanisms by which blood clots, is itself a highly complex subject. The review article by Ku [15] outlines the important considerations, which in the current work will be largely simplified. The focus is on the clotting processes and features such as pulsatility, wall elasticity and non-Newtonian[1] effects are not considered. These simplifications aid understanding of the clotting processes since the flow field is more predictable, but such effects can be included in future in order to examine their effect on the thrombotic deposition.

Established methods of computational fluid dynamics solve the incompressible Navier-Stokes equations in order to obtain descriptors of the flow field, such as the velocity distribution and derived quantities such as the shear stress. However, this is not the only available methodology. A competitive alternative is the lattice Boltzmann method, which was first presented in 1988 [17]. Instead of directly solving the Navier-Stokes equations, this method considers a discretised form of the Boltzmann equation in order to describe the evolution of particle distributions confined to a lattice with discrete velocities. The details of this are described in Chapter 2. In terms of the merits of the different methodologies, these are largely problem specific, but for the current project, the lattice Boltzmann method has certain advantages. The explicit nature of the code and the simplicity of its implementation and boundary conditions enable

[1] For the size of vessels used in this project (8mm) the non-Newtonian effects are negligible [15, 16].

the geometry of the domain to be altered during the simulation, without the need for remeshing. In this respect, blood clots can be represented as solid nodes, which will then directly affect the flow field and encourage or prevent further deposition. Solidification models have previously been used in lattice Boltzmann modelling to represent coral growth [18-20] and snow deposition [21].

Validation is of utmost importance to numerical models. It is often difficult to perform experiments with blood because of issues associated with safety, reproducibility and cost. A recent PhD project in this department [22] involved experiments using hypercoagulable milk; a well-validated blood analogue[1]. Since the chemistry of milk clotting is far less complex than that of blood, a set of simple models could be devised which provide a foundation for the subsequent development of more detailed thrombosis models. Despite its simplicity, the milk clotting model does appropriately represent the 'hydrodynamic' parts of the clotting process, and agreement between the experimental and numerical results for milk clotting gives confidence in the methodology adopted.

1.4 Project Description

The aim of this project is to develop clotting models using the lattice Boltzmann method.

In developing the clotting models, this project aims to describe a lattice Boltzmann framework for the simulation of thrombosis, encompassing features such as the activation of platelets and clotting factors in specific pathologies. The examples used are atherosclerotic plaques and damaged vessel walls, which can initiate and/or favour the growth of blood clots. DVT is considered by modelling the hypoxic damage of the valve endothelium and subsequent thrombosis.

---

[1] Further details can be found in Chapter 5.

This work aims to form the foundation on which more detailed models can be built, incorporating the existing work and expanding the complexity as desired.

Finally, this project also aims to evaluate the suitability of the lattice Boltzmann method for modelling such processes and to highlight the limits and difficulties involved.

Chapter Two: Lattice Boltzmann Simulations

2.1 The Lattice Boltzmann Method

The lattice Boltzmann method evolved from the theory of lattice gases in the late 1980s. Lattice gas methods are represented on the microscopic level whereas lattice Boltzmann methods are represented on a mesoscopic scale, the advantages of which will be highlighted. The aim of this section is to briefly describe the evolution from lattice gas methods to lattice Boltzmann methods. Details of the mathematics will be omitted and can be found in the cited literature. It must be emphasised that in the context of this project, the lattice Boltzmann method was simply used as a tool for the simulation of flow and thrombosis, and hence it is only appropriate to present an overview of the development and theory.

The lattice gas method for solving fluid flows was introduced in 1986 by Frisch *et al.* [23] and Wolfram [24]. It involves representing discrete particles on a grid or lattice. The evolution of the lattice involves a streaming process and a collision process at each discrete time step. First, the particles are propagated to the neighbouring lattice sites depending on the discrete velocities. Following this, the particles collide in order to define their new momentum and both mass and momentum are conserved locally. A schematic of this method is shown in figure 2.1. An exclusion principle permits only one of each of the particle velocities to reside on each lattice point at each time step.

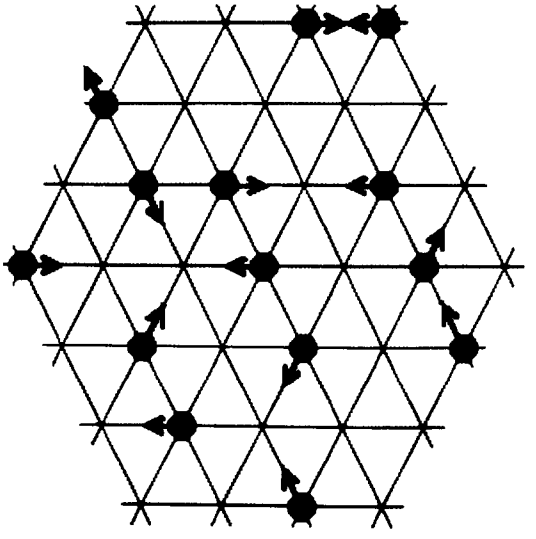

Figure 2.1: Representation of particles moving through a lattice and colliding as in the lattice gas method. Image taken from [25].

Certain disadvantages of this method were soon recognised; statistical noise, lack of Galilean invariance, high viscosity (therefore upper bound on Reynolds numbers) and an unphysical equation of state (depending upon the velocity) [26-29]. Succi [28] provides further details on these issues.

Shortly after, the lattice Boltzmann method emerged [17, 30, 31] which circumvents these issues if the collision operator is chosen appropriately [32, 33]. The lattice Boltzmann equation can be derived either by starting with the equations of the lattice gas method and performing a Chapman-Enskog expansion [28, 34] or by discretising the Boltzmann equation itself [35, 36]. Instead of tracking the motion of individual particles, this method examines the evolution of particle distributions as governed by the lattice Boltzmann equation (2.1).

$$f_i(\vec{x} + \Delta t\vec{c}_i, t + \Delta t) = f_i(\vec{x}, t) + \Omega_i \qquad \textbf{2.1}$$

f_i is the *distribution* of particles travelling with a discrete velocity $\vec{c}_i$ where i represents the number of discrete velocities and Ω_i is the collision operator.

In this project, the collision operator is represented by a Bhatnagar Gross Krook (BGK) operator [32] as in equation 2.2.

$$\Omega_i = \omega(f_i^{eq}(\vec{x}, t) - f_i(\vec{x}, t)) \qquad \textbf{2.2}$$

ω is the relaxation parameter and f_i^{eq} is the equilibrium distribution function which can be calculated from the macroscopic values of density, ρ and velocity, $\vec{u}$ as given in equation 2.3.

$$f_i^{eq}(\rho, \vec{u}) = t_p \rho \left(1 + \frac{\vec{c}_i \cdot \vec{u}}{c_s^2} + \frac{(\vec{c}_i \cdot \vec{u})^2}{2c_s^4} - \frac{\vec{u} \cdot \vec{u}}{2c_s^2}\right) \qquad \textbf{2.3}$$

The speed of sound, c_s and the shear viscosity, ν are given by equations 2.4 and 2.5 respectively [32] and the distributions are weighted according to the

lattice in use (represented by t_p, where p is the square modulus of the particle velocity).

$$c_s = \frac{1}{\sqrt{3}} \qquad \textbf{2.4}$$

$$\nu = \frac{1}{6}\left(\frac{2}{\omega} - 1\right) \qquad \textbf{2.5}$$

The evolution of the distributions is modelled using the lattice Boltzmann equation (2.1), the BGK collision operator (2.2) and the local macroscopic density and velocity values as given by equations 2.6 and 2.7.

$$\rho(\vec{x},t) = \sum_i f_i(\vec{x},t) \qquad \textbf{2.6}$$

$$\vec{u}(\vec{x},t) = \frac{\sum_i f_i(\vec{x},t)\vec{c}_i}{\rho(\vec{x},t)} \qquad \textbf{2.7}$$

The macroscopic values are computed at every lattice point at every time step and inserted in equation 2.3 to compute the equilibrium distributions and hence the new distributions. This follows the propagation and collision process described for the lattice gas method and the collision process involves relaxation to the local equilibrium distribution. This scheme is of second order accuracy in time and space [32]. Figure 2.2 shows a schematic of the algorithm used in computing fluid transport with this method, adapted from the review article by Nourgaliev *et al.* [37].

The lattice Boltzmann equation has been shown to satisfy the incompressible Navier-Stokes equations under conditions of low Mach and Knudsen numbers[1] [27, 32, 38-41].

The compressibility error is of the order of the square of the Mach number [40]. In fact, due to the equation of state (eqn. 2.8), in order to obtain a pressure gradient to drive the flow, an associated density gradient must exist along the length of the simulation domain. The scheme is therefore said to be 'weakly compressible'[2].

---

[1] Mach number, $M = u/c_s$, Knudsen number, $K_n = l_{mfp}/l_M$, where l_{mfp} is the mean free path and l_M is the shortest scale at which macroscopic variations can be appreciated [28].

[2] More advanced methods can avoid this "compressibility error", for example [42].

$$P = \rho c_s^2 \qquad \textbf{2.8}$$

With this method, a simplified 'computer fluid' is represented, which on average, behaves accordingly to satisfy the Navier-Stokes equations. The micro-dynamics of the system are represented by distributions and the knowledge of the individual particle trajectories is replaced by distributions. Further details of the lattice Boltzmann method and mathematical details of its derivation can be found in the literature [27-29, 34].

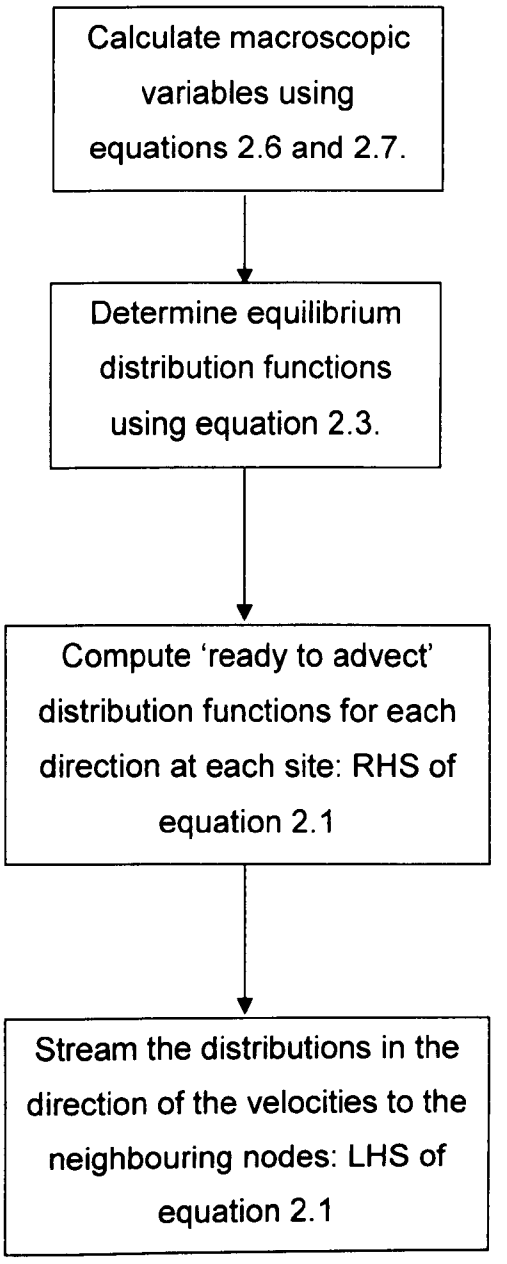

Figure 2.2: Stream and collide algorithm used by the lattice Boltzmann method.

2.2 Advantages of the Lattice Boltzmann Method

There are several advantages of using the lattice Boltzmann method, some of which favour its use over the more traditional CFD methods that directly solve the Navier-Stokes equations. The aim here is not to present a review of the exhaustive number of applications of the lattice Boltzmann method; these can be found in review articles [27, 34, 37]. Rather, the commonly reported advantages of this method are presented.

Because the scheme is explicit and local in space, it is highly suited to both vector and parallel computing [27, 34]. The lattice Boltzmann method is often described as being advantageous in the simulation of flows in complex geometries [34]. This is based on the ease at which geometries can be created, simply by defining occupied lattice points. However, such geometries can often only be captured with sufficient resolution by using highly irregular meshes [43]. Boundary conditions can be easily implemented, which supports the argument that this method is advantageous for flows in complex geometries [34].

It has been reported that multiphase and multicomponent flows can be more easily solved using the lattice Boltzmann method due to the tracking of the boundaries between fluids of different phase or components [33, 34, 37]. This also applies to the simulation of complex and moving boundaries in the simulation of particulate suspensions [44, 45].

The momentum flux tensor is tracked during simulations which allows for the more simple derivation of the stress tensor[1], which proves useful in turbulence modelling [43].

In 2003, Nourgaliev *et al.* [37] presented a critical review in response to "*unnecessary confusion*" in the growing body of lattice Boltzmann literature. This was aimed at "*eliminating further misunderstandings and misusage (sic) of the method*". This review praises the method for its simplicity in programming,

[1] The details of this are given in Chapter 5 along with appropriate references.

but claims that it cannot match the requirements on accuracy and stability typical of advanced CFD codes.

In his book of 2001, Succi [28] provided a clear summary defining four classes for applications; "*don't use*", "*can use*", "*should use*" and "*must use*". In the "*don't use*" class sit simulations of strongly compressible flows and those with substantial heat transfer effects. The "*can use*" class relates to the preference of the user and the ease of implementation. An example given is turbulent flows in simple geometries. The "*should use*" class encompasses applications such as multiphase flows in grossly irregular geometries due to the ease of creating the geometry and handling the boundary conditions. The final class, "*must use*", was at the time, said to be "*dilute*". The only possible application was that of suspended particles; however the introduction of more complex physics or massively parallel computing options could lead to the promotion of applications from the aforementioned, lower classes.

Several comparisons have been made between simulations performed using the discretised Navier-Stokes equations and the lattice Boltzmann method. Publications are aimed at comparing the accuracy of the results of both methods [46-50], some of which compare the computational efficiency [48-50]. In conclusion, these results show that the lattice Boltzmann method is accurate when compared to the results of alternative solvers and on a comparable level in terms of performance. Hence it was concluded that the choice of solver should be made based on the problem specifics.

Lockard *et al.* described the results obtained with the commercial lattice Boltzmann code PowerFLOW as "*disappointing*" in comparison with those obtained using a conventional CFD code [51]. Turbulent aerodynamic simulations were performed and the discrepancies between the results obtained with both methods were attributed to the insufficient grid resolution near the surface of the airfoil. This was restricted by the computational limitations and the imposed regular grid.

A recent comparison of methods was provided in 2006 by Geller *et al.* [52]. Laminar 2D flows were simulated in complex geometries with lattice Boltzmann

methods and the results were compared to those using finite volume and finite element solvers of the Navier-Stokes equations. The lattice Boltzmann code contains several extensions; local grid refinement, second order boundary conditions and multiple relaxation time models, whilst using a sparse, indirect addressing approach computing the distributions only for the fluid nodes. In the case of complex geometries, where a significant proportion of the domain is occupied by solid obstacles, a direct increase in the performance results[1]. The conclusions of this work are that the results of the lattice Boltzmann method were of comparable accuracy to the alternative methods, and, in the case of the transient simulations, were obtained at lower computational expense (CPU time). For simulations performed with a small but finite Mach number, the advantage of this method was "*significant*". However, the lattice Boltzmann computations of steady flow were slower.

2.3 Medical Applications of the Lattice Boltzmann Method

Interest in using the lattice Boltzmann method for simulation of physiological behaviour is constantly increasing. Over the duration of this project, the number of publications has more than tripled[2]. The following review discusses this work.

The PhD thesis of Artoli [53] investigates the suitability of the lattice Boltzmann method for simulating haemodynamics. This detailed body of work explored issues such as accuracy and performance of the method, particularly for haemodynamic features such as pulsatility. Artoli demonstrated that patient specific geometries could be obtained from magnetic resonance angiogram data and used in the simulations. The work of this thesis was presented in supporting publications [54, 55].

The group in Amsterdam have also been active in proposing and developing an environment which connects the patient scan to diagnosis through a path

---

[1] This technique is incorporated into the solver used in this project as will be discussed in later sections.

[2] Based on the number of publications known to the author.

involving simulation of the flow field with the lattice Boltzmann method [56]. This includes features such as image segmentation, mesh generation and interactive tools allowing for appropriate regions of the geometry to be selected and adapted. Pulsatile flow simulations in 3D physiological geometries can then be performed on parallel computers [57].

A significant proportion of work in Geneva has focused on the flow patterns in 2D models of aneurysms and the effects of stents [58-60]. Stents are commonly used in the treatment of aneurysms to reduce the flow and promote thrombosis. This ultimately reduces the pressure inside the aneurysm thus preventing its rupture. More recently, this group have focused their efforts upon modelling thrombotic processes within the aneurysm [61, 62]. The non-Newtonian properties of blood have been incorporated [61] and clotting is modelled via the aggregation of red blood cells, the concentration of which is treated as a passive scalar, in regions of low shear stress. The results of this study demonstrate that clotting occurs when the stent is in place because of the reduced wall shear stresses.

The work performed at Sheffield Hallam University is very different from that of the previous two groups in that blood flow is considered on a mesoscale [63, 64]. On this scale, the motion of individual blood cells is important and they cannot be treated as a continuum. Blood is modelled as multiple immiscible fluids where the individual particles are deformable, interacting drops. The authors claim that the lattice Boltzmann method has an advantage over the more traditional methods and this is in agreement with the discussions presented in section 2.2. The method was presented in the first publication [63] and some validation was presented in a subsequent paper [64]. Of interest are the simulation results on the website which show animations of the results obtained in these two publications [65].

Simulation of flows through heart valves was first performed in 1998 by Krafczyk *et al.* [66] using fixed valve leaflets at different opening angles in 3D. This work was developed in 2001 by Krafczyk *et al.* [67] where simulations were performed with moving leaflets in 2D.

In 2002, Fang *et al.* [68] described a model which could simulate distensible blood vessels. Boundary conditions were developed for moving and elastic walls and the results of steady flow simulations were of very high accuracy whereas those with pulsatile flow were "*comparable with those of the aortic flows observed experimentally*". Researchers from the same group later simulated particle suspensions in a 2D stenotic artery [69]. The diameter of the parent vessel was only $68\mu m$ which is one order of magnitude larger than the size of the blood cells.

Boyd *et al.* [70] investigated the difference between the bounce-back boundary condition and an extrapolation boundary condition in the context of arterial flows. The geometry considered was a curved stenosis in the carotid artery. Results indicated that the extrapolation boundary condition gave greater boundary resolution and the authors concluded that such boundary conditions are necessary in such complex geometries. Subsequent work by Boyd *et al.* [71] analysed the velocity and shear stresses in the region of a growing plaque. This study demonstrated that regions of low velocity and shear stress persisted during the growth under pulsatile conditions suggesting that the growth of the plaque maintains flow conditions that will encourage further growth.

The mesoscale was investigated in work by Migliorini *et al.* [72] who modelled leukocyte rolling and adhesion and the effect of red blood cells, by simulating suspensions of rigid particles. This work was advanced by Sun *et al.* [73] and Sun and Munn [74].

In 2005, Beronov and Durst [75] demonstrated the use of the lattice Boltzmann method for simulation of the flow field within physiological geometries obtained from clinical data. This supports the earlier work of Artoli [53]. In 2006, Chen *et al.* [76] also adopted this approach. Coronary artery geometries were obtained from intracoronary ultrasound angiography. The resolution of the lattice was increased in the near wall regions and the overall wall shear stress distributions were seen to be very similar to those produced with a conventional CFD code.

2.4 Implementation

The lattice Boltzmann BGK method described in section 2.1 is used for solving the flow in the simulations of this project. The specific lattice used is the D3Q19 lattice. This terminology [32] is commonly used where the number following the letter D represents the number of dimensions and that following the letter Q is the number of discrete velocities. A schematic of this lattice is shown in figure 2.3.

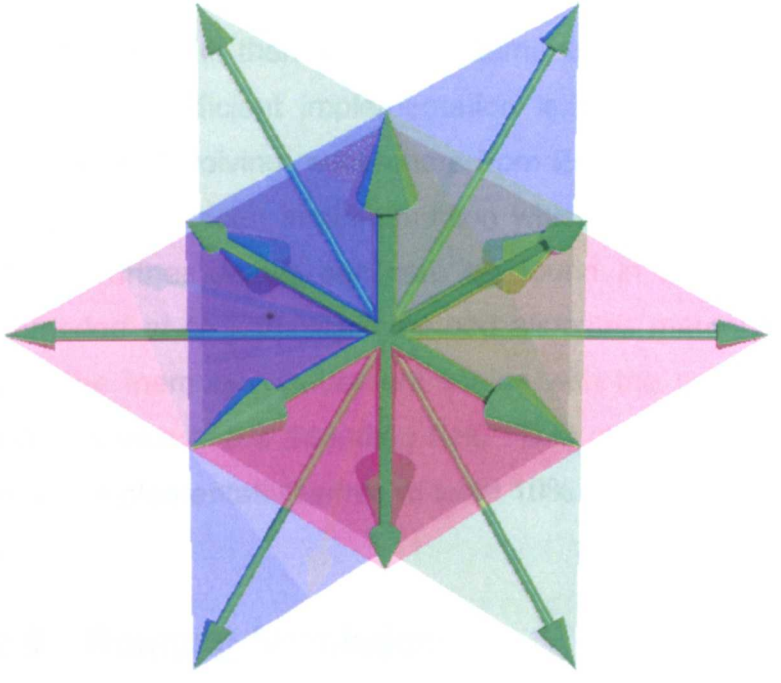

Figure 2.3: D3Q19 lattice showing velocities and directions related to the central lattice point. Image taken from [77]. One of the velocities is zero hence no arrow is shown.

For this lattice, the weights shown in equation 2.3 are $t_0 = 1/3$, $t_1 = 1/18$ and $t_2 = 1/36$ relating to the zero velocity position, the axial directions and the diagonal directions respectively. The axial distance between lattice points is 1 and the components of the discrete velocities, $\vec{c}_i$ in equations 2.1 and 2.3 are of magnitude 0 or 1. This lattice is used for both the 2 and 3 dimensional simulations since in 2 dimensions periodic wall boundary conditions are used in the 3rd dimension.

The equations and method described in section 2.1 are implemented in FORTRAN90 following the algorithm shown in figure 2.2. Geometry is created using an input file which stores a list of all the occupied lattice points. Such an input file can be created by hand for simple, small geometries, or with software such as Matlab for the larger geometries. As described in the previous section, medical scan data can also be used to create patient specific geometries. This was performed as part of this project, but this was predominantly a learning exercise.

In the duration of this project two codes have been used. The first is known as BEST[1]. This implementation allocates memory for the occupied lattice sites and then masks them with 'if' statements in the proceeding calculations. The later, more efficient implementation is part of an international development consortium involving researchers from Europe and Japan. This code is based on a sparse vector implementation which was first described by Schulz *et al.* [78]. Further details can also be found in a publication of this project by Bernsdorf *et al.* [79]. This method allocates memory only for the fluid nodes, thus the memory requirement scales with the number of fluid nodes and not with the size of the bounding box. This method is more efficient than the full matrix implementation when at least 10% of the geometry is occupied [79].

2.5 Running Simulations

Several platforms were used for running simulations in this project. The NEC SX-6i vector machine was used primarily. This is a single-CPU vector processor machine with a peak performance of 8 GFLOPS. For the final 6 months of the project, access to the SX-8 machine was provided. This has 4 CPUs, each with a peak performance of 16 GFLOPS. This machine allows for parallel computing, but the MPI version of the code with all the extensions required to simulate clotting was not available during this project. Both of these machines are located in C&C Research Laboratories, NEC Europe Ltd. and more information can be found on the web [80].

---

[1] The main authors of this code are Joerg Bernsdorf, NEC Europe Ltd. and Thomas Zeiser, Friedrich-Alexander-Universität Erlangen-Nürnberg.

2.6 Boundary Conditions

2.6.1 Wall boundary conditions

In the lattice Boltzmann method, boundary conditions are required to obtain the 'missing' velocity distributions along the boundaries. Considering the wall boundaries, distributions to be propagated from within the fluid are known, but those from outside of the simulation domain are clearly not. A no-slip condition is required along the walls of the domain, which will result in zero velocity. Succi [28] refers to two types of no-slip boundary conditions; on-grid and mid-grid, which are named according to where the position of zero-velocity lies. The on-grid method involves reversing all the populations sitting on a boundary node. The mid-grid method however involves reflecting the distributions about a mid point between the boundary node and the fluid node as illustrated in figure 2.4.

The on-grid method described by Succi [28] is of first order accuracy, whereas the mid-grid method is of second order, but this can be disputed since there are many ways of setting the distributions resulting in a conflict of definitions. It is interesting to recognise that both the above methods are described as being 'bounce-back' boundary conditions and the original idea behind this was that incoming distributions are reflected on the boundary nodes at the next timestep [81], however, this cannot be the case for the methods described above. Many variations of the bounce-back boundary condition exist depending upon the distributions and the timesteps at which they are used and so care must be taken.

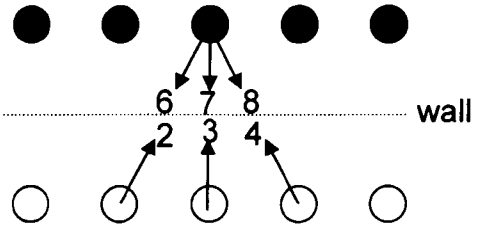

Figure 2.4: Boundary nodes (filled circles) and fluid nodes (open circles) and distribution exchanges for no-slip condition for the mid-grid method. Distributions 6, 7, 8 on the boundary are set to equal those of 2, 3 and 4 of the fluid nodes.

The method used in BEST is the mid-grid method, thus the missing distributions on the boundaries are set to equal their mirror images from the adjacent fluid nodes. This step is performed before the propagation and relaxation steps.

In the new sparse code, the boundary conditions are computed in a pre-processing step. The distributions of the fluid nodes adjacent to the boundary nodes simply change direction, but, this occurs during the propagation step where the propagation *direction* is altered. This is equivalent to the mid-grid method as described below. An adjacency-vector is used to store the neighbouring link that a distribution will travel along in the propagation step. In the pre-processor, distributions from fluid nodes that would have been sent to the corresponding link in a solid node have their destination changed so that the new link is on the same fluid node but pointing in the opposite direction. Since the propagation step occurs after the relaxation step, it is the *relaxed* distribution that is mirrored at the next time step. Figure 2.5 shows an illustration of this process.

The location of the point of zero velocity is the position at which the momentum cancels and, in this simple example, can be thought of as the position where the arrows instantaneously change direction. The distribution velocities are such that in one timestep, the distribution can travel to the neighbouring node.

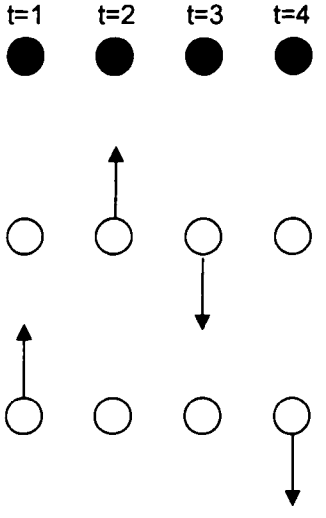

Figure 2.5: Illustration of boundary condition used in the sparse lattice Boltzmann code. The arrows represent one of the velocity distributions and its time-dependent motion is shown. Boundary nodes are represented by filled circles and fluid nodes are represented by open circles.

The arrow in the second column of figure 2.5 (t=2) must exactly reflect somewhere to result in the change in momentum seen at the next timestep. This means that the distribution must travel both to this location and back again in one timestep, hence the position of zero velocity must be located exactly between the wall node and the fluid node. Slight deviances from this will occur because it is the relaxed distribution seen in the following timestep, but this is a good approximation, as will be illustrated later in this chapter.

Concerning the accuracy of the above two schemes, without performing a detailed study on the position of zero velocity, it is perhaps not possible to say. Bounce-back boundary conditions are typically said to be of first order accuracy [82], however, He *et al.* [82] demonstrated that the simple bounce-back condition whereby a particle colliding with the wall simply reverses its direction is of second order accuracy if the wall is assumed to be at the half-way point between the fluid and the boundary nodes. This was numerically demonstrated to be true for both a flat tube and a tube inclined at 45 degrees [83].

In 1995, Noble *et al.* [84] demonstrated that the bounce-back condition is inferior for modelling stationary walls. They concluded that the position of the wall is unknown and moves with a speed dependent on the relaxation parameter. Problems were seen to occur for values of $\omega < 1$. However, within the current project, it is the higher Reynolds numbers and hence higher values of ω that are required and in practice, the value is kept above 1.7.

More complex boundary conditions are available in the literature and can lead to second [84-87] and possibly third [88] order accuracy. Further investigation of such schemes was not possible within this project. However, the simple bounceback scheme has been favoured for its easy implementation [34, 82] and efficiency [83] and so is considered a good compromise, particularly in the case where improved accuracy is gained in simple geometries by assuming the wall to be at the half-way position.

2.6.2 Inlet boundary conditions

The inlet boundary condition used in both codes can be chosen to be either plug flow or parabolic flow in either 2 or 3 dimensions. The boundary condition to prescribe parabolic flow with a circular cross section was implemented as part of this project. The inlet velocity distribution is used to obtain the equilibrium distribution functions which are then set to equal the distribution functions for further propagation and collision. The density values used in the inlet column are equal to those at the following downstream position. This method will produce errors when the resolution is coarse and the achieved velocity profile will not be exactly equal to the theoretical profile. However, rescaling can be performed in order to obtain the desired velocity profile and hence Reynolds number, but this often is not necessary for the finer grids used in this project.

In order to obtain improved stability, the inlet velocity profile is ramped over a specified number of iterations which follows a sinusoidal variation between the initial values of zero and the final required values.

2.6.3 Outlet boundary conditions

The outlet boundary condition used in both codes is a constant density, hence a constant pressure. The distributions are set to equal the equilibrium distributions where the velocities are calculated as an average of the two values upstream of the outlet.

2.6.4 Initial conditions

The initial conditions used are to initialise the entire domain with zero velocity and constant density (equal to the constant value used for the outlet boundary condition). The initial distributions are set equal to the density divided by 19, since there are 19 directions in the lattice in use.

2.7 Simulation Parameters

A sufficient amount of information has been presented in this chapter on the lattice Boltzmann method and the details specific to the codes used in this project. It is now appropriate to discuss the issues relating to running simulations, namely choosing appropriate values of the free parameters in order to obtain the desired results.

The parameters in the lattice world are connected to those in the real world through the use of dimensionless parameters. The most commonly used dimensionless parameter is the Reynolds number, which indicates the magnitude of inertial forces relative to the viscous forces, as shown in equation 2.9 [89].

$$\mathrm{Re} = \frac{u_{av} D}{\nu} \qquad \textbf{2.9}$$

In equation 2.9, u_{av} is the average velocity in the axial direction, D is a typical length scale, which, in this project will be taken to be the diameter of the vessel and ν is the kinematic viscosity, defined in equation 2.10, where μ is the dynamic viscosity and ρ is the density of the fluid. Flows with low Reynolds numbers can be described as creeping, where inertial effects are negligible whereas flows of a very high Reynolds number can indicate turbulence.

$$\nu = \frac{\mu}{\rho} \qquad \textbf{2.10}$$

The Reynolds number of the simulation must first be known, along with the remaining parameters in real units, which depend upon the vessel geometry and fluid properties. The conversion to lattice units is made by choosing combinations of the velocity and viscosity based on the size of the grid.

The grid size must be chosen with care such that accuracy is obtained, but this must be balanced with the computational time, particularly in the case of a

regular grid as is used in this project. The minimum grid size should be chosen using a mesh refinement study as shown in Chapter 3 for the simulation of flow through a stenotic tube.

When the grid is chosen, the lattice distance in real units can easily be obtained, but it must be remembered that the position of zero velocity and hence the position of the real wall in the simulation is offset from the physical wall (location of the occupied lattice points used to represent the wall) by half a lattice unit, for the boundary conditions used in this project. This means that if there are, for example, 82 lattice points across the diameter of a tube, the total distance between the walls is 80 lattice units. If the real diameter of the tube is $8mm$ then the real distance between two lattice points, termed the lattice length scale is $L = 1 \times 10^{-4} m$. The dimensions of a lattice in this project are referred to as lx, ly and lz, where these values represent the number of lattice points in the x, y and z dimensions respectively. The flow is directed along the x direction.

The velocity and viscosity in lattice units must be chosen with regard to the constraints described previously in this chapter. The relaxation parameter, which determines the viscosity through equation 2.5 must be greater than 1 due to the associated error in the bounce back boundary condition, as described in section 2.6.1. Since a lower relaxation parameter produces lower Reynolds numbers, this limit is rarely met. In practice, for this project, the relaxation parameter, $\omega > 1.7$, in the majority of simulations. Regarding the upper limit of the relaxation parameter, this is not so clearly defined, but it has been discovered in this project (results not shown) that if the relaxation parameter is too high, the code will become unstable. However, this limiting value depends upon the other simulation parameters in use. The absolute limit of this value is 2, since equation 2.5 shows that negative viscosities would be produced with higher values.

The lattice velocity must be chosen such that the Mach number is low, as discussed in section 2.1. Values found in the literature are 0.15 [42] and 0.20 [52]. This results in values of the lattice velocity of either $u_{av} = 0.0866 LT^{-1}$ or

$u_{av} = 0.1155LT^{-1}$. In this project, unless otherwise stated, the limiting peak velocity[1] is $u_p = 0.05LT^{-1}$.

The lattice timescale can be obtained using the length scale and either the velocity or viscosity values in both real and lattice units. The following example illustrates this, where the length scale is $L = 1 \times 10^{-4} m$ as in the previous example and the lattice and real velocities are $u_{av} = 0.05LT^{-1}$ and $u_{av} = 0.1ms^{-1}$ respectively. A similar procedure is followed (using the real and lattice values of density) in order to obtain the mass in lattice units, M.

$u_{av} = 0.05LT^{-1} = 0.1ms^{-1}$ Equate the velocities

$0.05(1 \times 10^{-4} m)T^{-1} = 0.1ms^{-1}$ Substitute in the length scale

$5 \times 10^{-6} T^{-1} = 0.1s^{-1}$

$T = 5 \times 10^{-5} s$

If a simulation is being performed of an experiment of a known real time, the time step can be used in order to calculate the number of iterations to be performed, otherwise, the number of iterations is chosen to achieve convergence, as will be discussed in a later section of this chapter.

The above discussions not only indicate the limits on the parameters, but more importantly, how they are related to each other. If the length scale is chosen for a particular simulation, the time step cannot be chosen separately, rather the limits on the lattice velocity and viscosity must first be considered. This can often present difficulties if a large Reynolds number is required. This is discussed by Nourgaliev *et al.* [37] who state that often the only way of obtaining such values is by increasing the grid size in order to increase the lattice diameter. However, Hoekstra [90] claims that the relaxation parameter should be increased "*close to its limiting value*" in order to maintain a manageable computational mesh.

---

[1] The limiting values of lattice velocity and viscosity used in this project are sufficiently far from those in the literature and this is because of the advised values given by Joerg Bernsdorf, NEC Europe Ltd. at the start of the project.

Significant work has been performed on selecting simulation parameters for the lattice Boltzmann method and this involves optimising the accuracy and performance of the simulations in order to obtain a minimal simulation time. Artoli [53, 91, 92] provided detailed discussions on these issues which led to the work of Abrahamyan *et al.* in 2006 [93]. This study presents a method which involves specifying the required simulation error and execution time in order to determine the space and time discretisations for time harmonic flows. Such methods were not employed in this project and each simulation was treated separately based on the requirements. Issues such as accuracy and performance will be addressed in subsequent sections.

2.8 Assessing Convergence

This section relates to the time convergence of simulations, not the space convergence. Space convergence is described in Chapter 3 for the simulations of flow through stenosed vessels.

Convergence in time ensures that a sufficient number of iterations have been performed. The fluid is ramped at the inlet from an initial stationary state to that specified by the boundary condition. Firstly, a sufficient number of iterations must have been performed to propagate the resulting wave from the inlet to the outlet and secondly, stability of this wave must be ensured.

The first check of convergence involves analysing the average velocity, measured over the cross section at a specified x value. These results are written to an output file during the simulation and can be plotted against the iteration number as shown in figure 2.6.

In order to check the convergence, the method used was to analyse the mean relative magnitude of the oscillations about the mean of the average velocity. The mean of the average velocity and the associated oscillations are found over the final period. If this value is of order 1×10^{-3} or less, the number of iterations is deemed sufficient. In practice, this value was at least an order of magnitude smaller than this since automatic termination of the simulation was not possible.

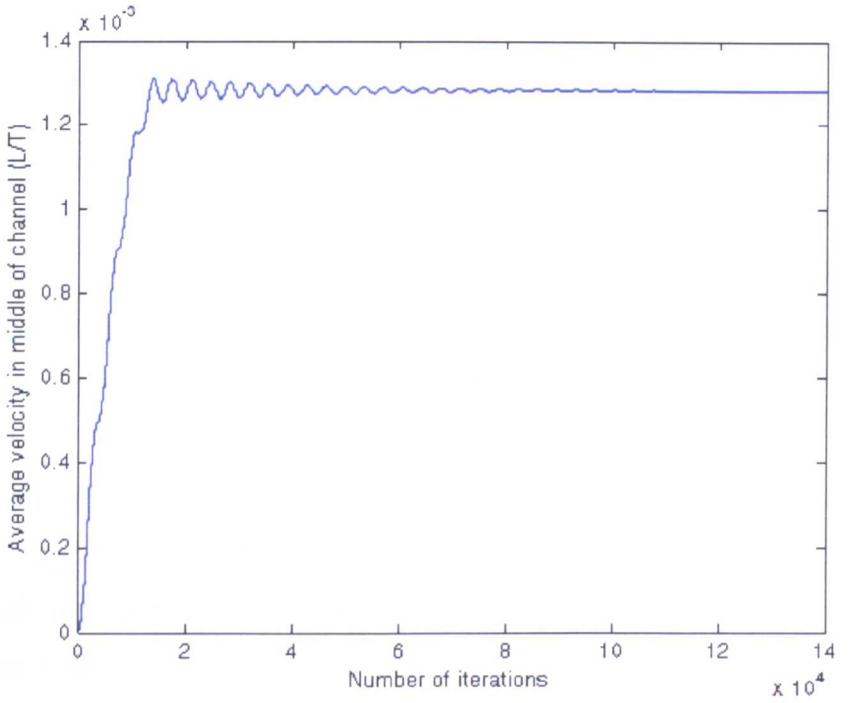

Figure 2.6: Variation in average velocity in the middle of a channel versus number of iterations. Ramping time is seen in first portion of graph.

In this project, studies have been performed which investigate the effects of iterating the simulation further. In the examples studied, no benefit was seen when iterating beyond those required to obtain convergence as described in this section.

The convergence is also examined by analysing the average velocity variation along the length of the domain at the final iteration, representing the compressibility error. For channel flow, a linear increase in the average velocity is observed which is attributable to the pressure drop observed in a channel and the Bernoulli relation. The inlet and outlet values are compared in order to obtain the magnitude of the increase relative to that at the inlet. The criterion used in this case is that the relative increase must be less than 1%.

2.9 Performance

The issue of performance will become more relevant when developments are made in the code, as will be described in the appropriate chapters. This section

identifies how the simulation time can be estimated from the performance of the code.

At the end of a simulation, a figure is reported representing the number of million lattice site updates per second ($MLUPS$) that have been performed. In the sparse code, the performance is independent of the geometry and is typically $26MLUPS$ for the fluid flow simulation on the SX-6i machine. This is almost doubled when the SX-8 is used and the sparse code provides further improvement depending on the geometry.

If the performance is known, the simulation time can be calculated from the grid size and number of iterations. One update corresponds to performing one iteration on a single lattice point. For example, with the above performance and a geometry of dimensions $lx = 1000$, $ly = 100$, $lz = 100$, performing 10,000 iterations would take approximately 64 minutes. The performance figure can obviously be used in the reverse direction to calculate the number of iterations that can be performed in a given time. Such matters are of extreme importance when running large simulations on multi-user platforms such as the SX machines at NEC.

2.10 2D Channel Flow

In order to obtain an appreciation of the magnitude of the errors present, some simple channel flow simulations were performed with a variety of different lattice sizes. The velocity profile in a 2D channel is given by equation 2.10, where r and R are the 2D versions of the radial position and the radius respectively, μ is the dynamic viscosity and $\frac{dp}{dx}$ is the pressure gradient in the channel.

$$u(r) = -\frac{R^2}{2\mu}\frac{dp}{dx}\left(1 - \frac{r^2}{R^2}\right) \qquad \textbf{2.10}$$

This can also be expressed in terms of the peak velocity, u_p as shown in equation 2.11.

$$u(r) = u_p\left(1 - \frac{r^2}{R^2}\right) \qquad \textbf{2.11}$$

In two dimensions, the peak and average velocities are related by equation 2.12.

$$u_p = \frac{3}{2}u_{av} \qquad \textbf{2.12}$$

Equations 2.11 and 2.12 are more meaningful than equation 2.10 in this project since it is the peak velocity that is specified in the simulations as the inlet boundary condition as opposed to a pressure gradient.

A set of simulations were performed which involved discretising the mesh whilst keeping the Reynolds number at a constant value of 10. As described in section 2.7, if the grid size is changed whilst the Reynolds number is constant, either the lattice velocity or viscosity must change. Simulations were performed first with a constant viscosity, then with a constant velocity. In each case the error in the pressure gradient was compared to the analytical value obtained from equations 2.10-2.12, using the simulated average velocity in the centre of the channel. The results can be seen in table 2.1. For the case of constant viscosity, $\omega = 1.8210$ (to 4 d.p.) was used and in the constant velocity simulations, $u_p = 1\times10^{-2}\,LT^{-1}$.

	$lx = 64, ly = 16$	$lx = 128, ly = 32$	$lx = 256, ly = 64$	$lx = 512, ly = 128$
Error in pressure gradient, % (ω)	6.5037×10^{-1}	1.4858×10^{-1}	4.8744×10^{-2}	2.8788×10^{-1}
Error in pressure gradient, % (u_p)	4.1303×10^{-1}	1.6386×10^{-1}	1.1744×10^{-1}	8.0822×10^{-2}

Table 2.1: Pressure gradient errors and their variation with discretisation via either constant velocity or viscosity, indicated by the brackets.

Overall, the results in table 2.1 indicate that the accuracy of the solution, determined by the pressure gradient increases as the mesh is refined. However, the slight increase in the finest grid for the simulation with constant viscosity has unknown origin. A more detailed investigation would use a larger number of lattices. The aim of this study is not to perform a formal grid convergence test but merely to demonstrate the processes outlined in section 2.5 appropriate to 2D channel flow and to obtain estimates of the errors involved in the simulations. As well as measuring the pressure gradient, the velocity profiles were analysed at various positions in the channel as was the centreline velocity variation along the length of the channel. These plots are shown in figures 2.7 and 2.8 for the different grids in the case of constant viscosity. Qualitatively, no difference was seen between these plots and those with constant velocity.

Figure 2.7 shows the obvious result that the parabolas become smoother and better defined with a fine grid. Discrepancies exist in the outlet region due to the effects of the boundary and this must be remembered for future simulations.

The trends in figure 2.8 show that in the middle region of the channel, the peak velocity applied at the inlet is approximately obtained. However, near the inlet, a region of lower velocity exists, the relative magnitude of which decreases as the grid is refined. The outlet region also suffers and the region of stability in between these regions does not appear to alter with the grid size.

In order to investigate the position of the wall, the points of zero velocity were obtained by extrapolation of the values of the inner two fluid points for each wall. For this study, the grid size chosen had dimensions 320×82 and 3 different values of the relaxation parameter were used, both above and below the normal limit of $\omega = 1.7$. The Reynolds number was approximately 30. Table 2.2 shows the results obtained. These appear to suggest that values of $\omega = 1.5$ can be used with acceptable errors in the channel width. This is in agreement with the results of Nobel *et al.* [84] who found that the relaxation parameter produced moving walls for values below 1. As described previously, in this project, such low values of the relaxation parameter will not be used since it is

the higher Reynolds number regime that is of interest. It is, however, reassuring to observe the magnitude of the errors in this particular situation.

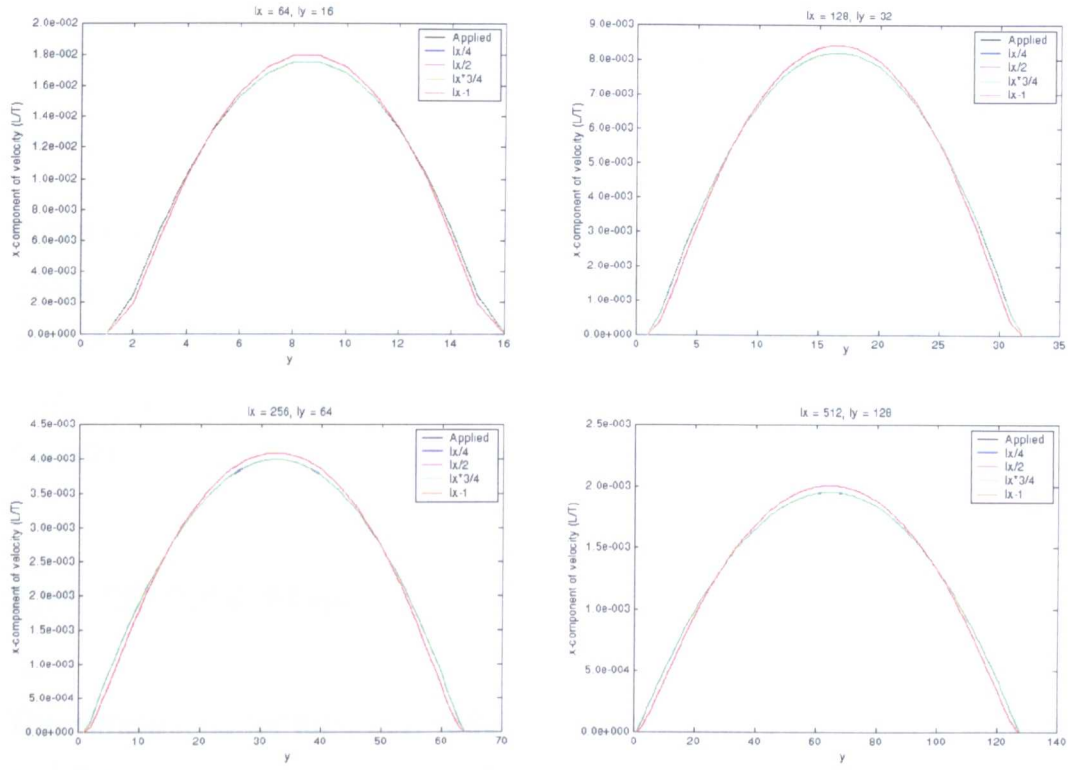

Figure 2.7: Variation in velocity profiles for the simulations with constant viscosity with various grid sizes.

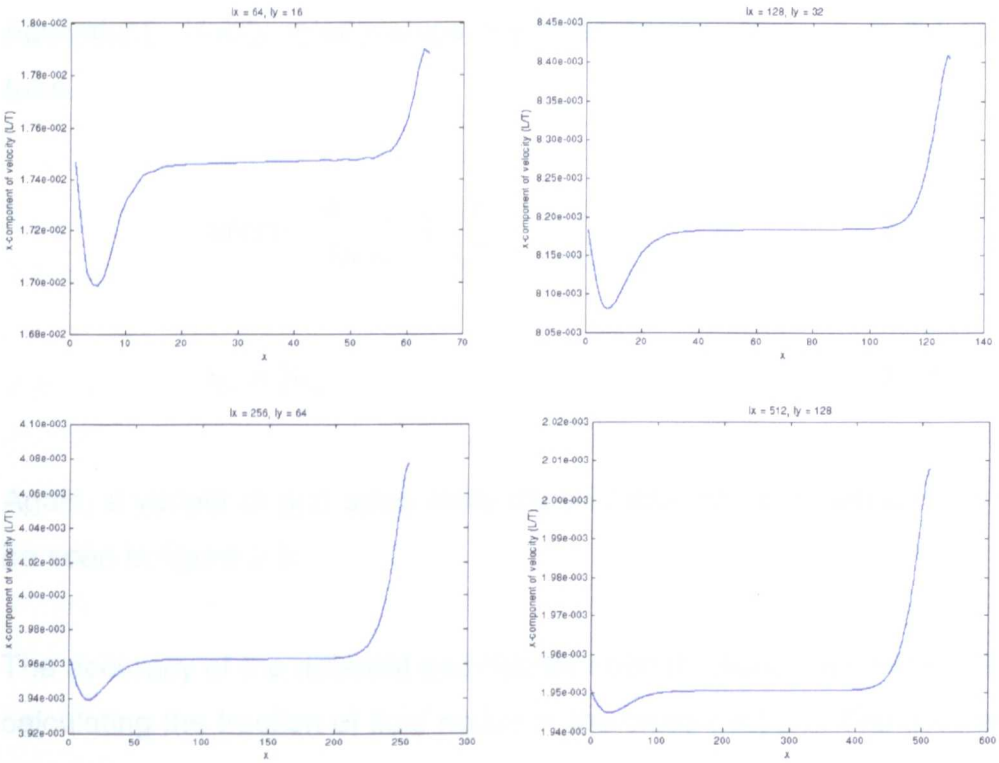

Figure 2.8: Variation in centreline velocity for the simulations with constant viscosity with various grid sizes.

Omega	Wall 1	Wall 2	Width of channel	Error in width of channel (%)
1.50	1.493102	81.506898	80.013796	0.017
1.85	1.493555	81.506445	80.012890	0.016
1.99	1.494533	81.505467	80.010934	0.014

Table 2.2: Wall positions for various values of the relaxation parameter.

Further investigations (results not shown) indicated that no significant difference exists in the measured channel width between simulations performed with decreasing relaxation parameter through either a change in the velocity or a change in the Reynolds number. The results of table 2.2 are likely to vary as the grid is changed, but such investigations were not performed.

2.11 3D Tube Flow

The simulations for tube flow require more attention than those of channel flow and there are two main reasons for this; firstly, the representation of a cylinder using voxels is likely to affect the flow simulations and secondly, it is the 3D simulations that are of interest in the stenotic flow studies in Chapter 3. The equivalent velocity relationships are given below. Here R is the radius of the tube.

$$u(r) = -\frac{R^2}{4\mu}\frac{dp}{dz}\left(1-\frac{r^2}{R^2}\right) \qquad \textbf{2.13}$$

$$u_p = 2u_{av} \qquad \textbf{2.14}$$

Again, a variety of grid sizes were chosen and the cross-sections of these can be seen in figure 2.9.

The accuracy of the different geometries seen in figure 2.9 can be compared by calculating the fraction of fluid nodes in the cross section. The theoretical value of this fraction for a perfect circle is $\frac{\pi}{4}$ and the errors in the fraction compared to

this value are shown in table 2.3. Simulations were performed at a Reynolds number of 100 with a constant relaxation parameter of $\omega = 1.95$ for the different grids. The errors in the pressure gradients are also shown in table 2.3, where the simulated pressure gradient was calculated over the central half of the model length. These simulations had a constant length of $400L$ which essentially means that tubes of different *real* lengths are being modelled. However, the effect of this dimension is assumed to be negligible in comparison to that of the discretisation in the cross section, particularly when figure 2.9 is considered.

The accuracy of the flow simulation compared to the analytical solution for Poiseuille flow in a cylinder will be most dependent upon the accuracy of representing a cylinder geometrically, which is ultimately dependent upon the number of lattice points in the cross-section.

Few conclusions can be drawn from the results shown in table 2.3. The behaviour could be attributed to the fact that the geometry of the coarse grid is heavily affected as seen in figure 2.9 leading to unpredictable behaviour which does not represent the expected flow field. The three coarsest grids are visibly poor and it may well be expected that their accuracy does not follow the expected trends.

The pressure gradient was measured and compared to the analytical value calculated from the simulated average velocity measured over a cross-section halfway along the length of the tube and equations 2.13 and 2.14.

It is appreciated that there are many criticisms concerning the results presented in this section, but the aim of this study was not to perform a formal grid conversion test from which to extract detailed results, instead, an estimate of the errors involved was required in the case where the geometry creation by voxels can produce errors. However, this exercise has highlighted some issues that must be considered when accurate results are required, as in the case of Chapter 3. Improvements in the implementation will of course be met if more accurate wall boundary conditions are used.

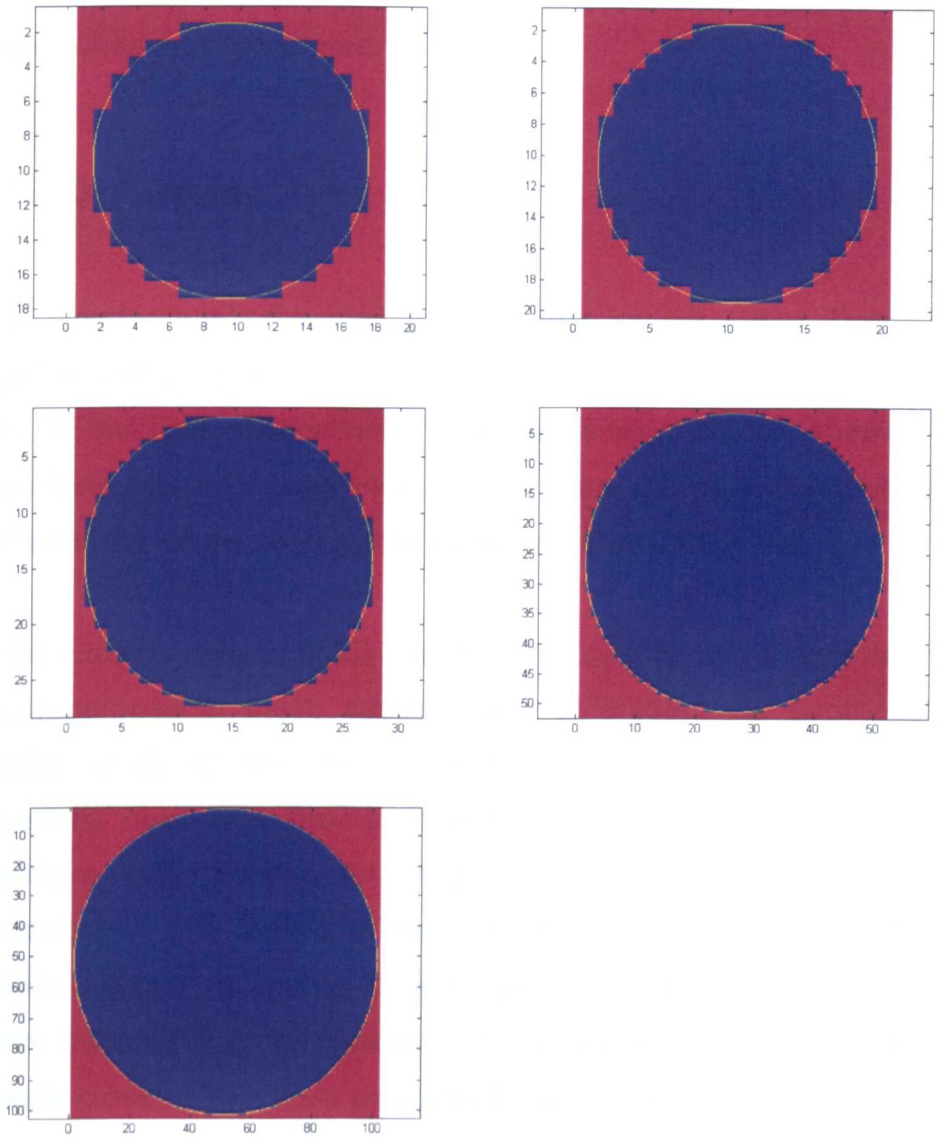

Figure 2.9: Cross sections of tube geometries. Left to right and top to bottom, lattice diameters: 16, 18, 26, 50, 100. Yellow line shows the analytic circular cross section.

ly	Error in fraction of fluid nodes (%)	Error in pressure gradient (%)
18	3.45	3.18
20	0.60	4.92
28	1.71	2.17
52	0.64	2.13
102	0.077	2.15

Table 2.3: Variation in error in fraction of fluid nodes and pressure gradient with different lattice sizes.

The conclusions concerning the velocity profiles in the previous section for channel flow also apply here. With a finer grid, the profiles more accurately

represent the analytic solutions. In this study, both axial and diagonal profiles were plotted and considered.

2.12 Discussion

This chapter has presented a description of the lattice Boltzmann method together with a review of the work of the major contributors to research in the field of medical applications. The remainder of this chapter focused on describing the techniques used in setting up and performing simulations. The details of the codes used in this project were also reviewed.

Some example results of 2D channel and 3D tube flow were presented and the major purpose of these sections was to present the appropriate analytical results, which will be used in the more detailed simulations to follow. The equations describing flow in 2 and 3 dimensions will be applicable in the upstream and downstream regions of the more complicated stenosis geometries. The results of these studies did not provide grid convergence results but used a variety of grid sizes in order to obtain an estimate of the errors involved and the accuracy of the geometry in the 3D case where the circular cross section must be created from voxels.

The results of this chapter do however lead to some important conclusions. A finer grid produces more accurate simulations of the velocity profile, but this requires more computational time due to the number of lattice points and the speed of convergence. For the simulations performed there appears to be no significant difference between the discretisations performed via either velocity or viscosity variation. With the values of relaxation parameter used, the walls lie within an acceptable range. The boundary regions can contain large errors and results must be taken sufficiently far from these problematic areas.

Tube and channel flow will not be considered further in this project, but for the stenotic flow studies, detailed flow parameters will be required for comparison with experiments and full grid convergence investigations are therefore performed.

Chapter Three: Flow through Stenoses

3.1 Literature Review

The presence of an atherosclerotic plaque in an artery can significantly affect the flow field therein. It can be shown [15, 94] how such arterial narrowing can lead to flow separation resulting from a decelerating flow and a diverging area distal to the plaque. Associated with separation are areas of recirculation and stagnation, which must be considered in detail as they will dictate the initial deposition patterns in the case of thrombosis. Raised fluid velocity through the stenosis leads to an increase in the wall shear stress, which can cause platelet activation. The flow field downstream of an occlusion will be dependent upon the size and shape of the constriction and the Reynolds number of the flow. Post-stenotic flow fields may encourage the progression of the plaque in regions of low or oscillatory shear stress [95, 96]. Turbulent flow fields can be detected non-invasively to assist diagnosis of localised atherosclerotic plaques [97, 98], which increases the need for a knowledge of the relationship between the plaque and the flow.

Many previous studies have focused on the flow effects of stenotic occlusions, both experimentally and numerically. Numerical simulations carry the advantage that additional physical parameters such as wall shear stress and residence time can be accurately derived; experimental estimates of wall shear stresses are difficult to obtain and only accurate to within 20-50% [15]. However, there are several reasons why discrepancies may arise between the results of experimental and numerical work, including limitations of the adopted numerical methods and specification of appropriate boundary conditions [99].

The review which follows presents the results of both *in vitro* experiments and numerical simulations of flow in stenosed vessels. The purpose of this is primarily to establish an understanding of the current progress in this subject and to portray the sensitivity and complexity of this topic. Comparisons with the results of the current study are not possible because of the difference in geometrical and fluid parameters chosen. However, comparisons will be made with experimental data produced in this department in a previous project by Smith [22]. In all literature reviewed, the Reynolds number is calculated using

the diameter and average velocity of the parent vessel. The percent stenosis is measured by area, unless otherwise stated.

Azuma and Fukushima [100] presented experimental results of flow in smooth stenotic vessels in 1976. Both axisymmetric and non-symmetric models were studied under conditions of steady and pulsatile flow with Reynolds numbers in the range 250-1500. For the steady flow experiments it was observed that, as the degree of axisymmetric occlusion increased, the critical Reynolds number, representing that at which laminar flow breaks down, decreased. This relationship was observed to be almost linear in the region where the occlusion varied in the range from 0-40% by diameter. As the Reynolds number increased, the flow field downstream of the stenosis passed through a transitional regime involving the formation of steady, laminar vortices, fluctuations of the separated region followed by vortex shedding and localised turbulence. The non-symmetric stenosis consisted of a hemispherical "*bulge*" on one side of the vessel. This produced a horse-shoe vortex around the constriction at intermediate Reynolds numbers, then turbulence at the higher Reynolds numbers. The effect of pulsatility was seen to facilitate the production of vortices and increase the range of the turbulent region in the upstream direction.

In 1978, Cassanova and Giddens [97] presented the experimental results of disordered flow in rigid tubes containing axisymmetric stenoses, using both steady and pulsatile conditions. In this detailed study, the effect of stenosis size and geometry was investigated using Reynolds numbers in the range 318-2540. Sharp-edged occlusions were created with thin brass plates and contoured occlusions were constructed from acrylic. The flow was visualised by the introduction of a fine stream of dye in the inlet region. The overall conclusions of this work were that the sharp-edged stenosis produced a much larger disturbance of the flow than the contoured stenosis at a given Reynolds number and for both types of stenosis the disturbance was increased as the degree of occlusion increased. This is in accordance with later work by Hyun *et al.* who also concluded that step expansions create greater levels of disturbance than smooth stenoses [101] and also the work of Azuma and Fukushima [100] described previously. The effect of pulsatility in the work of Cassanova and

Giddens [97] was also reported to induce disturbances at a lower degree of occlusion for a given Reynolds number and this was verified by analysing the energy spectra. As no results were presented for the lower Reynolds numbers, the Reynolds number at which the disordered flow developed could not be identified for these geometries.

Similar studies were presented in 1983 by Ahmed and Giddens [98] who used steady flows of Reynolds numbers in the range 250-2000. Sinusoidal-shaped occlusions of 25, 50 and 75% were investigated and the results were visualised using laser Doppler anemometry and flow visualisation. For the 75% stenosis, the flow was laminar at $\mathrm{Re} = 250$, showed periodic oscillations at $\mathrm{Re} = 500$ and became turbulent at $\mathrm{Re} = 1000$. Once again, the onset of disturbance was observed at a lower Reynolds number for a higher degree of occlusion. The recirculation length measured for the 75% stenosis was greater for a Reynolds number of $\mathrm{Re} = 1000$ than for $\mathrm{Re} = 500$. However, with the onset of turbulence, as the Reynolds number is increased further, the reattachment point was observed to move upstream. This effect was also reported by Smith [22] and is related to the breakdown of the stability of the shear layer between the jet and surrounding fluid in the throat of the stenosis [102].

In 1997, Bluestein *et al.* [103] performed experiments and numerical simulations of blood flow through stenoses with Reynolds numbers in the range 300-3600. The focus of this paper was on correlating the observed flow patterns with previously measured platelet deposition results. This section of the work will be revisited in Chapter 6. Concerning the flow simulations, an axisymmetric, sinusoidal stenosis with an occlusion of 84% was used with steady flow conditions. A finite element code (FIDAP) was used to solve the Navier-Stokes equations with the $k - \varepsilon$ turbulence model. The mesh was refined in the wall region to increase the accuracy of results (particularly the shear rate) and a total of 4600 nine-node quadrilateral elements were used. Reynolds numbers of 300, 900, 1800 and 3600 were investigated, all of which showed a core jet through the stenosis and symmetrical recirculating vortices in the expansion region. Similar to Ahmed and Giddens [98], Bluestein *et al.* [103] noted a decrease in the recirculation length up to the Reynolds number of 1800, followed by a slight increase for $\mathrm{Re} = 3600$. However, the recirculation length

was not seen to increase with Reynolds number in the laminar range (given as $\mathrm{Re}=300$, $\mathrm{Re}=900$ and $\mathrm{Re}=1800$, based on the upstream flow conditions). The numerical results were compared to experimental data obtained using digital particle image velocimetry (DPIV) and these were presented at the laminar Reynolds number of 300 and the turbulent Reynolds number of 3600. The positions of separation and reattachment points were in very good agreement and the characteristic inlet, stenosis and recirculation zone velocity profiles were tightly overlapped.

Bluestein *et al.* extended this work in 1999 [104] using the same geometry and similar methods as in the previous publication [103]. This article also focused on the relationship between flow patterns and thrombus formation and will therefore be revisited in Chapter 6. The Reynolds numbers used in this study fell in the range 300-1800. This more recent publication [104] identified a weakness in their earlier publication [103] stating that the steady flow model was "*unable to capture the unsteady vortex phenomena in the recirculation region known to occur under these conditions.*" The non-Newtonian properties of blood were modelled; the viscosity was shear rate dependent which is important for accurately capturing the dynamics of shed vortices in a low shear environment. A "*quasi-unsteady*" flow condition was implemented at the inlet by applying a velocity fluctuation of 5% over a period of 10ms. This is a method in which unsteady flow can be triggered, as will be discussed in section 3.5. Again, the $k-\varepsilon$ turbulence model was used for the numerical simulations and DPIV was used in the experiments, but with a more accurate set-up capable of capturing the unsteady flow. Results of the flow visualisation studies indicated the periodic shedding of vortices distal to the stenosis from a Reynolds number of 375. The location of the site at which vortices were produced, along with their size and duration, varied with Reynolds number. As the Reynolds number increased, the size of the measured vortices decreased and the orientation of their path line changed from being parallel to the axial direction to being parallel to the wall of the downstream edge of the stenosis, as can be seen in figure 3.1. Vortices were also seen to move upstream and closer to this wall such that for $\mathrm{Re}>1000$, the site of vortex initiation is very near the stenosis throat. This phenomena enhances platelet deposition as will be discussed in Chapter 6.

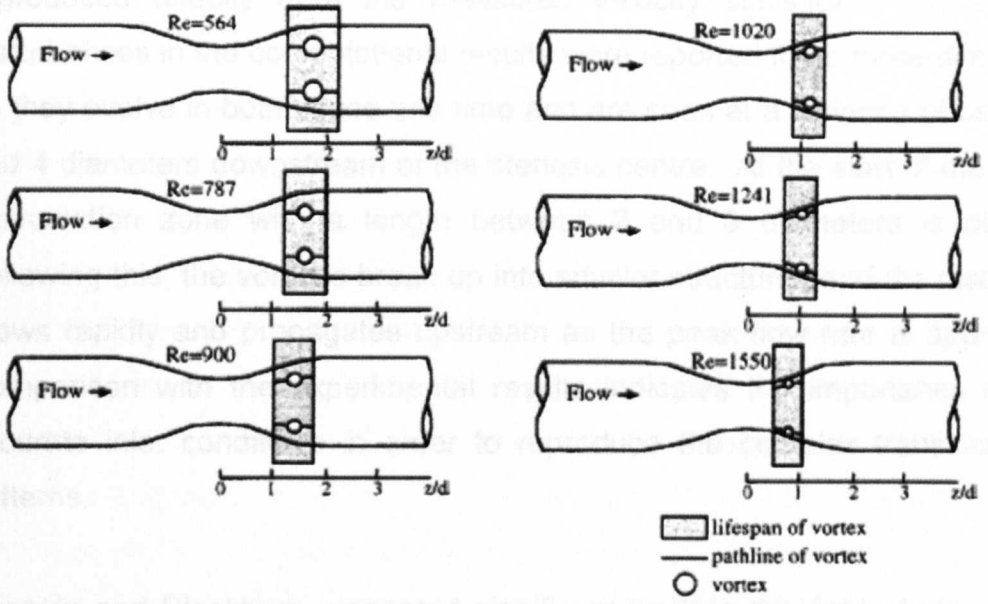

Figure 3.1: Schematic drawing of the relative location, pathline and size of the vortices observed at different Reynolds numbers. Diagram taken from Bluestein et al. [104].

In 2002, Lee and Xu described the results of a 3D coupled fluid-wall interaction model using ABAQUS and CFX [105]. The pressure field was obtained in the flow simulation, which was then fed into the wall model to compute the associated displacement. A 45% axisymmetric stenosis model was used with sinusoidal inflow conditions at a mean Reynolds number of 580 hence the flow was treated as laminar. The compliant nature of the vessel walls altered the resulting velocity profiles due to mass conservation and the region of separated flow was seen to be larger in width and length. Results were also presented using a rigid wall and static flow with a compliant wall. This allowed for model validation with existing literature and analytical solutions.

Further comparisons of numerical simulations and experiments were presented by Beratlis *et al.* in 2005 [99]. Pulsatile flow through a 50% smooth, symmetric stenosis (placed within a rectangular channel) was used at an average Reynolds number of 570. Laser Doppler velocimetry (LDV) was used to prescribe the appropriate inlet conditions to be used in the direct numerical simulation (DNS), which solved the Navier-Stokes equations on a non-uniform grid containing approximately 1.4×10^{6} nodes. Flow disturbances were triggered with an inlet boundary condition containing a laminar component taken from the experiments and a random component which is superimposed. These random fluctuations mimic those present in the experiments which could not be

reproduced directly from the measured velocity statistics. The observed disturbances in the computational results were reported to be three-dimensional as they evolve in both space and time and are seen at a distance of between 3 and 4 diameters downstream of the stenosis centre. At the start of the cycle, a recirculation zone with a length between 2 and 3 diameters is observed. Following this, the vortices break up into smaller structures and the disturbance grows rapidly and propagates upstream as the peak flow rate is approached. Comparison with the experimental results indicates the importance of using accurate inlet conditions in order to reproduce the complex transitional flow patterns.

Sherwin and Blackburn presented significant work in the field of stenotic flow simulations in 2005 [106]. The primary aim of this work was to examine the stability of steady and pulsatile flows and the subsequent transition to turbulence. A smooth, 75%, axisymmetric, sinusoidal constriction was used and two types of pulsatility were employed (one of a sinusoidal form and one being more representative of physiological waveforms) along with the Navier-Stokes equations. Reynolds numbers in the range 400-800 were investigated for the case of steady flow, 250-500 for the sinusoidal flow and 500-550 for the physiological flow. Stability analyses were conducted by decomposing the velocity into a base flow and a perturbation flow in order to examine the stability of the perturbation linearised about the base flow. For the simulations with steady flow, the stability analyses concluded that the critical Reynolds number at which instabilities were seen was 722. This is in agreement with the results of Ahmed and Giddens [98] who used the same geometry. DNS were also performed in order to characterise the flow properties. At a Reynolds number of 750, long-period fluctuations were observed, associated with a slow flapping of the jet and axial movement of a region of localised turbulent breakdown. The critical Reynolds number reported for the physiological flow was 535. For the pulsatile simulations considered, instability occurred through a "*period-doubling bifurcation, and the nature of the instability was identified as alternating tilting of vortex rings generated during sequential pulsatile cyclic ejections from the stenotic constriction.*"

As outlined in this literature review, there are many factors that affect the nature of the flow downstream of an occlusion. Both numerical and experimental investigations have been reported using a variety of techniques. To summarise, it has been demonstrated that a larger percentage occlusion leads to more disturbed flow [97, 98, 100] and a more abrupt stenosis will cause disturbances at a lower Reynolds number than a smooth stenosis [97, 101]. Pulsatility will also induce instabilities at a lower Reynolds number than steady flow [97, 100, 106]. However, there are many other factors that contribute to the stability of the flow field that have not been mentioned. Curvature of the artery has been shown to augment the increased flow resistance and wall shear stress due to stenoses [107]. The structure of the stenosis [108] and the inlet boundary conditions used are also important considerations [99, 104, 108].

3.1.1 Stenosis Severity

In 1987, the North American Symptomatic Carotid Endarterectomy Trial (NASCET) was set up in order to assess the benefits to patients undergoing endarterectomy treatment of carotid stenosis and subsequent results have been presented [109]. The study has concluded that treatment is beneficial for patients with severe stenosis (defined as 70-99% by diameter), that those with symptomatic moderate stenosis (50-69%) display only a moderate reduction in the risk of stroke and patients with stenosis of less than 50% do not benefit [110]. Stenotic occlusions can be confidently identified using imaging techniques such as ultrasound if the radius reduction is 50% or greater [106], equivalent to a 75% by area occlusion.

However, the use of just a single parameter has been criticised by several authors. Yao *et al.* [107] demonstrated substantial differences between the flow patterns and shear stresses in curved compared to straight arteries. Such differences in the flow field may result in different pathologies such as thrombosis, further plaque development or plaque rupture. The authors emphasised the need for both curvature and percent stenosis to be considered in assessing stenosis severity. Stroud *et al.* [108] investigated effects such as stenosis morphology and surface irregularity, suggesting consideration of these

additional factors in the clinical assessment. The results of this study showed that two vessels with the same percent stenosis but differing plaque morphologies produce significantly different flow fields and wall shear distributions. In 2001 Chua *et al.* [111] described a scaling technique that could be used to normalise the wall shear stresses produced under different flow conditions to fit on to a single generic curve. This was suggested as a referencing method that could be used by clinicians to aid the decision regarding treatment. This article produced results for both steady and pulsatile flows, but only axisymmetric sinusoidal stenoses were investigated.

3.2 Lattice Boltzmann Simulations of Flow through Stenoses

This section describes the methods used and results obtained in the current project when simulating flow through stenosed vessels using the lattice Boltzmann method. All simulations were performed to match the experimental flow visualisation work of Smith [22]. The vessel diameter was 8mm, with an axisymmetric square-edged occlusion of 75% by area and length 5mm. The inlet length was 16mm and the outlet length 80mm. These parameters are representative of the geometry of an idealised human femoral artery and the average Reynolds number therein is approximately 550 [22]. Figure 3.2 shows the stenosis model geometry used. The walls of the vessel were rigid and the flow treated as incompressible. The complexity of the $\mathrm{Re} = 550$ flow in the experimental studies of Smith [22] proved initially challenging for the simulations since the occlusion produced transitional behaviour. For this reason, a lower Reynolds number of 100 was used in the first instance since experimental data for this more stable, laminar flow were also available. The results of the flow simulations for both Reynolds numbers are discussed separately in the following sections.

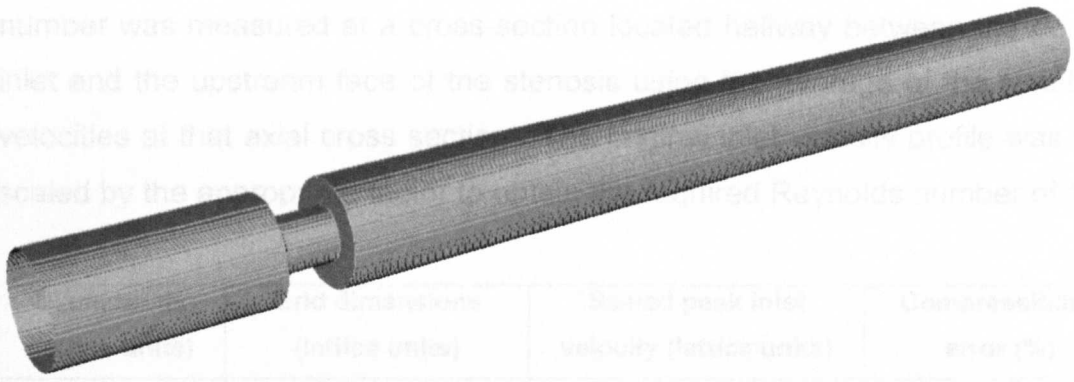

Figure 3.2: Geometry of stenosis model used for the lattice Boltzmann flow simulations. Inlet length is 16mm, outlet length is 80mm. Tube diameter is 8mm with a 75% by area stenosis 5mm in length.

3.3 Laminar Simulations: Re = 100

3.3.1 Grid convergence study

In order to choose the appropriate grid size to use for the simulation of stenotic flow at this Reynolds number, and for accurate comparison with the experimental results, a full grid convergence study was performed. As described in Chapter 2, for a given spatial discretisation the requisite Reynolds number can be achieved by appropriate selection of the relative magnitudes of viscosity and velocity, in lattice units. In this particular study, the viscosity was kept constant and the lattice velocity was altered accordingly to compensate for the changes in spatial discretisation. The relaxation parameter was $\omega = 1.95$, which allowed for the full range of lattice sizes to be reached, without producing compressibility errors caused by high values of velocity. For each simulation, convergence was assessed by measuring the average fluctuation of the average velocity about the mean value, as described in Chapter 2. The compressibility error between inlet and outlet was calculated for each simulation by simply measuring the mean velocity near the inlet and outlet regions and computing the relative increase. The parameters used for this investigation are shown in table 3.1 along with the compressibility errors. For each simulation, the approximate peak inlet velocity was calculated using the formula for Reynolds number and methods described in Chapter 2. Since a precise measurement of the resulting flow features was required yet the inlet boundary conditions specify only the equilibrium distributions for the velocities and not the actual density distributions, rescaling was performed. The simulated Reynolds

number was measured at a cross-section located halfway between the domain inlet and the upstream face of the stenosis using the average of the simulated velocities at that axial cross section. The original inlet velocity profile was then scaled by the appropriate factor to obtain the required Reynolds number of 100.

Diameter/dx (lattice units)	Grid dimensions (lattice units)	Scaled peak inlet velocity (lattice units)	Compressibility error (%)
16	204x18x18	0.05503132959	4.1
32	406x34x34	0.02695590701	0.75
48	608x50x50	0.01776649634	0.31
64	810x66x66	0.01340995140	0.23
80	1012x82x82	0.01068729963	0.18
96	1214x98x98	0.00890313390	0.09

Table 3.1: Scaled peak inlet velocity values used for corresponding grid sizes for Re = 100 discretisation study and associated compressibility errors.

Table 3.1 shows that even though the convergence criterion was satisfied, there was a significant compressibility error for the simulation with the coarsest grid. Because of this, and the fact that it was very difficult to obtain the results needed, this simulation will be omitted from further discussions.

Within this laminar flow regime, the converged result indicates that there is a stable axisymmetric toroidal vortex situated immediately downstream of the stenosis, as shown in figure 3.3. The measured parameters used for the discretisation study were the recirculation length and the position of the centre of the vortex, both of which are measured in relation to the downstream face of the stenosis. The recirculation zone was measured using Tecplot to identify the extent of reverse flow in the recirculation region. Figure 3.4 shows a plot of the results.

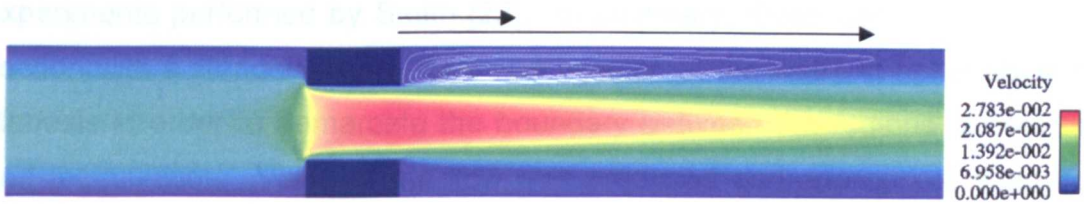

Figure 3.3: Typical laminar flow pattern seen downstream of a stenotic occlusion. Cropped two-dimensional slice through three-dimensional result is shown. Upper arrow indicates measure of centre of vortex and lower arrow indicates the recirculation length. Streamlines are shown only in the upper half of the recirculation zone.

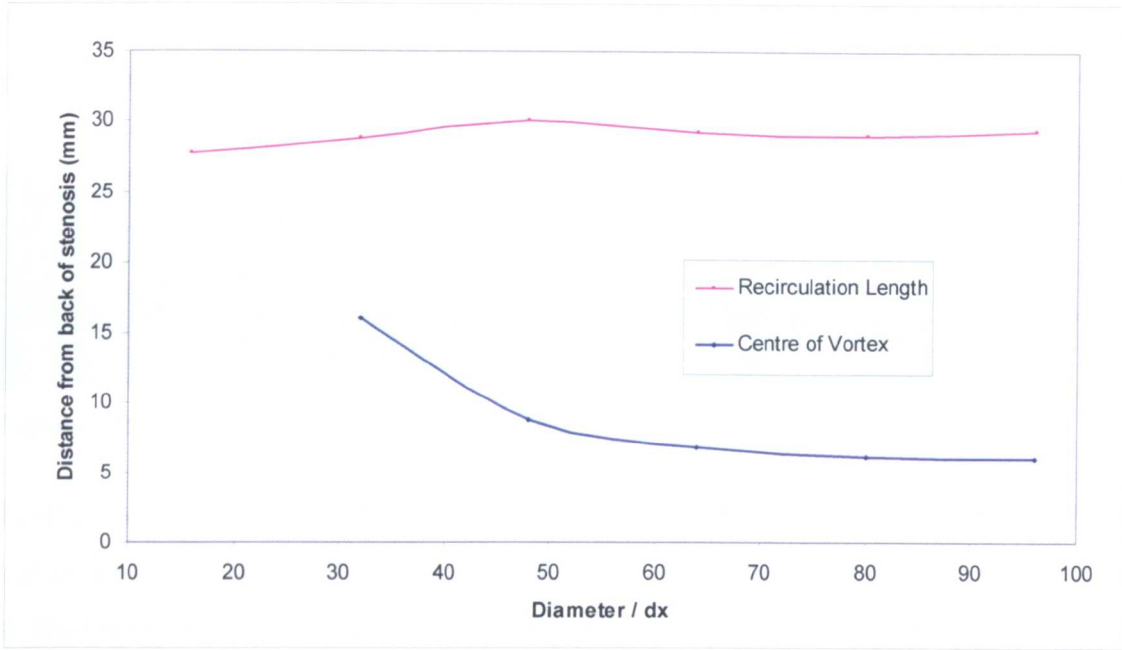

Figure 3.4: Results of grid convergence study for stenosis geometry at Re = 100. Recirculation length and centre of vortex position plotted against discretisation.

Figure 3.4 shows that the position of the centre of the vortex converges as the spatial resolution of the mesh is increased, changing by 1.6% as the grid is refined from 80 to 96 points across the diameter. The recirculation length varies within a window of $\pm$ 2.5% of the mean value. The finest grid reported $(1214 \times 98 \times 98)$ represents the limit for these analyses on the SX-6, due to memory allocation restrictions: the results are considered mesh invariant at this resolution, and all further analyses and discussions will be based on this grid. The relevant grid spacing and timestep in SI units are $L = 8.3333 \times 10^{-5} m$ and $T = 2.9383 \times 10^{-5} s$ respectively.

3.3.2 Comparison with experimental results

The simulations described in the previous section were based on the experiments performed by Smith [22]. In summary, these used an acrylic test section with a stenosis insert. Dye was injected at the wall just upstream of the stenosis in order to demarcate the boundary between the regions of core flow and recirculation. Video of the flow was produced and appropriate snapshots taken to enable accurate measurement of the recirculation region, as seen in

figure 3.5. It was not possible to measure accurately the position of the centre of the vortex in these experiments.

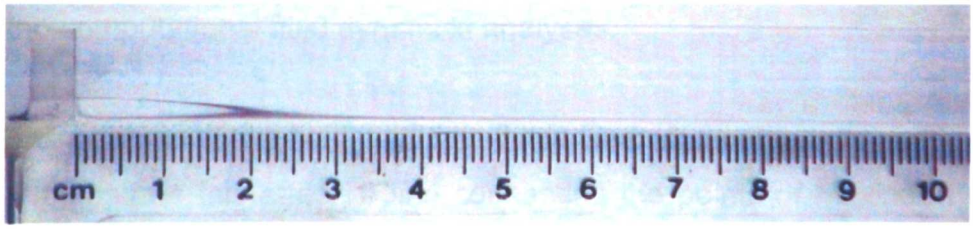

Figure 3.5: Photograph of flow visualisation results for Re = 100 stenosis experiment.

Further to this, simulations were performed by Smith [22] using CFX, a finite volume based Navier-Stokes solver. A converged flow solution was obtained in a geometry similar to that described for the lattice Boltzmann simulations. These results were also independently assessed for grid convergence.

Upon further investigation it was observed that, because the results were not axisymmetric, the reattachment point and the centre of the vortex were not uniquely defined in the three dimensional computational fluid dynamics analyses. For the lattice Boltzmann simulations, two limiting values of the reattachment length can be observed. The first is defined by the axial position at which the cross section shows a complete circle of reverse flow and the second, defined by the first occurrence of the complete absence of flow reversal at any point on the cross section. From each of these, the position of zero wall velocity is extrapolated. Figure 3.6 illustrates the two regions described.

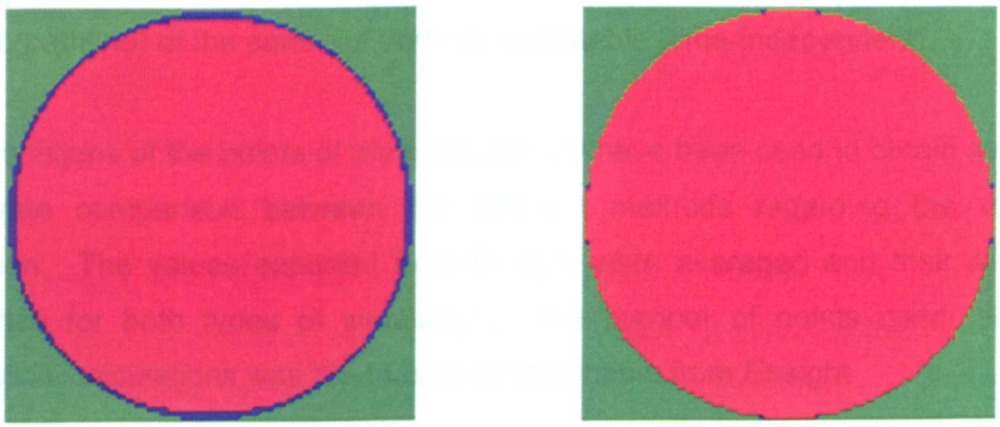

Figure 3.6: Cross sections of post-stenotic flow region for Re = 100 simulation coloured by magnitude of velocity in the axial direction. Red shows positive, blue negative and green zero regions. LHS illustrates complete circle of recirculating flow, RHS shows the presence of reverse flow further downstream at much fewer lattice points.

The CFX solution also exhibited a slight asymmetry of the recirculation zone, although less apparently associated with the geometric structure of the mesh. Two limiting values of the recirculation length were thus obtained from each of the computational fluid dynamics analyses.

The position of the centre of the vortex was also not axisymmetric. In order to demonstrate this effect, a line connecting the points of maximum vorticity was created using Ensight. Figure 3.7 shows the result for the lattice Boltzmann simulation and figure 3.8 shows the equivalent image for the CFX solution.

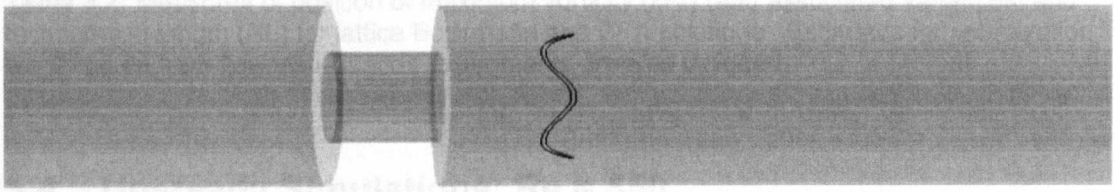

Figure 3.7: Lattice Boltzmann geometry showing line connecting positions of maximum vorticity.

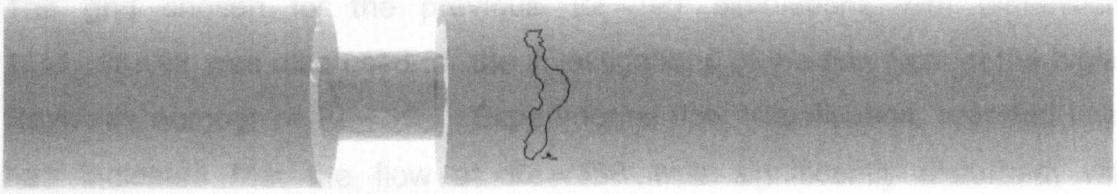

Figure 3.8: CFX geometry showing line connecting positions of maximum vorticity.

The positions of maximum vorticity were analysed further for the lattice Boltzmann simulations and were found to be Reynolds number dependent. Using a Reynolds number of 30, the vortex was almost axisymmetric. The locus (pathline) of the centre of vorticity was stable (time-independent).

The locations of the points of maximal vorticity have been used to obtain a more accurate comparison between the different methods regarding the vortex location. The values exported from Ensight were averaged and their ranges reported for both types of simulation. The number of points used for the statistical calculations was the maximum obtainable from Ensight.

Table 3.2 shows the measurements of recirculation length and position of maximum vorticity for the lattice Boltzmann and CFX solutions alongside the experimental estimate from figure 3.5.

	Lattice Boltzmann (± 0.05mm)	CFX (± 0.05mm)	Experiment
MV: Mean	5.30mm	4.91mm	
MV: Min	4.62mm	4.25mm	
MV: Max	6.01mm	5.43mm	
Standard deviation	0.47mm	0.36mm	
No. of sample points	965	143	
RL: Mean	29.0mm	27.3mm	25-30mm
RL: Min	28.6mm	25.9mm	
RL: Max	29.4mm	28.6mm	

Table 3.2: Measures of position of maximum vorticity (MV) (and associated variances) and recirculation length (RL) for lattice Boltzmann and CFX solutions. Estimates for recirculation length taken from flow visualisation experiments are also included.

3.4 Unsteady Simulations: Re = 550

The grid chosen for the previous $\mathrm{Re} = 100$ simulations with dimensions $1214 \times 98 \times 98$ was also used for the investigations of the flow field at the higher Reynolds number of $\mathrm{Re} = 550$. Experimental flow visualisation, reported later, had indicated that the flow at $\mathrm{Re} = 550$ was significantly disturbed, with complex, time-dependent characteristics. This is challenging for the numerical flow solution, and the results are very sensitive to simulation parameters such as lattice velocity and viscosity. A variety of techniques were used in order to obtain solutions that agreed with the experimental flow visualisation results and these will be described in turn in the following sections.

3.4.1 Standard simulation

As discussed in Chapter 2, lattice Boltzmann simulations are in principle dimensionless and the analyst is free to choose, subject to accuracy and stability constraints, two independent parameters (a length scale and a velocity) effectively fixing the units of length and time that will be used to represent the physical system. In the simulations reported in this section, the length scale is fixed by the choice of the grid size ($1214 \times 98 \times 98$), which represents the upper limit that can be handled within memory allocation limits on the SX-6. For the

75% by area constriction, the spatial average velocity at a cross-section through the stenosis is four times higher than that in the parent tube. The profile within the stenosis is likely to be relatively flat (spatially undeveloped), but making the conservative assumption of fully developed (parabolic) laminar flow, the peak velocity at any point in the domain will be eight times the nominal average inlet velocity. To keep compressibility errors within acceptable bounds, it is recommended that the Mach number should be less than 0.1 anywhere in the domain. Since the speed of sound is $1/\sqrt{3}$ (taken approximately and conservatively to be 0.5) in lattice units (see Chapter 2), this implies that the average inlet velocity should not exceed 0.5 x 0.1 / 8 = $0.00625\,\mathrm{L}T^{-1}$. Consequently, for a Reynolds number of 550, a kinematic viscosity of 96 (characteristic length) x 0.00625 / 550 = $0.00109\,\mathrm{L}^2T^{-1}$. Using the relationship between kinematic viscosity and relaxation factor, ω, from Chapter 2 gives a relaxation parameter of 1.987.

The fluid being modelled is water, with a kinematic viscosity of $\nu = 1.01\times10^{-6}m^2s^{-1}$ [89]. The diameter of the acrylic tube used in the flow visualisation experiments is $D = 8mm$, hence the corresponding length and timescales in SI units are $L = 8.3333\times10^{-5}m$ and $T = 7.4974\times10^{-6}s$ (to 5 s.f.). The simulation was executed for 2×10^5 iterations, limited by reasonable CPU time on the SX-6. The computation of 2×10^5 iterations represents a *real* time of approximately 1.5*s*.

Simulations were performed with a range of ramping times to investigate whether this parameter affected the steady state solution, in particular with respect to its stability. Three sets of results were produced using ramping times of 3×10^4, 6×10^4 and 1×10^5 iterations. Figure 3.9 shows plots of the average velocity over the entire simulation time.

In order to compare the magnitudes of the oscillations seen in figure 3.9, the average relative deviation from the mean value was calculated for the non-ramping time. Table 3.3 shows the results obtained.

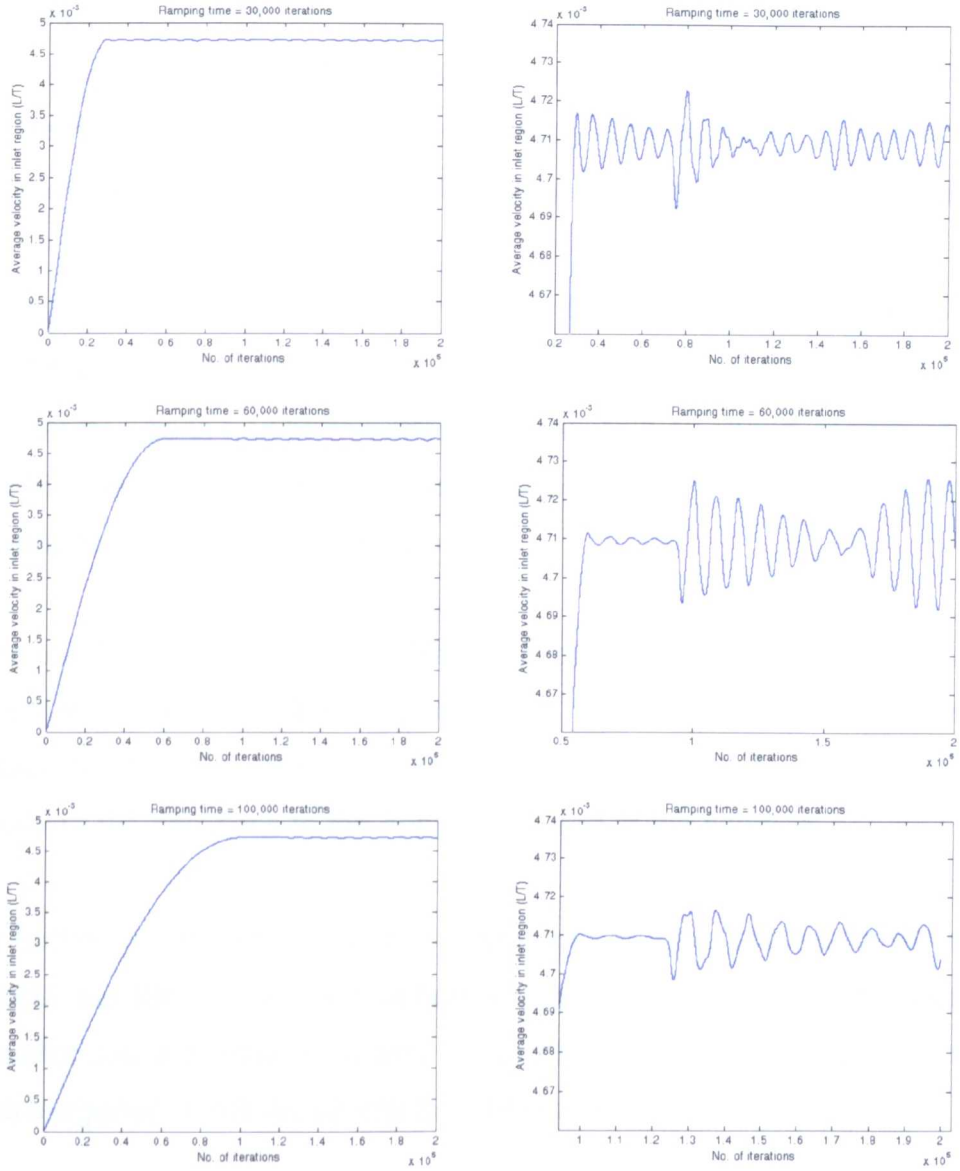

Figure 3.9: Variation in average velocity in inlet region for different ramping times, against iterations. RHS plots show enlargements of the constant velocity sections.

No. of iterations used for ramping ($x10^4$)	Average relative oscillation about the mean velocity
3	$6.7909x10^{-4}$
6	0.0011
10	$5.2901x10^{-4}$

Table 3.3: Variation in average relative velocity with varying ramping times.

In Chapter 2 the convergence of the simulations was assessed by calculating the average relative deviation from the mean value and ensuring that this parameter was of order 1×10^{-3} (0.1%) or below. Table 3.3 shows that this

condition is satisfied for the ramping times of 3×10^4 and 1×10^5 iterations, but not with that of 6×10^4 iterations. The advised ramping time is half the number of iterations being performed for a steady state solution: all further discussions relate to the results produced with a ramping time of 1×10^5 iterations.

The simulation using a ramping time of 1×10^5 iterations was advanced in time and the results were analysed at intervals of 1×10^5 iterations until a total of 5×10^5 iterations had been performed. Figure 3.10 shows images of the velocity distribution at subsequent times and figure 3.11 shows the variation in the average velocity over this time period.

Figure 3.11 suggests that the variations in the average velocity may be increasing with the number of iterations. Table 3.4 shows the recorded relative oscillations in the average velocity, averaged over the period which extends from 1×10^5 iterations to the appropriate end of the solution.

A further 3×10^5 iterations were performed and the average relative oscillation about the mean velocity reached a value of 0.0015. This suggests that the oscillations are increasing and the method used previously for analysing the convergence of results cannot be used for unsteady results.

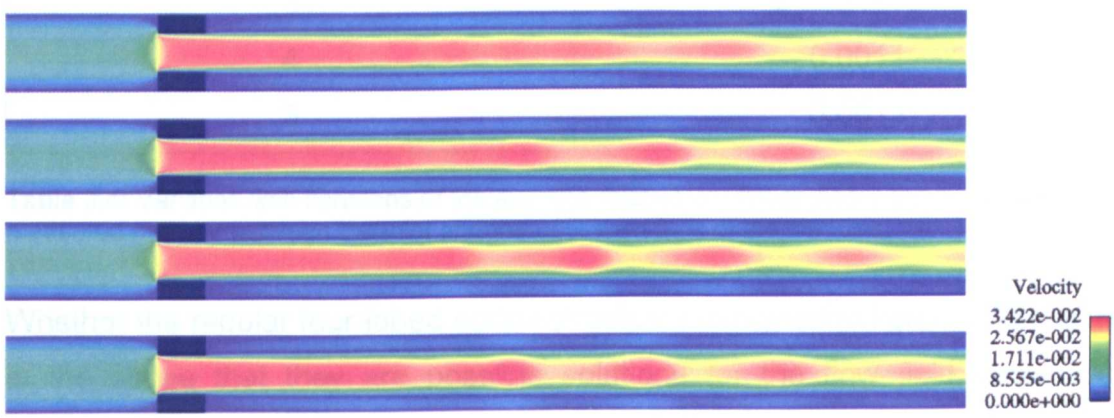

Figure 3.10: From top to bottom, velocity results after; 2×10^5, 3×10^5, 4×10^5 and 5×10^5 iterations.

Due to the increasing magnitude of the oscillations, it was believed that the structure of pulsatile vortices seen in figure 3.10 may become unstable.

However, a further 3×10^5 iterations were performed, thus totalling 1.1×10^6 iterations and no qualitative differences were observed in the results.

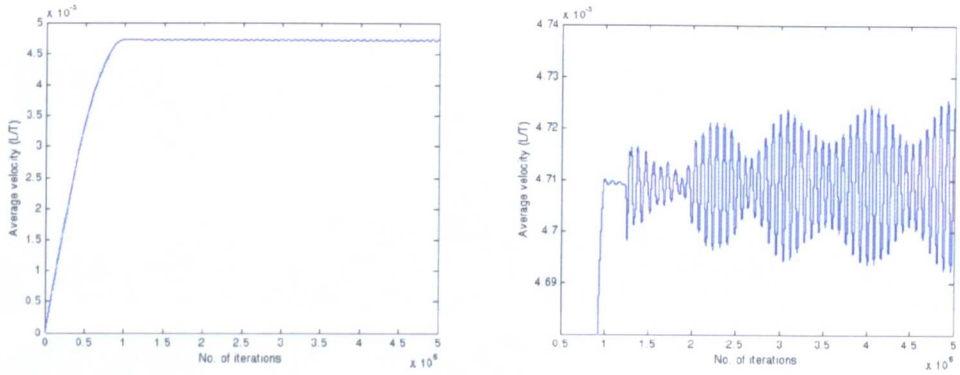

Figure 3.11: Variation of average velocity measured halfway between the inlet and the upstream face of the stenosis with increasing iterations.

The results of this simulation have been analysed in more detail by viewing cross-sectional slices of the velocity distribution. These are shown in figure 3.12. The slices shown were chosen due to their regular, highly symmetric patterns found in the regions near the vortices and the streamlines of these vortices can be seen in figure 3.13.

Number of iterations ($x10^5$)	Average relative oscillation about the mean velocity
2	$5.2901x10^{-4}$
3	$9.2051x10^{-4}$
4	0.0011
5	0.0013

Table 3.4: Variation with iterations of the average relative oscillation about the mean velocity measured halfway between the inlet and the upstream face of the stenosis.

Whether the regular four-lobed vortex structures indicated in figure 3.12 are real in the sense that they are possible solutions for the flow field under ideal conditions, or whether they are numerical artefact associated with the regular mesh (or perhaps more likely with the inadequacy of the representation of a circular section on the regular LB grid), there is no evidence of them either in the literature or in the flow visualisation studies. In practice, the flow at a Reynolds number of 550 is temporally disturbed, and the following sections

describe the methods used to trigger flow instabilities to achieve solutions that were qualitatively comparable to observation.

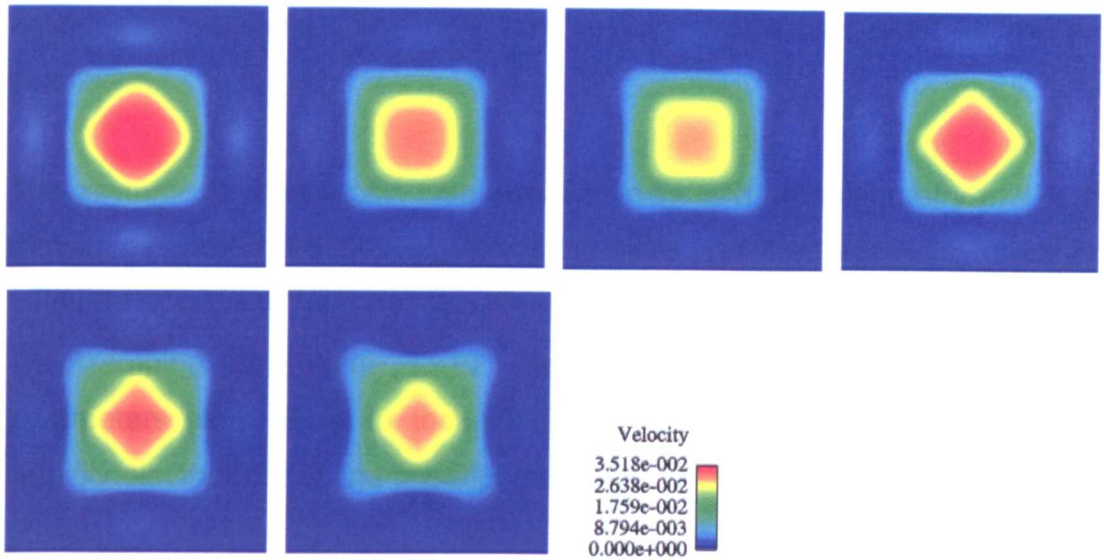

Figure 3.12: Cross-sectional slices coloured by velocity. Top to bottom and left to right, x = 636, 669, 685, 791, 981, 1145. End of domain is at x = 1214.

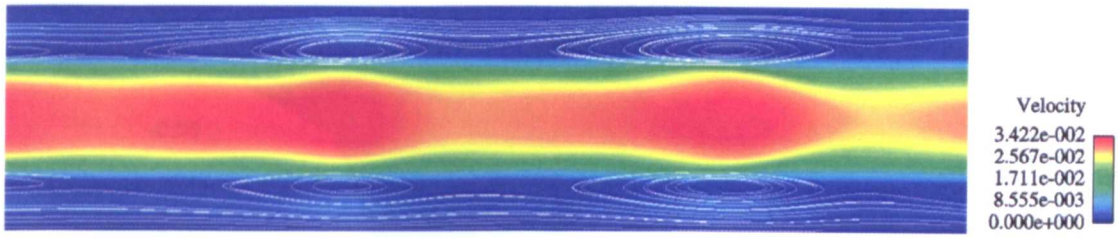

Figure 3.13: Streamline plot showing the location of vortices.

3.4.2 Asymmetric inlet velocity profile

In order to try and produce the unsteady flow patterns identified in the flow visualisation experiments, the applied inlet velocity profile was altered slightly so as to make it asymmetric, whilst conserving volume flow. This is a common technique used for triggering anticipated instabilities in numerical simulations [99, 104], since highly symmetric geometries and boundary conditions can act to dampen any irregularities that would be present in experimental conditions.

The asymmetric profile used in this study was created by multiplying a parabola by a straight line symmetric about the origin. The result is a three-dimensional

sin-type graph with negative values in the first half and positive values in the second half, as shown in figure 3.14. This was then normalised so that the peak value was 1% of the peak of the original parabola. This new normalised result was then subtracted from the original parabola to create a slightly asymmetric parabola. The new inlet velocity profile was used for the entire simulation.

The asymmetric inlet profile was applied, firstly with an asymmetry of 1%, then with an asymmetry of 39.5%. This latter value was the largest asymmetry that could be applied without the occurrence of negative velocity values at the inlet. The ramping time was 3×10^4 iterations and the remaining simulation parameters were equal to those used in section 3.4.1. Figure 3.15 shows velocity distributions at the onset of instability.

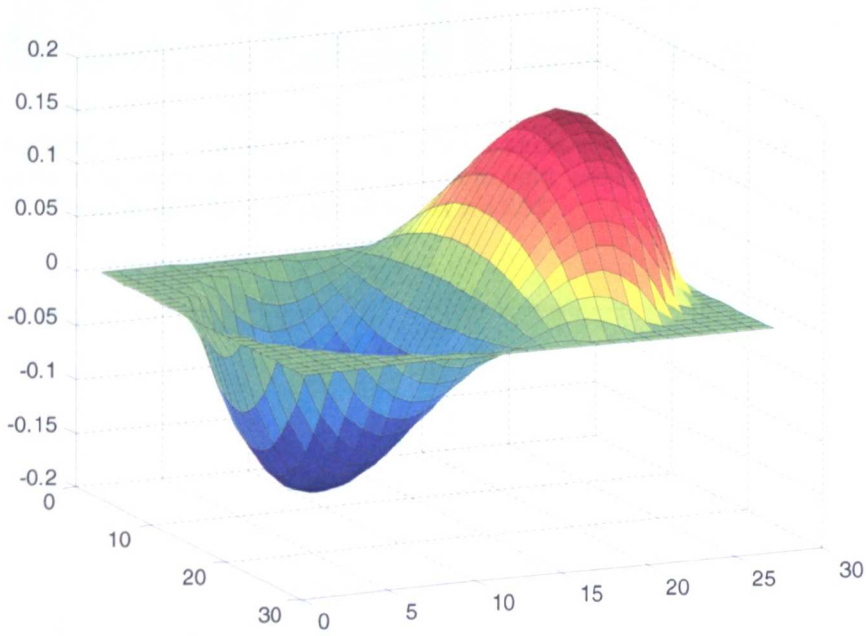

Figure 3.14: Example of paraboloid multiplied by a straight line, symmetric about the origin.

Figure 3.15 shows that an asymmetric inlet velocity profile can be used to trigger instabilities in the flow field and the results produced are dependent upon the magnitude of the asymmetry applied. However, cross-sectional slices were analysed as before and figure 3.16 shows that once again, highly symmetrical shapes are produced in the velocity field upstream of the disturbed region. Figure 3.17 shows a plot of average velocity versus iterations halfway along the inlet for the case of an asymmetry of 1%.

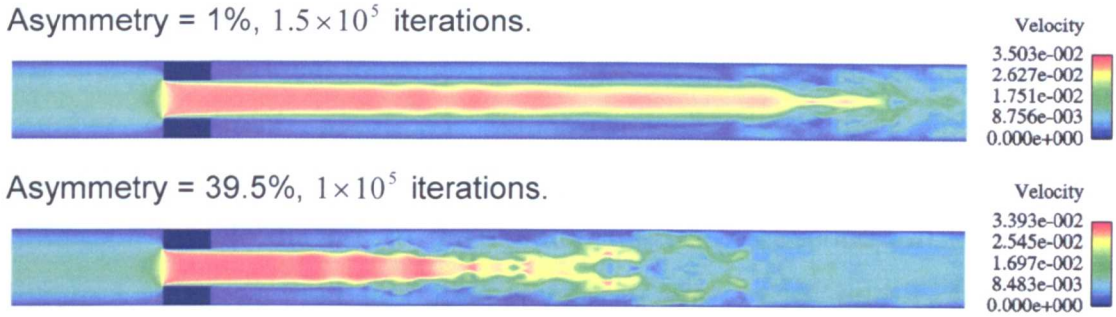

Figure 3.15: Velocity distribution produced at the onset of turbulence triggered using an asymmetric inlet velocity profile.

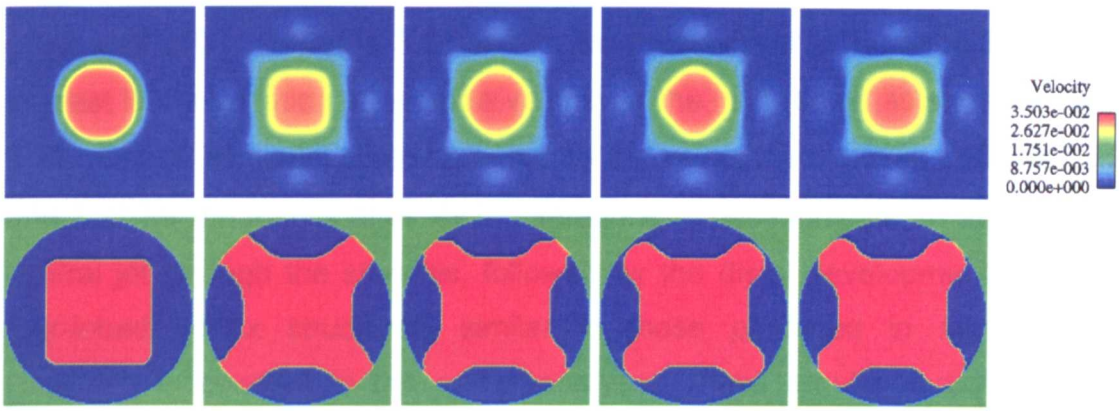

Figure 3.16: Cross sectional slices of Re = 550 simulations using 1% asymmetry in inlet velocity profile after 1×10^5 iterations. Upper images show velocity in full colour scale, lower images show the magnitude of the velocity, *u*. Left to right, slices displayed are x = 287, 553, 577, 589, 611. Downstream face of stenosis is at x = 253.

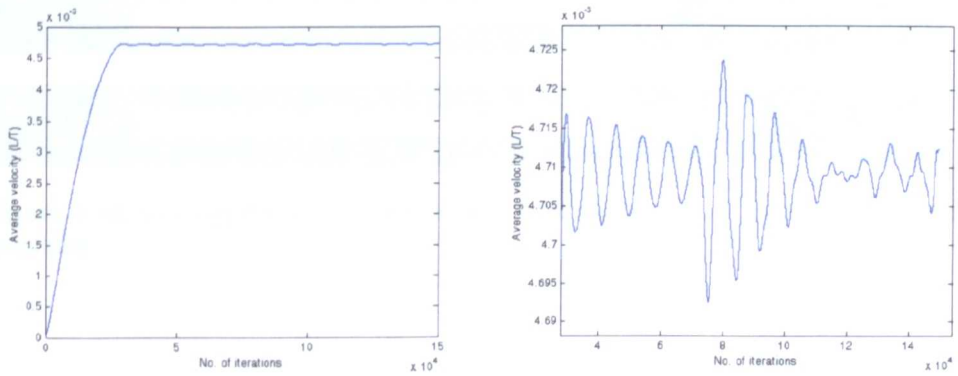

Figure 3.17: Variation in average velocity halfway down inlet region over 1.5×10^5 iterations with 1% asymmetry at inlet.

3.4.3 High Mach number simulation

Section 3.4.1 describes analyses in which the Mach number constraint is satisfied. In this section, results are presented for an analysis with an average inlet velocity of $0.025LT^{-1}$. Simple calculations suggested that this could

produce a local Mach number of 0.35, but in practice (examining the results of the analysis) the local maximum was 0.26. This analysis, violating the Mach number constraint, produced results indicating disturbed flow that was qualitatively more similar to the experimental observations, and to those produced by introducing an asymmetry, than that described in section 3.4.1. Figure 3.18 shows the distribution of velocity after 2×10^5 and 4×10^5 iterations, with a ramping time of 3×10^4 iterations. The relaxation parameter is 1.95, therefore the corresponding length and timescales are $L=8.3333\times10^{-5}m$ and $T=2.9383\times10^{-5}s$. Figure 3.18 shows the presence of instabilities, but also of interest is the variation of average velocity in the inlet region as shown in figure 3.19. Cross- sectional slices coloured by the velocity are shown in figures 3.20 and 3.21 for the results after 4×10^5 iterations. These indicate an axisymmetric central jet through the stenosis, followed by the distal development of regular four-lobed vortex structures, similar to those produced in section 3.4.1. However, in contrast to the earlier analyses, these regular vortices become unstable within the flow domain modelled, and degenerate into a disturbed pattern of flow that is qualitatively similar to that observed experimentally.

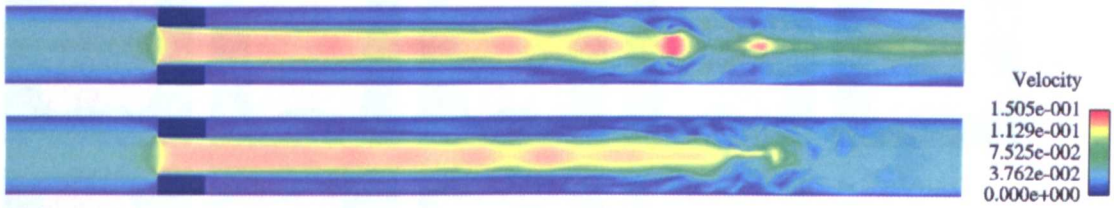

Figure 3.18: Velocity distribution in centre of z axis after 2×10^5 (upper) and 4×10^5 (lower) iterations.

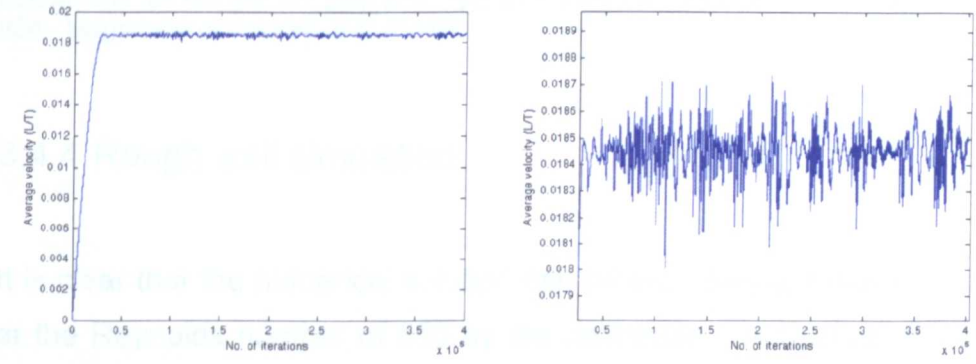

Figure 3.19: Variation in average velocity halfway between inlet and upstream face of stenosis over 4×10^5 iterations for high Mach number simulation.

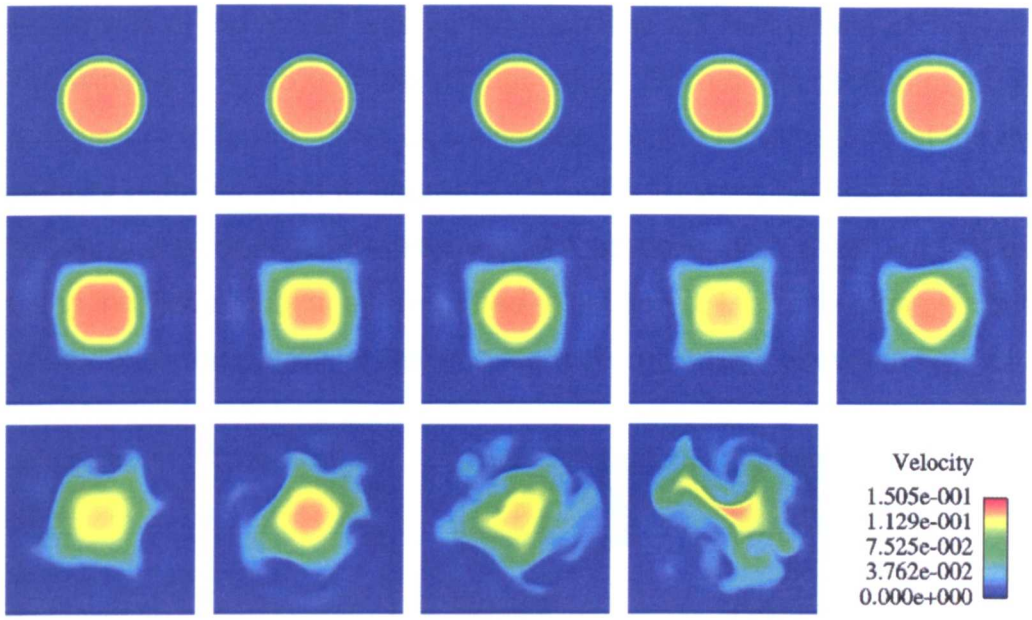

Figure 3.20: Cross sectional slices coloured by velocity for Re = 550 simulation with high Mach number. Top to bottom and left to right: x = 254, 255, 262, 277, 298, 395, 559, 595, 625, 674, 734, 783, 873, 934.

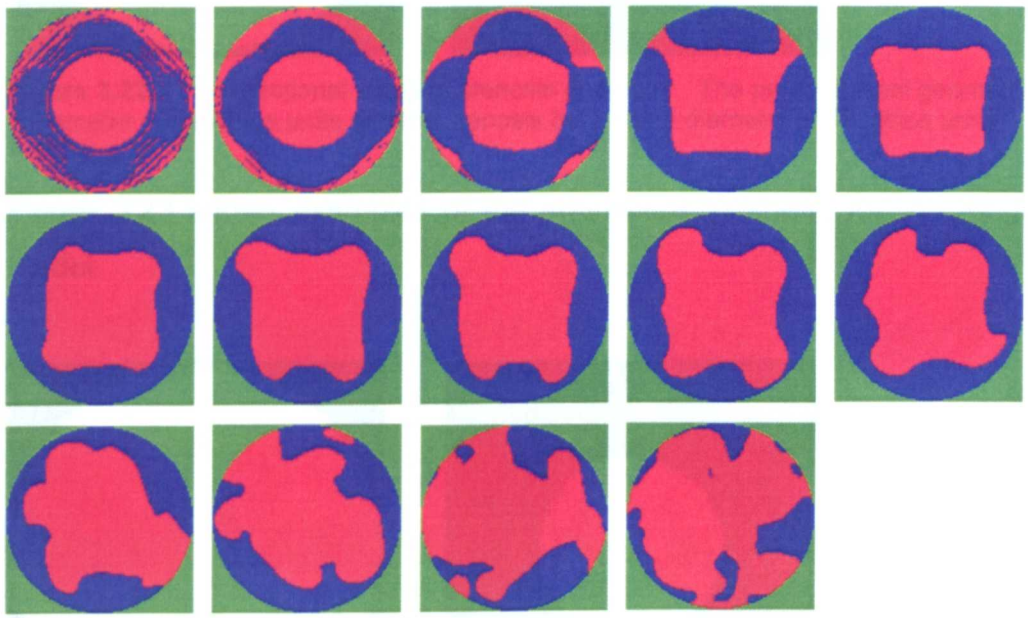

Figure 3.21: Cross sectional slices for Re = 550 simulation with high Mach number. Top to bottom and left to right: x = 254, 255, 262, 277, 298, 395, 559, 595, 625, 674, 734, 783, 873, 934. Magnitude of velocity, *u* is shown.

3.4.4 Rough wall simulation

It is clear that the numerical solution can be provoked to produce disturbed flow at the Reynolds number of 550 by the deliberate introduction of instabilities or symmetry-breaks. The final method adopted to break symmetry was the introduction of small geometrical irregularities at the wall. The geometry of the

entire wall of the model was varied such that the radius was chosen at random in a window of ± 1.5% of the original value. Each cross section of the geometry is therefore different. This was instigated by the hypothesis that the symmetric velocity patterns seen in figures 3.12 and 3.16 were caused by the slightly flat edges of the idealised geometry which approximates a circle in cross-section using individual cubes, as described in section 3.4.1. The cross sections of the geometry in the parent vessel and stenosis region are shown in figure 3.22.

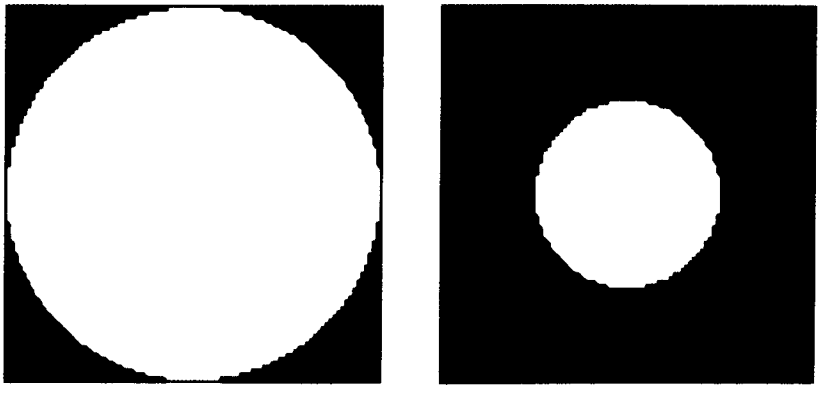

Figure 3.22: Cross sectional slices of stenosis geometry. The parent vessel geometry (left) has a diameter of 96 lattice units and the stenosis bore has a diameter of 48 lattice units.

Figure 3.23 shows examples of the equivalent geometry for the rough walled model.

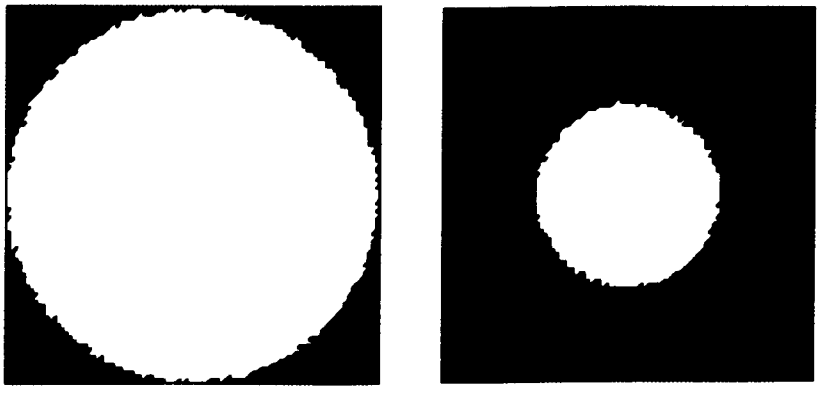

Figure 3.23: Cross sectional slices of stenosis geometry with rough wall.

A simulation was performed using the parameters described in section 3.4.1. Results of the flow field velocity after 8×10^4 iterations are shown in figure 3.24.

Figures 3.25 and 3.26 show cross-sectional slices coloured by the velocity. In conclusion, these results are similar to those in sections 3.4.2 and 3.4.3 in that prior to the disturbed region, regular four-lobed structures exist.

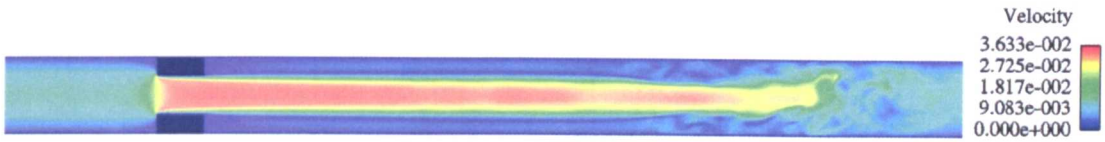

Figure 3.24: Slice through centre of z-axis coloured by axial component velocity after 8×10^4 iterations with the rough walled model.

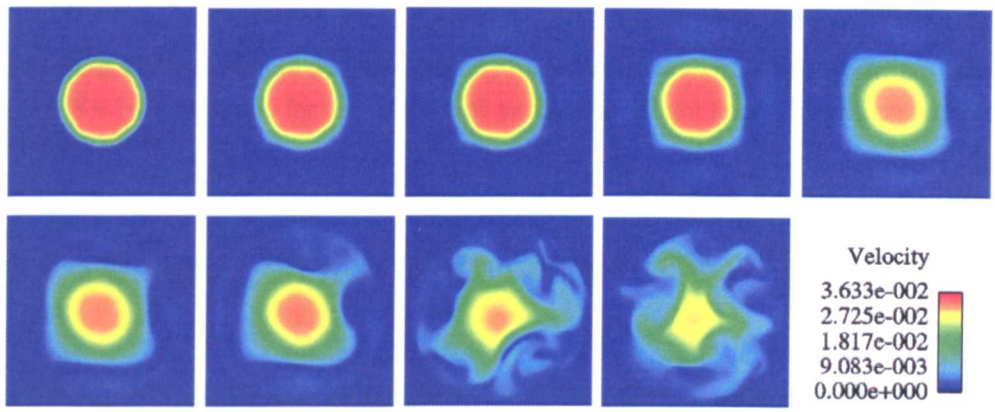

Figure 3.25: Cross-sectional slices coloured by velocity for Re = 550 simulation with rough wall. Top to bottom and left to right: x = 258, 307, 326, 401, 746, 758, 801, 928, 958.

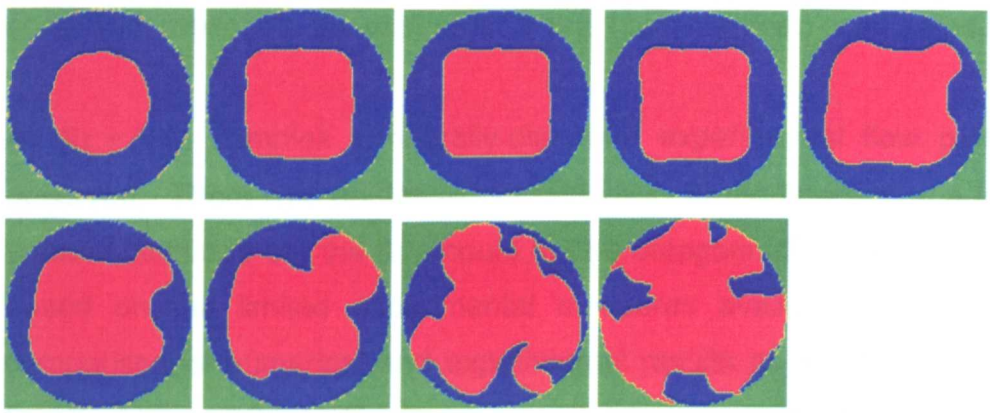

Figure 3.26: Cross-sectional slices coloured by magnitude of velocity, *u* for Re = 550 simulation with rough wall. Top to bottom and left to right: x = 258, 307, 326, 401, 746, 758, 801, 928, 958.

Figure 3.27 shows the variation in average velocity with iterations for the first 8×10^4 iterations and the criterion for convergence is satisfied. Following this, 1.6×10^6 iterations were performed so that the characteristics of the flow could be fully assessed. This is equal to a real time of approximately 12s and took approximately 150 hours of CPU time on the SX-6. These results are presented in the following section.

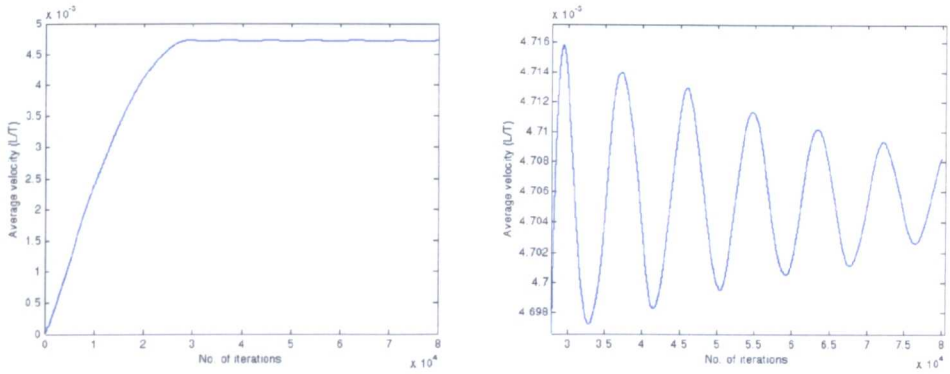

Figure 3.27: Variation in average velocity halfway between inlet and upstream face of stenosis over 8×10^4 iterations for the rough wall simulation. Right image shows enlargement of non-ramping time.

3.4.5 Comparison with experimental results

The results obtained in section 3.4.4 using a rough-walled stenosis geometry were chosen as being the most appropriate to use in further comparisons. This is because this triggering factor is likely to be most representative of the experimental conditions, although there are probably many more destabilising conditions present in the experiments that have not been considered.

At $\mathrm{Re} = 550$, complex temporally-disturbed experimental flow patterns were observed. There was no consistent periodicity in the flow patterns (no obvious vortex shedding), but the flow could not be categorically described as turbulent based on the limited experimental measures available. Good qualitative comparison of numerical and experimental results at $\mathrm{Re} = 550$ is illustrated in figures 3.28 and 3.29. The 'reattachment point' fluctuates temporally and has a range of 15mm-65mm in the simulations and 30mm-55mm in the experiment for the results shown. The detailed flow structure at any instant in time was apparently random, but the overall characteristics were similar. The experimental results were captured from video of the flow visualisation study.

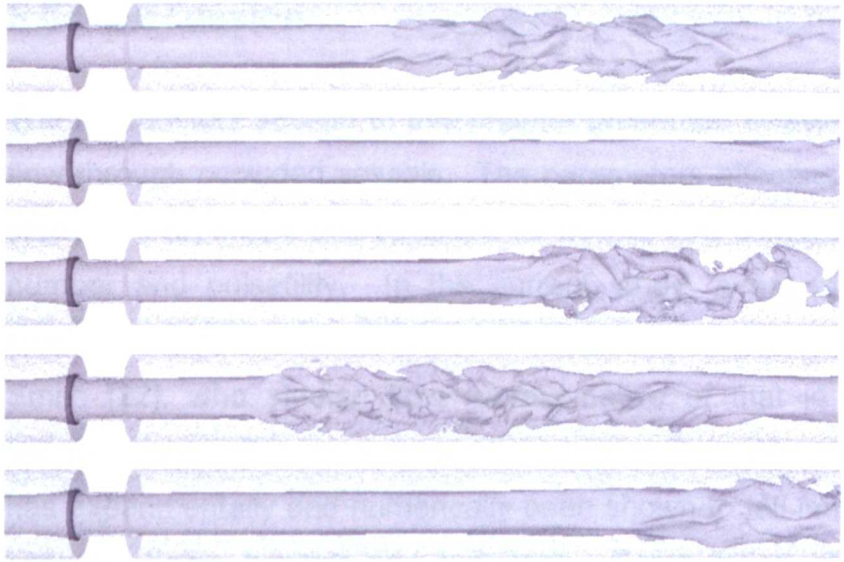

Figure 3.28: Lattice Boltzmann flow simulation results at Re=550. Isosurface of velocity shown inside core fluid domain. Arbitrary snapshots in time are shown to demonstrate the overall behaviour.

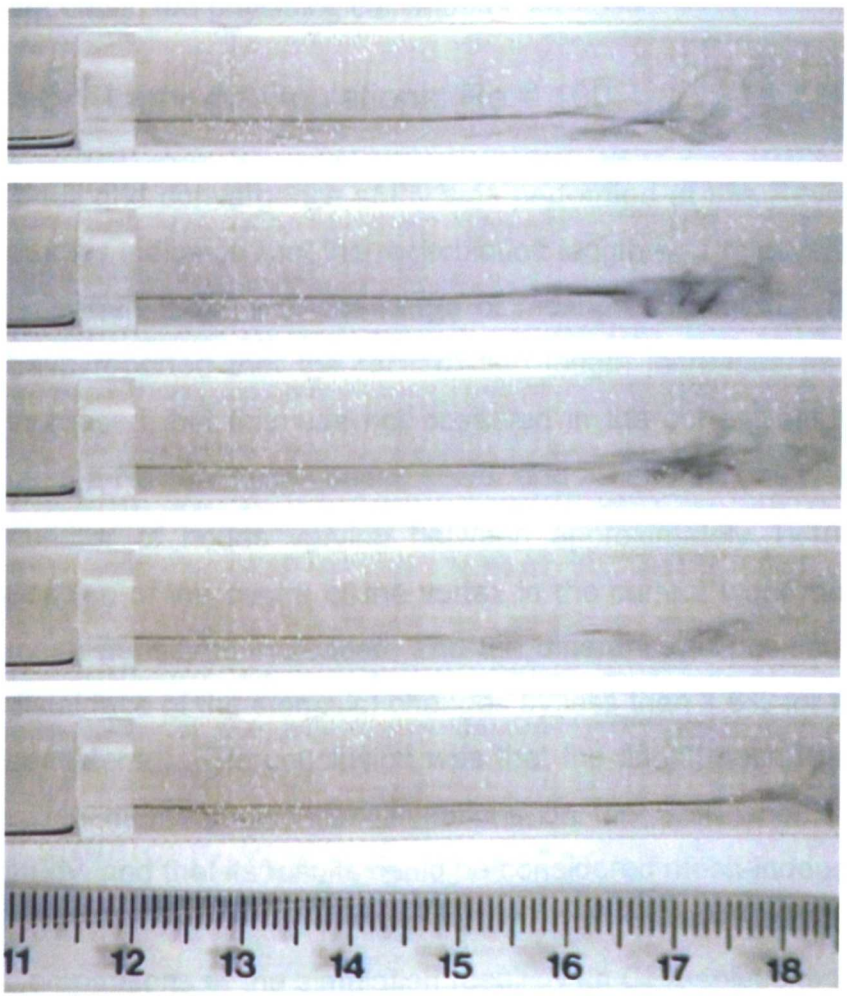

Figure 3.29: Flow visualisation results at Re = 550. External tube wall can be seen. Snapshots are shown to demonstrate the overall behaviour.

3.5 Discussion

The introductory section of this chapter presented a review of the literature on flow through occluded vessels. The parameters affecting the flow field include stenosis size, shape and structure as well as flow conditions such as Reynolds number and pulsatility. In the current study, a set of geometric and flow conditions were chosen to allow for comparisons with the experimental work of Smith [22], who studied flow representative of that in an idealised human femoral artery. The appropriate physiological Reynolds number is 550, and this has experimentally and numerically been shown to fall in the transitional region between being laminar and turbulent. Computation of flow in this regime presents many challenges and, in this study, two Reynolds numbers have been investigated, firstly $\mathrm{Re} = 100$ which clearly lies in the laminar region and secondly, the physiological value of $\mathrm{Re} = 550$.

3.5.1 Laminar simulations: Re = 100

A full grid convergence study was performed at this Reynolds number. These studies indicated that the recirculation length was relatively constant, varying by less than 2.5% over the range of meshes computed. Thornburg *et al.* [112] have reported that the recirculation length increases as the mesh density is increased, but this was not observed in the current study. This investigation used a Navier-Stokes based solver and 2D simulations were performed with the number of nodes varying between approximately 1×10^4 and 3×10^4. The position of the centre of the vortex in the current work moves upstream as the mesh density is increased, and the difference in position (measured from the distal face of the stenosis) changes by less than 1.6% for the two finest meshes considered. The conclusion was that the finest mesh that could be supported within memory-allocation limitations on the SX-6 should be adopted for this study, and that its results could be considered mesh-independent.

Comparisons of the simulation results with CFX solutions indicated a difference of approximately 10% in the location of the centre of the vortex, although the solution was not axisymmetric and the standard deviation of the position was of the same order. Differences in the computed recirculation length were approximately 6%, and again this difference was of the order of the range of

values based on asymmetry of the solutions. Comparisons with the experimental flow visualisation results indicated good agreement of the location of the reattachment point, although experimental resolution was such that it could not be used to discriminate between the accuracies of the lattice Boltzmann and CFX simulations.

3.5.2 Unsteady simulations: Re = 550

In order to numerically reproduce the unsteady results observed experimentally at this Reynolds number, a method of triggering the instabilities was required. Before this was attempted, a simulation was performed which yielded highly symmetric flow patterns throughout the domain. It was believed that these were caused by the high degree of symmetry in the geometrical and flow parameters. However, it is also believed that this is characteristic of the flow prior to the onset of flow instabilities with the associated break up of symmetric structures with powers of two[1].

A number of methods were used to trigger the unsteady, time-dependent flow field, including (separately) the adoption of an asymmetric inlet velocity profile, a high Mach number and an irregular wall. All produced qualitatively similar results, effectively breaking the symmetry and producing disturbed flow regimes. The results of section 3.4.4 used a rough wall and hence indicate that the symmetry of the geometry is not a contributor to the regular vortex structures observed upstream of the disturbed region. Figures 3.28 and 3.29 show many similarities. The unsteady nature of the flow seen experimentally is captured in the simulations. The onset of disturbance, marked by the recirculation region is shown to oscillate up and down the tube and this is also noted in the numerical study by Sherwin and Blackburn [106].

In order to make a more detailed comparison between the two sets of results, a full study of the flow solutions should be performed to extract statistical data to characterise the flow disturbances. This is considered beyond the scope of the current work, for which the focus is the development of the modelling framework for integration of biological processes.

---

[1] Based on discussions between Joerg Bernsdorf, NEC Europe Ltd. and Jovan Jovanovic, LSTM Institute of Fluid Mechanics, Erlangen.

Chapter Four: Diffusion

4.1 Introduction

The thrombosis models developed in this study rely heavily on the process of diffusion. As will be discussed in Chapter 5, the simplest model studied, in which clot formation is triggered by the age of the fluid, uses a passive scalar to trace this parameter. In the more complex models in subsequent chapters, further developments are made to simulate the transport of pro-coagulant proteins of the coagulation cascade as well as normal and activated platelets. These are also represented as species concentrations, because their density is similar to that of the elements of the carrier fluid, blood. This is a common technique employed for representation and simulation of the process of thrombosis; therefore it is necessary to be able to incorporate a reliable convection-diffusion algorithm into the lattice Boltzmann fluid flow solver.

BEST, the lattice Boltzmann code used for the majority of the simulations presented in this thesis, includes an implementation of the diffusion algorithm reported in Flekkoy [113] and Flekkoy *et al.* [114]. It was found that, with this implementation, there was a lower bound on the diffusion coefficient, below which the scheme became unstable (exhibiting negative species concentrations). In order to address this issue a (more stable and potentially less diffusive) first order upwind scheme was introduced and results compared with those for the Flekkoy model.

The emphasis in the current programme of work is on the development of the framework for modelling the interaction of physical and biochemical processes in thrombosis. Nevertheless, diffusion of chemical species is one of the important physical processes, and limitations in the diffusion model will limit the potential for realistic simulation of these events. This chapter outlines the work performed in assessing the strengths and weaknesses of the original model proposed by Flekkoy [113, 114] in relation to other standard diffusion models. However, it should be noted that the framework under development is not tied to any particular diffusion model and that incorporation of alternative diffusion algorithms at some point in the future would not require any changes to the model infrastructure.

A review of the literature was performed in order to outline previous lattice Boltzmann simulations with convective-diffusive systems.

4.2 Literature Review

This brief review aims to explore the methods of previous researchers choosing to model convective-diffusive systems in lattice Boltzmann simulations. Of interest in this study is the simulation of passive-scalar tracer species. These species require knowledge of the velocity field in order to calculate the new concentration distributions, but do not feedback the concentration distributions for subsequent calculations of velocities. As will be discussed later in this chapter, any scheme for solving the convection-diffusion equation can be used alongside the lattice Boltzmann algorithm for solving the flow. In the literature, there appear to be two methodologies; the first is the direct incorporation of the species transport equation into the lattice Boltzmann schema and the second is the invocation of a separate convection-diffusion solver using the velocity fields from the LB solution at each time increment.

Cali *et al.* reinterpreted the lattice Boltzmann equation in order to model tracer diffusion [115] in 1992. In this model, tracer dynamics are included by considering a 4D face-centred hypercubic lattice. The distributions are then projected onto a 3D lattice to obtain the flow field which results in the self-transport of the fourth component of the flow, such that it is convected as a passive scalar by the 3D flow. Further details of the 4D face-centred hypercubic lattice can be found in the book by Succi [28]. The diffusion coefficient is therefore equal to the kinematic viscosity. This model was demonstrated with simulations of diffusion in fractal media and convective-diffusion in parabolic flow.

In 1996, Weimar and Boon [116] took advantage of the fact that transport of a fluid using the lattice Boltzmann method introduces a numerical diffusion of the advected species. The diffusion is controlled by introducing additional diffusive steps. The species transport is performed using distributions on a reduced grid. The distributions and directions are calculated as shown in table 4.1.

Direction	Transported distribution of species
$\rightarrow$	$D+\frac{ux}{2}$
$\uparrow$	$D+\frac{uy}{2}$
$\leftarrow$	$D-\frac{ux}{2}$
$\downarrow$	$D-\frac{uy}{2}$
$\bullet$	$1-4D$

Table 4.1: Velocity configuration for the species and weights depending on the diffusion coefficient D and the velocity $\mathbf{u}=(u_x,u_y)$, taken from Weimar and Boon [116].

The additional diffusion step can be performed one or more times by transporting a fraction D to each of the neighbours, with the rest fraction as given in table 4.1. The range of diffusion coefficients that can be used in this model are $\frac{1}{2}|\mathbf{u}|<D<\frac{1}{4}$ in order to avoid instabilities.

In 2000, van der Sman and Ernst [117] presented a lattice Boltzmann convection-diffusion scheme for use on irregular lattices. The transport of the tracer is directly related to that of the fluid; hence the diffusion coefficient is again equal to the kinematic viscosity. The results were compared to more traditional finite difference and finite element methods. This scheme accurately resolves the analytical solution of a 1D benchmark problem if the grid Peclet number is low $(Pe\leq 1)$, but spurious oscillations are seen if larger values are used. These can be reduced using grid refinement methods, which locally reduce the grid spacing and hence the local grid Peclet number, which is defined as $Pe(x)=\frac{u\Delta x(x)}{D}$. This agrees with work to be described later in this chapter. Results of this model are shown for the case of a moving 1D Gaussian distribution of species and a 2D Gaussian moving at an angle to the grid with grid Peclet numbers of up to 1000. The disadvantage of this model however is that the diffusion coefficient is equal to the kinematic viscosity, but in practice, this can be set in order to obtain the required diffusion before setting the

kinematic viscosity. Grid refinement is clearly an advantage of this model as will be discussed in later sections of this chapter.

Merks *et al.* [118] analysed the limits of the moment propagation method of solving the convection-diffusion equation within a lattice Boltzmann solver. This method transports a single scalar between lattice points based on the local velocities and the probability of transport governs the diffusion coefficient. A single scalar at each lattice point reduces the computational load compared to having many directions of scalars. The moment propagation method was then adapted by adjusting the tracer in accordance with the equilibrium distribution of a stationary fluid, which allowed for higher Peclet numbers to be reached, with an increase factor in the range 1.3-1.7. Both methods were analysed against the Taylor-Aris solution for dispersion in 3D parabolic flow with excellent agreement.

Further lattice Boltzmann models are available [113, 114, 119, 120] and will be discussed in later sections of this chapter.

4.3 The Convection Diffusion Equation

The convection diffusion equation can be written in vector notation as shown in equation 4.1.

$$\frac{\partial \phi}{\partial t} = D\nabla^2\phi - \mathbf{u}\cdot(\nabla\phi) \qquad \textbf{4.1}$$

In equation 4.1, ϕ represents the concentration of the species, D is the diffusion coefficient and $\mathbf{u}$ is the vector of velocity. For simplicity of the following discussions, this is expanded as shown in equation 4.2.

$$\frac{\partial \phi}{\partial t} = D\left[\frac{\partial^2\phi}{\partial x^2} + \frac{\partial^2\phi}{\partial y^2} + \frac{\partial^2\phi}{\partial z^2}\right] - u\frac{\partial \phi}{\partial x} - v\frac{\partial \phi}{\partial y} - w\frac{\partial \phi}{\partial z} \qquad \textbf{4.2}$$

where u, v and w represent the x, y and z components of velocity respectively.

4.4 Flekkoy Model

The transport of species in the convection-diffusion algorithm proposed by Flekkoy [113] and Flekkoy *et al.* [114] is directly analogous to the transport of distributions within the lattice Boltzmann method. This preserves the "*algorithmic simplicity*" of the BGK models.

The previously described flow equations used in the lattice Boltzmann method (eqns. 4.3 and 4.4) are shown along with the associated transport equations used for the convection and diffusion of the massless species (eqns. 4.5 and 4.6)

$$f_i(\vec{x}+\Delta t\vec{c}_i, t+\Delta t) = f_i(\vec{x},t) + \omega(f_i^{eq}(\vec{x},t) - f_i(\vec{x},t)) \qquad \textbf{4.3}$$

$$f_i^{eq}(\rho,\vec{u}) = t_p\rho\left(1+\frac{\vec{c}_i\cdot\vec{u}}{c_s^2}+\frac{(\vec{c}_i\cdot\vec{u})^2}{2c_s^4}-\frac{\vec{u}\cdot\vec{u}}{2c_s^2}\right) \qquad \textbf{4.4}$$

$$\Delta_i(\vec{x}+\Delta t\vec{c}_i, t+\Delta t) = \Delta_i(\vec{x},t) + \omega_D(\Delta_i^{eq}(\vec{x},t) - \Delta_i(\vec{x},t)) \qquad \textbf{4.5}$$

$$\Delta_i^{eq} = t_i\phi\left(1+\frac{\vec{c}_i\cdot\vec{u}}{c_s^2}\right) \qquad \textbf{4.6}$$

Δ_i represents the set of distributions for the tracer species.

The kinematic viscosity and diffusion coefficient are determined by the relaxation parameters through the following relationships.

$$\nu = \frac{1}{6}\left(\frac{2}{\omega}-1\right) \qquad D = \frac{1}{6}\left(\frac{2}{\omega_D}-1\right) \qquad \textbf{4.7}$$

Flekkoy measured the relaxation of a sinusoidal concentration profile in order to obtain the diffusion coefficient and found agreement with the implemented

diffusion coefficient for values greater than approximately $D = 1 \times 10^{-4} L^2 T^{-1}$ [113]. In 1995, Flekkoy identified regions of negative concentration for diffusion coefficients lower than this value [114].

In the model implemented in the lattice Boltzmann code used in this study, a reduced lattice was used for the species. This is based on work by Stockman *et al.* [121] and considers transport along only the Cartesian directions.

4.5 Limitations of the Flekkoy Model

In order to test the limits of the Flekkoy model, a set of two-dimensional simulations have been devised. These explore the range of diffusion coefficients that can be used and also monitor the subsequent transport of the species through the domain. In section 4.6, other standard convection-diffusion algorithms are described along with corresponding results to allow for comparisons to be made.

4.5.1 Continuous injection of a source at one lattice point

A 2D channel of dimensions 200×40 was used with plug flow at a Reynolds number of approximately 2. Periodic wall boundary conditions were applied and the converged flow solution obtained. Following this, a source of species with a concentration of $1 ML^{-3}$ (mass concentration) was placed in the middle of the channel and the converged species distribution obtained. As the diffusion coefficient of the species is lowered, the magnitude of the negative concentration values increases and the criterion used in this study was that after 1×10^5 iterations, the ratio of the magnitudes of the maximum negative and maximum positive values must be lower than 0.1%. For the simulation parameters given above, the limiting diffusion coefficient was found to be $7 \times 10^{-4} L^2 T^{-1}$ (to the nearest $0.5 \times 10^{-4} L^2 T^{-1}$).

It was believed that this value would depend upon the lattice parameters used, but care must be taken because altering the lattice parameters for the same

equivalent real simulation has the effect of altering the conversion factors between lattice units and real units.

The grid size was doubled to 400×80 lattice points, hence either the velocity or the viscosity needed to change accordingly in order to keep the Reynolds number the same, hence the latter problem is a discretised version of the former. First the velocity was lowered and a limiting diffusion coefficient of $3.5 \times 10^{-4} L^2 T^{-1}$ (to the nearest $0.5 \times 10^{-4} L^2 T^{-1}$) was found. Second, the viscosity was increased and a limiting value of $7 \times 10^{-4} L^2 T^{-1}$ (to the nearest $0.5 \times 10^{-4} L^2 T^{-1}$) was found. In terms of the values in *real* units, the latter values are equal, being half the original limiting value.

This means that regardless of the parameters changed when using a finer grid, the limiting value of diffusion coefficient is inversely proportional to the number of grid points across the width of the channel, hence using a finer grid allows for lower diffusion coefficients to be used. To verify this conclusion, two further simulations were performed using the original grid dimensions of 200×40 but with different combinations of velocity and viscosity. The *real* limiting diffusion coefficients remained constant; hence no reduction in the limiting value was seen. In all these cases, the ratio of lattice velocity and limiting diffusion coefficient was found to be constant with a value of approximately 1.4. An example of the converged concentration distribution using the limiting value of diffusion coefficient (grid Peclet number) is shown in figure 4.1 for the original lattice parameters. It must be remembered that improvements can be seen, i.e. lower diffusion coefficients can be obtained if a finer grid is used.

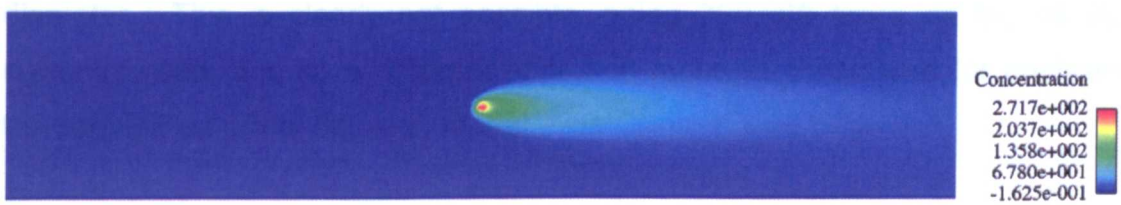

Figure 4.1: Converged concentration distribution for continuous source injection with minimum stable diffusion coefficient.

In order to extend this investigation, a higher Reynolds number of approximately 100 was chosen and the original grid of dimensions 200×40 was used. The

Reynolds number was increased by increasing the lattice velocity to $0.05LT^{-1}$ which is the upper limit for lattice Boltzmann simulations. The limiting diffusion coefficient was found to be $3.5\times10^{-2}L^2T^{-1}$ (to the nearest $0.5\times10^{-2}L^2T^{-1}$). The ratio of lattice velocity and limiting diffusion coefficient is again approximately 1.4 as for all the previous simulations.

The real Peclet number is equal to the lattice Peclet number because this is a dimensionless parameter and is given by the following equation:

$$Pe = \frac{ul}{D} \qquad \textbf{4.8}$$

where u is a typical velocity, l is a typical length scale and D is the diffusion coefficient.

It is not appropriate in this case to consider what the typical length scale may be because the problem is detached from real length scales by the periodic boundaries. However, in lattice units, the ratio of u and D in the limiting case has been found to be constant at approximately 1.4. This means that the *real* Peclet number can only be increased if the grid is refined. More importantly, for a particular *real* problem, the *real* diffusion coefficient can only be reduced by refining the grid. As an indicator of how severe this problem is, a quick calculation shows that for a 2D channel, for a Reynolds number of 100 using the flow parameters of the stenosis problem (Chapter 3), to achieve a typical *real* diffusion coefficient of order $1\times10^{-13}m^2s^{-1}$ for the components of blood [122], approximately 30 million lattice points would need to be used across the diameter. This is clearly not possible, being 300,000 times as big as that currently used, and so a different approach must be considered for analysing the capabilities of the diffusion model.

Instead of imposing such a strict limit on the *real* diffusion coefficient, a more relaxed approach can be considered relating to the activity within the domain. This is the topic of the following section.

4.5.2 Convection of a single finite mass of species

It is perhaps more appropriate to consider how an injected mass of species is transported out of the domain, rather than observing the behaviour of a constant source. If a clottable species is produced somewhere in the domain, it should be washed out unless it is trapped within an area of retarded or recirculating flow. The diffusion coefficient can be chosen by specifying limits on the amount of the species that must be present within a given area when the transported mass has reached the outlet. Three theoretical approaches have been considered and will be used to obtain new lower limits for the *real* diffusion coefficients, based on the model parameters.

If a mass M_0 is injected to an infinitesimally small region of space (area or volume) at time t_0, for the case of zero velocity, a solution exists for the concentration as a function of time and radial distance from the source. The solution must satisfy the diffusion equation given below in plane polar (radial) coordinates.

$$\frac{\partial \phi}{\partial t} = D\nabla^2 \phi \qquad \textbf{4.9}$$

$$\frac{\partial \phi}{\partial t} = D\left[\frac{\partial^2 \phi}{\partial r^2} + \frac{1}{r}\frac{\partial \phi}{\partial r}\right] \qquad \textbf{4.10}$$

In equation 4.10, symmetric diffusion is assumed and angular variations are not considered.

The solution for the 2D diffusion of a point mass is formulated by assuming a Gaussian distribution and adapting the equivalent 3D solution [123]:

$$\phi(r,t) = M_0 \frac{\exp\left(-\frac{r^2}{4Dt}\right)}{(4\pi Dt)} \qquad \textbf{4.11}$$

To verify that this is a solution of the diffusion equation, equation 4.11 is inserted into equation 4.10.

For completeness, the equivalent solution for 3D spherical diffusion [123] is:

$$\phi(r,t) = M_0 \frac{\exp\left(-\frac{r^2}{4Dt}\right)}{(4\pi Dt)^{\frac{3}{2}}} \qquad \textbf{4.12}$$

This can also be inserted into equation 4.10 for verification.

These equations (4.11 and 4.12) represent the solution for diffusion in the absence of convection. The coefficients of diffusion of the blood-related chemical species in the carrier fluid are quoted in the literature and are generally very low (e.g. for platelets, $1.6\times10^{-13} m^2 s^{-1}$ [122]) causing numerical instability in the lattice Boltzmann simulations. In the context of the current project, there is a natural characteristic timescale represented by the transit time through the domain of an element of fluid in the bulk flow. Test simulations are described below, based on the stenosis geometry reported in Chapter 3 ($1214\times98\times98$) where the characteristic times are $t_{100} = 2.7\times10^5$ iterations = 1.89s for a Reynolds number of 100 and $t_{550} = 4.9\times10^4$ iterations = 0.34s for a Reynolds number of 550, in the case of $\omega = 1.95$. Taking the simplest possible approach, if the system is to be convection-dominated the Peclet number must be maintained above unity, and thus if the characteristic length is taken to be that of the domain, the requisite diffusion coefficient must be less than $D = 0.4274 L^2 T^{-1}$ with a Reynolds number of 100 and $D = 2.3504 L^2 T^{-1}$ with a Reynolds number of 550. Of course the area of interest for clot simulation is the recirculation zone, and in this region the true Peclet number, using real diffusion coefficients and typical length and velocity scales, is of the order of $Pe = 1\times10^8$.

To develop an appreciation of the performance of the diffusion models a series of simple test cases were studied. Assuming that in the bulk flow diffusion is negligible, it is reasonable to specify that the code must be able to handle a diffusion coefficient that would correlate to a reduction in concentration of a

marker species in a small bolus of fluid of less than 1% as it is convected through the fluid domain. Unfortunately the analytical solution available corresponds only to the diffusion of the theoretical point delta function, and in practice this cannot be achieved on a discrete grid. Three approximations were considered, each yielding slightly different values of the '1% diffusion limit' for this problem.

1) If a species is injected at a point, the initial concentration there is theoretically infinite. However, in a discrete grid, the smallest area over which a mass of species can be injected is 1 square lattice unit, hence the concentration is finite. If a concentration of 1 (mass/area) is injected to a single lattice point, the injected mass, M_0, is also 1 (lattice units). Equation 4.12 can be used, assuming that the theoretical situation, where an infinite concentration is injected, can be approximated. The simplest approach is to calculate the diffusion coefficient that would correspond to the reduction of the concentration at the centre from unity to 0.99 over the characteristic time, for which, the following values are obtained.

Re = 100: $D = 2.99 \times 10^{-7} L^2 T^{-1} = 2.97 \times 10^{-10} m^2 s^{-1}$

Re = 550: $D = 1.64 \times 10^{-6} L^2 T^{-1} = 1.63 \times 10^{-9} m^2 s^{-1}$

These values have been converted from lattice to SI units using the discretisation parameters for the stenosis model and the viscosity of blood, just to obtain an estimate of the corresponding values.

2) Instead of considering the peak concentration of the diffused species, an alternative condition is to constrain an integral of the concentration so that a stated percentage of the mass should be conserved within a certain area over the characteristic time. This requires integrating equation 4.12 to find the mass between two specified limits. The condition imposed is that 99% of the injected mass must be within an area encompassed by a radius of 0.5 lattice units, hence the original injection area, and this yields diffusion coefficients as follows.

Re = 100: $D = 5.03 \times 10^{-8} L^2 T^{-1} = 5.00 \times 10^{-11} m^2 s^{-1}$

Re = 550: $D = 2.77 \times 10^{-7} L^2 T^{-1} = 2.75 \times 10^{-10} m^2 s^{-1}$

3) The final approximation considered involves first the computation, using the governing equation, of a concentration profile containing the same total mass as that of a uniform 'block' of concentration injected over an area of 1 lattice unit. This profile would have evolved from the initial delta function over a time t_1, and would evolve further over time to another, more diffuse profile and a conservation condition can then be applied. The condition imposed is that the mass of species at the end of the simulation (time *t*) within a circle of radius of 0.5 lattice units is 99% of the mass applied. The difference between this approach and the 2nd approach is that the initial condition in the simulation is equivalent to a theoretical solution after time t_1. This means that the final solution will be at time $t_2 = t_1 + t$ where t_1 must be calculated. Two simultaneous equations must be solved based on the condition described above and the condition that the profile at time t_1 has a mass of only $1 \times 10^{-6} M_0$ in the tails. Therefore there is very little difference between the mass injected in the simulation over a square area and the mass within a circle of radius 0.5 lattice units of the Gaussian solution which is assumed to be formed from the infinite pulse after time t_1. This is best understood with a diagram (figure 4.2).

In this approach, it is assumed that the injected 'block' is equivalent to a Gaussian where the mass in the tails, defined as the region outside of the circle of radius 0.5 lattice units, is only $1 \times 10^{-6} M_0$. This Gaussian will be equivalent to a Gaussian profile formed from an infinite pulse with a certain diffusion coefficient after a certain time, t_1. This leads to one of the simultaneous equations. The second equation comes from ensuring that at time t_2, 99% of the mass is in an area of circle radius 0.5 lattice units. The time t is that given previously as the average transport time for fluid passing through the domain. Solving these equations gives the following values of diffusion coefficient:

Re = 100: $D = 3.35 \times 10^{-8} L^2 T^{-1} = 3.33 \times 10^{-11} m^2 s^{-1}$ $\quad t_1 = 1.35 \times 10^5 : t_2 = 4.05 \times 10^5$

Re = 550: $D = 1.42 \times 10^{-6} L^2 T^{-1} = 1.41 \times 10^{-9} m^2 s^{-1}$ $\quad t_1 = 2.45 \times 10^4 : t_2 = 7.35 \times 10^4$

Figure 4.3 shows the concentration profiles for the Re=100 case. It must be remembered that it is the *area* integral of these curves that is used to calculate the mass within the required regions and not just the radial integral.

Simulation:

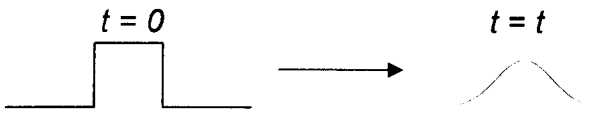

Theory:

Approach 3:

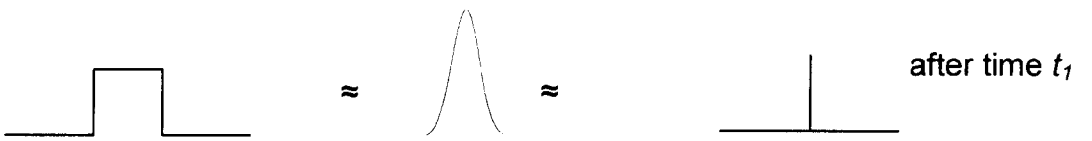

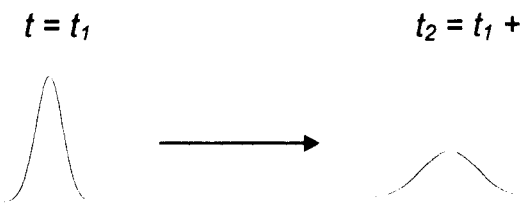

Figure 4.2: Diagrammatic representation of approach 3 described in text regarding the spread of Gaussian curves.

The conclusion of this work is that it might be possible to increase the diffusion coefficients slightly, from those typical of the blood elements, whilst still maintaining the essential characteristics of the problem.

In order to view the theoretical work in light of the capabilities of the LB code, a 2D simulation was performed where a mass of 1 unit was applied to a converged flow solution for 1 iteration. The lattice had dimensions of 1214x98

(hence equal to a 2D version of the lattice used for the 3D stenosis model) and a Reynolds number of 100 was used.

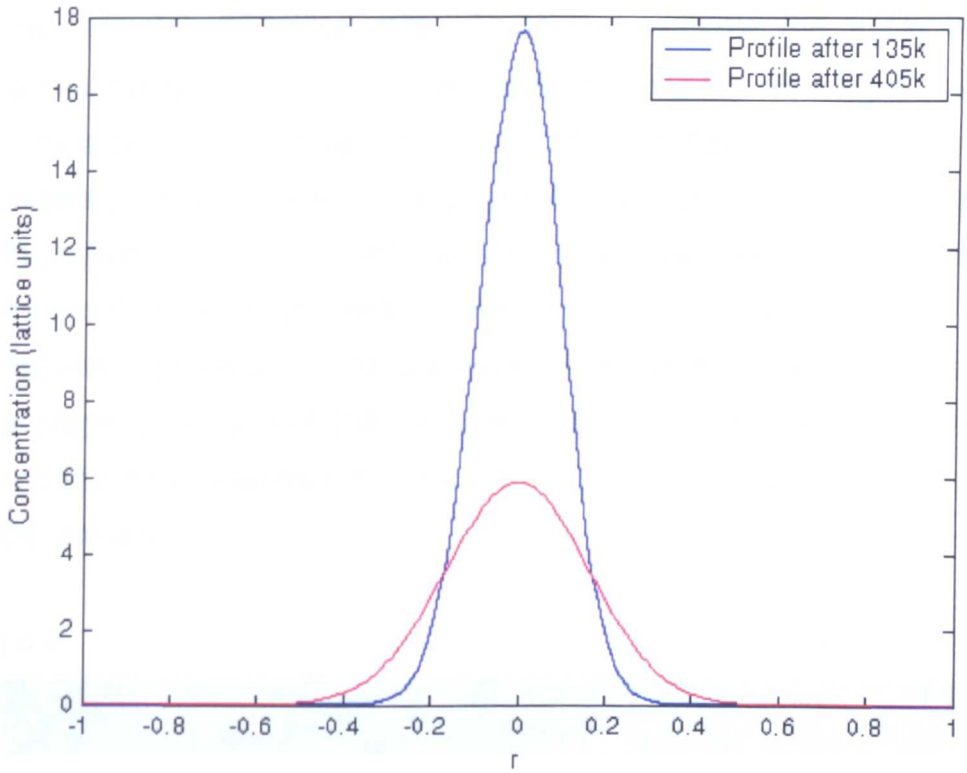

Figure 4.3: Profiles corresponding to approach 3 for Re = 100. Profile after 1.35×10^{5} iterations is equivalent to the 'block' profile applied in the simulation as regards its extent.

The diffusion coefficient used was the lowest stable value, found to be $5\times10^{-4}\,L^{2}T^{-1}$ (to the nearest $0.5\times10^{-4}\,L^{2}T^{-1}$) = $4.97\times10^{-7}\,m^{2}s^{-1}$. This is at least two orders of magnitude higher than that indicated by the calculations presented above to correspond to a '1% diffusion limit' for this system. Taking the length of the domain to be the characteristic length, this results in a Peclet number of $Pe = 855$. The subsequent transport was then monitored. In order to obtain a faster flow convergence, bounceback wall boundary conditions were used. This is more appropriate when considering the realistic simulations and clotting models. This simulation was performed to provide a *qualitative* illustration of the amount of diffusion present. Figure 4.4 shows the species being transported from the inlet to the outlet. Note how the colour bar scale changes.

Given the above calculations, the results were no surprise. It is visually clear that the system is diffusion dominated, and that 99% of the original mass is not

contained within the area surrounding 1 lattice point. The simultaneous equations formulated for approach 3 can be used to calculate the associated radius within which 99% of the species exists and this results in a value of approximately 60 lattice units. As another example, the profile of the species concentration after 1.6×10^5 iterations is plotted in figure 4.5 and should be compared to the theoretical profiles plotted in figure 4.3 where the scale is 4 orders of magnitude larger. Figure 4.4 suggests much faster transport through the system and this is because a parabolic inlet velocity profile is used. This means that fluid in the centre of the domain will be travelling at 1.5 times that of the average velocity. All theoretical calculations were performed using the average velocity, but this error is negligible in these circumstances. It is important to remember that a clottable species could be injected anywhere in the domain.

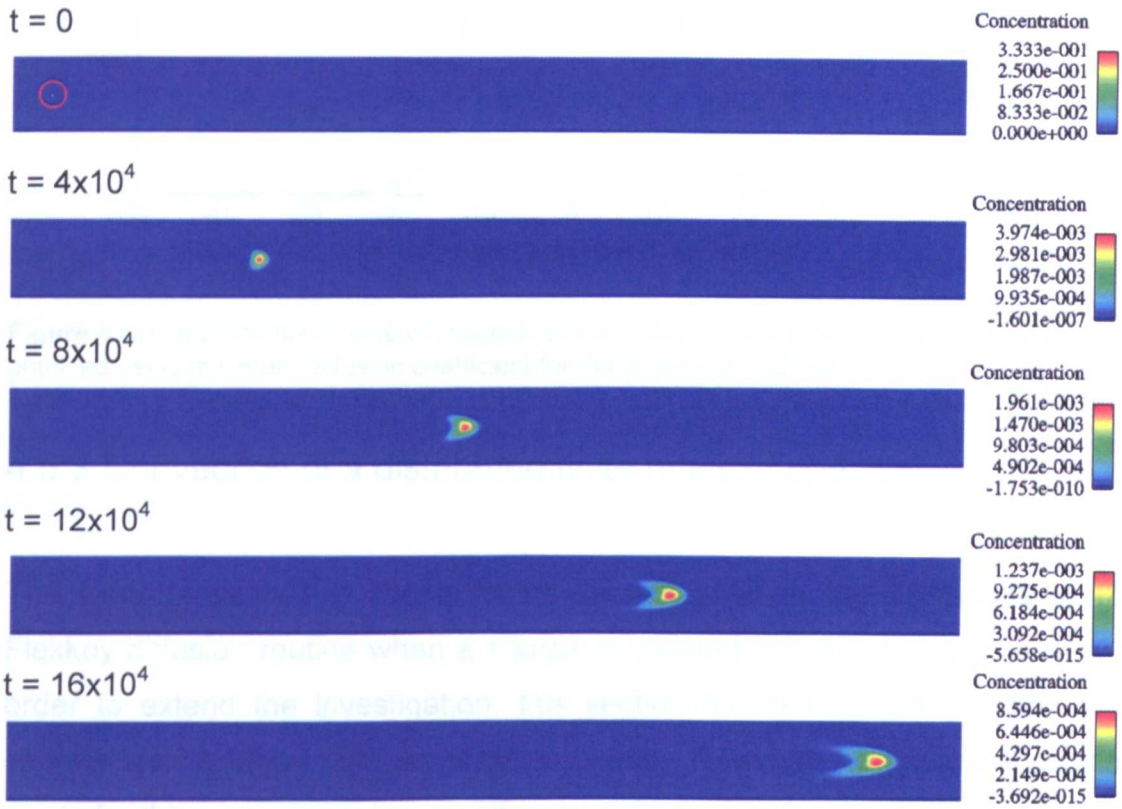

Figure 4.4: Downstream transport of species injected to a single lattice point with limiting diffusion coefficient. Red circle in first image indicates location of injection.

The techniques used in this section have the advantage that approximations to the theoretical solutions exist. However, this simulation may be unstable due to the small injection area and associated high gradients. For this reason, a larger injection area will be considered in the following section. All methods reported

in this chapter can however be used to compare different convection-diffusion algorithms since the advantages or disadvantages of the techniques will be present in all cases.

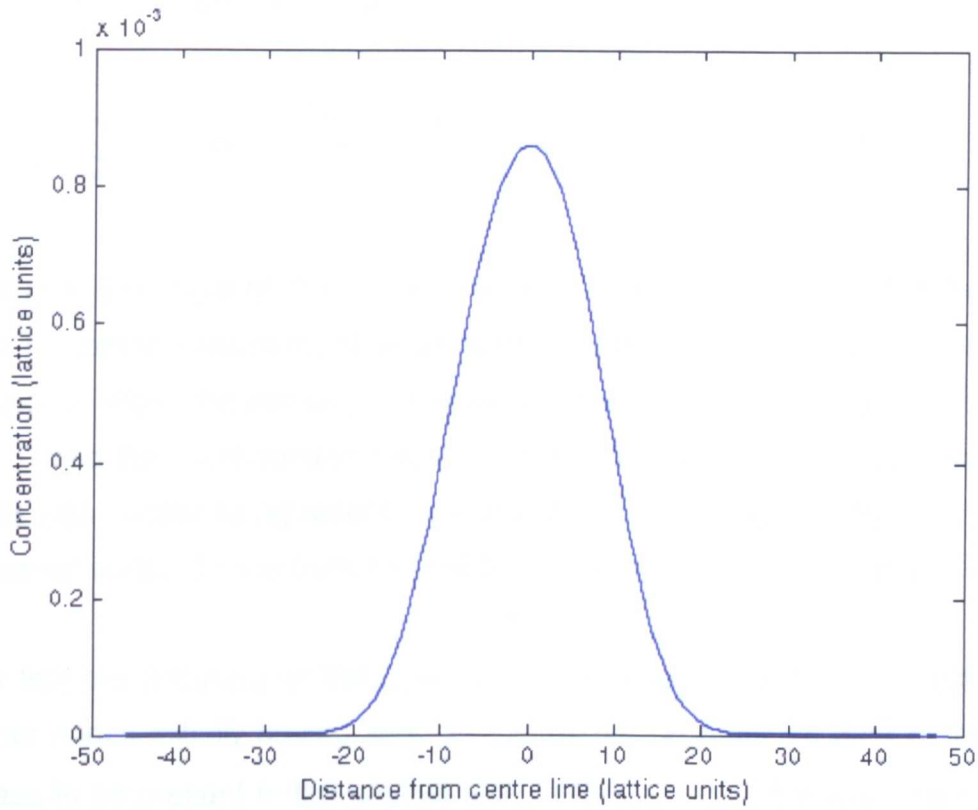

Figure 4.5: Concentration profile of injected species after 1.6×10^5 iterations. LB solution obtained using minimum diffusion coefficient for this particular grid size.

4.5.3 Convection of a distributed finite mass of species

The work presented in the previous section showed the limitations of the Flekkoy diffusion routine when a source is injected to a single lattice point. In order to extend the investigation, this section focuses on the injection of a species over a larger number of lattice points. However, no analytical solution exists for this problem and so an alternative method of comparison is required.

A solver has been written in Matlab which can be used to predict the values of diffusion coefficient needed for this new problem. This uses radial symmetry for simplicity, which allows for the use of a one-dimensional model. The equation to be solved is that given previously (4.10) for diffusive transport. A numerical representation, based on a first order backward Euler (implicit) discretisation in

time and a second order central difference in space, is presented in equation 4.13.

The implicit Matlab code was used to solve a discretised version of equation 4.10, where h represents the spatial discretisation.

$$\left[\frac{-2rD+Dh}{2rh^2}\right]\phi_{i-1,j}+\left[\frac{h^2+2Ddt}{h^2dt}\right]\phi_{i,j}+\left[\frac{-2rD-Dh}{2rh^2}\right]\phi_{i+1,j}=\frac{1}{dt}\phi_{i,j-1} \qquad \textbf{4.13}$$

There is a singularity at $r = 0$ but this is dealt with by ensuring that the mass in the system is conserved, thus an approximate to an area integral is solved for the case when the species is injected over a circular area. The first node is at $r=0$ and the initial condition is that the first 5 nodes have a concentration of 1. This was chosen to represent a circle with a diameter approximately 10% of the channel width. This is then allowed to diffuse for a set number of time steps.

To test the accuracy of the code, a single node (node 1) was injected to; all other nodes initially having zero concentration. In order for 99% of the original mass to be present in the original area, after 2.7×10^5 iterations (transport time for fluid at Re=100), a diffusion coefficient of approximately $1\times10^{-8}L^2T^{-1}$ to the nearest $0.5\times10^{-8}L^2T^{-1}$ was needed. The theoretical work presented in the previous section suggested that a value in the range $3\times10^{-8}-3\times10^{-7}L^2T^{-1}$ was needed, depending on the criterion used.

This was repeated using the initial condition described above for injecting over 5 points and the initial and final masses in the original injection area were compared. The injection region was almost 50 lattice points away from the outlet, to minimise boundary effects. Using the same criterion that 99% of the initial mass must be within the initial area ($\pi r^2=\pi\times4.5^2=20.25\pi$), a diffusion coefficient of $8.5\times10^{-8}L^2T^{-1}$ to the nearest $0.5\times10^{-8}L^2T^{-1}$ was needed. When directly comparing the results using the implicit Matlab code, it can be seen that if the injection area is larger, a *larger* diffusion coefficient can be used. This is presumably because the enclosed region of species simply cannot diffuse because there is no gradient. Figure 4.6 shows a radial concentration plot after

2.7×10^5 iterations for the limiting diffusion coefficient along with the results using higher and lower diffusion coefficients.

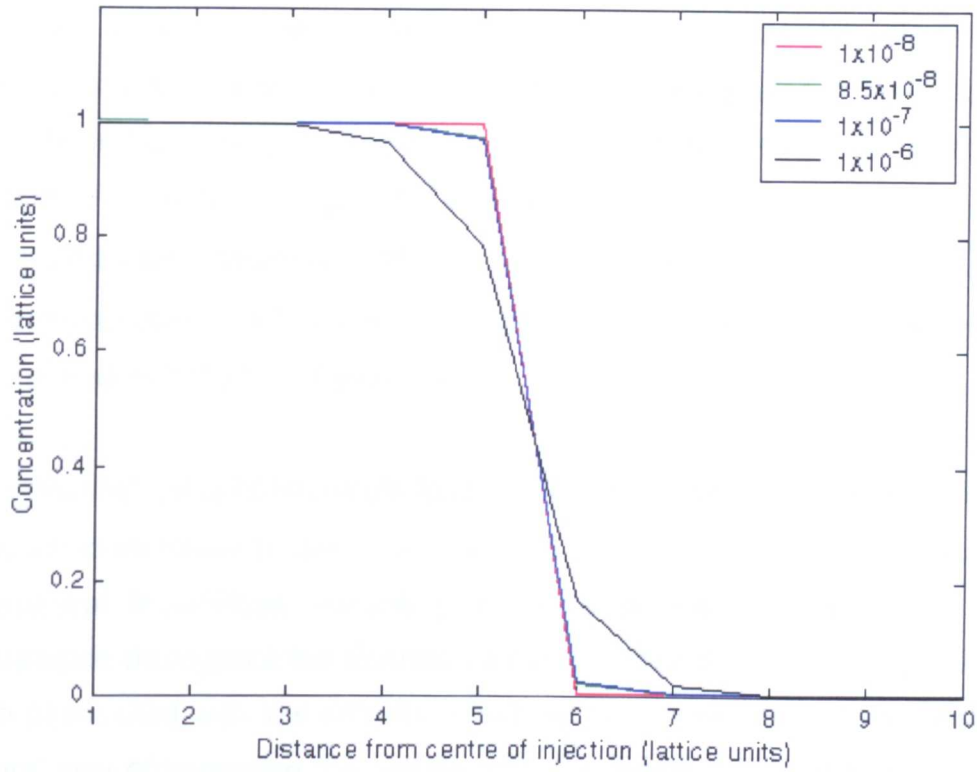

Figure 4.6: Concentration profiles for 5 injected points with different diffusion coefficients. Results obtained using implicit code for solving the diffusion equation.

An equivalent simulation was performed using the LB code: a 9×9 square block of species was injected near the inlet of a 2D channel with flow at Re = 100, in a grid with dimensions 1214×98. An attempt was made using the limiting diffusion coefficient of $8.5 \times 10^{-8} L^2 T^{-1}$. This produced negative values with a magnitude of 23% of the peak positive value, which is clearly inappropriate. The diffusion coefficient was then raised until this ratio became less than 0.1%, which occurred at $4 \times 10^{-4} L^2 T^{-1}$ to the nearest $0.5 \times 10^{-4} L^2 T^{-1}$.

When a single lattice point was injected to, the limiting diffusion coefficient was found to be $5 \times 10^{-4} L^2 T^{-1}$ to the nearest $0.5 \times 10^{-4} L^2 T^{-1}$. This therefore supports the hypothesis that the numerical problem associated with stability improves if a bigger injection area is used. This is not related to the issue discussed in the previous section concerning the theoretical limit of diffusion coefficient and the dependence on injection area. However, this study shows that for such a block, the diffusion coefficient required to transport 99% of the original mass to the

outlet is $8.5\times10^{-8}L^2T^{-1}$ whereas the lowest possible value that can be simulated is $4\times10^{-4}L^2T^{-1}$. For the injection to a single lattice point, the corresponding values are $1\times10^{-8}L^2T^{-1}$ and $5\times10^{-4}L^2T^{-1}$ respectively. This shows that as the injection area is increased, not only does the theoretical value relax slightly, but the numerical limit also improves. This essentially makes it easier to simulate the theoretical values, apart from the fact that the difference is still several orders of magnitude. Figure 4.7 shows the larger block convecting to the outlet with the limiting diffusion coefficient of $4\times10^{-4}L^2T^{-1}$. In terms of real units, this is approximately $3.97\times10^{-7}m^2s^{-1}$. The colour legends in figure 4.7 should be compared with those in figure 4.4.

In conclusion, it is not possible to obtain the low physical diffusion coefficients of the blood elements (order $1\times10^{-13}m^2s^{-1}$ [122]). The Flekkoy model suffers from numerical instabilities, exhibiting negative species concentrations that can propagate throughout the domain, under conditions of high Peclet number that are associated with low diffusion coefficients. It has been shown that the only 'pure' way of improving the results with this model is to use a larger grid. The motivation of this section was to explore the practical limitations of the Flekkoy model in the context of the modelling of the process of thrombosis. It is argued that the important physical characteristics of the problem might be adequately represented providing that the diffusion coefficient is sufficiently low that the diffusion of the species is 'not excessive', by some criterion. Two arbitrary criteria have been set to monitor the application of the Flekkoy model. The first is that negative species concentrations have been limited to 0.1% of positive values.

The conclusions of this study are very sensitive to the choice of this parameter: a reduction in achievable diffusion coefficient of four orders of magnitude is possible if this criterion is relaxed to 23%. The second arbitrary criterion of 1% has been chosen for the allowable dispersion of the species from a stated region of interest, and again the conclusions are sensitive to this parameter and a relaxation would allow a higher diffusion coefficient to be used whilst still capturing the physical characteristics.

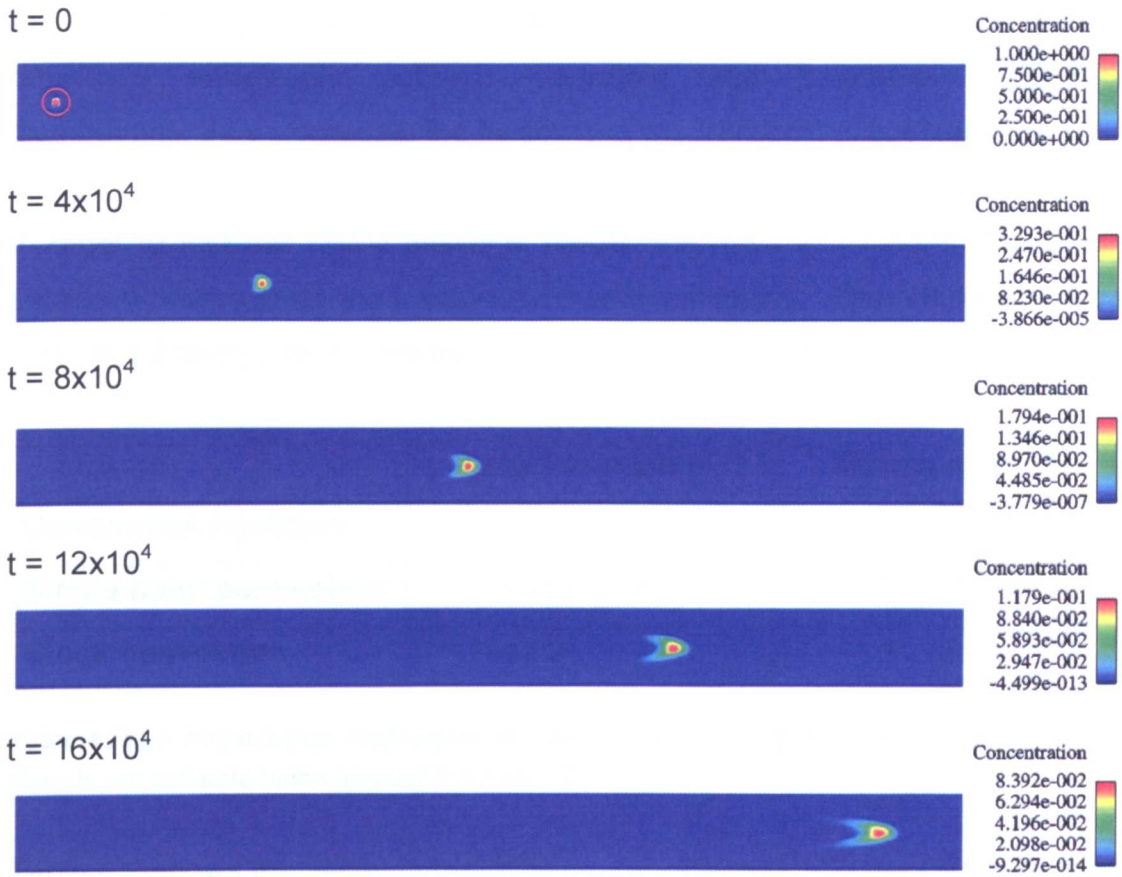

Figure 4.7: Downstream transport of species injected to a 9x9 square block with limiting diffusion coefficient. Red circle in first image indicates location of injection.

Firmer conclusions for a specific problem, including that of the sharp-edged stenosis that is the subject of study in this thesis can only be made by examining its own unique characteristics. Given sufficient relaxation of the imposed (an opposing) criteria it might be possible to obtain a usable model of a particular system. However, it has been demonstrated that the constraints on the Flekkoy model are such that it is worthwhile exploring alternative diffusion models, and this is the subject of the following sections.

4.6 Comparisons with Other Methods

4.6.1 Ginzburg diffusion model

A convection-diffusion algorithm developed by Ginzburg [119, 120] was implemented in the lattice Boltzmann source code[1], and was made available to

[1] This task was performed by Jan Linxweiler of the Technische Universität Carolo-Wilhelmina zu Braunschweig.

the current programme of study towards the end of the project. This model considers anisotropic collision operators and anisotropic equilibrium distributions, thus increasing the flexibility of the transport of species.

In order to test this newly available model, the main simulations described in section 4.5 were performed, under the same conditions. The results are shown in table 4.2 alongside the results using the Flekkoy model.

	Flekkoy model	**Ginzburg model**
Continuous injection	$7\times10^{-4}\,L^2T^{-1}$	$6\times10^{-4}\,L^2T^{-1}$
Single point convection	$5\times10^{-4}\,L^2T^{-1}$	$2\times10^{-4}\,L^2T^{-1}$
Block convection	$4\times10^{-4}\,L^2T^{-1}$	$1.5\times10^{-4}\,L^2T^{-1}$

Table 4.2: Limiting diffusion coefficients for Flekkoy and Ginzburg convection-diffusion models. Results are accurate to the nearest $0.5\times10^{-4}\,L^2T^{-1}$.

Table 4.2 shows that slight improvements are obtained with the Ginzburg model in terms of the minimum diffusion coefficients that can be obtained, but the improvements are not sufficient to allow for the true diffusion coefficients of the blood elements to be used.

4.6.2 Central differencing model

A more traditional method of solving the convection-diffusion equation has been investigated, which uses central differencing methods for obtaining the gradient terms of the discretised form of the convection-diffusion equation. For this study the velocity distributions at each timestep were taken from the lattice Boltzmann flow solution, and the convection diffusion equation was solved in a separate step, assuming that the species concentrations were scalars that did not affect the flow. In practice, and for efficiency, this equation was solved concurrently with the flow solve.

The convection-diffusion equation to be solved is given in equation 4.14, which is as given previously in section 4.3.

$$\frac{\partial \phi}{\partial t} = D\nabla^2 \phi - \mathbf{u}.(\nabla \phi) \qquad \textbf{4.14}$$

In equation 4.14, ϕ represents the concentration of the species, D is the diffusion coefficient and $\mathbf{u}$ is the vector of velocity. For simplicity of the following discussions, this is expanded as shown in equation 4.15.

$$\frac{\partial \phi}{\partial t} = D\left[\frac{\partial^2 \phi}{\partial x^2} + \frac{\partial^2 \phi}{\partial y^2} + \frac{\partial^2 \phi}{\partial z^2}\right] - u\frac{\partial \phi}{\partial x} - v\frac{\partial \phi}{\partial y} - w\frac{\partial \phi}{\partial z} \qquad \textbf{4.15}$$

where u and v represent the x and y components of velocity respectively.

The gradients are calculated using the following equations, which show those in the x direction [124]. Similar results are obtained for the orthogonal directions.

$$\frac{\partial \phi}{\partial x} = \frac{\phi_{i+1,j-1} - \phi_{i-1,j-1}}{2h} \qquad \textbf{4.16}$$

$$\frac{\partial^2 \phi}{\partial x^2} = \frac{\phi_{i-1,j-1} - 2\phi_{i,j-1} + \phi_{i+1,j-1}}{h^2} \qquad \textbf{4.17}$$

The central-difference approximation to the convection-diffusion equation is unconditionally unstable in the absence of diffusion [124]. This suggests that a limit exists depending on the velocity and diffusion coefficient. The central-difference approximation is of second order accuracy in space.

Implementation of equation 4.15 in the LB code involved using the adjacency vector to obtain the node numbers of the neighbouring nodes, in order to calculate the gradients. The value of h is always 1 in the current LB code and the default option is $dt = 1$, although this can be altered, as explained later. The inlet and outlet boundary conditions were also changed to account for the fact that only concentrations, and not distributions, are set.

In order to test the implementation, the 3 examples performed in section 4.6.1 (to test the Ginzburg model) were repeated. Table 4.3 shows comparisons between the results of the central-difference approach along with the previously obtained results from the Flekkoy and Ginzburg models.

	Flekkoy model	Ginzburg model	Central difference model
Continuous injection	$7\times10^{-4}L^2T^{-1}$	$6\times10^{-4}L^2T^{-1}$	$2.5\times10^{-4}L^2T^{-1}$
Single point convection	$5\times10^{-4}L^2T^{-1}$	$2\times10^{-4}L^2T^{-1}$	$9\times10^{-4}L^2T^{-1}$
Block convection	$4\times10^{-4}L^2T^{-1}$	$1.5\times10^{-4}L^2T^{-1}$	$8.5\times10^{-4}L^2T^{-1}$

Table 4.3: Limiting diffusion coefficients for Flekkoy, Ginzburg and central difference convection-diffusion models. Results are accurate to the nearest $0.5\times10^{-4}L^2T^{-1}$.

Failure of this model was again noted by the presence of large negative concentration values. These results show that there is an improvement in the first example, but the limiting value is actually worse than either the Flekkoy or the Ginzburg model for the remaining examples. Some minor investigations were performed using larger timesteps, therefore calling the diffusion routine at set intervals, but this made the results worse.

To verify this work outside the implementation in the LB flow solver, a simple example was performed using the same convection-diffusion equation in Matlab but with a simple specified flow distribution. A 2D problem with plug flow was solved with the injection of a species near the inlet. The units were equivalent to lattice units and a 50×50 grid was used. The velocity was altered and for each value, the limiting diffusion coefficient reported, using the same error criterion as for the previous examples. Two scenarios were considered, one where 100 iterations were performed for all parameter sets and another where the number of iterations was chosen (based on the velocity) such that the species could transport (by convection) a distance of 25 lattice units. The results for both cases are shown in a plot of limiting diffusion coefficient versus velocity in figure 4.8. The reason that the two lines in figure 4.8 differ is that the results are analysed after a different numbers of iterations. The errors present (negative values) are likely to amplify with a larger number of iterations, so it is perhaps more appropriate to consider the blue line (100 iterations). The gradient of this line is approximately 0.5 and this is in exact agreement with the limit given by Paolucci and Chenoweth [125] of $0\le Pe_\Delta\le2$, where Pe_Δ is the grid Peclet number, which in lattice units is simply given by $Pe_\Delta=\frac{u}{D}$, where u

is the lattice velocity and D is the diffusion coefficient. The other limit given by Paolucci and Chenoweth [125] is $\frac{Ddt}{h^2} \leq \frac{1}{2}$. With dt and h equal to 1 (giving best results as described above), this places an upper bound on the diffusion coefficient, but this is the opposite end of the scale to that being investigated.

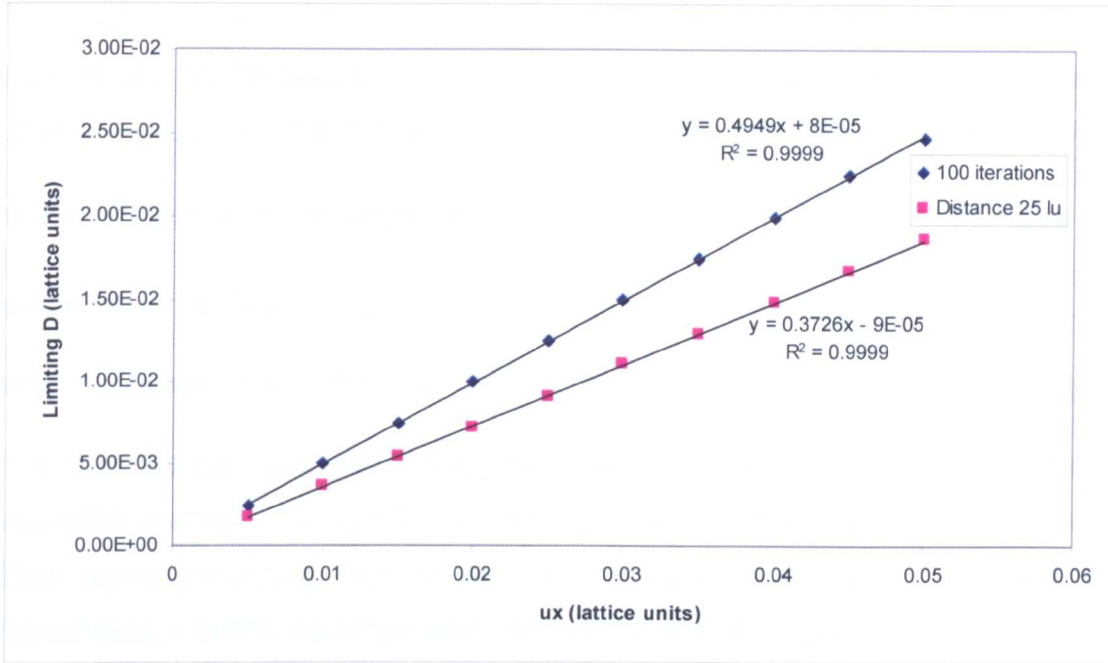

Figure 4.8: Plot to show limiting diffusion coefficients and variation with velocity. Results for 100 iterations and the appropriate number of iterations to travel 25 lattice units are shown.

4.6.3 Upwind model

Paolucci and Chenoweth [125] state that the upwind approximation of the convective term, although of only first order accuracy in space, is stable for all Peclet numbers up to infinity. The upwind gradient for use in the convective term is calculated using equation 4.18 [124, 125].

$$\frac{\partial \phi}{\partial x} = \phi_{i,t-1} - \phi_{i-1,t-1} \qquad \textbf{4.18}$$

The upwind method was introduced into the Matlab code for testing purposes and also into the LB solver. A diffusion coefficient of zero could be obtained without any negative values appearing. The three examples were repeated using this method to allow for further comparisons. The results of these are

shown in figures 4.9-4.11 alongside the previous results. The timestep was altered for the upwind model to check if any improvements could be made.

The results show that with the upwind approximation, even with a diffusion coefficient of zero, there is still a significant amount of diffusion, which occurs in the direction of the flow. This is excess diffusion caused by the convection term. Equation 4.15 shows that if there is a gradient present, a finite mass of species will be transported to the next node at the next time step. With the upwind calculation of the gradient, the concentration transported each timestep in the 1D case in the absence of diffusion, is $udt\left[\frac{\phi_{i,t-1}-\phi_{i-1,t-1}}{h}\right]$. In the case of a single point of injection as the initial condition of a concentration of 1, the amount transported to the next node at the next timestep is $\frac{udt}{h}$. The value of h is 1 in the LB code, which suggests that the value of dt can be adjusted to equal the inverse of u so that all of the species is transported to the next node. This works providing the velocity is constant everywhere. To test this hypothesis, a further example was used as described below.

Flekkoy model

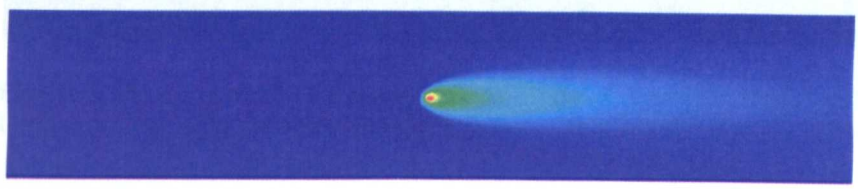

Central difference model

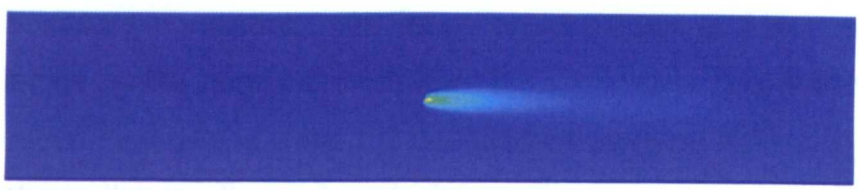

Upwind model

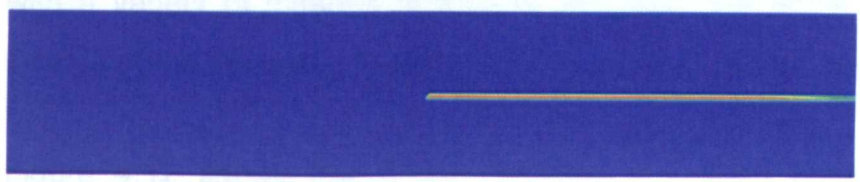

Figure 4.9: Comparison between Flekkoy, central difference and upwind models for first example using plug flow and continuous injection to a single lattice point. Results show converged species distributions.

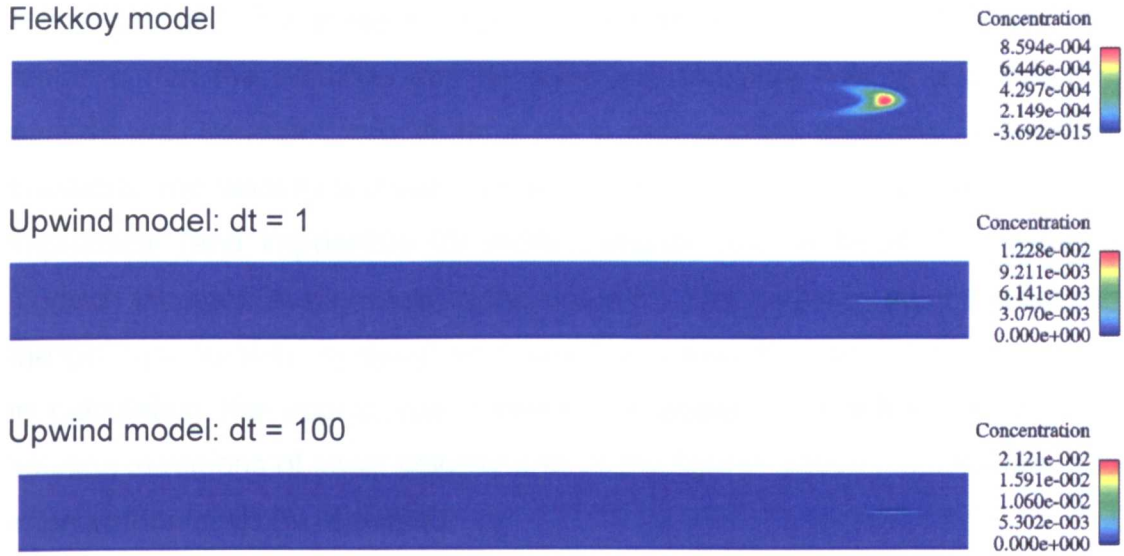

Figure 4.10: Comparison between Flekkoy model and upwind model with varying timesteps for second example using parabolic flow with a single point of injection in time and space.

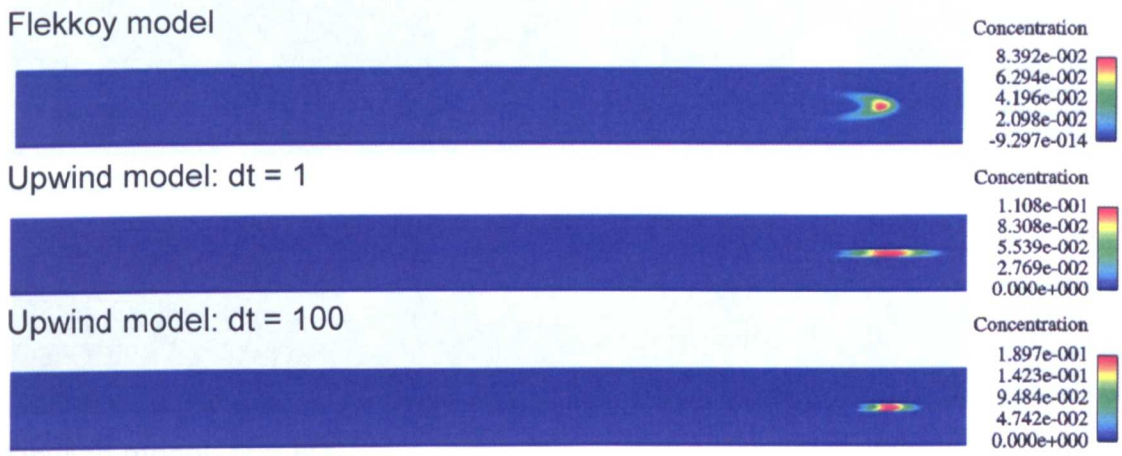

Figure 4.11: Comparison between Flekkoy model and upwind model with varying timesteps for third example using parabolic flow with a block injection as initial conditions.

To obtain the required constant velocity, plug flow was used with periodic wall boundary conditions. An initial concentration of $1ML^{-3}$ was injected to four lattice points near the inlet after the converged flow field was obtained. The lattice dimensions were 200×40 and the velocity was $1 \times 10^{-3} LT^{-1}$. Figure 4.12 shows the results produced with the Flekkoy model and with the upwind model with a variety of different timesteps, including one equal to 1000, being the inverse of the timestep. Results are shown after 1.6×10^{5} iterations.

Figure 4.12 shows that if the timestep is chosen correctly, calculated by inverting the velocity, the species can be transported without diffusion to the end of the domain. Improvements are seen using a timestep of 800 rather than

a timestep of 1, but these are not as great as expected. This is a very good result in that the diffusion can be removed, but plug flow in a channel with periodic wall boundary conditions is not a very realistic example. If the flow is parabolic, the velocity will vary across the width of the channel, thus making it impractical (and impossible for more complex velocity fields) to choose the 'correct' timestep at all points in the domain. The timestep must be such that the Courant number[1] is less than 1, which requires the use of the peak velocity in calculating the appropriate timestep. However, this will compromise the solution in regions of lower velocity and as the figures above indicate, only slight improvements will be observed.

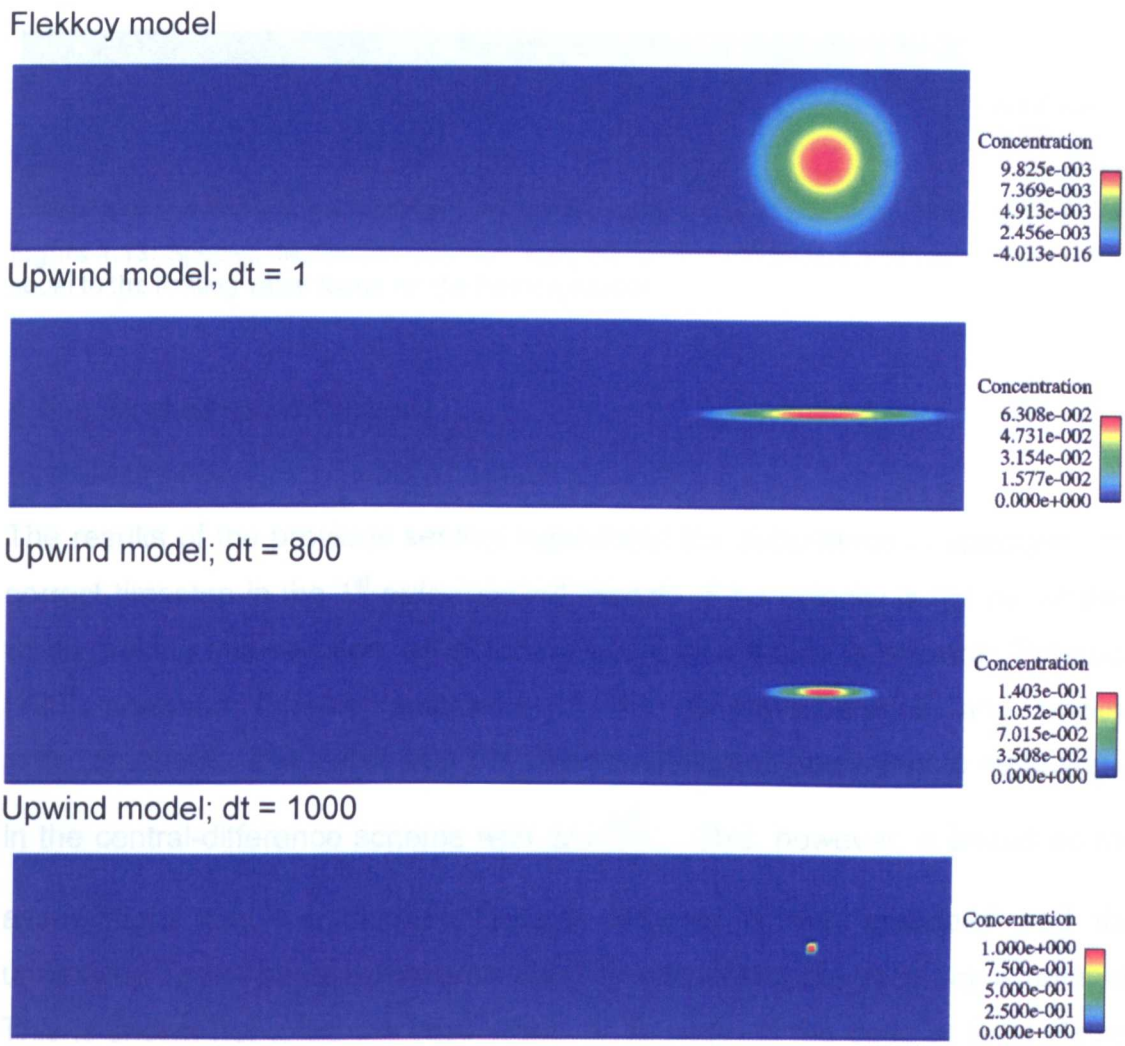

Figure 4.12: Species distributions produced in plug flow with periodic boundary conditions. Results of Flekkoy model are shown alongside upwind model with various timesteps.

[1] The Courant number is $C = \frac{u\Delta t}{\Delta x}$.

To observe the diffusion present with a diffusion coefficient equal to the limiting value of the Flekkoy model, a simulation was performed using the upwind model. The results are shown in figure 4.13 after 1.3×10^{5} iterations, which can be compared to those in figure 4.12. The results are actually worse with the upwind model than with the Flekkoy model because the excess diffusion in the flow direction is superimposed on the prescribed diffusion, producing an elliptical distribution as shown in figure 4.13. This difference must be related to the accuracy of the schemes used; the upwind model being 1st order and the Flekkoy model being 2nd order.

Upwind model; dt = 1, $D=2\times10^{-4}\,L^{2}T^{-1}$

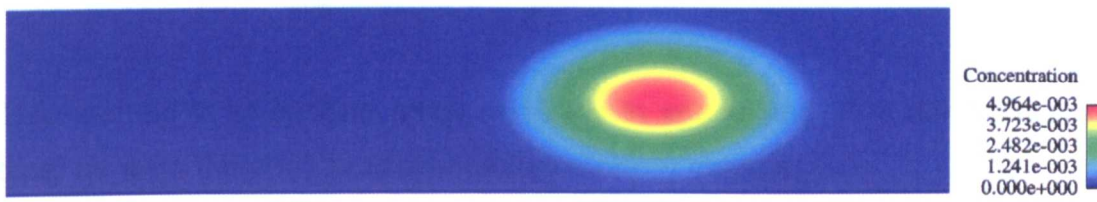

Figure 4.13: Species distribution obtained using the upwind model and a diffusion coefficient equal to the limiting value found for the Flekkoy model.

4.6.4 Numerical diffusion

The results of the previous section highlighted the importance of specifying the correct timestep in the 1st order upwind model. If the velocity is not considered when making this decision, an excess amount of diffusion is present. Patankar [126] analyses the characteristics of the central-difference and upwind approximations. It is stated that the upwind scheme is equivalent to replacing D in the central-difference scheme with $D+\frac{u\delta x}{2}$. This, however, is based on the assumptions that the central-difference scheme is the "*standard*" and the underlying Taylor-series expansion used for calculating the accuracy is reliable. This is shown not to be the case when δx is large, in the case of large Peclet numbers. Patankar [126] claims that at high Peclet numbers, the central-difference scheme "*has little to offer*". The excess diffusion observed in the previous section is described as being the "*common view of false diffusion*". Further discussions of the upwind method and central-difference schemes,

along with the development of a more stable solution are provided by Brooks and Hughes [127].

In order to investigate the "*common view of false diffusion*", alternative models have been considered for the problem of transporting a single block of species, these are a second order upwind approach and an implicit model.

The gradient using the second order upwind approach is calculated using equation 4.19 [128], where h is assumed to be 1.

$$\frac{\partial \phi}{\partial x} = \frac{-3\phi_{i,j-1} + 4\phi_{i-1,j-1} - \phi_{i-2,j-1}}{2} \qquad \textbf{4.19}$$

This method is of second order accuracy in space and 1st order accuracy in time, as were the central difference and Flekkoy models.

The implicit method is calculated by solving the following equation (4.20), which is a rearrangement of the explicit form of equation 4.15, using the central-difference approach for calculating the gradient, which gives second order accuracy in space:

$$2\phi_{i,j-1} = -udt\phi_{i-1,j} + udt\phi_{i+1,j} + 2\phi_{i,j} \qquad \textbf{4.20}$$

This is solved by solving the matrix equation $[k]\{\phi\} = \{b\}$ where $\{\phi\}$ is the matrix of concentrations to be found, $[k]$ is a matrix of coefficients containing information about the indices of the elements of $\{\phi\}$ and $\{b\}$ is the left-hand-side of equation 4.20, i.e. the solution at the previous timestep.

The 1D problem, constructed in Matlab, involved using a diffusion coefficient of zero and completing a sufficient number of iterations to convect the species to the next node, using a timestep of 1. The aim of this study is to investigate the amount of excessive diffusion present in the system when purely convective transport is required and the original hypothesis was that using a higher order upwind scheme or an implicit scheme would minimise the excess diffusion

reported in section 4.6.3 for the upwind model caused by velocity and timestep mismatches. The central-difference approach cannot be tested here for comparison because, with no diffusion, this scheme is unconditionally unstable [124]. The upwind method was however used, with a timestep of 1. The velocities used were 1, 0.5 and 0.25. These are much higher than those typical of LB simulations, but the results will be the same and fewer iterations are needed, therefore the simulation time is reduced. The concentration distributions are shown in plots in figures 4.14-4.16.

Figures 14.14-14.16 do not appear to show any improvement when using either the 2nd order upwind scheme or the implicit scheme. The best result is obtained when the 1st order upwind approach is used with a velocity of 1, since the ideal timestep is 1.

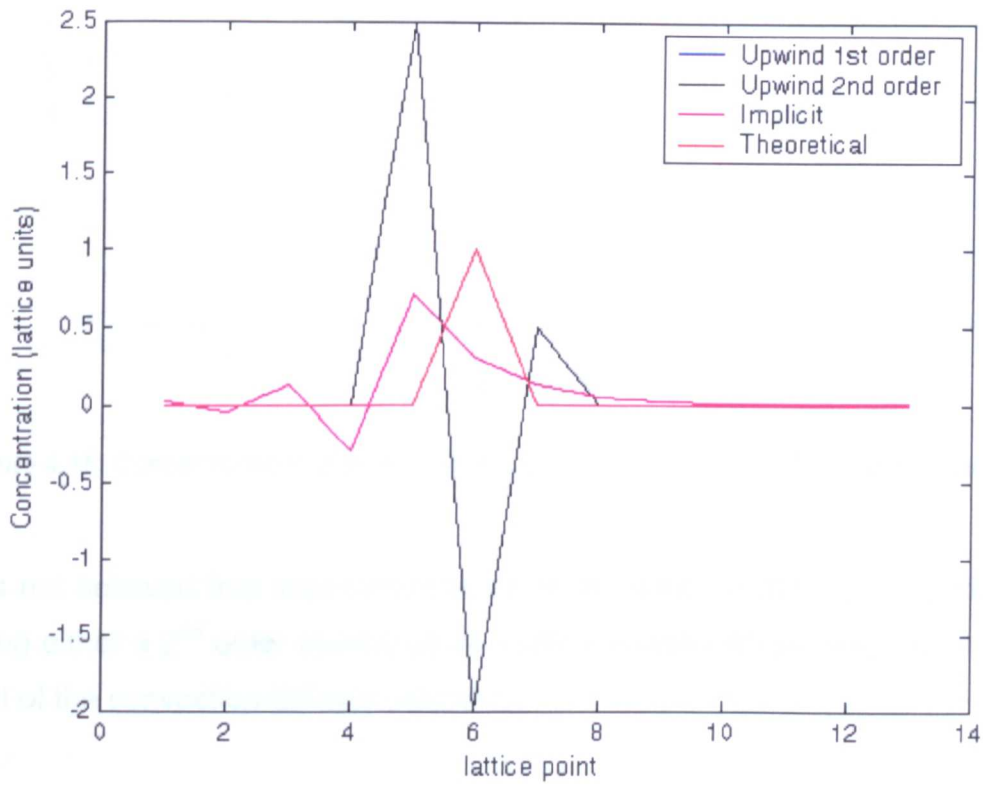

Figure 4.14: Concentration profiles for different schemes with $u = 1LT^{-1}$ after 1 iteration. Upwind plot lies directly beneath theoretical.

All schemes were then tested using different timesteps and a velocity of $u = 0.25LT^{-1}$. Figures 14.17-14.19 show that for the upwind scheme, the results improve as the timestep is increased to 4, thus matching the inverse of the velocity. The results of the 2nd order upwind scheme are difficult to interpret, but

appear to show an improvement when the timestep is increased from 1. However, the optimal timestep is not 4 as for the 1st order upwind scheme. The implicit scheme shows improvements with increasing timestep as regards the correct convection of the species, but the peak concentration worsens. The timestep cannot be increased further due to the limit on the Courant number; the maximum timestep for this example is 4.

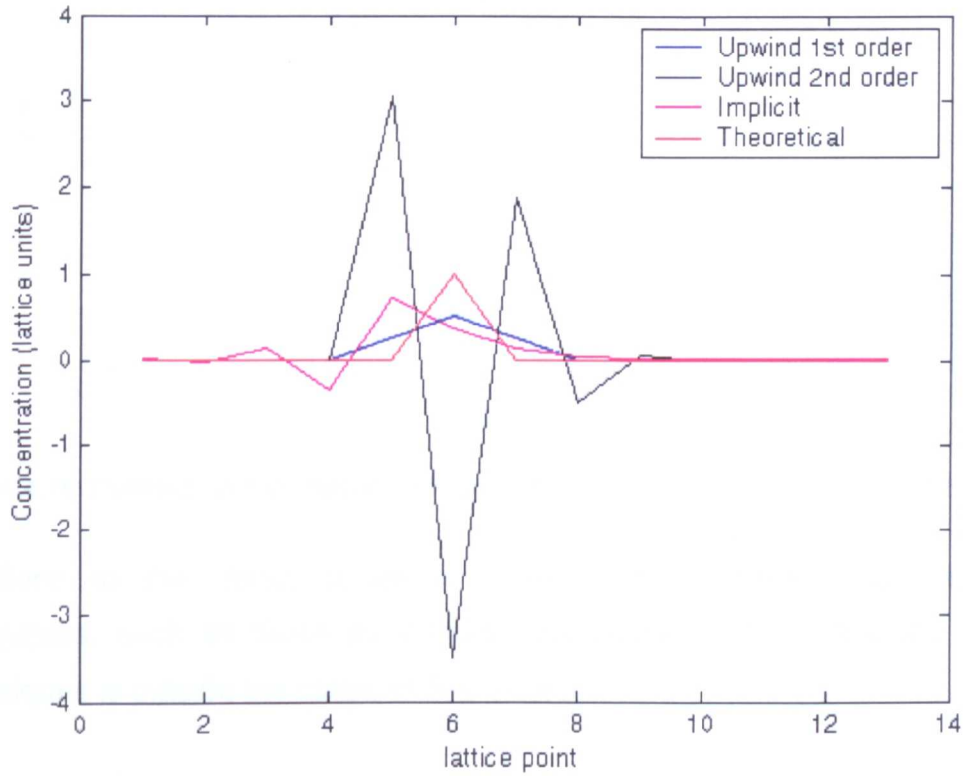

Figure 4.15: Concentration profiles for different schemes with $u = 0.5LT^{-1}$ after 2 iterations.

It is not believed that improvements would be seen *for this type of problem* by using either a 2nd order upwind or an implicit scheme for solving the convective part of the convection-diffusion equation.

The 1st order upwind model is the most stable for large Peclet numbers, but the presence of excess diffusion is clearly seen. The 1st order upwind scheme can be optimised by increasing the timestep to a value equal to the inverse of the peak velocity in the model. However, this is not a realistic solution since the velocity field will not generally be constant. It must be remembered that all the results presented in this section were for zero diffusion. This is the best way of testing the significance of excess diffusion [126].

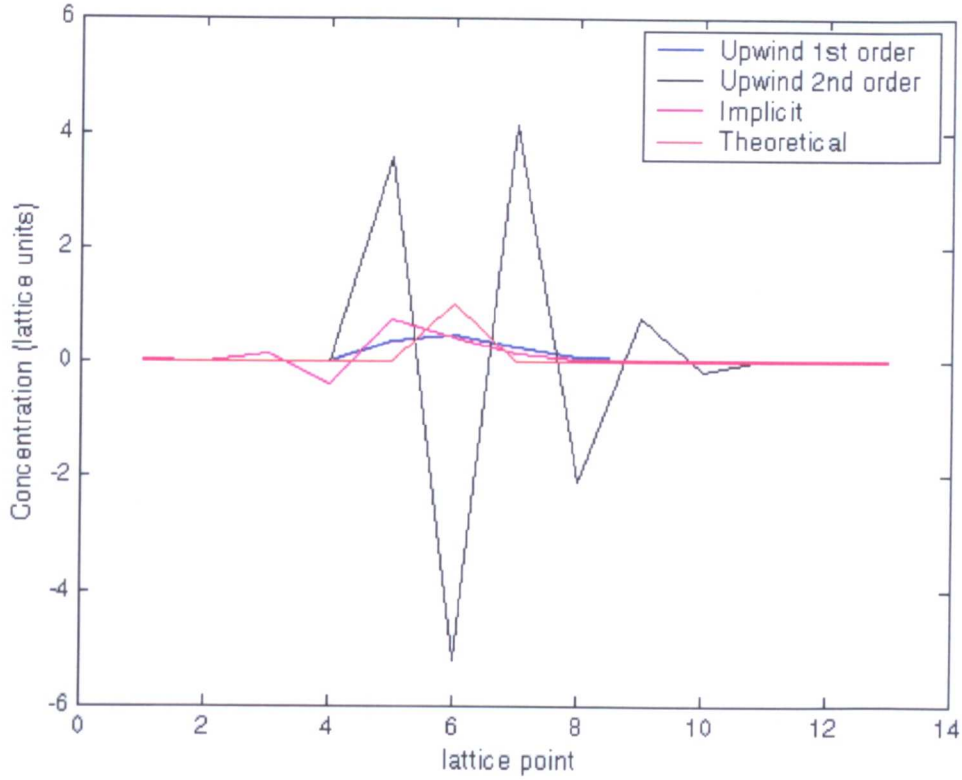

Figure 4.16: Concentration profiles for different schemes with $u = 0.25LT^{-1}$ after 4 iterations.

Solutions to the above problems have been suggested with stabilising techniques, such as those by Brooks and Hughes [127]. A study of such techniques is outside the scope of this project.

Secondary to the "*common view of false diffusion*" is the "*proper view of false diffusion*" [126], which is frequently termed numerical diffusion. Numerical diffusion is often related to flows at an angle to the lattice. If a uniform grid is used, pure convection is only possible if the velocity vectors point to the neighbouring nodes. If this is not the case, at the following iteration, the species should be transported to a position located between lattice points. This is not possible and the only option is to split the concentration of the species so that a certain fraction goes in one direction and the remaining fraction goes to another lattice point. However, this is equivalent to diffusing the species and will have an associated diffusion coefficient.

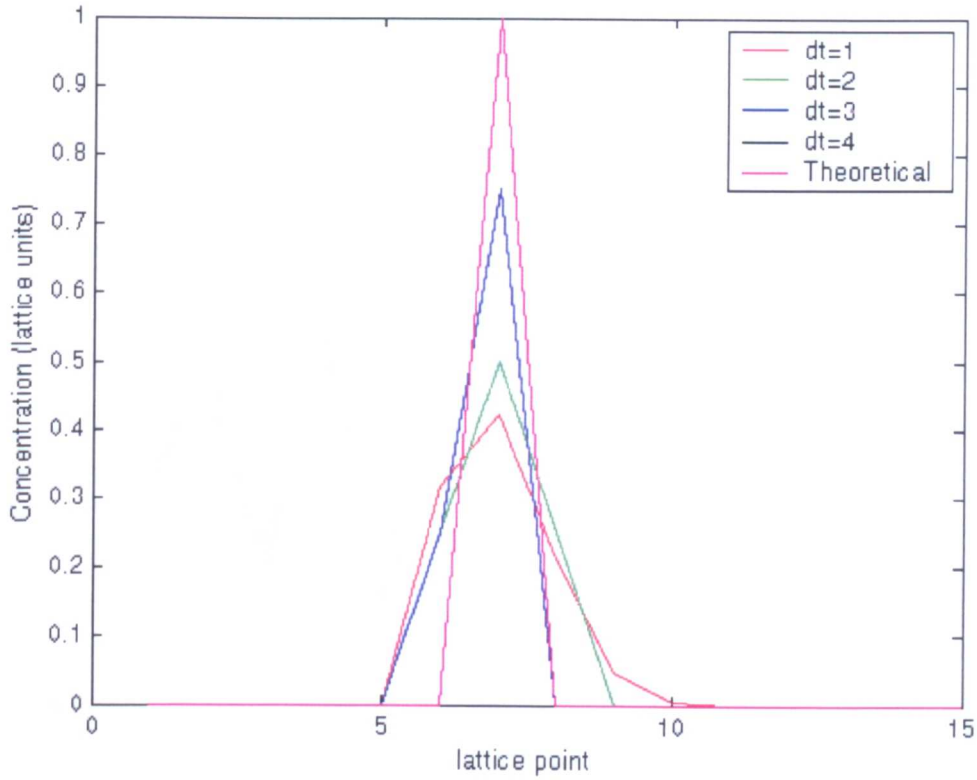

Figure 4.17: Concentration profiles for the 1st order upwind scheme with $u = 0.25LT^{-1}$ after 4 iterations. Timestep is varied as shown. The dt = 4 profile lies directly beneath the theoretical solution.

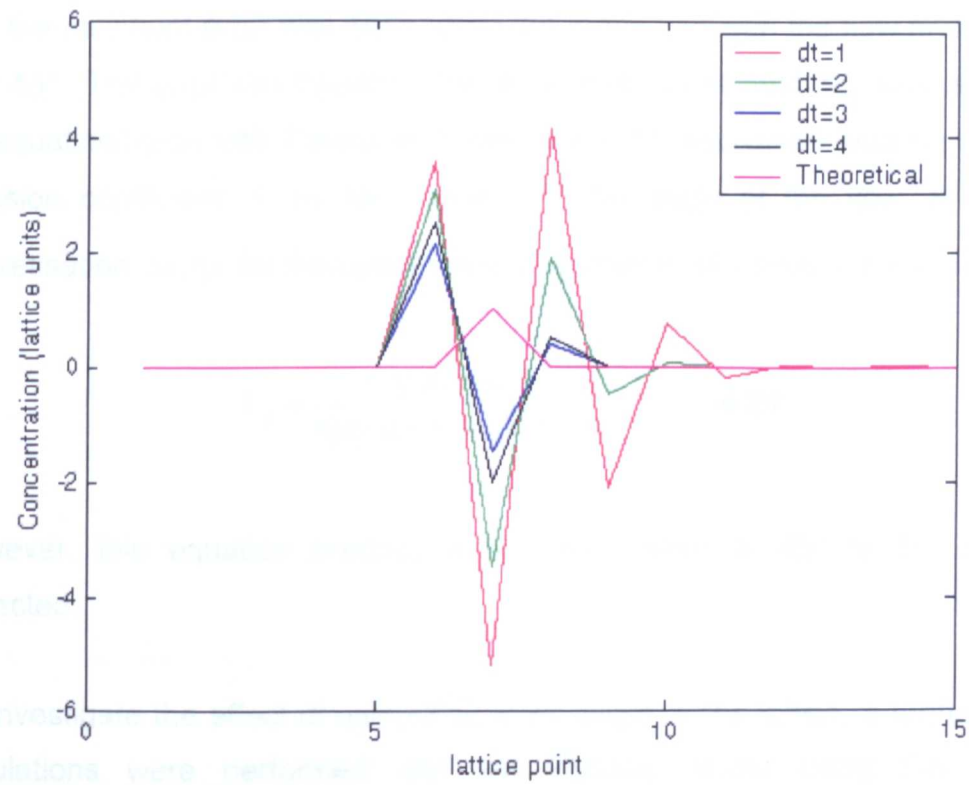

Figure 4.18: Concentration profiles for the 2nd order upwind scheme with $u = 0.25LT^{-1}$ after 4 iterations. Timestep is varied as shown.

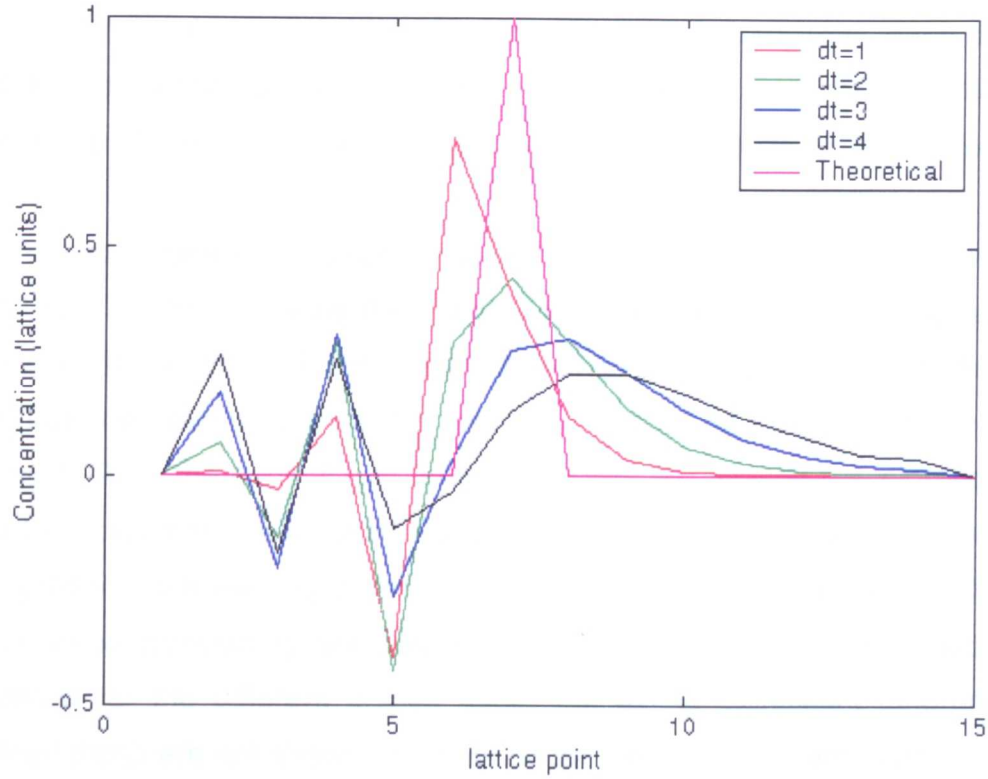

Figure 4.19: *Concentration profiles for the implicit scheme with* $u = 0.25LT^{-1}$ after 4 iterations. Timestep is varied as shown.

Raithby [129, 130] analysed the upstream differencing approach and claimed that the minimum error was seen when the angle between the flow and the grid was 45°. The error was based on the amount of flux through the axial surfaces. An equation by de Vahl Davies and Mallinson [131] was given[1] relating the false diffusion coefficient, Γ_f to the velocity V, the angle of the flow, θ and the discretisation $\Delta x, \Delta y$ for the upstream approximation of convection method as:

$$\Gamma_f = \frac{V\Delta x\Delta y \sin(2\theta)}{4\left[\Delta y \sin^3\theta + \Delta x \cos^3\theta\right]} \qquad \textbf{4.21}$$

However, this equation predicts a *maximum* error at 45° to the grid, as expected.

To investigate the effect of using flow at an angle to the lattice, a further set of simulations were performed with the Flekkoy model using the original

[1] The original article could not be obtained, but the form of the equation agrees with that given by Patankar [126].

parameters from section 4.5.1 and the limiting diffusion coefficient of $7\times10^{-4}\,L^2T^{-1}$. Angles of 15°, 30° and 45° were investigated, each time, the converged flow solution was obtained before injecting the continuous source in the middle of the channel and iterating until the species distribution converged.

In order to compare the results of different flow angles, two types of plots were created. The first showing the concentration along a line perpendicular to the flow direction at different distances, the second showing the concentration along the flow line measured from the source. The first type of plot can be seen in figure 4.20 for the original grid parameters with the limiting diffusion coefficient and the flow along the horizontal direction. This shows the expected Gaussian-like profiles obtained along the perpendicular lines, with the magnitude of the peak value decreasing with distance from the source. Similar plots were obtained for the different angles used, but as no significant difference was noticed these are not shown. In order to compare the concentration distribution at different angles, the second type of plot was produced as can be seen in figure 4.21.

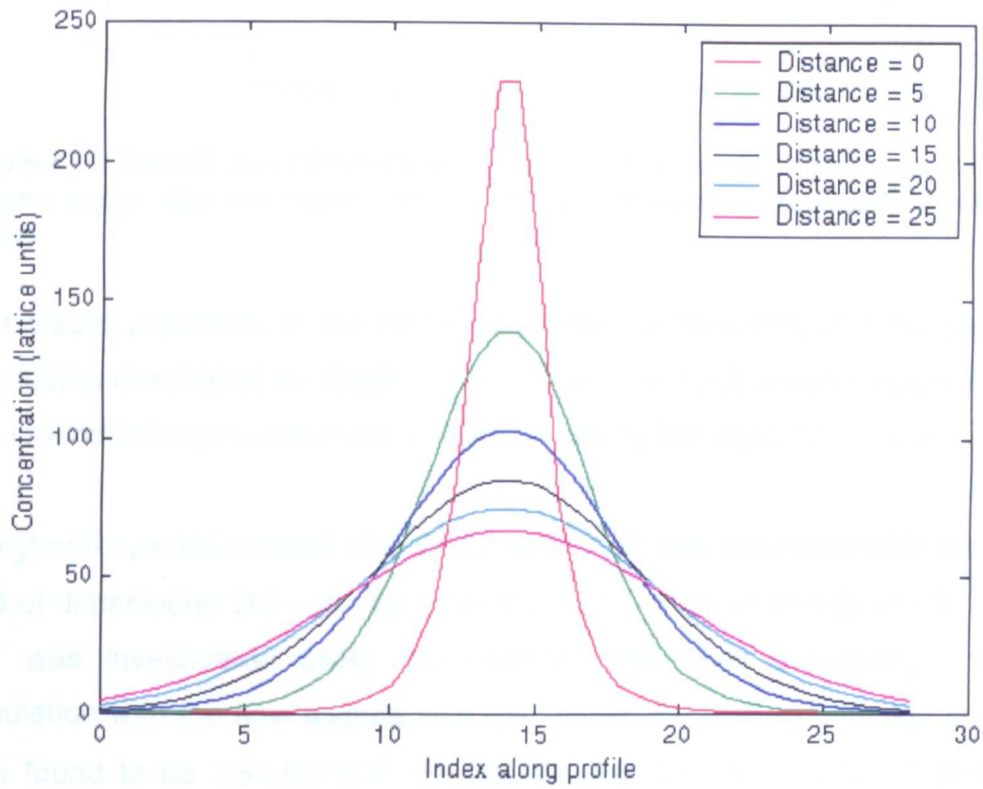

Figure 4.20: Perpendicular concentration profiles at different distances from the source. Results obtained using Flekkoy model. Flow is aligned with the lattice.

This suggests that the diffusion coefficient, which is limited by the algorithm, is too high for the problems of false diffusion to be recognised for this particular grid size. To test the grid dependence of this particular plot, an equivalent was produced using the finer grid of dimensions 400×80 lattice points and this is shown in figure 4.22.

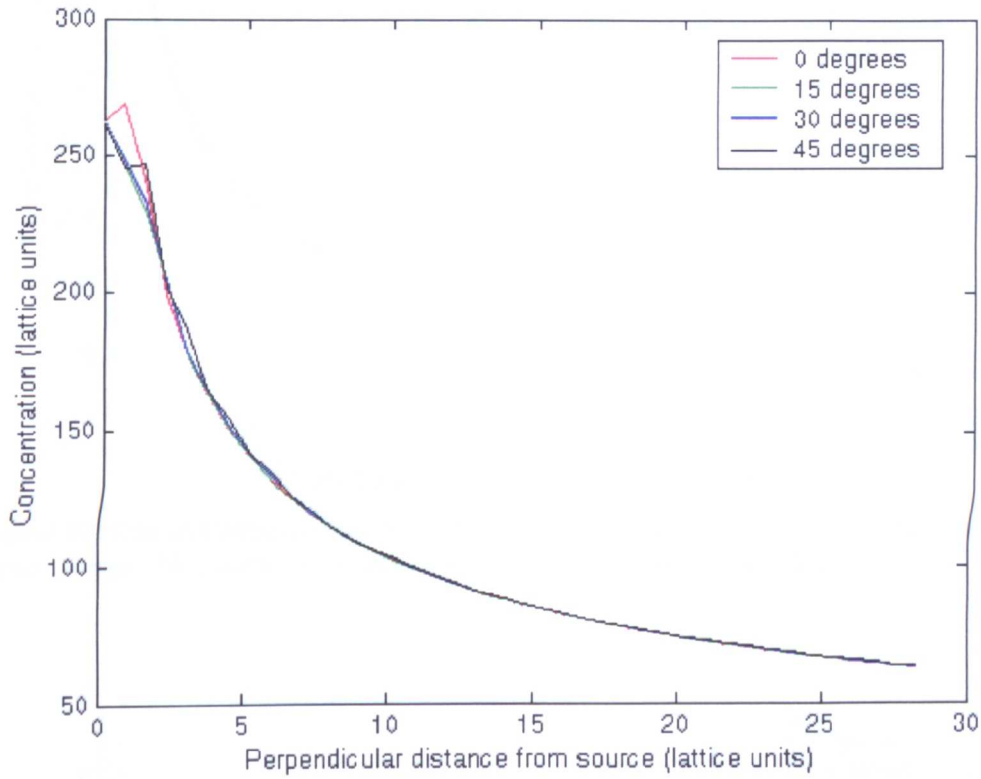

Figure 4.21: Concentration profiles measured along the flow direction from the source for different angles. Grid dimensions 200×40, Re = 2. Results obtained using the Flekkoy model.

The results presented in this section suggest that false diffusion, caused by the flow being directed at an angle to the grid is of a much smaller magnitude than the real diffusion present in the system limited by the algorithm in use.

A higher Reynolds number of approximately 100 was also used with the original grid of dimensions 200×40, as in section 4.51. Flow at angles of 15°, 30° and 45° was investigated using the methods described previously. For the simulation with the flow aligned with the lattice, the limiting diffusion coefficient was found to be $3.5 \times 10^{-2} L^2 T^{-1}$ (to the nearest $0.5 \times 10^{-2} L^2 T^{-1}$). A plot of the concentration profiles measured along the flow direction from the source for the quoted angles is shown in figure 4.23, which again shows no significant discrepancies indicating the presence of false diffusion.

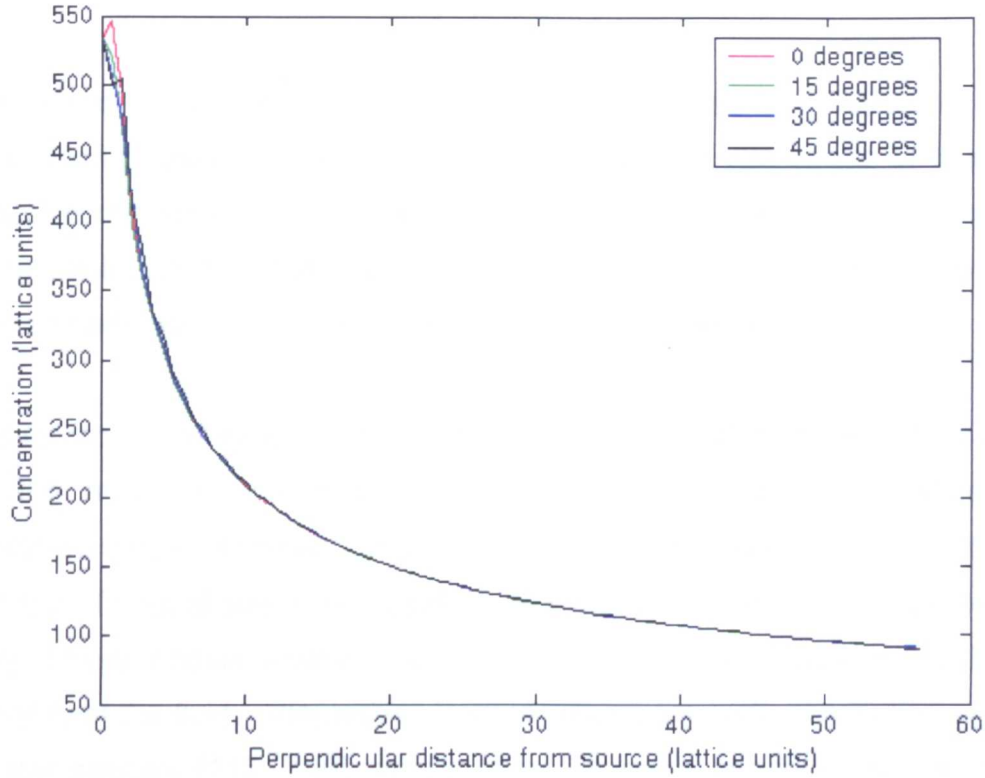

Figure 4.22: Concentration profiles measured along the flow direction from the source for different angles. Grid dimensions 400×80 , Re = 2. Flekkoy model used.

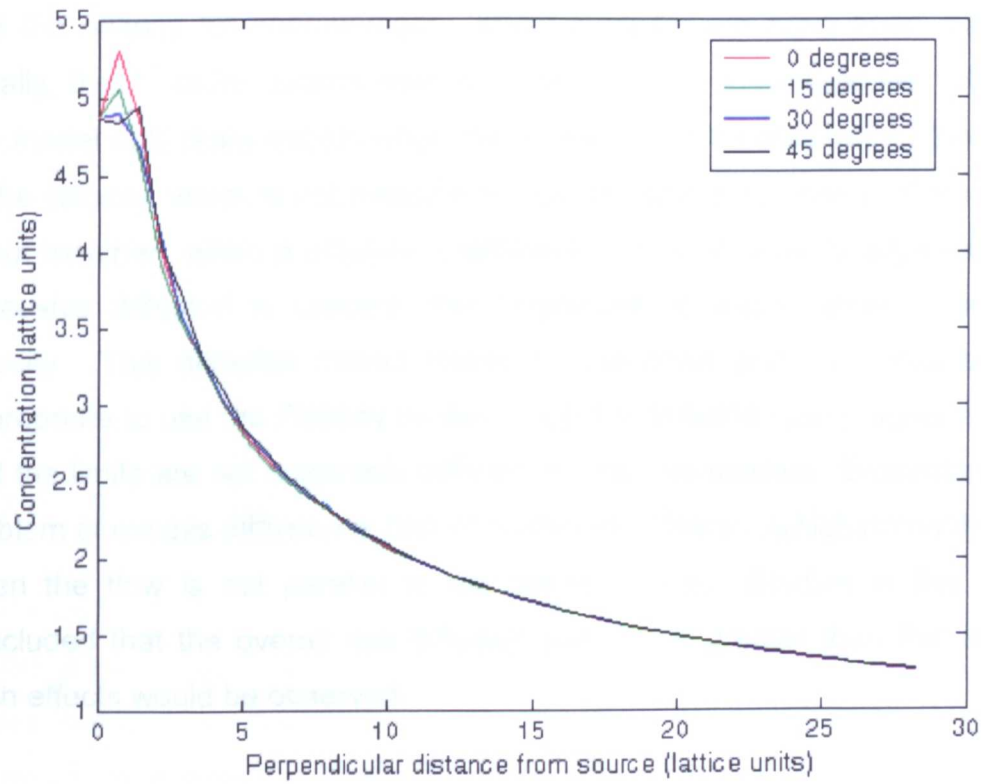

Figure 4.23: Concentration profiles measured along the flow direction from the source for different angles. Grid dimensions 200×40 , Re = 100. Flekkoy model used.

4.7 Discussion

The introductory section of this chapter explained the relevance of the convection-diffusion equation to the core problems addressed in this thesis. Although the focus of this chapter was not to implement improved routines, some basic implementations were performed in order to assess the relative merits of alternative schemes compared with the Flekkoy model.

The literature available on the topic of convection-diffusion algorithms is vast, but the review in this chapter concentrated specifically on methods used alongside lattice Boltzmann solvers. As discussed, it was sometimes the case that the LB equations were modified to include the transport of species [115, 117]. These models however have a diffusion coefficient equal to the kinematic viscosity of the fluid. Alternatives involve solving separate distribution equations for the species [113, 116], which allow for more control over the diffusion coefficients, or the more advanced moment propagation method [118].

A considerable amount has been learnt about the limitations of diffusion models and the options for improvement. Many comparisons have been made and initially, the 1^{st} order upwind scheme seemed to be advantageous. However, this model only really excels when the timestep can be matched to the inverse of the velocity, which is not possible in most realistic simulations. If the velocity is not matched, when a diffusion coefficient of zero is used, a large amount of excessive diffusion is present, the magnitude of which depends upon the velocity. This diffusion cannot easily be quantified and so it may be more appropriate to use the Flekkoy model, since this scheme has a higher accuracy and the limits are not massively different for the two models. Secondary to the problem of excess diffusion is that of numerical diffusion, which primarily occurs when the flow is not parallel to the lattice in use. Studies in this chapter concluded that the overall real diffusion was much greater than that at which such effects would be observed.

The excess diffusion present in the upwind model is a result of the loss of accuracy in this method, being of only first order [127]. Figures 4.10-4.12 show excess diffusion only in the flow direction since this is the only non-zero

component of velocity and it is this convective term that uses the 1st order upwind approach and the diffusion set in the model is zero. The excess diffusion can be quantified relative to the central-difference approach by incrementing the true diffusion coefficient by an amount $\frac{u\Delta x}{2}$ [126, 129]. This implies that the upwind scheme is equivalent to the central-difference scheme when the diffusion coefficient is incremented by $\frac{u\Delta x}{2}$. Patankar [126] disputes this since the central-difference approach is not suitable for use as a comparison. This also does not match the results of figure 4.12 which show that the excess diffusion can be removed with the choice of an appropriate timestep. Such excess diffusion only along the flow direction is not observed with the Flekkoy model[1] since this model had a finite diffusion coefficient, limited by the stability of the scheme itself. It is not possible to set a zero diffusion coefficient in this model without the species concentration being heavily populated with negative values.

The Flekkoy model was found to improve only if the grid was refined. The real Peclet number can only be increased by increasing the number of grid points across the diameter.

The techniques used for analysing the limits of the various diffusion models were based on requirements for simulating thrombosis. In the more complex situation of blood clotting, various species can be released from individual locations in the domain, thus giving very high gradients. This explains the reason for choosing point sources of injection in this chapter. The purpose of these analyses was not to test the accuracy of the convection-diffusion algorithms used, since this is performed in the original articles. Rakotomalala *et al.* [132] have previously validated the dispersion in a BGK lattice Boltzmann simulation with the Flekkoy model. The diffusion coefficients of the elements of blood are well documented and remain several orders of magnitude lower than those that can be obtained within the simulation. It may well be the case that some of the methods outlined in the literature review would prove to be more

[1] This is also true for the results using the Ginzburg model, which are qualitatively similar to those of the Flekkoy model, but with slightly less diffusion present.

successful in reproducing these small amounts of diffusion, but until they have been implemented and analysed using the same methods, comparisons cannot be made. However, the techniques used to develop the thrombosis models in this project are such that the diffusion model exists to supply the appropriate concentrations to be updated based on the rules in use.

The availability of a diffusion algorithm with improved stability might improve the physical accuracy of simulations, but it would not affect the development of the framework for modelling the process of thrombosis which is the primary purpose of this thesis. For the remainder of this project, the Flekkoy model will be used, since, although limited by a lower bound on the diffusion coefficient, the point at which instabilities arise is clear. The lowest diffusion coefficients obtained in this chapter are of the order $1 \times 10^{-4} L^2 T^{-1}$ which is in agreement with the limits reported by Flekkoy [113, 114] and the alternative implementations considered do not offer significant benefit.

Chapter Five: Milk Clotting Model

5.1 Introduction

As will be detailed in the following chapters, the process of blood clotting is extremely complex. Involved are a series of chemical reactions with associated feedback and inhibition, the balance of which controls the production of the final enzyme thrombin. As a first step towards modelling blood clotting, a model of milk clotting was developed. The details of this will be described in subsequent sections, but the virtues of the use of a milk clotting model as an analogue for part of the blood clotting process can be outlined. Milk is readily available and, as an experimental medium, is safer and more reliable when reproducibility of results is required. Reproducibility is greater because of the reduced complexity of the underlying chemistry. The chemistry of the clotting process is also more completely documented in the literature. This benefit allows simpler numerical clotting models to be developed. The reduced complexity provides a higher degree of accuracy, since fewer assumptions are required.

Milk was the primary medium of choice in the present study as access is available to a large body of experimental milk clotting data [22] for validation of the generated models.

This chapter introduces the details of the milk clotting process along with previous results and then describes the numerical models developed in this study. Validation is then provided, which gives confidence in the modelling processes when considering the more detailed clotting phenomena specific to blood.

5.2 Literature Review

The use of milk as a blood analogue was first reported by Jollès [133] in 1975 and the similarities between milk clotting and the final stages of blood clotting were outlined. Experimental verification was first provided by Lewis and Macleod in 1981 [134] and subsequently by others [135, 136].

For blood, the final stage of the coagulation cascade involves thrombin-mediated enzymatic conversion of fibrinogen to insoluble fibrin monomers, which polymerise, forming a fibrin scaffold. Likewise, for milk, addition of the enzyme chymosin (rennet) to milk converts the substrate κ-casein into insoluble para-κ-casein which aggregates, forming a milk clot.

The clotting of milk essentially involves 3 stages; enzyme action, aggregation and clot structure rearrangement [137]. The first two stages are described below.

5.2.1 Enzyme action and aggregation

Before clotting is possible, an enzyme (either chymosin or rennin) must act upon the substrate κ-casein. This substrate forms part of the casein molecule which itself contributes to approximately 80% of the total protein present in milk [138]. The enzyme is free to diffuse throughout the fluid and the rate of diffusion controls the rate of reaction with the κ-casein micelles [139]. The action of the enzyme on the substrate produces a hydrophobic moiety (para-κ-casein) which complexes with casein to form the strands of the clot and a hydrophilic moiety known as caseino(glyco)peptide [133]. When the substrate has been acted upon by the enzyme, changes occur which allow for the onset of coagulation. One theory, introduced by de Kruif *et al.* [140], is that the action of the enzyme causes cutting of the "*hairs*" of the κ-casein molecules which decreases their hydrodynamic radius. The κ-casein "*hairs*" are believed to provide a short range repulsion and when cut, van der Waals' attractive forces dominate resulting in attraction between the micelles. If the energy of this attraction continues to increase beyond the thermal energy, aggregation can take place. It is not possible to separate the two phases of enzyme action and aggregation because aggregation is initiated before complete conversion of the κ-casein substrate [137].

There is a reported delay between the addition of the enzyme and the onset of clot formation and the methods and techniques used for evaluating this vary. A

combination of experimental and theoretical work is reported in the literature and the major conclusions are discussed below.

Payens *et al.* [141] have defined the clotting time as the lag period between the addition of the enzyme and the moment at which the clot becomes visible. They considered the increase in the number of particles of clotting product and their work predicts a lag period in the formation of multiple particles which they believe is due to the difference in reaction order rates of enzyme production and flocculation. A linear relationship between $\ln(e^{-1})$ and $\ln(t)$ is demonstrated using experimental data where e is the enzyme concentration and t is the clotting time and this leads to the relationship $te^{\gamma} = C$ where γ and C are constants. The authors derive a condition for the clotting time as $t\sqrt{\frac{k_s V}{2}} = C$ where k_s is the flocculation rate constant and V is the rate of production of clottable particles, found to be proportional to e. This leads to the assumption that the clotting time is inversely proportional to the square root of the enzyme concentration and hence the parameter γ is 0.5. However, experimental results suggest that the parameter γ is closer to 1. This is believed to be due to the fact that the flocculation rate constant increases with enzyme concentration, i.e. k_s is not constant. In a subsequent paper [139], Payens verified this and suggested that γ lies in the range 0.92-1.00.

Another consideration regarding the presence of a measurable clotting time is the issue concerning the amount of substrate that must be destroyed before coagulation can take place. Dalgleish [137] discovered that in excess of 80% of the κ-casein had to be hydrolysed by chymosin before a distinct tendency towards aggregation could be seen. Experiments show that aggregation had not started after 60% of the clotting time had elapsed at which stage at least 80% of the κ-casein is split. Stress is placed on the importance of defining a minimum amount of proteolysis required before a micelle is considered capable of aggregating but this essentially implies that the process of enzymic reaction is not complete at the start of aggregation. Dalgleish also presents an equation relating the clotting time to the enzyme concentration, as shown below:

$$t_c \sim \frac{A}{[e]} + B \qquad \textbf{5.1}$$

where A and B are constants and e again is the enzyme concentration.

This follows the variation observed by Payens *et al.* [141], apart from the addition of a constant term. The techniques used incorporate a critical value of proteolysis which therefore takes account of the concentration of enzyme required to initiate aggregation.

So far, the importance of the concentration and the time since addition of the enzyme to the fluid has been explained in terms of the chemical processes at play. It is now appropriate to discuss the sequence of events which are followed once the fluid is deemed 'clottable'. The major effect reported is the change in viscosity observed as the milk changes its state. Scott Blair and Oosthuizen [142] report an initial fall in viscosity, which they believe is caused by decomposition of part of the casein, then an increase caused by the formation of aggregates. They attempt to apply simple equations to the early stages which result in the observed decrease in viscosity. The viscosity decrease at low rennet concentration is found to be zeroth order, then at higher rennet concentrations and after longer times, the reaction passes to first order[1].

De Kruif *et al.* [140] report the same trend in viscosity and assign the fall to the decrease in micelle size upon removal of the κ-casein "*hairs*". As mentioned previously, the removal of the "*hairs*" enables the Van der Waals attraction between micelles to dominate over the repulsive forces present. The subsequent increase in viscosity is assigned to the formation of aggregates. This agrees with the hypothesis provided by Scott Blair and Oosthuizen [142].

To summarise, it is hypothesised that the viscosity falls due to κ-casein decomposition, but this can only happen if a sufficient fraction of the κ-casein is lysed. This requires a certain minimum enzyme concentration and a certain amount of time. The viscosity then increases as aggregates start to form. This

[1] No details concerning magnitudes are given because values will be experiment dependent.

brief description includes the presence of a lag period as stated by Payens *et al.* [141].

It is now appropriate to discuss the Sheffield experimental work with milk clotting on which the lattice Boltzmann model will be based.

The first major piece of work was performed by Keggen [143] in 1996 and this involved the study of milk clot deposition on heart valves. A variety of mechanical and tissue valves were evaluated *in vitro* with varying enzyme concentrations and the resulting clots were compared with the thrombus formation found on explanted valves. The milk clotting patterns resembled thrombus in terms of location and, for most valves studied, the extent of milk clot and thrombus were similar. The limitations of the model as a direct analogue of blood were outlined. These are based mainly on the difficulty of simulating the complicated reactions involved with blood clotting. However, the investigator emphasised the potential for application to the design of improved valve configuration.

The *in vitro* work of Keggen [143] illustrated the value of coagulation studies using enzyme treated milk and this provided the justification for further extension of the technique and subsequent *in vitro* studies by Smith [22]. Although Smith developed a simple numerical representation and performed some preliminary numerical studies, the primary purpose of his work was to produce experimental data for validation of clotting models in the context of the simplified 'coagulation cascade' of enzyme-activated milk. The geometry studied was a sharp-edged stenosis, with flow rates in the physiological range. Clot formation was recorded using photography, clot casting and clot mass calculation.

5.2.2 Residence time models

The previous section described the process of milk clotting and highlighted some experimental work. The dominant factor governing the deposition of milk clot is the clotting time. This has been shown to be dependent upon the

enzyme concentration, which is a second variable to consider in the model. However, due to the design of the experimental studies by Smith [22], there is no need to include enzyme concentration in the models. Smith [22] introduces an appropriate amount of enzyme (rennet) to the system upstream of the region of interest such that clottable fluid is detected 10s after ejection at the outlet of the experiment. This is to prevent the formation of clot in the bulk flow region (which would only serve to occlude the system), but to allow for clots to be produced in recirculation zones in a reasonable timeframe. The clotting time is therefore calculated using the average velocity in the system and the length of the experimental flow vessel. Further details concerning these experiments will be given in a later section, where necessary. This experimental set up reduces the complexity of the models to be generated, since only the residence time or 'age' of the fluid needs to be known.

The use of residence time models in general is well documented in the literature and different techniques have been used for calculating the residence time. In 1953, Danckwerts demonstrated that a set of residence-time distribution-functions could be defined and measured for a variety of systems [144]. The notion behind this was based on consideration of the amount of tracer entering and leaving the domain, hence providing information on the amount of tracer still present within the domain. This analytical work was illustrated with plots of the fraction of tracer leaving the domain versus time for flow through beds of porous solids, flow in pipes, reactors and blenders. Danckwerts, using previous work of Spalding [145] clarified this work in 1958 [146] by explaining that if a pulse of a tracer is injected at the inlet of a system, a plane in the domain can be monitored over time to provide the variation of the average age of the material at that plane. However, this is only applicable in the steady state context, since this variable is independent of time.

In 2000, Józsa and Krámer described a technique for measuring residence times using finite difference methods [147]. This incorporated a zeroth order reaction model and a uniform source term of species used to trace the age of the fluid. This method will be described in more detail in the following section since it has been adopted for use in this study.

In 2004, Jongen presented a detailed review of residence time models and criticised some of the common computational methods of estimating residence time [148]. These were based on the fact that tracer species are typically used. These are capable of estimating the residence time of the tracer as opposed to that of the underlying fluid, which essentially have different diffusion mechanisms. The value of the tracer diffusion coefficient is of little use and does not have a defined value, unless experiments using real tracers are being simulated. Jongen then proceeded to illustrate an alternative method which defines the age of the fluid in a purely kinematic sense as a "*tagging variable*" based solely on the velocity of the underlying fluid. The advantages and disadvantages of this type of method compared to those using tracer species for the simulation in this study will be discussed in a later section of this chapter.

Residence time models have been used to predict the location of thrombosis in physiologically representative geometries. In 1996, Kunov *et al.* [149] demonstrated a particle tracking method for obtaining residence times with application in a model of a stenosed artery. Particles were seeded at the inlet and convected by the previously computed flow field as non-diffusing passive scalars. Validation was performed by comparing the results to analytical solutions for both spatially and temporally varying flows and agreement was found to within 1%. The authors then proceeded to track the motion and residence time of platelets that were activated if the shear stress at any instant was supra-threshold. This led to results identifying regions where activated platelets would reside for extended periods of time, which is ultimately related to the likelihood of deposition and aggregation. Although this model considered the residence time and prediction of possible platelet deposition regions, it did not attempt to model the deposited platelets in any way.

Friedrich and Reininger [150] proposed a model for simulating the clot growth on indwelling catheters. They validated this with experimental data. Following comparison of the experimental clot growths with the distribution of streamlines, shear rate and residence time they stated that "*...the residence time is the single most important flow factor for fibrin coagulation and thus probably for thrombus formation.*"

Residence time was modelled numerically in the same way as it was measured experimentally; using dye washout techniques. The local concentration of the dye is therefore proportional to the residence time at that location.

The Navier-Stokes equations were used and coagulation was simulated using a mathematical viscosity model based on the work of Tippe and Müller-Mohnssen [151], which describes the time-course of the viscosity increase of blood when the final reaction between fibrinogen and thrombin is considered. The fibrin concentration $c(t)$ can be expressed in terms of the rate coefficients (equation 5.2) and is used in the calculation of the viscosity of the clot (equation 5.3).

$$c(t) = 1 + \frac{[k_2 \exp(-k_1 t) - k_1 \exp(-k_2 t)]}{(k_1 - k_2)} \qquad \textbf{5.2}$$

$$\mu(t) = s_2 . [c(t)]^m - f_2'(t) \qquad \textbf{5.3}$$

k_1 and k_2 are rate constants dependent upon thrombin, s_2 is a scale factor, m is an exponential coefficient describing the effect of the spatial fibrin cross-linking on the viscosity of the solution and f_2' is a function representing the reduction in viscosity due to high shear rates breaking the molecules. This was found to be best represented by a step function.

Friedrich and Reininger [150] simplified the above equations by using $m = 1$, $s_2 = \mu_0$ and $f_2'(t) = 0$. In this model, it was not possible to convert fluid to solid elements based on their viscosity and so the threshold value of $5mPas$ was used as a saturation value of the fibrin polymerisation process.

The results of Friedrich and Reininger's experimental study [150] showed growth of clot within a recirculation zone, which proceeded until the entire region was replaced by a solid fibrin clot of the same geometrical form as the recirculation zone. The numerical results were said to give a region of solid elements "*identical in size, form and localization.*" Whilst the experimental results suggested that low shear stresses as well as long residence times are

necessary for the initiation of clot formation, the computational simulation required only residence time of the fluid to yield "*identical*" results.

The problems with models based purely on residence time were outlined by Narracott *et al.* in 2005 [152]. Computational models typically employ no-slip boundary conditions at the walls. This leads to very slow moving fluid in these regions associated with very large residence times. The experimental work of Friedrich and Reininger [150] demonstrated large shear rates and hence no coagulation in the wall regions. Consideration of purely residence time in their numerical work did not result in clot in these regions and residence time was concluded to be the "*only necessary variable*". To avoid the spurious effects of high residence times at the walls, Narracott *et al.* [152] devised a scheme whereby a source of clottable fluid is generated on a surface away from the wall in order to represent the activation of blood. The target was to represent clotting on a metal coil in an aneurysm, and the (natural) wall of the vessel was assumed not to be a source of activated blood.

This review outlines the processes involved in milk clotting and simplifications made in the *in vitro* experimental work, which allow simulations to be performed using a residence time model. A review of similar models previously used for clotting studies has been presented along with the options available for obtaining residence time.

The following work presents the progress made in the lattice Boltzmann simulations of milk clotting using a residence time model and the results of this are compared to those produced experimentally.

5.3 Aging Model

5.3.1 Description of aging model

Fluid residence time is a governing variable in the clotting model. All fluid within the domain is deemed clottable (it is assumed that mixing has taken place upstream) and detail of the enzymatic reaction between rennet and κ-casein is

not considered. Fluid age is determined by adding a constant concentration of a tracer species to every node in the model at each timestep, hence the local concentration of the species is proportional to the fluid age at that node[1]. This differs from the experimental technique whereby rennet is injected upstream and normal untreated milk already in the system is replaced with clottable milk. However, the simulation technique is efficient, involving only one species. At $\mathrm{Re} = 550$ there is strong convective mixing, and the start-up condition is relatively insignificant.

This method is equivalent to a zeroth order reaction, which can represent the reactions occurring in the process of milk clotting. This is obviously simpler than the relationships discussed in the literature review of this chapter, but a sufficient amount of enzyme is presumed as discussed above. The reaction being considered is the conversion of κ-casein to para-κ-casein catalysed by the enzyme, rennet. κ-casein is present in milk and para-κ-casein forms the strands of the clot. The approximation made in the aging model is that this reaction takes place at a given rate, thus the age of the fluid dictates its state. Obviously, the age of the fluid increases linearly with time and this is where the similarity lies. A reaction model can be used if the two species considered are κ-casein and para-κ-casein and the concentration of para-κ-casein increases at a constant rate, thus describing a zeroth order reaction as shown below:

$$\kappa - casein \xrightarrow{rennet} para - \kappa - casein$$

$$A \rightarrow B \text{ (at rate } k\text{)}$$

$$[A]_{new} = [A]_{old} - k$$
$$[B]_{new} = [B]_{old} + k$$

It is assumed that the amount of rennet everywhere in the domain is constant and that all fluid ages at a constant rate, hence the concentration of para-κ-casein also increases at a constant rate. These assumptions mean that only the concentration of para-κ-casein is required, which is directly captured by the aging species.

---

[1] This part of the model was introduced in the source code by Joerg Bernsdorf, NEC Europe Ltd.

The inlet boundary condition of the model imposes a concentration of zero and the outlet condition extrapolates the upstream values and applies the average of two nodes. Bounceback conditions are used on the walls in the same manner as for the fluid.

This method is chosen over particle-tracking methods due to its algorithmic simplicity and increased computational efficiency. Previous studies have adopted similar methods to this with some success [22, 147, 152].

The aging species is a passive scalar tracer, transported by convection and diffusion. The diffusion coefficient describes the rate of mixing between 'old' and 'young' fluid, and is an important parameter that must be chosen carefully. Excessive diffusion limits the maximum age of any fluid element in a recirculation zone. The need for a finite amount of diffusion to represent the mixing of different types of milk strengthens the argument for using this type of method rather than one using particle tracking methods [148]. A purely convective model would result in excessive clotting along the domain walls as discussed by Narracott *et al.* [152].

5.3.2 Testing and validation of aging model: 2D channel

In order to validate this as a method for modelling the residence time of fluid, simulations of parabolic flow in a 2D channel were considered for a variety of Peclet numbers. The Peclet number is given in equation 5.4.

$$Pe = \frac{ul}{D} \qquad \textbf{5.4}$$

where, u is the average velocity, l is a typical length scale and D is the diffusion coefficient. This is similar to the equation for calculating the Reynolds number and the same velocity and length scale are used.

Flow velocity is maximal in the centre of the channel, falling parabolically to zero at the walls. Therefore, after a certain time has elapsed, the 'youngest' fluid will be found in the centre at the inlet and the 'oldest' fluid will be found near the

outlet walls. The Peclet number was varied in the range $13.5 - 1.35 \times 10^5$, resulting from diffusion coefficients in the range of $1 \times 10^{-6} - 0.01$. This will result in convection dominated transported as discussed in Chapter 4. For this study, the algorithm described by Flekkoy [113] was used. The grid size chosen for this simulation was 200×42 and the Reynolds number was approximately 10. The converged flow solution was obtained after 4×10^4 iterations without the aging species and this was used for restarting with the aging model. For each simulation, convergence in the plot of mean concentration along the length of the channel was obtained, with convergence requiring fewer iterations for the lower Peclet numbers, due to the increased speed of information transfer via diffusion. Convergence of the results is logical because there must exist a certain period in which all fluid is replaced by new fluid from the inlet. An analytical solution for the problem of pure convection was formulated in Matlab and figure 5.1 shows the results obtained.

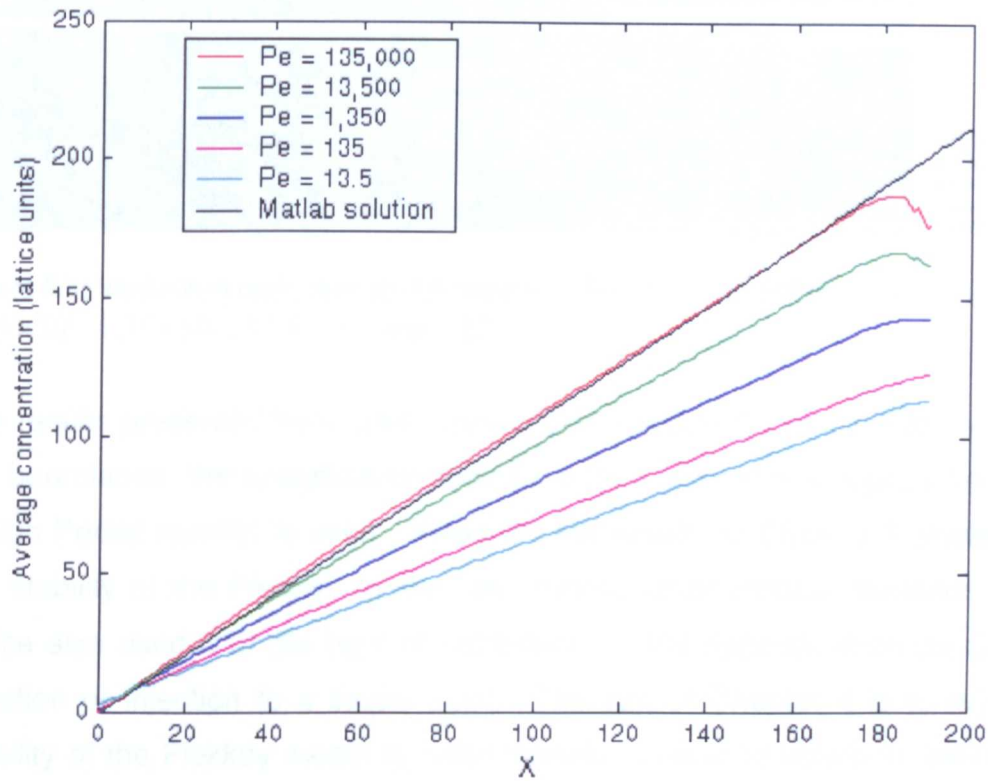

Figure 5.1: Variation in mean concentration of aging species along channel length for various Peclet numbers. Matlab prediction of pure convective flow is also shown.

The increase in gradient with increasing Peclet number in figure 5.1 is expected, because a higher Peclet number implies less diffusion and hence the

slow moving fluid at the walls increases the mean concentration across the channel. Colour images of the concentration distribution were also compared and as the Peclet number was increased, the effect of the parabolic variation in velocity could be more easily seen as shown in figure 5.2.

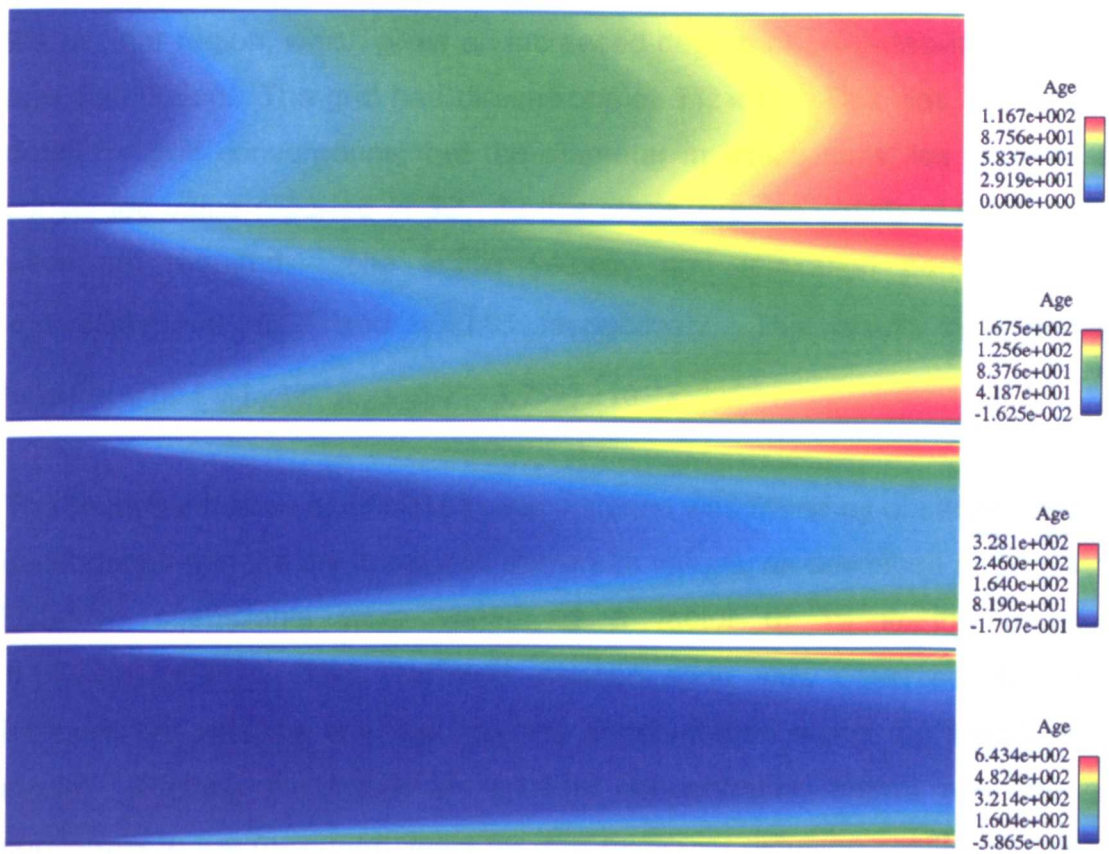

Figure 5.2: Variation in aging species distribution for Peclet numbers of (top to bottom) 1.35×10^{1}, 1.35×10^{2}, 1.35×10^{3} and 1.35×10^{4}.

The results presented here, particularly those in figure 5.1, show that away from the boundaries, the analytical solution for pure convection is approached when a high Peclet number is used. However, the results of Chapter 4 showed that the stability of the Flekkoy model, and indeed other models, depends on the lattice size used and the type of conditions on the species, such as constant injection or injection to a single point. The aim of Chapter 4 is to relate the stability of the Flekkoy model to other models in order to obtain an estimate of the practical limits that exist in this kind of problem. However, these limits are problem specific and the stability can not be generalised from the results presented in Chapter 4. For this reason, further discussions on this topic are required for the aging model, in the case of the stenosis geometry.

5.3.3 Testing and validation of aging model: 2D stenosis

For a significant part of the initial testing of the aging model, a 2D representation of the stenosis geometry with a Reynolds number of 100 was used. The 2D flow field is qualitatively similar to that produced in 3D and falls in the laminar region, which gives an increased degree of predictability of the fluid age distribution. The grid had dimensions of 532×82. This was not tested in detail for grid convergence, but the diameter in lattice units lies close to the converged value reported in 3D. At this stage, precise details of the flow field were not required. The lattice velocity and relaxation parameter were $u_{av} = 5.3419 \times 10^{-3} LT^{-1}$ and $w = 1.95$ respectively. This results in length and timesteps of $L = 1 \times 10^{-4} m$ and $T = 3.7393 \times 10^{-5} s$.

The limiting diffusion coefficient in this instance was found by observing the age distributions and the minimum and maximum values, as described in Chapter 4. Diffusion coefficients were varied by a factor of 10 in the range of $0.1 - 1 \times 10^{-5} L^2 T^{-1}$. The maximum concentration was observed at regular intervals, as was the average species concentration along the length of the model. Plotting the maximum species concentration shows how the age converges to the maximum value for that particular diffusion coefficient and the plots of average age along the length of the model indicate how the solution converges throughout the entire domain, with the maximum age within the recirculation zone converging dependent up the diffusion coefficient. Figures 5.3-5.6 show the plots of the average species concentration along the length of the model at different times for the diffusion coefficients used.

Figures 5.3-5.6 clearly show the presence of the recirculation zone for the lower diffusion coefficients and the effect on the convergence of age. The stenosis is located between horizontal positions of 82 and 131 and this can be seen as a drop in the average value of age since a value of zero is measured for the extra obstacles in this region and the values either side increase as the diffusion coefficient is reduced. Results are not shown for $D = 1 \times 10^{-5} L^2 T^{-1}$ since this produced an excessive amount of negative ages.

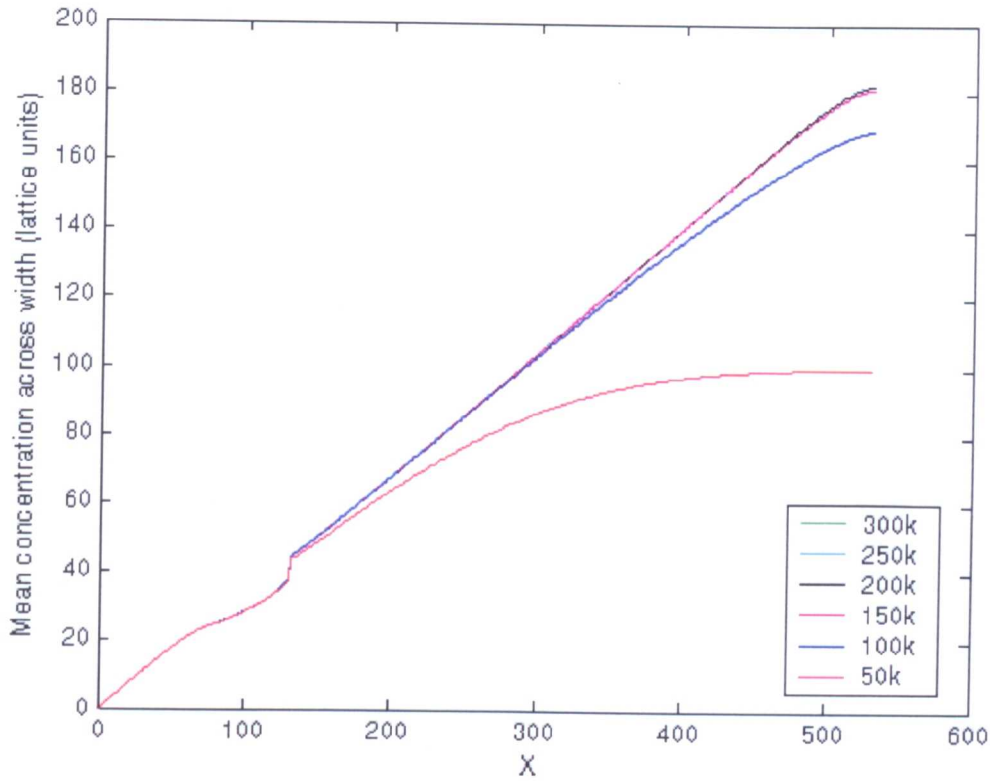

Figure 5.3: Convergence of mean species concentration in 2D stenosis geometry for $D = 0.1L^2T^{-1}$.

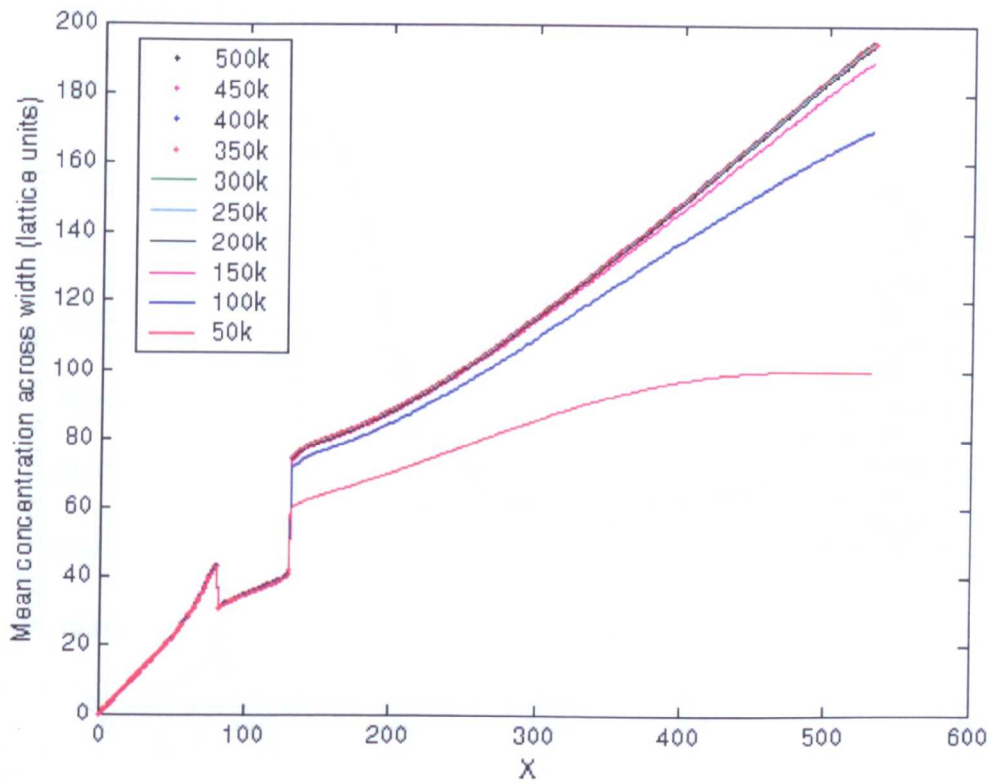

Figure 5.4: Convergence of mean species concentration in 2D stenosis geometry for $D = 0.01L^2T^{-1}$.

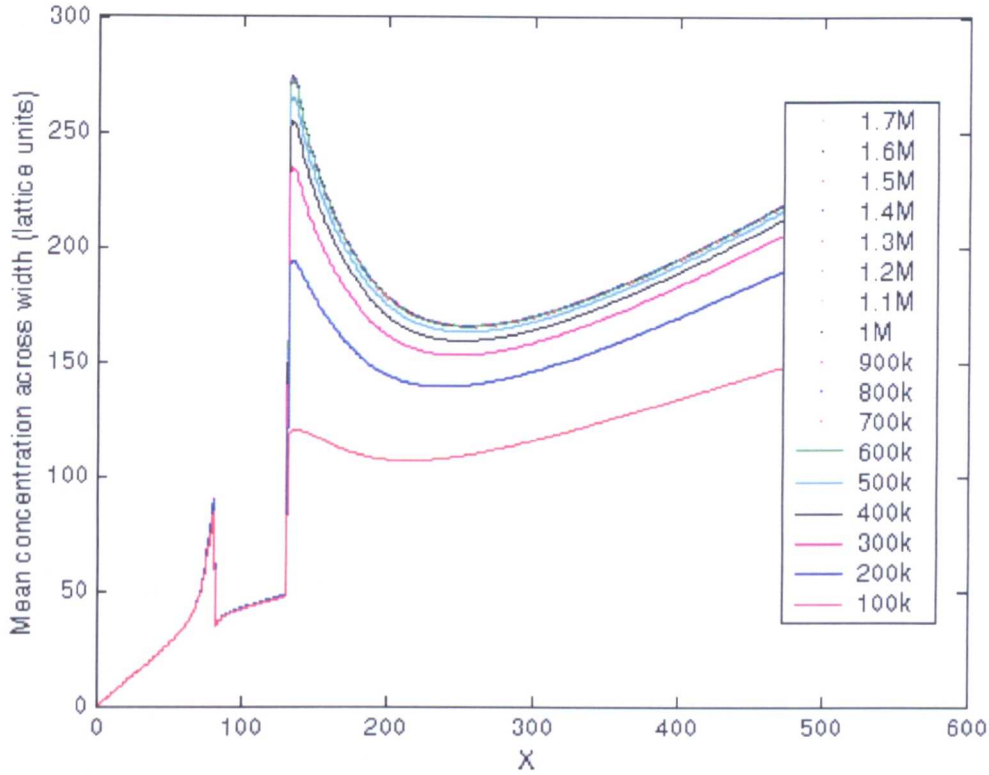

Figure 5.5: Convergence of mean species concentration in 2D stenosis geometry for $D = 1 \times 10^{-3} L^2 T^{-1}$.

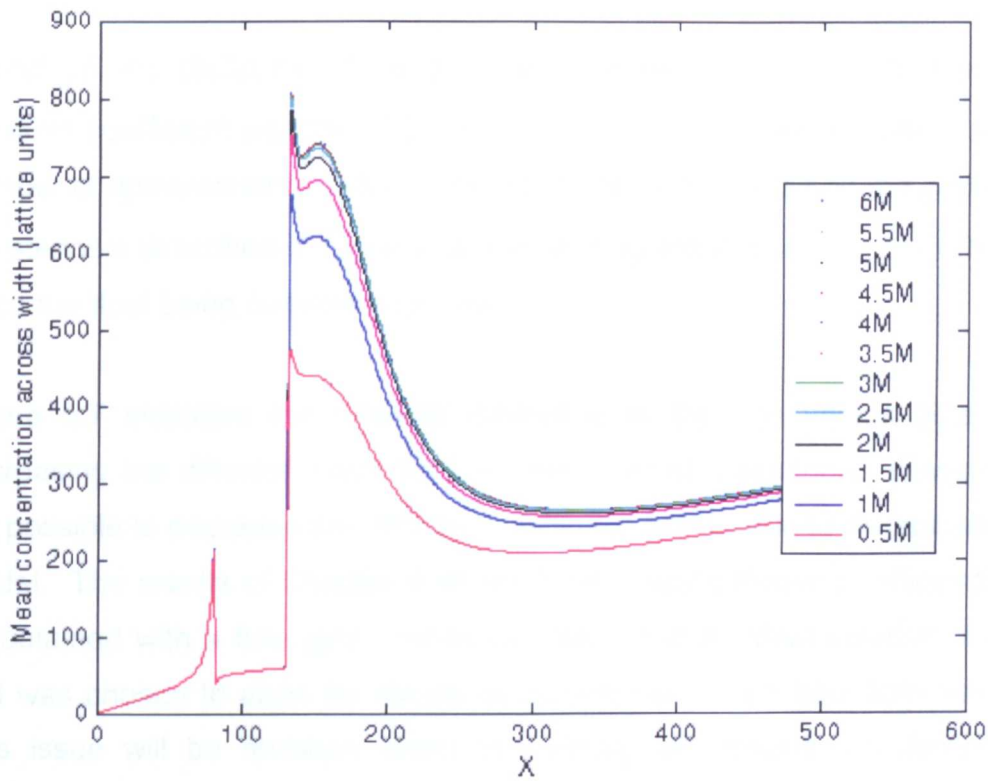

Figure 5.6: Convergence of mean species concentration in 2D stenosis geometry for $D = 1 \times 10^{-4} L^2 T^{-1}$.

Figure 5.7 shows the convergence of the maximum age for the diffusion coefficients used.

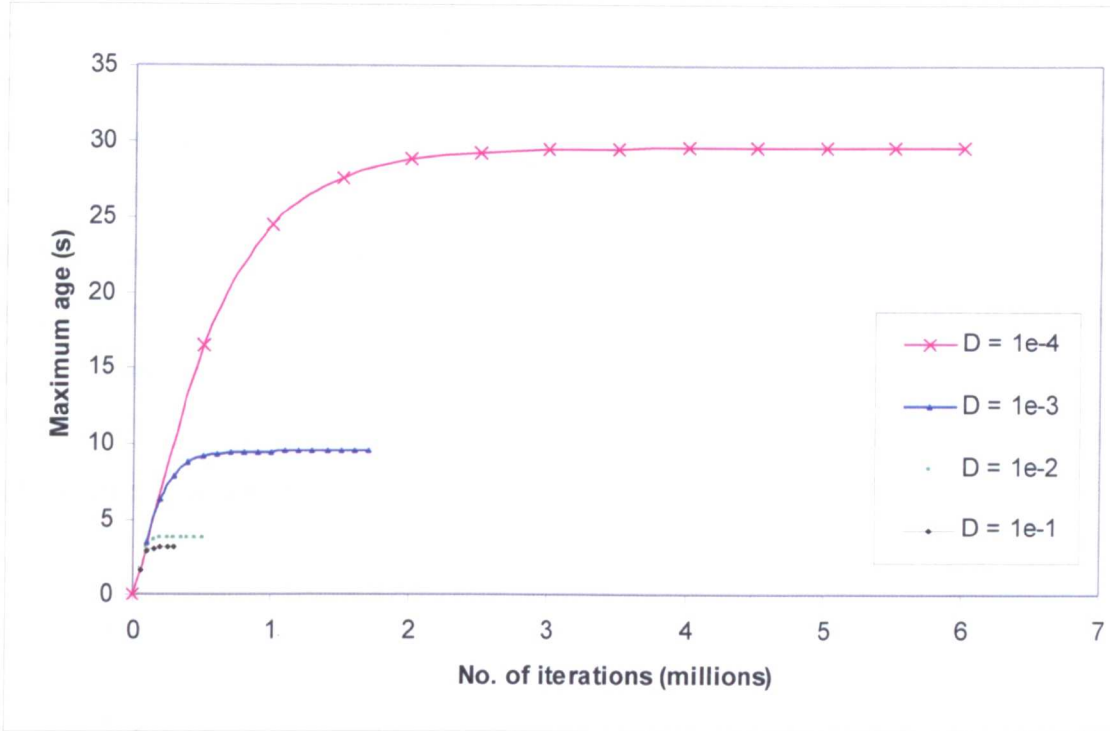

Figure 5.7: Convergence of age for different diffusion coefficients in 2D stenosis geometry.

Based on the presence of negative age values in the domain, the limiting diffusion coefficient was found to be $D = 1 \times 10^{-4} L^2 T^{-1}$. This results in a Peclet number of approximately 4280. In terms of *real* units, based on the geometry of the stenosis described in Chapter 3, this limiting value is $D = 2.6743 \times 10^{-8} m^2 s^{-1}$ since the fluid being considered is milk.

Figure 5.7 indicates the sizeable difference in the age values obtained by decreasing the diffusion coefficient by one order of magnitude. However, it is not possible to decrease the diffusion coefficient further due to instabilities in the model. The results of Chapter 4 showed that lower diffusion coefficients could be obtained with a finer grid. However, this is not an ideal solution since this grid was chosen to allow for results to be obtained in a reasonable timeframe. This issue will be revisited when the clotting simulations are discussed in section 5.6.6.

5.3.4 Testing and validation of aging model: 3D stenosis

As in the previous section, the limiting diffusion coefficient was required for the case of the 3D stenosis. Similar tests were performed at the Reynolds number of 100 but rather than simply using multiples of 10, intermediate values were also investigated. For this simulation, the grid size used was the converged grid used in Chapter 3 for the flow simulations $(1214 \times 98 \times 98)$. The length and timesteps were $L = 8.3333 \times 10^{-5} s$ and $T = 2.5967 \times 10^{-5} s$ respectively, as once again, the fluid considered is milk. The limiting diffusion coefficient in this case was measured to be $D = 5 \times 10^{-5} L^2 T^{-1}$ which is equivalent to $D = 1.3371 \times 10^{-8} m^2 s^{-1}$. With this diffusion coefficient it is possible to obtain ages of approximately 60s as shown in figure 5.8.

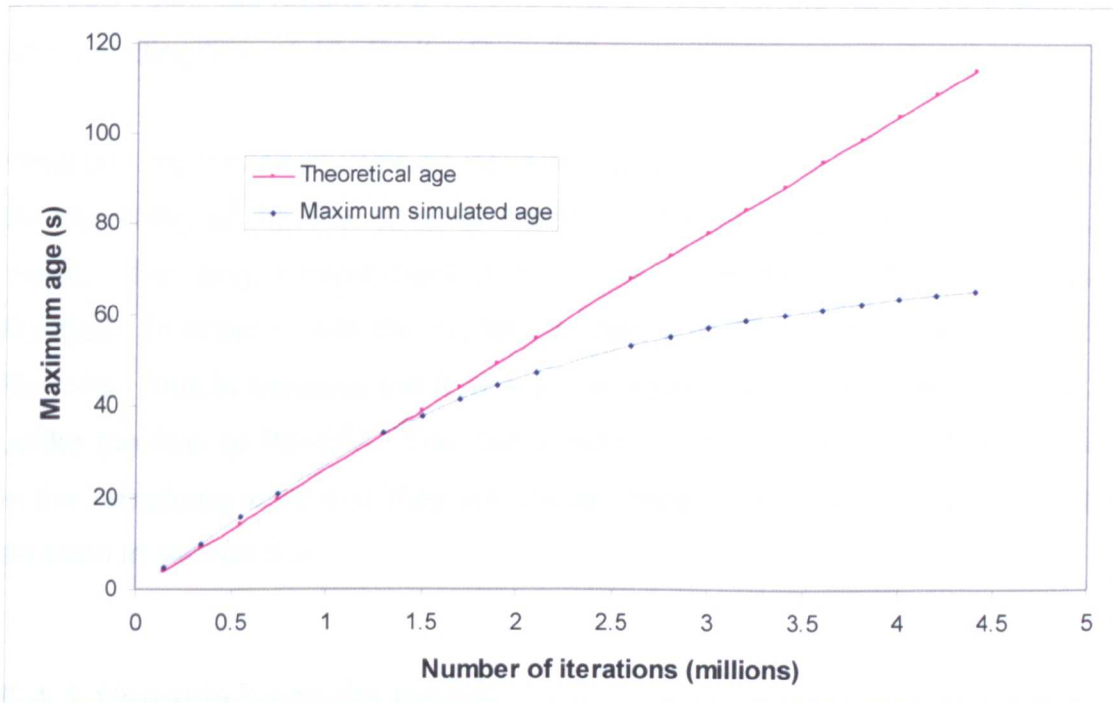

Figure 5.8: Convergence of age in 3D stenosis geometry with smallest diffusion coefficient possible. Theoretical age assumes zero diffusion.

Further discussions on this topic will take place in later sections of this chapter, particularly for the case of the higher Reynolds number of 550 since much of the work depended upon the clotting model in use.

5.4 Clotting Model

A variety of clotting models were introduced into the lattice Boltzmann source code in order to reproduce the results obtained experimentally using milk. The methods used and the results obtained are described in the sections which follow.

In the experiments performed by Smith [22], the total experiment time was 600s and the clotting times were chosen such that clot was produced 10s after the enzyme-activated milk left the outlet of the test section. Taking account of differences between the experimental and numerical upstream distance between the inlet and stenosis results in an offset of the clotting time since the fluid entering the simulated inlet should already have a non-zero age. Using the average velocities results in a clotting time of 185s for the Re = 100 experiment and a clotting time of 42s for the Re = 550 experiment.

However, reproducibility was an issue for experimental results at Re=100 due to the sensitivity of the flow to small vibrations, therefore comparisons cannot be made. The only comparisons that will be made are for the 3D results at Re=550. In order to test the models, a variety of 2D results were produced at Re=100. This is because the flow is more predictable and similar to that in 3D, unlike the flow at Re=550. The experimental clotting times are not considered in the remaining work and they are chosen based on the limiting values of age as seen in section 5.3.

5.4.1 Variable viscosity model

The viscosity model employs a linear relationship between the age of the fluid surrounding a given lattice point and the dynamic viscosity. The initial viscosity is based on the properties of the milk used in the experiments and the final viscosity was chosen arbitrarily with the requirement for a sizeable increase from its fluid value. Consideration of the resulting relaxation parameter is required at this stage. The viscosity of the fluid is altered locally, dependent on

age[1], by allowing a variable relaxation parameter to be used in the lattice Boltzmann relaxation algorithm. This has the advantage that clotted fluid can be transported within the model, behaving as a highly viscous fluid, which is realistically feasible. Sufficient experimental data allowing for a more accurate viscosity-residence time relationship to be derived, such as described in the literature [140, 142], is not available for this model.

5.4.2 Solidification model

The simplest clotting model involves using a threshold value of age and clotting any fluid nodes that exceed that value. The age distribution is available at every iteration as described previously. Any fluid nodes reaching the threshold value are transformed into solid nodes and no further mass transport is allowed. Within the lattice Boltzmann framework this means a fluid node becomes an obstacle node and the solid surface boundary condition is applied[2]. An extra variable is used to store the location of the solid particles and the iteration at which that node solidified is also stored. During the following iterations the flow field and age distribution adapt to the new geometry, while further clotting on adjacent fluid nodes may occur. This is a major advantage of using such a model, but has the disadvantage that the solid nodes will remain fixed and cannot be transported by the fluid nodes.

5.4.3 Proximity condition

For this model, a further condition is applied to the solidification model: for a fluid node to transform into a solid node, it must be adjacent to a wall, the stenosis or another clot particle. This criterion prevents detached clots from growing in regions such as the centres of vortices, where they have nothing to adhere to. If isolated clots developed in the experiments, such as those described by Parmentier *et al.* [153], it is likely that they would be transported downstream by the fluid nodes. The solidification model does not permit this,

---

[1] This was introduced into the LB source code by Joerg Bernsdorf, NEC Europe Ltd.
[2] This was introduced into the LB source code by Joerg Bernsdorf, NEC Europe Ltd.

but the solidification proximity model simply prevents the formation of such clots.

5.5 Shear Stress

It is hypothesised that experimental milk clots are susceptible to physical damage caused by the shear stress of the adjacent flow field [154]. This would act to break up certain parts of the clot such that they would be stripped from the wall and travel downstream; a situation analogous to the formation of emboli *in vivo*. In contrast to the situation which applies in the blood clotting process, shear stress cannot contribute to the clottability of the fluid as no such activation mechanism exists.

It is not straightforward to determine a particular value of shear stress that will damage existing clots and it has been shown that such a value will depend upon a large number of other variables such as pH, enzyme concentration and temperature [155-157]. There is a large body of literature on the strength of milk clot following renneting [156, 158-161], but in the current project, the main focus is on the level of shear stress that prevents a clot from forming. The data in the literature is reported over much longer timescales than required to inform the simulations, and is relevant only to the study of the structural characteristics of the clot as it ages. This is not important for the current study.

5.5.1 Lattice Boltzmann implementation of shear stress

The stress tensor can be computed from the density distributions and their equilibrium values, without computing velocity gradients. This was demonstrated in 1994 by Ladd [44] and has been used extensively in more recent work [162-164]. This is particularly useful because only local quantities are being calculated using variables already available in the relaxation routine. The governing tensor equation is given below[1]:

---

[1] Calculation of these values was already present in the source code, implemented previously by Peter Lammers, High Performance Computing Center, Stuttgart (HLRS), Germany.

$$\sigma_{\alpha\beta} = -\rho c_s^2 \delta_{\alpha\beta} - \left(1 - \frac{\omega}{2}\right) \sum_i f_i^{(1)} c_{i\alpha} c_{i\beta} \qquad \textbf{5.5}$$

where $f_i^{(1)} = f_i - f_i^{eq}$

The stress tensor is given by White [89] as:

$$\sigma_{ij} = \begin{vmatrix} -p + \tau_{xx} & \tau_{yx} & \tau_{zx} \\ \tau_{xy} & -p + \tau_{yy} & \tau_{zy} \\ \tau_{xz} & \tau_{yz} & -p + \tau_{zz} \end{vmatrix} \qquad \textbf{5.6}$$

where σ_{ij} is the stress in the *j* direction on a face normal to the *i* axis and the τ values are the viscous stresses. For a Newtonian fluid, the viscous stresses are proportional to the element strain rates and the coefficient of viscosity and for incompressible flow, the τ values are defined as:

$$\tau_{xx} = 2\mu \frac{\partial u}{\partial x} \quad \tau_{yy} = 2\mu \frac{\partial v}{\partial y} \quad \tau_{zz} = 2\mu \frac{\partial w}{\partial z} \qquad \textbf{5.7}$$

$$\tau_{xy} = \tau_{yx} = \mu\left(\frac{\partial u}{\partial y} + \frac{\partial v}{\partial x}\right) \qquad \tau_{xz} = \tau_{zx} = \mu\left(\frac{\partial w}{\partial x} + \frac{\partial u}{\partial z}\right) \qquad \tau_{yz} = \tau_{zy} = \mu\left(\frac{\partial v}{\partial z} + \frac{\partial w}{\partial y}\right)$$

Examination of equations 5.5 and 5.6 implies that the τ values (viscous stresses) are given by:

$$\tau_{\alpha\beta} = -\left(1 - \frac{\omega}{2}\right) \sum_i f_i^{(1)} c_{i\alpha} c_{i\beta} \qquad \textbf{5.8}$$

Hence the velocity gradients given in 5.7 do not need to be calculated. The viscous stress tensor can therefore be calculated directly by making a few extra calculations in the relaxation routine. The difficulty comes in using this tensor appropriately. A scalar value of the shear stress is required. White [89] defines the shear stress in 2D as:

$$\tau = \mu \frac{du}{dy} \qquad \textbf{5.9}$$

White also defines the expressions in 5.7 as the generalisation of 5.9 to three-dimensional viscous flow. One particular analysis [165] was implemented and the theory behind this will now be described.

The maximum shearing stress for a particular lattice point can be determined by finding the direction cosines of a plane on which the derivatives of the shear stress are zero. The three values of maximum shear stress are given by the following equations:

$$\tau = \pm\frac{1}{2}(S_y - S_z) \qquad \tau = \pm\frac{1}{2}(S_x - S_z) \qquad \tau = \pm\frac{1}{2}(S_x - S_y) \qquad \textbf{5.10}$$

where S_x, S_y and S_z are the principal stresses calculated at each lattice point. The principal stresses are found by determining a set of perpendicular axes in which the shear stresses vanish. These axes are termed the principal axes. The principal stresses can be determined from the stresses in an alternative, known axes system, such as the Cartesians used in the lattice Boltzmann code. Calculation of the principal stresses requires solution of the following cubic equation:

$$S^3 - (\sigma_x + \sigma_y + \sigma_z)S^2 + (\sigma_x\sigma_y + \sigma_y\sigma_z + \sigma_x\sigma_z - \tau_{yz}^2 - \tau_{xz}^2 - \tau_{xy}^2)S - (\sigma_x\sigma_y\sigma_z + 2\tau_{yz}\tau_{xz}\tau_{xy} - \sigma_x\tau_{yz}^2 - \sigma_y\tau_{xz}^2 - \sigma_z\tau_{xy}^2) = 0 \qquad \textbf{5.11}$$

where the three *S* solutions are the principal stresses. This requires careful consideration when choosing the original stress values to be used. The stress tensor given previously is:

$$\sigma_{ij} = \begin{vmatrix} -p + \tau_{xx} & \tau_{yx} & \tau_{zx} \\ \tau_{xy} & -p + \tau_{yy} & \tau_{zy} \\ \tau_{xz} & \tau_{yz} & -p + \tau_{zz} \end{vmatrix} \qquad \textbf{5.12}$$

The pressure terms, p are several orders of magnitude larger than the remaining components and therefore dominate all calculations. It has been demonstrated analytically that the principal stresses computed without the pressure terms are offset by the value of the pressure and hence, the maximum shear values computed in 5.10 are identical whether the pressure terms are used or not. However, there is a large difference in the accuracy between both solutions, due to the inevitable truncation of all stored values and so the pressure terms must not be used to compute the principal stresses.

A method for solving equation 5.11 has been implemented in the source code[1] [166] to obtain the principal stresses. Equation 5.10 can then be used to obtain the three maximum shear stresses and the required scalar is simply the maximum of these three values. A detailed performance analysis of this method has not been performed, but simulating 100 iterations of an empty 3D box suggests that the performance is approximately halved when the shear stress calculation is used[2]. This method was validated using a variety of geometries as shown in the following sections.

5.5.2 Validation of shear stress calculation: 2D channel

The analytical solution for the shear stress distribution for parabolic flow in a channel can be derived using either the theoretical or simulated velocities. In order to use the simulated velocities, a central difference approach must be taken to calculate the transverse gradient of the longitudinal velocity component. The shear stress is then calculated as before using equation 5.13 [89].

$$\tau = \mu \frac{du}{dy} \qquad \textbf{5.13}$$

For calculating the shear stress using the analytical velocity profile, the equation for 2D parabolic flow can simply be differentiated with respect to *y*, as follows.

---

[1] See Appendix 9.1 for details.
[2] This was discussed in detail with Joerg Bernsdorf, NEC Europe Ltd. and it is not believed that this can be improved.

$$u = u_{\max}\left(1-\frac{r^2}{R^2}\right) = u_{\max}\left(\frac{-4j^2-6ly+4jly+4j+3}{(ly-2)^2}\right) \qquad \textbf{5.14}$$

$$\frac{du}{dy} = \frac{du}{dr} = \frac{du}{dj} = \frac{-2ru_{\max}}{R^2} = -4u_{\max}\left(\frac{2j-ly-1}{(ly-2)^2}\right) \qquad \textbf{5.15}$$

where r represents a radial distance and j represents the vertical index as used in LB simulations. ly is the number of lattice points in the vertical direction.

The simulated pressure gradient can also be used to calculate the analytical shear stress profile. This is likely to be the most appropriate method since the inlet boundary condition applies the equilibrium distributions rather than the actual distributions, which would cause a slight error in the simulated velocity profile. The equations to be used for calculating all further analytical shear stress profiles are given below. The difference between 2D and 3D profiles arises from the differing theoretical parabolic equations.

$$\tau = r\frac{dp}{dx}\ \text{(2D)} \qquad\qquad \tau = \frac{r}{2}\frac{dp}{dx}\ \text{(3D)} \qquad \textbf{5.16}$$

where $\frac{dp}{dx}$ is the pressure gradient along the channel and r is the radial direction.

For the channel simulation and shear stress calculation, a lattice of dimensions 320×82 was used with $u_p = 8.0128\times 10^{-3}\,LT^{-1}$ and $\omega = 1.95$ hence a Reynolds number of 100 was obtained. Figure 5.9 shows the two sets of theoretical results along with the simulated results taken at the middle of the channel. This shows that strong agreement is seen between the analytical and simulated values of shear stress across the majority of the channel. There is, however, an issue regarding the wall. The wall in the simulation lies half way between the first fluid and the first solid node. This is the position where the velocity goes to zero. The shear stress is accurately calculated for all fluid nodes but if the shear stress on the wall is required, difficulties arise. The problem is that the

shear stress is not calculated between lattice points and the value on the real wall is an incorrect interpolation because the solid node has no real significance. It was decided that this is not a problem and the shear stress on the first fluid node can be used to represent the wall shear stress. Figure 5.10 shows the simulated shear stress plotted at the first fluid node alongside the theoretical value based on equation 5.15.

Figure 5.10 shows that discrepancies arise at the inlet and outlet and that the analytical shear stress measured at y = 2 (last fluid node) is lower than that at $y = 1.5$ (the real wall) by only 0.63% measured relative to the shear on the real wall. The approximate error in the simulated shear stress measured relative to that on the real wall is 0.33% in the middle region of the channel. If further accuracy is required for obtaining the wall shear, a larger number of lattice points must be used.

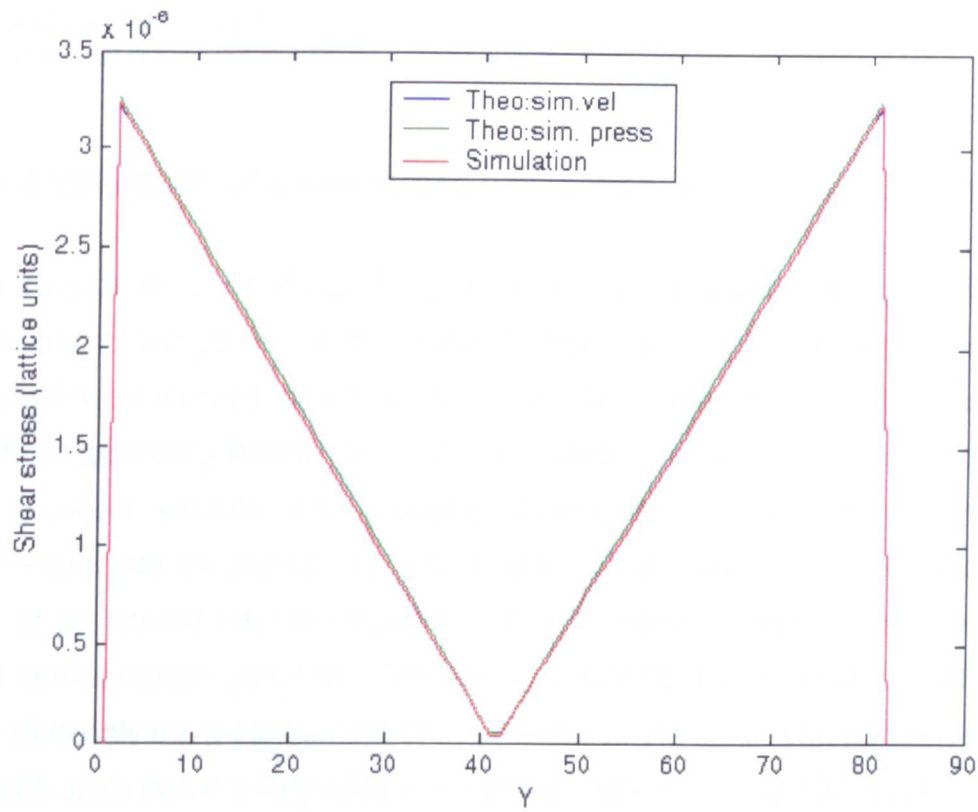

Figure 5.9: Distribution of shear stress across channel. Simulated and analytical results are shown.

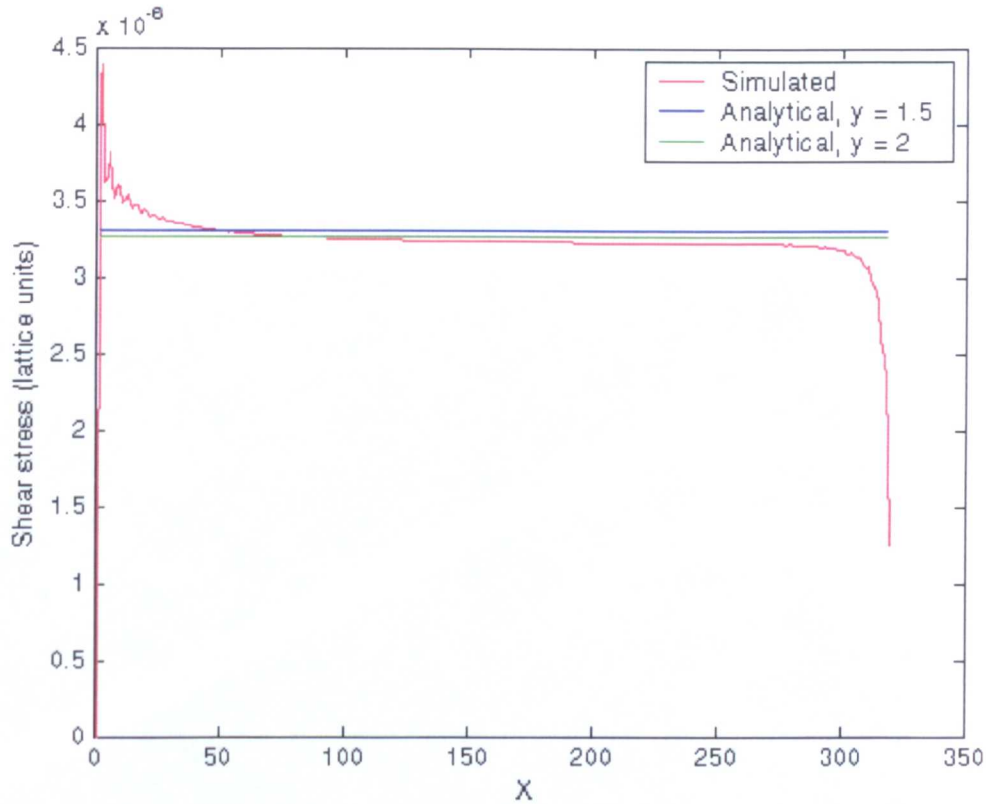

Figure 5.10: Distribution of shear stress along length of channel at last fluid node. Simulated and analytical results are shown.

5.5.3 Validation of shear stress calculation: 2D inclined channel

The solution of shear stress should be orientation independent, hence this is an essential investigation of the shear stress calculations implemented. The channel was inclined at an angle of $\tan^{-1}(0.5)$ relative to the horizon. The obstacle geometry had to be specifically created in Matlab. In order to obtain an accurate velocity and pressure distribution, a channel of dimensions 1145×664 with an angled inlet velocity distribution was used. This requires the use of an altered inlet boundary condition to allow for two dimensions of the inlet velocity to be specified. The previous inlet boundary condition in the code specified only the x-component of the velocity at the inlet. The parameters were chosen such that the Reynolds number was approximately 100, using the width of the channel measured perpendicular to the channel axis. Figure 5.11 shows the velocity distribution and the development to parabolic flow is clear.

A variety of velocity and shear stress profiles were taken in order to compute the analytical solutions. The results were analysed using profiles taken at

various locations along the length/width of the channel, perpendicular to either the channel wall or the global axes. The analytical solutions were obtained using the methods described for the straight channel. Figures 5.12-5.14 show the results obtained.

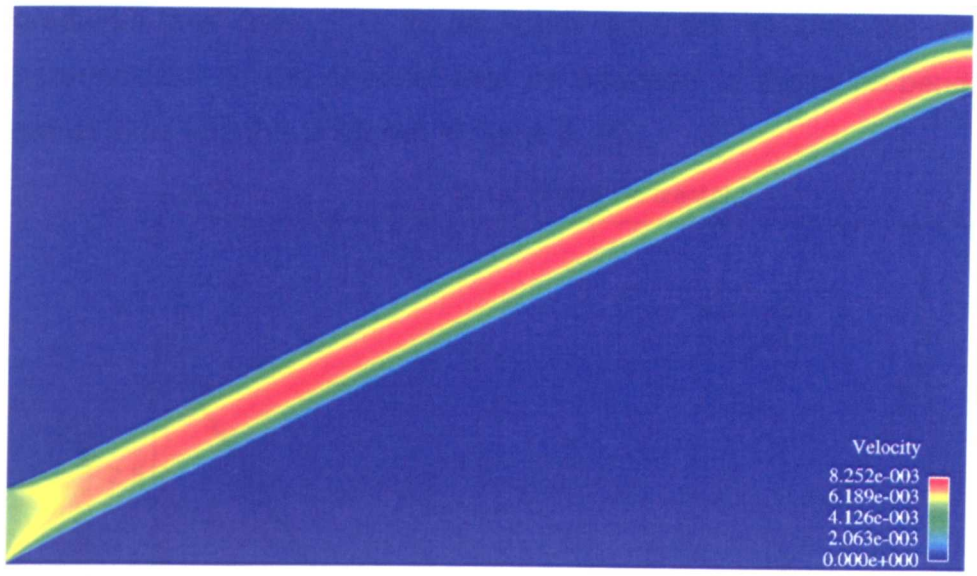

Figure 5.11: Velocity (magnitude) distribution in inclined channel at Re = 100. Values measured in lattice units.

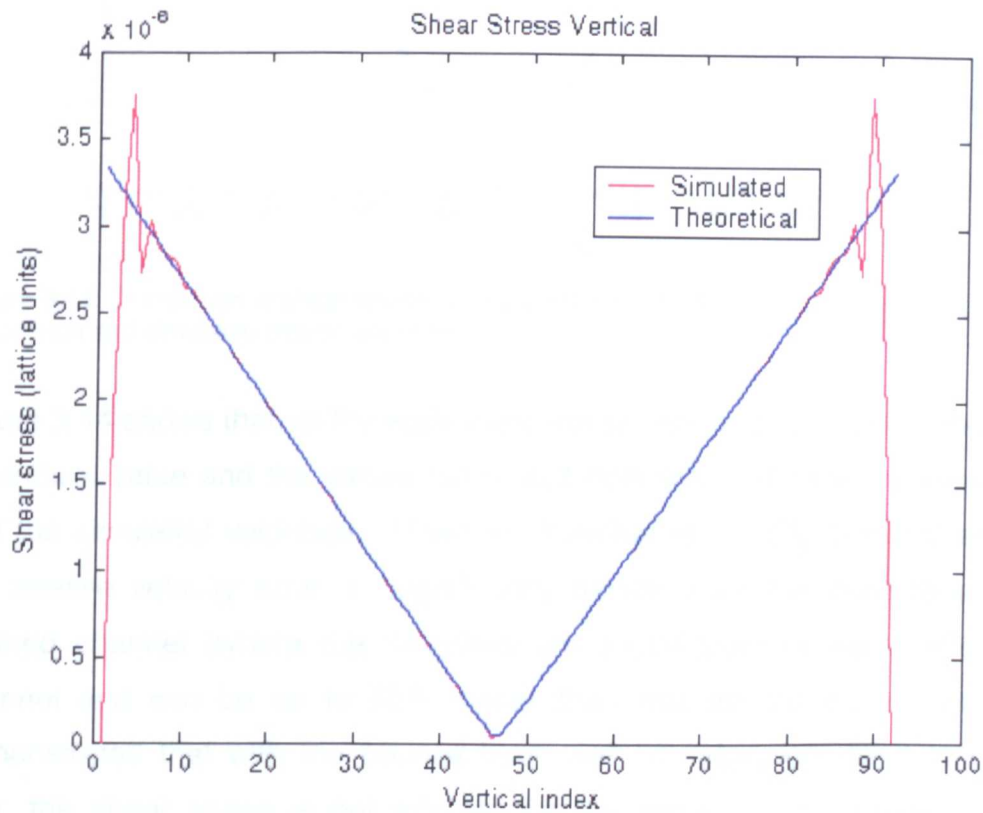

Figure 5.12: Distribution of shear stress across central vertical profile of the inclined channel. Theoretical and simulated results are shown.

The profiles obtained in figures 5.12 and 5.13 are oscillatory at the walls because, as the wall is approached, different parts of the wall are seen since the wall is made up of square elements and the relative distances from these change across the profile. The different wall nodes are contributing by different amounts as the profile is traversed. This is also true when the velocity gradients are used. It is far more accurate to use the profile that is perpendicular to the channel axis as opposed to those perpendicular to the global axes and this is shown in figure 5.14.

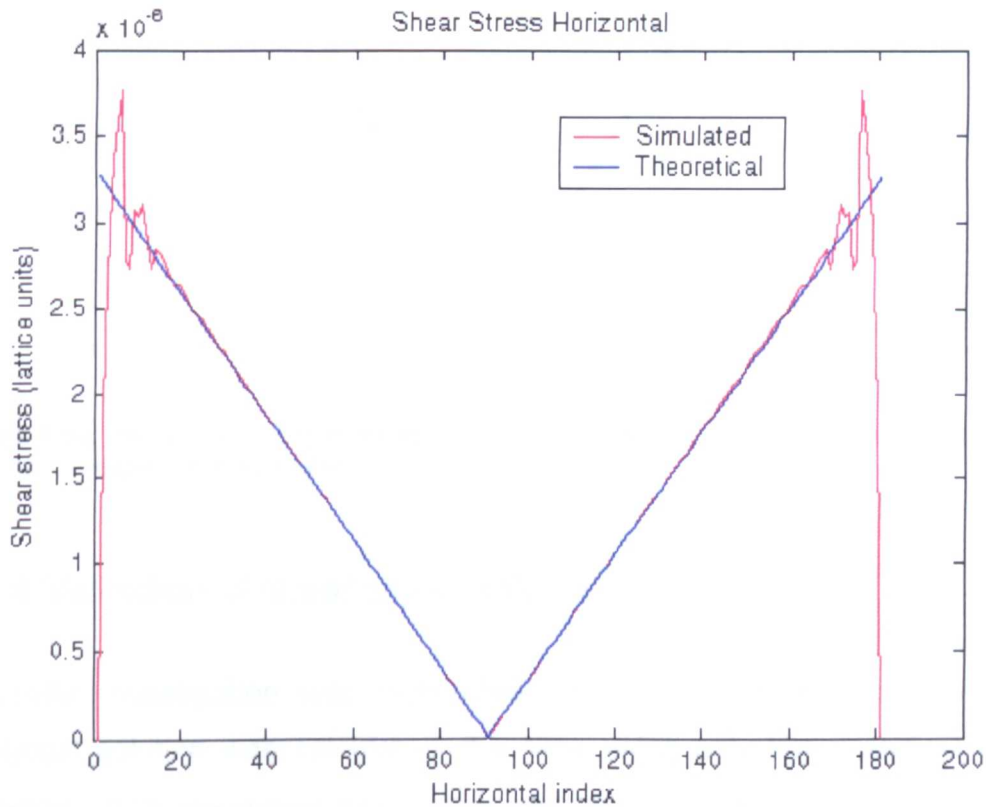

Figure 5.13: Distribution of shear stress across central horizontal profile of the inclined channel. Theoretical and simulated results are shown.

Figure 5.14 shows that, at the walls there are still some differences between the theoretical value and the values calculated both with the code implementation and the simulated velocities. However, Kandhai *et al.* [83] demonstrated that the *relative* velocity error is "*significantly higher*" near the boundaries of an inclined channel (where the velocities are small) than in the centre of the channel and can be up to 50% higher than that for flat walls. Artoli [53] demonstrated that with the bounce back wall boundary condition in channel flow, the shear stress is not affected by the slip velocity. However, in an inclined channel, due to the changing geometry, the velocity and hence shear stress profiles near the boundary will vary from the theoretical solutions.

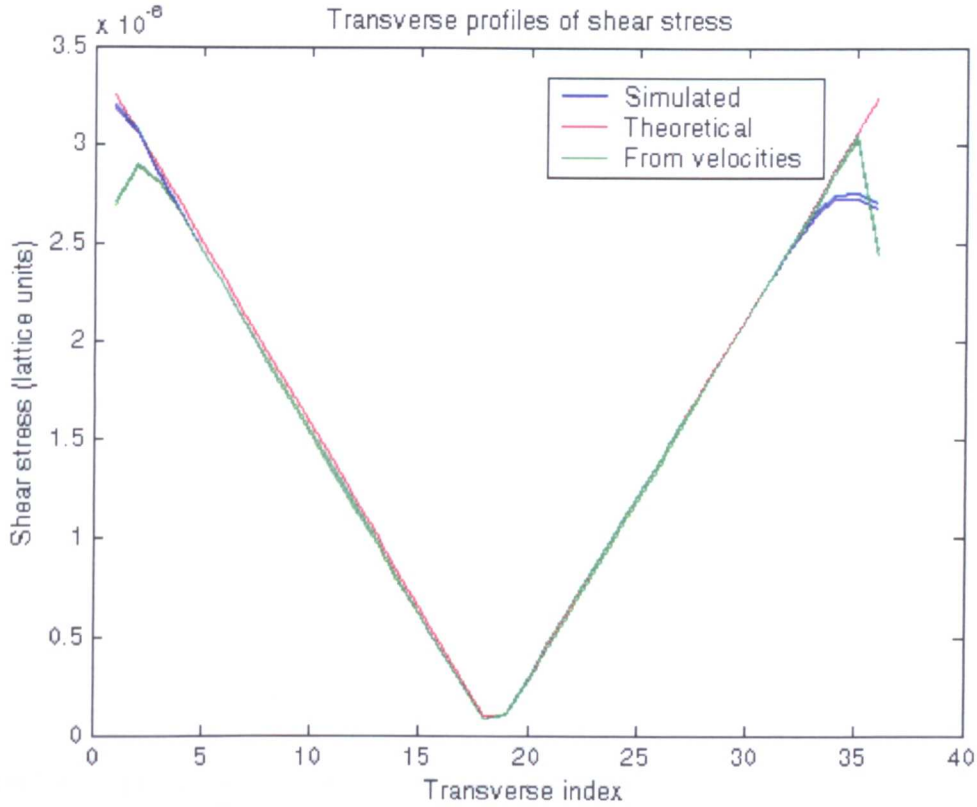

Figure 5.14: Distribution of shear stress across central transverse profile of the inclined channel. Theoretical and simulated results are shown.

5.5.4 Validation of shear stress calculation: 3D tube

A similar investigation was performed for parabolic flow in a tube. The analytical solution was calculated, this time using only the analytical velocity equation. The simulation parameters are $384 \times 98 \times 98$, $u_p = 8.9031 \times 10^{-3} LT^{-1}$ and $\omega = 1.95$ hence a Reynolds number of 100 was obtained. Figure 5.15 shows axial profiles and figure 5.16 shows diagonal profiles. These show some discrepancies near the wall. Previous reports on the simulation of tube flow in Chapter 2 indicated that the velocity profiles were highly accurate in both the axial and diagonal directions. However, the calculation of the shear stress involves the use of both the distributions and the equilibrium values, both of which will have an error at the wall compared to the theoretical solution. This is because the theoretical solution is based on a perfect circular cross section. Further manipulation of the stress tensor will lead to an increase of this error, hence placing it above those obtained for the velocities at the walls.

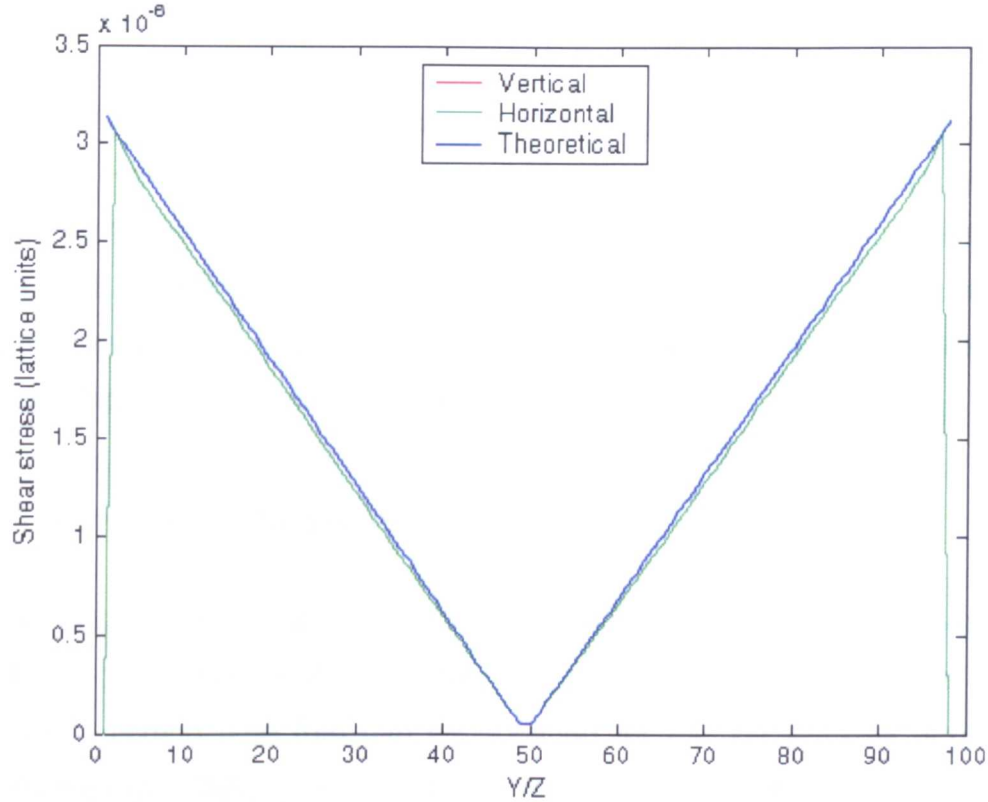

Figure 5.15: Axial profiles of shear stress taken from the simulated tube results. The vertical profile lies underneath the horizontal profile.

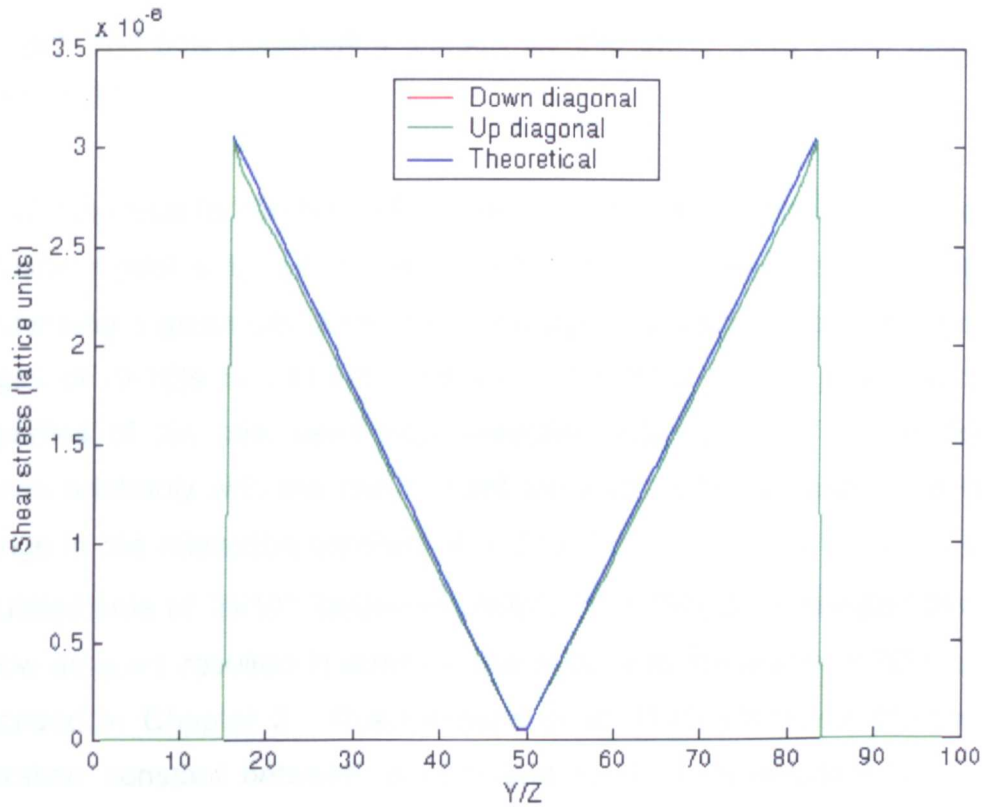

Figure 5.16: Diagonal profiles of shear stress taken from the simulated tube results. The down-diagonal profile lies underneath the up-diagonal profile.

5.6 Results

The results are presented, in turn, for the models described in the previous sections. However, it must be noted that a lot of the developmental work was performed for the 2D stenosis geometry at Re=100, hence this comprises the larger part of the validation. Based on the results presented in Chapter 4, the upwind model was used for the 3D Re=550 simulations in an attempt to improve the results obtained with the Flekkoy model.

5.6.1 2D viscosity model results

Due to instabilities in the diffusion model, the clotting time of 185s required for the Re = 100 experiment could not be obtained. Figure 5.7 shows that the maximum clotting time that can be obtained for the 2D stenosis geometry is approximately 30s, since the limiting diffusion coefficient was $D = 2.6743 \times 10^{-8} m^2 s^{-1}$. The chosen clotting time was chosen to be 10s in order to demonstrate the functionality of the model.

The grid and flow parameters chosen for this study were those described in section 5.3.3.

The clotting time for the lattice Boltzmann models is chosen to be 10s whilst the viscosity model employs a linear relationship between the age of the fluid surrounding a given lattice point and the dynamic viscosity over the respective ranges of (9-10)s and (1.2-100)mPa.s. The initial viscosity is based on the properties of the milk used experimentally [22] and the final viscosity was chosen arbitrarily with the requirement for a sizeable increase. The resulting change in the relaxation constant is a drop from $\omega = 1.95$ to $\omega = 0.66$ over the simulated time of 2×10^6 iterations. Noble *et al.* [84] demonstrated that values as low as $\omega = 1$ resulted in errors in the velocity at the wall in a 2D channel as described in Chapter 2. Rakotomalala *et al.* [132] employ a change in the relaxation constant between $\omega = 0.5$ and $\omega = 1.99$ in simulations of viscous mixing, stating that only values of $\omega < 0.30$ produce wall boundary effects. Since the change in the relaxation constant described above is only local, such effects are assumed to be negligible.

Figure 5.17 shows the results of the simulations performed using the viscosity model, the images displaying fluid with a viscosity of 100mPa.s. The extent of the high viscosity fluid is seen to increase with time, originating from the downstream face of the stenosis, within the recirculation zones. After approximately 11.18s seconds, a region of high viscosity fluid develops at the centre of the vortex. These two high-viscosity regions join as the clot size continues to increase. After approximately 11.63s, high viscosity fluid can be seen to develop from the outlet, growing along the walls until it reaches the primary clot. This wall growth is related to the slow moving fluid in the wall boundary layer, allowing residence times of sufficient magnitude to clot.

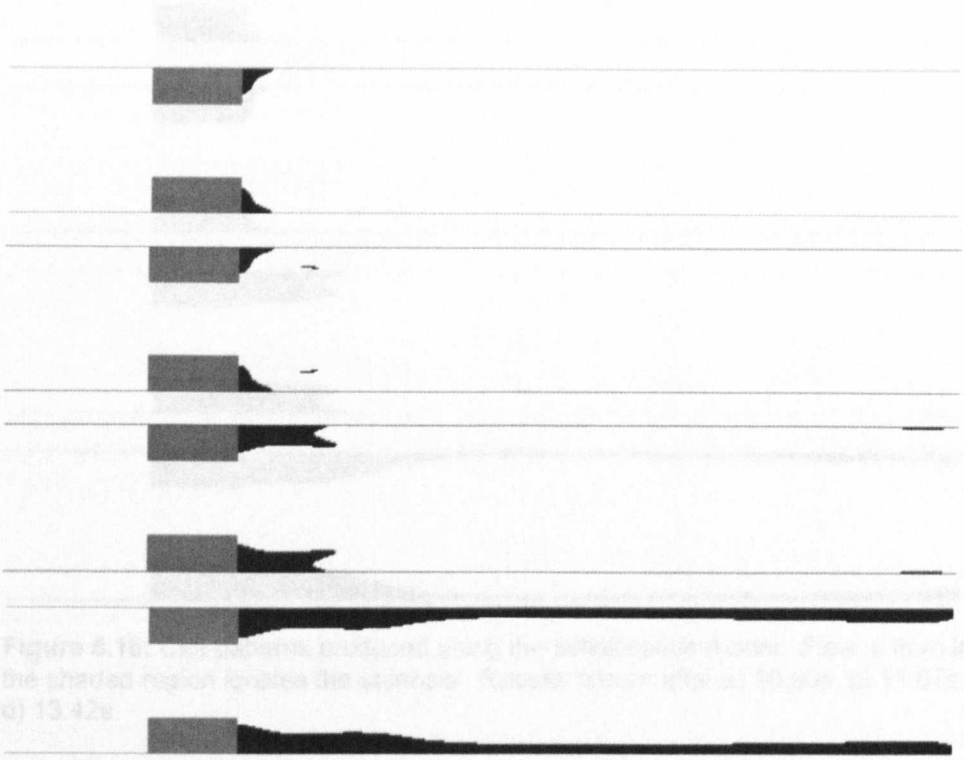

Figure 5.17: Clot patterns produced using the viscosity model. Flow is from left to right and the shaded region locates the stenosis. Clot is represented by fluid of maximal viscosity (100mPa.s). Results shown after approximately a) 11.12s, b) 11.18s, c) 11.63s and d) 14.32s.

5.6.2 2D solidification model results

Figure 5.18 shows the results obtained using the solidification model at a Reynolds number of 100. All simulation parameters were as described in the previous section.

Figure 5.18 demonstrates the existence of isolated clots in the centre of the vortex. This Reynolds number produces flow with closed streamlines and the

'hotspots' of age are in the corner distal to the stenosis and in the vortex centres since very little convective transport can occur in these regions.

Clot deposition was observed for this model as part of this study using the higher Reynolds number of 550 [79, 167, 168]. However, these results attempt to simulate the complex flow seen in Chapter 3 in just 2D, hence major differences result and will not be discussed further.

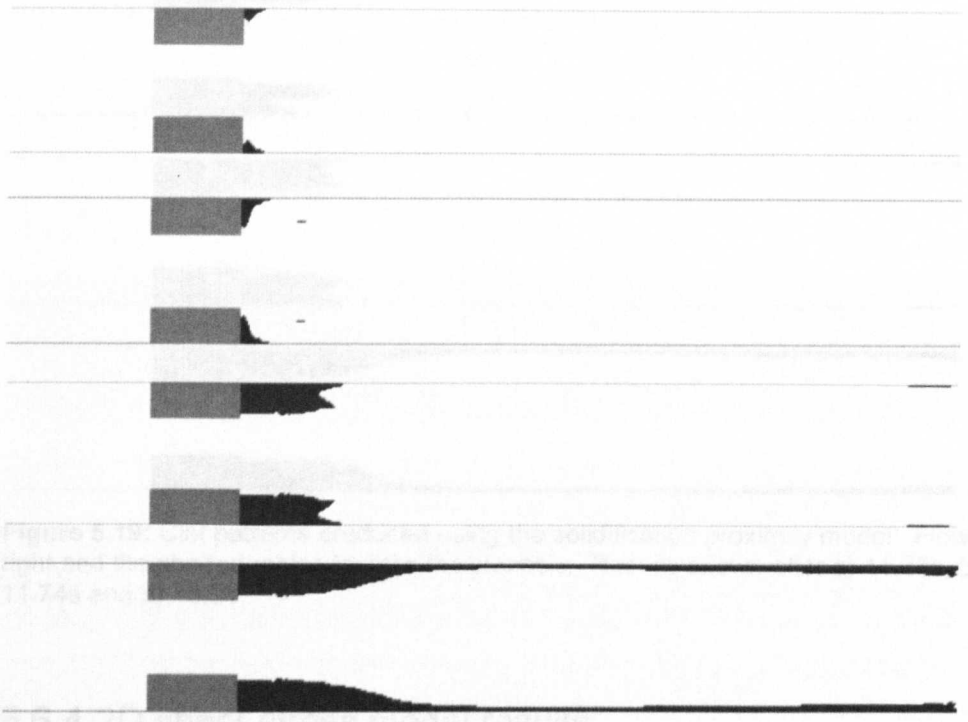

Figure 5.18: Clot patterns produced using the solidification model. Flow is from left to right and the shaded region locates the stenosis. Results shown after a) 10.90s, b) 11.07s, c) 11.74s and d) 13.42s.

5.6.3 2D proximity model results

The aim of this modification of the model was to prevent clot growth in isolated regions, such as the vortex centre as seen in figure 5.18. Figure 5.19 shows that isolated clots no longer form, but very rapid growth is observed between the vortex centre and the clot downstream of the stenosis. The ensuing clot growth continues in a similar fashion to that seen in the preceding models.

It is not likely that such a structure as that shown in figure 5.19 would be supported under the shear conditions resulting from the surrounding flow field. It is also likely that the mass of clot in this region would result in a positional

change in the deposition pattern. This latter point will not be considered, but the first point relating to the shear field can be addressed using the shear stress model described in section 5.5.

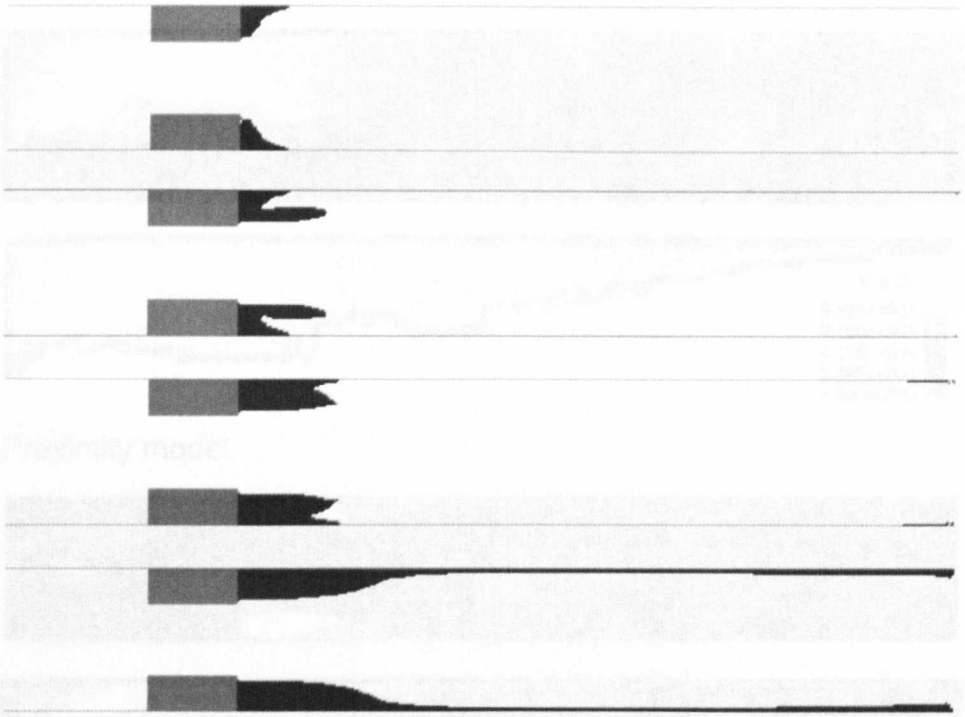

Figure 5.19: Clot patterns produced using the solidification proximity model. Flow is from left to right and the shaded region locates the stenosis. Results shown after a) 11.35s, b) 11.40s, c) 11.74s and d) 13.31.

5.6.4 2D shear stress model results

In order to compare the results of the previous models with those incorporating the limiting shear stress condition, a set of simulations were performed with all the relevant combinations of models. The parameters used in this study were a clotting time of 16.5s and a total experiment time of 30s.

Figure 5.20 shows the results of the different models. The effect of the shear stress threshold is clearly seen in figure 5.20. This was investigated in more detail in a simulation with a clotting time of 6.83s and a total time of 16.8s. The results are shown in figure 5.21. This shows that two types of clot form and the threshold shear stress is a very sensitive parameter.

Aging model

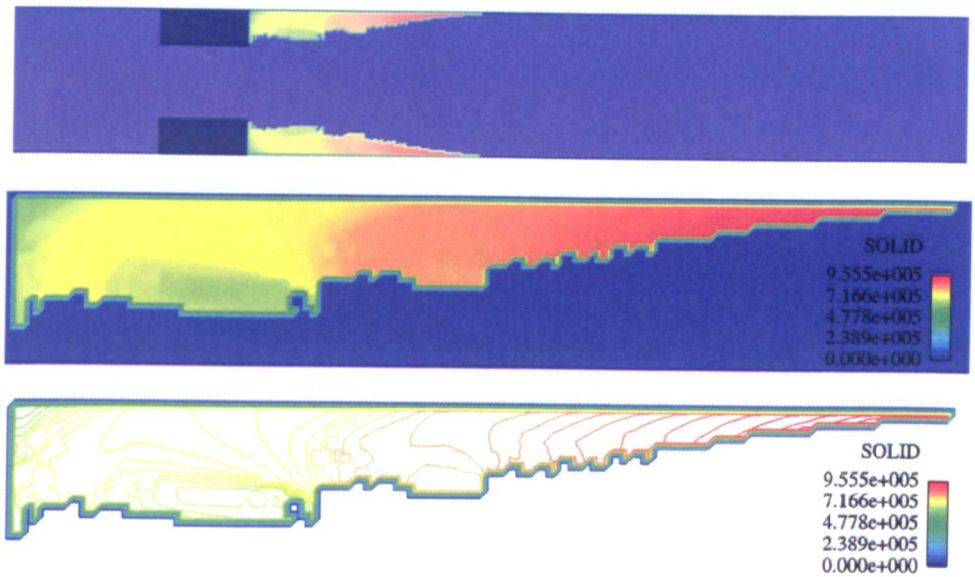

Proximity model

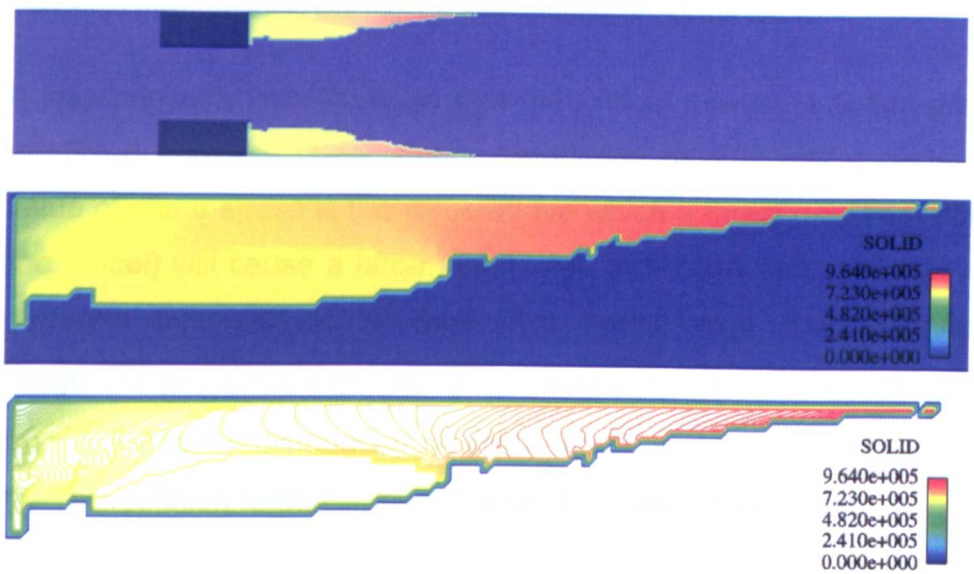

Shear stress model: low threshold

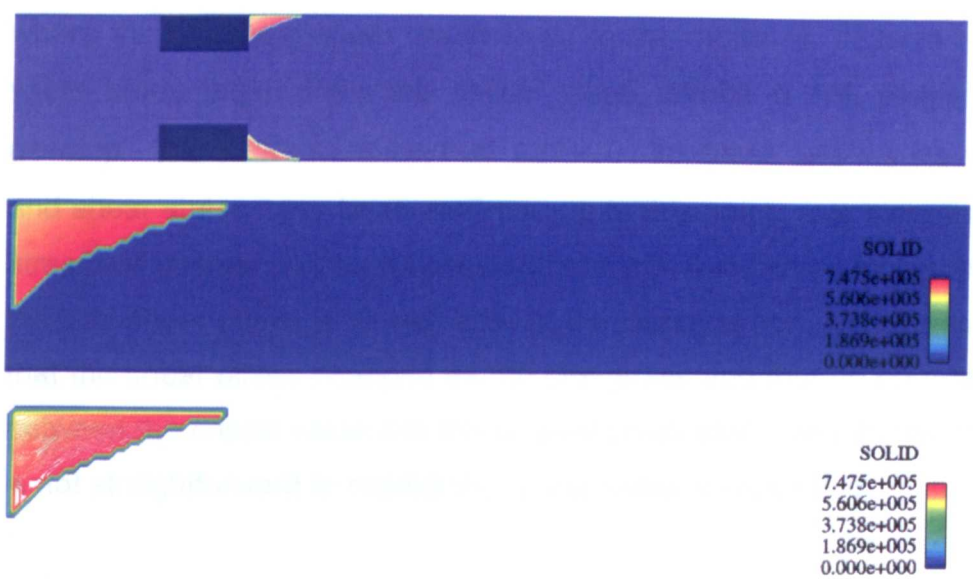

Shear stress model: high threshold

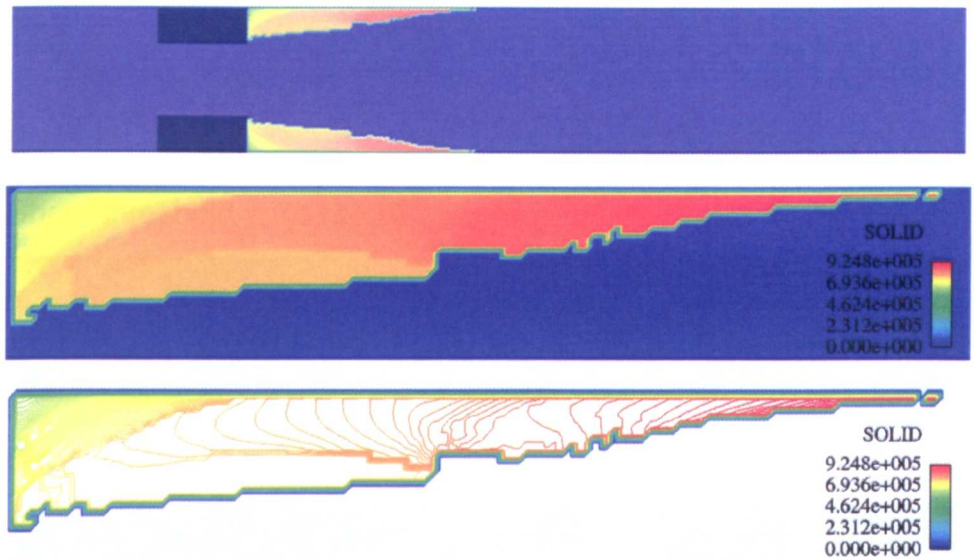

Figure 5.20: Clots produced using aging, proximity and shear stress models. Results are shown after 30s with a clotting time of 16.5s. Solid variable indicates iteration number at which the clot formed. Zoomed clot regions and contours of clot are shown.

It was originally hypothesised that the critical threshold shear stress could be predicted from the shear stress distribution prior to clot growth. The critical value of shear stress is the value above which a threshold shear stress (used in the model) will cause a large, connected clot to develop and below which, two separate regions of clot will form. The critical value of shear stress was in the range $(7.510 - 7.512) \times 10^{-6}\, ML^{-1}T^{-2}$. However, this value could not be identified from the original distribution of shear stress and the maximum shear stress in the recirculation region is much higher than the critical value.

The development of the clot has been investigated in greater detail for a case where the threshold shear stress used in the model is $7.52 \times 10^{-6}\, ML^{-1}T^{-2}$ this value being larger than the critical value, hence a full, single clot should develop. The total simulation has 4.87×10^{5} iterations and results of clot shape and shear stress have been analysed up to this point. It is clear that the shear stress will change as the clot develops and this is indicated by figure 5.22 where the wall shear stress is plotted against the distance from the stenosis. The fact that the shear stress changes as the clot grows and that no correlation is seen between the critical value and the original shear stress distribution means that it is not straightforward to predict the critical shear stress value.

Shear threshold = 1×10^{-5}

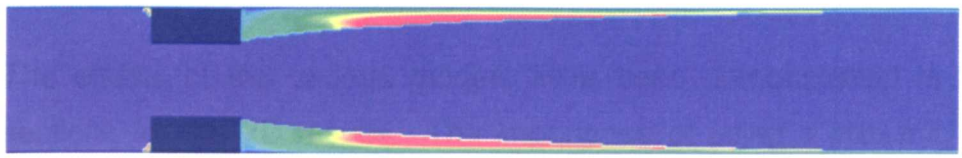

Shear threshold = 7.512×10^{-6}

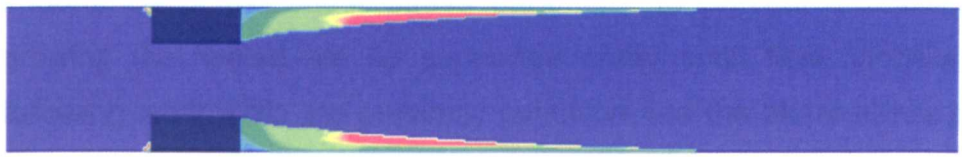

Shear threshold = 7.51×10^{-6}

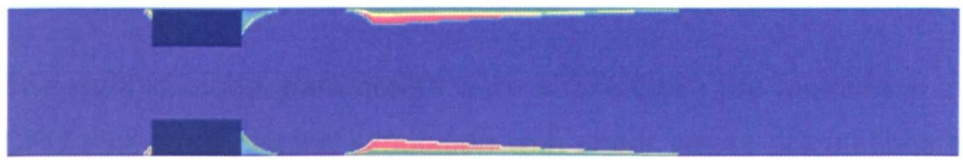

Shear threshold = 6×10^{-6}

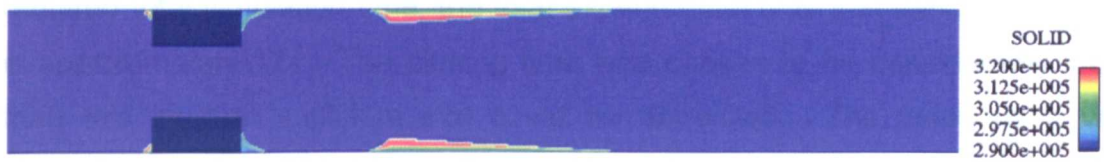

Figure 5.21: Clots produced using a variety of shear stress thresholds. Clotting time of 6.83s is used with a total experiment time of 16.8s.

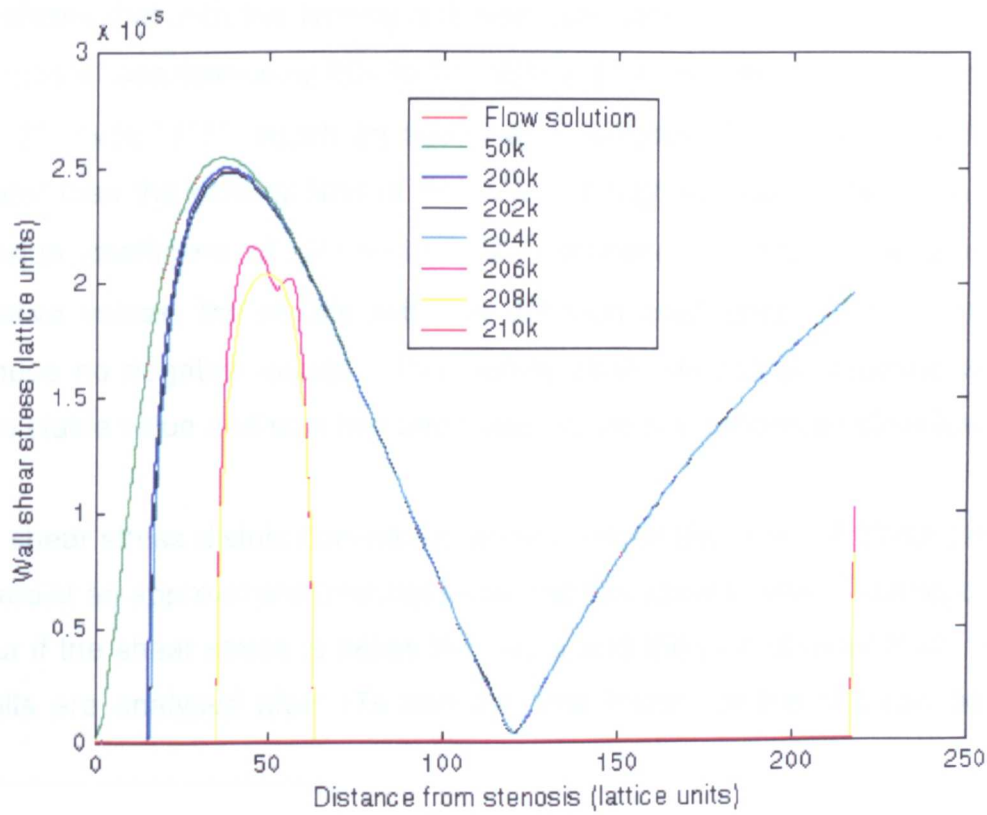

Figure 5.22: Distribution of 2D wall shear stress in recirculation zone during clot growth.

5.6.5 3D Re=100 stenosis results

The effects of the various models have been demonstrated in the previous sections for the 2D results. The importance of using a proximity condition to prevent the growth of isolated clots in the domain is demonstrated, as is the importance of the shear stress parameter to prevent unrealistic clots from growing that would not be supported under such flow conditions. For the following work, both the proximity condition and the shear stress condition are used together with the solidification model and this section presents the results of the clots produced in laminar flow at Re=100.

The clotting model parameters were chosen with the requirement that the total CPU time for a clotting simulation with shear stress calculations should be no longer than 1 week on the SX-6. Given the performance of the model and the required total simulation time, the total experimental time that can be simulated is approximately 17s. The clotting time was chosen to be considerably lower than this so that sufficient clot could be deposited. The value used was approximately 7s. The latter value is equated to a concentration value of the aging species that is used to determine the onset of clotting. The plot in figure 5.8 shows that with the limiting diffusion coefficient of $D = 5 \times 10^{-5} L^2 T^{-1}$ allows for ages of approximately 60s to be obtained. However, the results produced with $D = 1 \times 10^{-4} L^2 T^{-1}$ reach an age of approximately 30s[1], which is sufficiently greater than the clotting time of 7s. Even though simulations with the limiting diffusion coefficient of $D = 5 \times 10^{-5} L^2 T^{-1}$ produce an acceptable amount of negative values, the results with the diffusion coefficient of $D = 1 \times 10^{-4} L^2 T^{-1}$ produce no negative values. The clotting time can still be reached with this more stable value and so it has been used in the simulations which follow.

The shear stress distribution was analysed before the onset of clotting in order to predict an approximate threshold shear stress value to use. Clotting can only occur if the shear stress is below this value and the fluid is older than 7s. The results are analysed after 17s and the time history of the clot can be seen.

---

[1] This was reported in figure 5.7 for the 2D simulation. This was not repeated in 3D, but similar values are expected.

Simulations have been performed using threshold values of shear stress of $1\times10^{-6}\,ML^{-1}T^{-2}$, $5\times10^{-7}\,ML^{-1}T^{-2}$ and $1\times10^{-7}\,ML^{-1}T^{-2}$. Figures 5.23-5.25 show the results obtained.

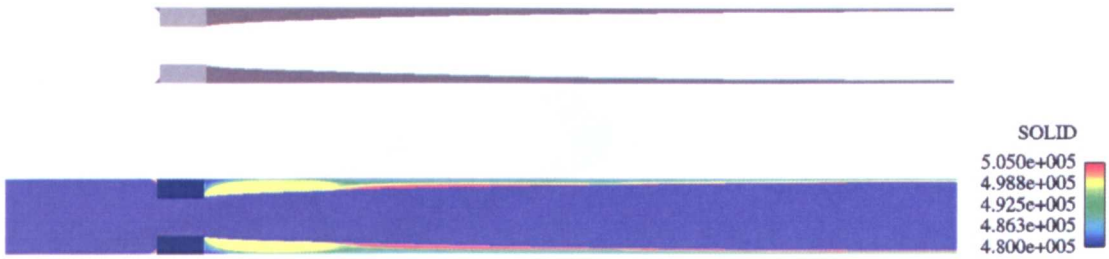

Figure 5.23: Greyscale image of clot produced in central z-slice after 17s (upper) and time history of clot growth (lower) in Re=100 3D simulation. The variable 'solid' indicates the iteration number at which that lattice point became solid, therefore new clots are shown in red and old clots (or no clots) are shown in blue. Shear stress threshold = $1\times10^{-6}\,ML^{-1}T^{-2}$.

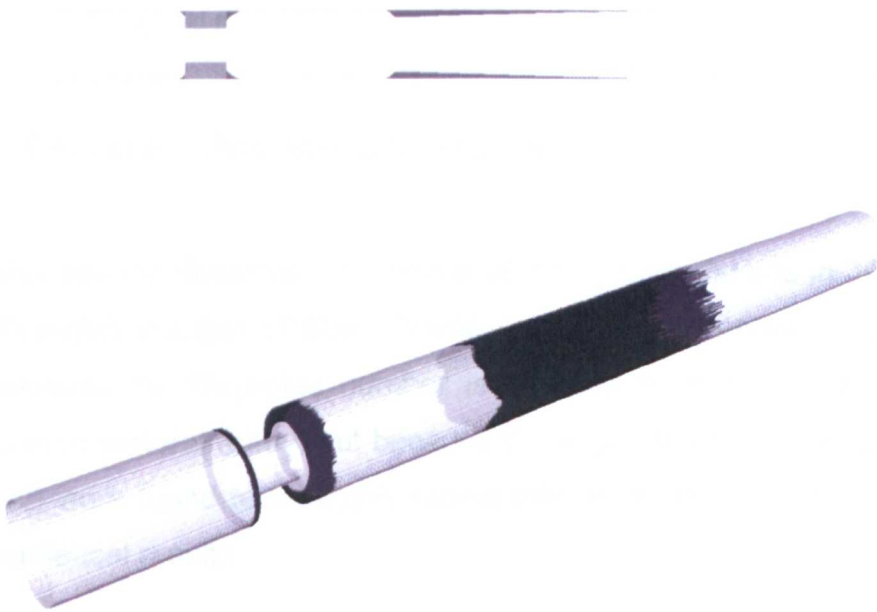

Figure 5.24: : Re=100 3D clot produced after 17s. Upper image shows clot in central z-slice, lower image shows 3D clot isosurface within isosurface of geometry. Clot is shown as darker region. Threshold shear stress = $5\times10^{-7}\,ML^{-1}T^{-2}$.

Figures 5.23 and 5.24 suggest that the *critical* shear stress threshold value lies between $5\times10^{-7}\,ML^{-1}T^{-2}$ and $1\times10^{-6}\,ML^{-1}T^{-2}$ because the shape of the clot changes in a fashion similar to the 2D simulations.

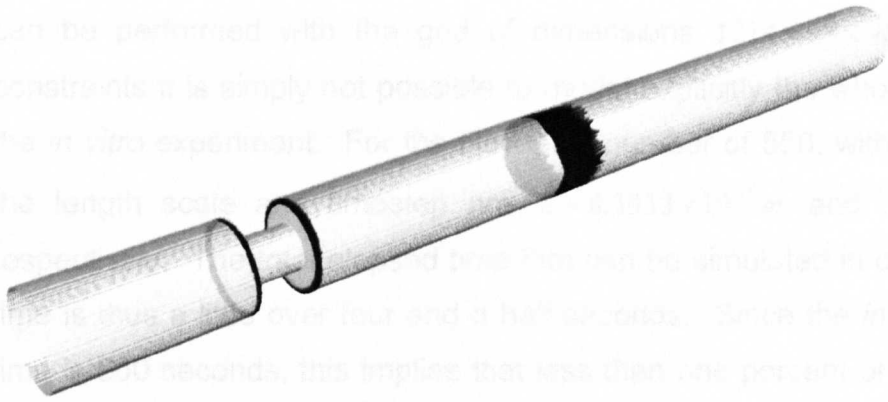

Figure 5.25: Re=100 3D clot produced after 17s. Upper image shows clot in central z-slice, lower image shows 3D clot isosurface within isosurface of geometry. Clot is shown as darker region. Threshold shear stress = $1 \times 10^{-7} ML^{-1}T^{-2}$.

5.6.6 3D Re=550 stenosis results

This section describes the results of the clot simulations in 3D using the higher Reynolds number of 550. These results are of greatest importance not only because the Reynolds number is representative of physiological flow in the human femoral artery, but because the experimental results produced by Smith [22] were found to be highly repeatable, thus allowing for comparison with the numerical results.

The complex flow field was seen to be in qualitative agreement with that of the flow visualisation studies in Chapter 3 and the established (but transient – arbitrary starting point) flow is used as the starting condition for the clotting simulations. For this highly-disturbed flow, diffusive transport is likely to be less important than convective transport and the age of the fluid in the lee of the stenosis will be significantly less.

In order to calculate the clotting time and the total simulation time to be used, as for the case of the lower Reynolds number flow solution in the previous section, the simulation time was restricted by only allowing for one week on the SX-6

machine. However, the performance of the code is such that $12.45 MLUPS$ are obtained for the whole domain. This figure can be used along with the total domain size in order to calculate the number of iterations that can be performed in one week[1]. This calculation indicates that approximately 7×10^5 iterations can be performed with the grid of dimensions $1214 \times 98 \times 98$. Under these constraints it is simply not possible to model explicitly the whole time course of the *in vitro* experiment. For the Reynolds number of 550, with this spatial grid, the length scale and timestep are $L = 8.3333 \times 10^{-5} m$ and $T = 6.6258 \times 10^{-6} s$ respectively. The total elapsed time that can be simulated in one week of CPU time is thus a little over four and a half seconds. Since the *in vitro* experiment time is 600 seconds, this implies that less than one percent of the real elapsed time can be simulated within the computational constraints. Although it would in principle be possible to increase the simulation time, already the CPU cost on the SX machine is significant and in any case a simulation that consumes more than this amount of CPU time is unlikely to be of great practical value for the foreseeable future.

There are several options for producing a representative simulation within the available constraints. The experimental clotting time is 42s and the experiment time is 600s, as discussed in section 5.4. One reasonable approach might be to maintain the ratio between the clotting time and the simulation time. In this case the clotting time to be used in the simulations for this grid would be 4.9×10^4 lattice time units, or 0.3247 seconds. There is, however, a fatal flaw in this approach. The average transport time through the domain is approximately 1.9×10^5 iterations, which equates to $1.2876 s$. Assuming a parabolic flow profile, even the fastest-moving fluid on the central axis would transport through the domain in $0.6438 s$, and this is longer than the clotting time. This means that, using this approach, without the shear stress condition, by the end of the simulation, all fluid in the domain would clot. This implies that the shear stress condition would be acting to prevent this behaviour as opposed to simply shaping the deposited clot (and, of course, the shear stress is zero on the axis for stable parabolic flow). Clearly this approach is inappropriate: although it maintains the ratio between clotting time and experimental time, it is impossible

[1] Further details on this calculation are given in Chapter 2.

to satisfy an equally reasonable constraint that the transit time through the domain should be a small proportion of the total simulation time

If an accurate comparison with the experiments is to be performed, the experimental and simulated times should be in agreement. In order to achieve this within sensible computational limitations, the lattice timestep needs to be increased. With the current grid, this would require reduction of the relaxation parameter, hence increasing the lattice viscosity. However, to obtain the required Reynolds number, the lattice velocity would have to increase proportionately. The restriction on the lattice velocity is related to the validity of Chapman-Enskog expansion, which is only valid in the limit of low Mach number. The compressibility error increases with the square of the Mach number as discussed in Chapter 2. However, if a compressibility error is permitted, since this will be small in comparison with the remaining errors present in the experiments, then an alternative approach can be considered.

The following guidance is given by White [89] concerning Mach numbers in traditional simulations:

Ma < 0.3:	*incompressible flow,* where density effects are negligible.
0.3 < Ma < 0.8:	*subsonic flow,* where density effects are important but no shock waves appear.

As described in Chapter 2, neglecting the considerations of the Chapman-Enskog analysis and hence the accuracy of the BGK approximation, the limit on the Mach number is 0.3 in order to neglect density effects. However, with the current grid, even if the lattice velocity was increased to a limit of Mach 0.3, the timestep would only increase to $T = 2.2963 \times 10^{-5} s$, which would mean that the simulation of the full experiment would take approximately 280 days on the SX-6 machine, thus 40 times longer than the required time.

The alternative solution to this problem is to reduce the grid size. The grid in consideration is that used for the Re=100 flow simulations which, from the results presented in Chapter 3, appeared to show convergence. Performing the necessary calculations, and permitting a Mach number of 0.3, means that the

full 600s experiment can be simulated if the grid is reduced so that 36 points represent the diameter of the parent vessel[1]. The grid size is therefore $456 \times 38 \times 38$.

Under these conditions it is possible to simulate the full 600s experiment reported by Smith [22], although it is appreciated that the accuracy of the LB scheme is now compromised The question immediately arises as to whether the computed flow field provides a reasonable approximation to that computed previously. Figure 5.26 illustrates the flow field.

2×10^5 iterations = 12.25s

4×10^5 iterations = 24.49s

6×10^5 iterations = 36.74s

8×10^5 iterations = 48.99s

1×10^6 iterations = 61.23s

Figure 5.26: Isosurface of flow shown in geometry for Re=550 simulation with coarse grid.

Figure 5.26 appears to show that the recirculation zone and hence the onset of disturbance is closer to the stenosis than that seen in the simulations shown in Chapter 3. This could be a result of the timescales used relative to the times at which results were captured. Figure 5.26 does not appear to show the

[1] This is based on the performance on the SX-6. In the latter part of this project, the SX-8 became available, resulting in an increase in performance by a factor of 2, hence a grid of diameter 44 lattice units could be used.

movement of the recirculation region seen in Chapter 3 and in the experimental results. An aliasing effect might be observed if the frequency of the oscillation of the recirculation zone is matched with the frequency at which results are captured. The timestep here is much larger than in the previous simulations, which may also give differences. However, Thornburg *et al.* [112] reported that the recirculation length moves downstream as the mesh density is increased. Since turbulence modelling is not available in the LB code, a full grid convergence study using averaged parameters has not been performed so it is possible that the results with this grid size are not converged. Nevertheless, and despite these criticisms, the results of this simulation are at least qualitatively comparable with those presented in Chapter 3. It is interesting to note that for the current simulations, in contrast with those for the finer grid, the unsteady flow was achieved without the need to introduce additional wall roughness. This might suggest that the unsteady flows observed both numerically and experimentally are the consequence of imperfect geometries and/or unstable boundary conditions. In practice, even though a stable flow might be the theoretical result at this Reynolds number, the flow is close to the breakdown of stability and, certainly in the experiments conducted by Smith [22], unsteady flow was observed.

The clotting time required, as discussed in section 5.4 is 42s. Chapter 4 demonstrated that as the grid size decreases, the limiting real diffusion coefficient also decreases. The clotting time to be used now depends upon the value that can be obtained with this grid size and might not be representative of that in the experiments. With a diffusion coefficient of $D = 5 \times 10^{-3} L^2 T^{-1}$, no negative values of concentration were observed, but the maximum age was only approximately 1.4s. For this grid, the average transport time through the domain is 1.29s. This has slightly improved the situation in that the clotting time is now longer than the average transport time, but much of the fluid will clot and the separation of these two times is not as great as desired. When the diffusion coefficient was reduced to $D = 1 \times 10^{-3} L^2 T^{-1}$, the negative values were sometimes as large as 20% of the peak concentrations and with a diffusion coefficient of $D = 5 \times 10^{-4} L^2 T^{-1}$, this value rose to 70%. These peak negative values were found in regions where the flow was highly disturbed and therefore depend (in an unpredictable fashion) on the flow field and hence simulation

time. The variation of the peak positive and negative values of concentration for the two lowest diffusion coefficients is shown in figure 5.27.

The diffusion coefficients of $D = 1 \times 10^{-3} L^2 T^{-1}$ and $D = 5 \times 10^{-4} L^2 T^{-1}$ are equivalent to real values of $D = 8.0646 \times 10^{-7} m^2 s^{-1}$ and $D = 4.0323 \times 10^{-7} m^2 s^{-1}$ respectively.

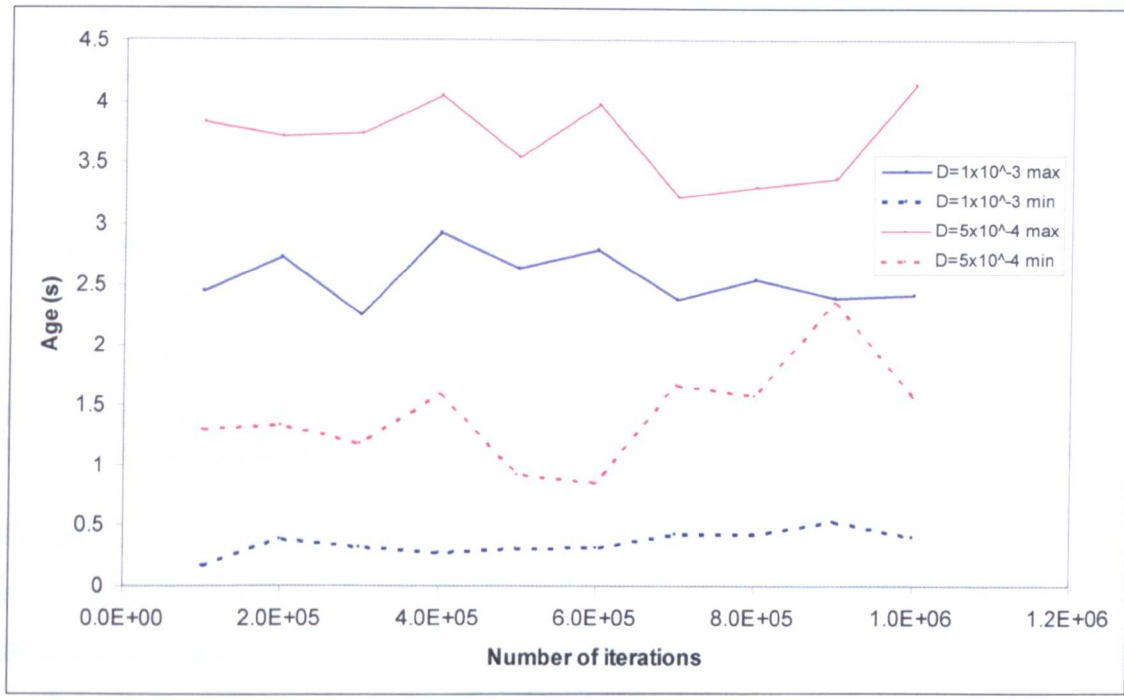

Figure 5.27: Variation in peak positive (solid lines) and peak negative magnitude (dotted lines) for $D = 1 \times 10^{-3} L^2 T^{-1}$ and $D = 5 \times 10^{-4} L^2 T^{-1}$ in Re=550 coarse grid aging simulation.

Figure 5.27 is interesting in that it indicates that, the age of the fluid does not increase with the number of iterations and that the peak negative value of age varies at random. The experimental clotting time of 42s cannot be achieved with either of these diffusion coefficients because of increased diffusive and convective transport between the recirculation zone and the core flow.

As the negative values of age only occur at a small number of individual lattice points, their presence will be ignored temporarily in order to investigate the patterns of clot deposition. The clotting time was varied as was the shear stress threshold for both diffusion coefficients. However, the results produced with the diffusion coefficient of $D = 5 \times 10^{-4} L^2 T^{-1}$ were not noticeably different than those for the diffusion coefficient of $D = 1 \times 10^{-3} L^2 T^{-1}$. Figures 5.28 and 5.29 show the

results obtained with the diffusion coefficient of $D = 1 \times 10^{-3} L^2 T^{-1}$ since these will be less affected by negative ages. In these figures, only slices through the z-axis are shown. The results in other planes were analysed but were found to be very similar.

No shear stress limit

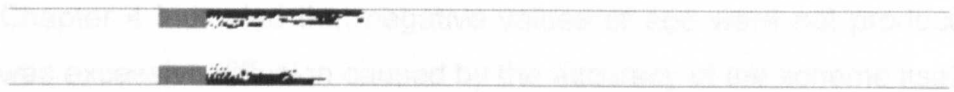

Shear threshold = 5×10^{-5}

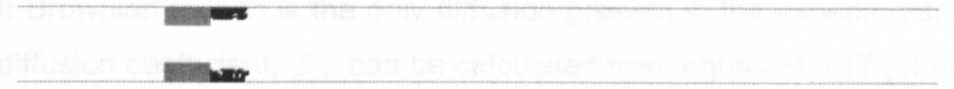

Shear threshold = 1×10^{-5}

Figure 5.28: Clots produced with a diffusion coefficient of $D = 1 \times 10^{-3} L^2 T^{-1}$ and a clotting time of 1.99s with a variety of shear thresholds for the coarse grid of dimensions 456x38x38.

Figure 5.29 shows that clotting starts along the walls at the outlet when the shear stress condition is not used. This is because the clotting time is 1.53s and the average transport time is 1.29s, hence the slower moving fluid at the walls will be older than the average residence time of fluid in the domain. Figures 5.28 and 5.29 appear to show isolated clots in the domain, but this is not the case as the clots are connected in other planes.

No shear stress limit

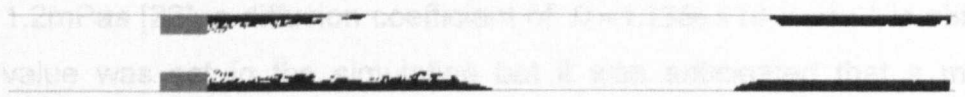

Shear threshold = 5×10^{-5}

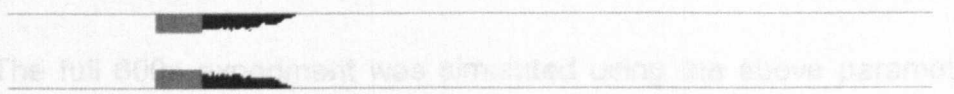

Shear threshold = 1×10^{-5}

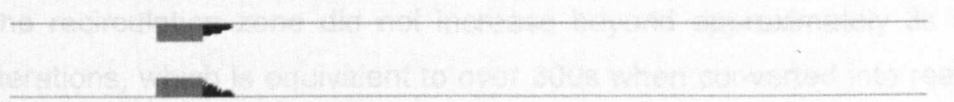

Figure 5.29: Clots produced with a diffusion coefficient of $D = 1 \times 10^{-3} L^2 T^{-1}$ and a clotting time of 1.53s with a variety of shear thresholds for the coarse grid of dimensions 456x38x38.

Figures 5.28 and 5.29 represent the 'best' simulations that can be performed under the specified computational constraints using the Flekkoy model.

To investigate whether further improvements could be made using a more stable diffusion model, the 1st order upwind model described in Chapter 4 was introduced into the aging routine of the LB source code. The results shown in Chapter 4 indicated that negative values of age were not produced, but there was excessive diffusion caused by the accuracy of the scheme itself.

If Brownian motion is the only diffusion present in the experimental system, the diffusion coefficient, D, can be calculated from equation 5.17 [169].

$$D = \frac{kT}{2\pi\mu a} \qquad \textbf{5.17}$$

where k is Boltzmann's constant $(1.38 \times 10^{-23} JK^{-1})$, T is the temperature (K), μ is the dynamic viscosity and a is the radius of the small particles suspended in the fluid.

In the case of clottable milk, it is appropriate to focus on the suspension of insoluble para-K-casein molecules in fluid as it is the aggregation of these particles that form the clot. The random motion of these clotting particles in the fluid suspension is considered to be equivalent to the mixing of old and new milk. With a micelle radius of 50nm [170] and a dynamic viscosity for milk of 1.2mPas [22], a diffusion coefficient of $D = 1.1366 \times 10^{-11} m^2 s^{-1}$ is obtained. This value was set in the simulation but it was anticipated that a much greater amount of diffusion would be present based on the work in Chapter 4.

The full 600s experiment was simulated using the above parameters and the largest ages in the model were found along the walls at the outlet. The age in the recirculation zone did not increase beyond approximately 3s after 5×10^6 iterations, which is equivalent to over 300s when converted into real time. This is of the same order as the ages shown in figure 5.27, the difference being that with the upwind methods, there are no negative ages present. There will

however be an error in the age distribution due to the limited accuracy of the upwind scheme.

For comparison with the results using the Flekkoy model, clotting results were obtained using the upwind method and the coarse grid of dimensions $456 \times 38 \times 38$ requiring approximately 3 days on the SX-8 machine or 6 days on the SX-6 machine. The theoretical diffusion coefficient of $D = 1.1366 \times 10^{-11} m^2 s^{-1}$ was set, but the studies presented in Chapter 4 suggest that there will be excess diffusion associated with the numerical scheme. A clotting time of 3s was chosen and the full 600s experiment was simulated. The average transport time through the domain is 1.29s and this simulation results in the largest clotting time currently available. As described previously, the largest ages are found at the outlet along the walls. Therefore the shear stress condition must be implemented in order to prevent total occlusion at the outlet. Figure 5.30 shows the results obtained.

Shear threshold ≈ 0.75mPa

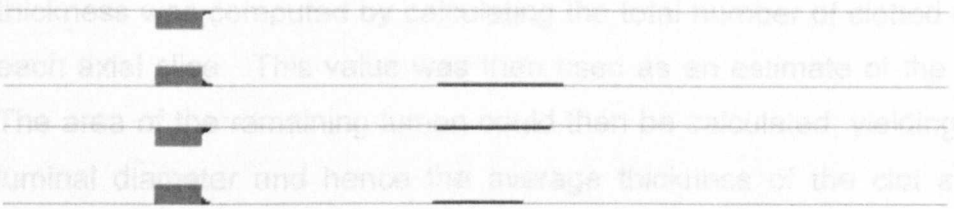

Shear threshold ≈ 1.5mPa

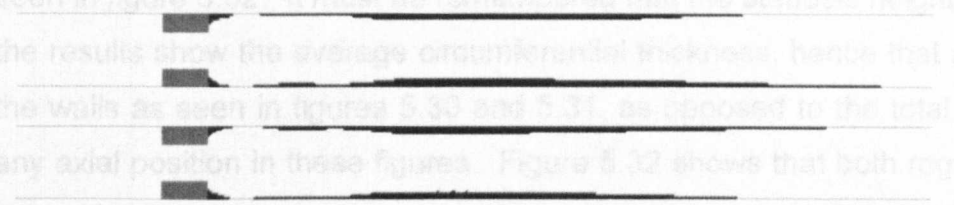

Figure 5.30: Perpendicular axial slices through 3D domain showing simulated clot at Re=550 with upwind method and clotting time of 3s. Results produced with different threshold shear stresses.

Figure 5.30 shows that the threshold shear stress can dramatically change the resulting clot deposition profile, but sufficient data is not available in the literature to allow for a prescribed value of shear stress to be used, as described previously in this chapter.

In order to examine the mesh sensitivity of this specific problem, a simulation was performed with twice the number of lattice points across the diameter, giving almost 8 times the number of lattice points overall; $911 \times 74 \times 74$. This simulation took approximately 4 weeks of CPU time on the SX-8. Such a simulation cannot be performed routinely, but acts to provide details of the accuracy of the previous, coarser grid. The clotting time was kept at 3s and the threshold shear stress used was approximately 1.5mPa. Figure 5.31 shows the results obtained, which should be compared to those seen in figure 5.30.

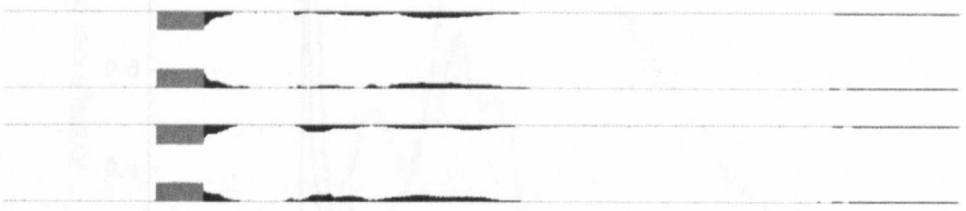

Figure 5.31: Perpendicular axial slices through 3D domain showing simulated clot at Re=550 with upwind method and clotting time of 3s. Shear threshold ≈1.5mPa. Fine grid of dimensions $911 \times 74 \times 74$ was used.

In order to compare these two sets of results more accurately, the average clot thickness was computed by calculating the total number of clotted nodes within each axial slice. This value was then used as an estimate of the area of clot. The area of the remaining lumen could then be calculated, yielding an average luminal diameter and hence the average thickness of the clot at each axial point. These values were then converted into *real* units and the results can be seen in figure 5.32. It must be remembered that the stenosis height is 2mm and the results show the average circumferential thickness, hence that along one of the walls as seen in figures 5.30 and 5.31, as opposed to the total clot seen at any axial position in these figures. Figure 5.32 shows that both regions of peak deposition are in approximate agreement, however, with the coarse grid, the secondary clot develops further upstream.

5.6.7 Comparing the diffusion routines

In order to investigate the limits of the two diffusion schemes in the context of achievable age in the flow simulations, two further analyses were performed with the upwind method. Firstly, the 2D stenosis at a Reynolds number of 100 was used with the upwind aging model to determine the range of ages that

could be obtained. Figure 5.33 shows the results alongside those obtained previously with the Flekkoy model. This shows that significantly greater ages can be obtained with the upwind method than with the Flekkoy model.

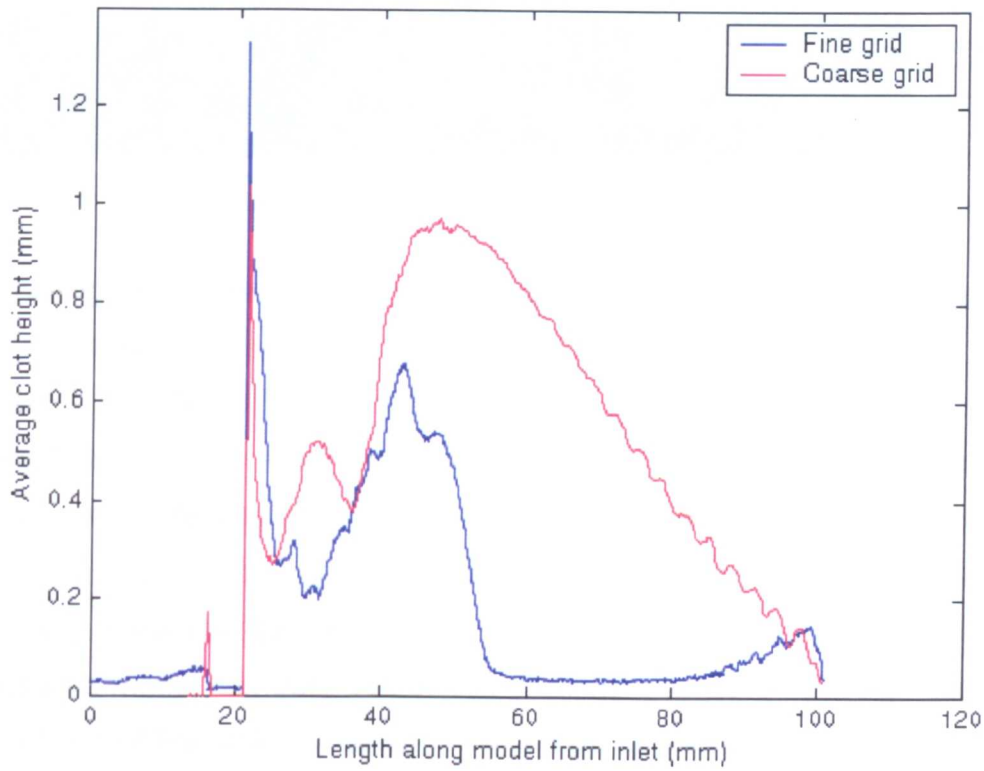

Figure 5.32: Profiles of clot thickness for the two grids described in text with distance from model inlet. Fine grid $911 \times 74 \times 74$, coarse grid $456 \times 38 \times 38$.

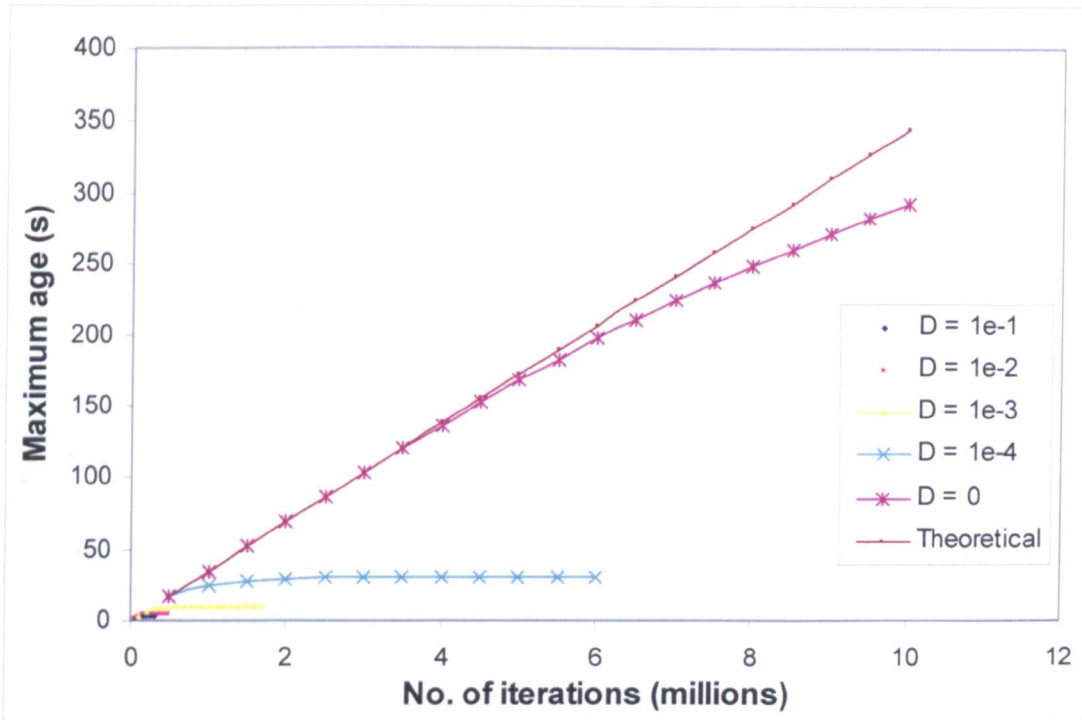

Figure 5.33: Maximum age in 2D Re=100 stenosis model for different diffusion coefficients. The zero diffusion results were obtained with the 1st order upwind method, all others used the Flekkoy model. Theoretical values assume zero diffusion.

However, these very high ages are only found in the corner immediately behind the stenosis, as shown in figure 5.34.

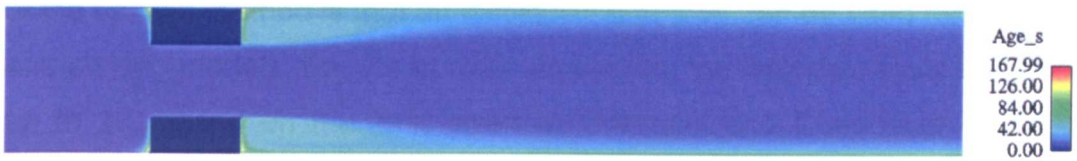

Figure 5.34: Age distribution using 1st order upwind scheme in 2D Re=100 stenosis model.

To investigate whether higher ages in the recirculation zone could be achieved with the upwind scheme, the original fine grid used for the flow studies presented in Chapter 3 was used to find the age limit for the Re=550 simulation. Figure 5.35 illustrates the limits of age immediately distal to the stenosis using the upwind model and the Flekkoy model, the latter with the limiting diffusion coefficient of $D = 1 \times 10^{-3} L^2 T^{-1}$. It shows the important result that the diffusion coefficient in the Flekkoy model limits the maximum age to approximately 3s but the upwind model can obtain ages of almost 50s, however, the age distribution will only be of first order accuracy. Note that for the coarser grids these limits were 1.5s and 3 s respectively. This implies that the upwind scheme yields greater return for a finer grid.

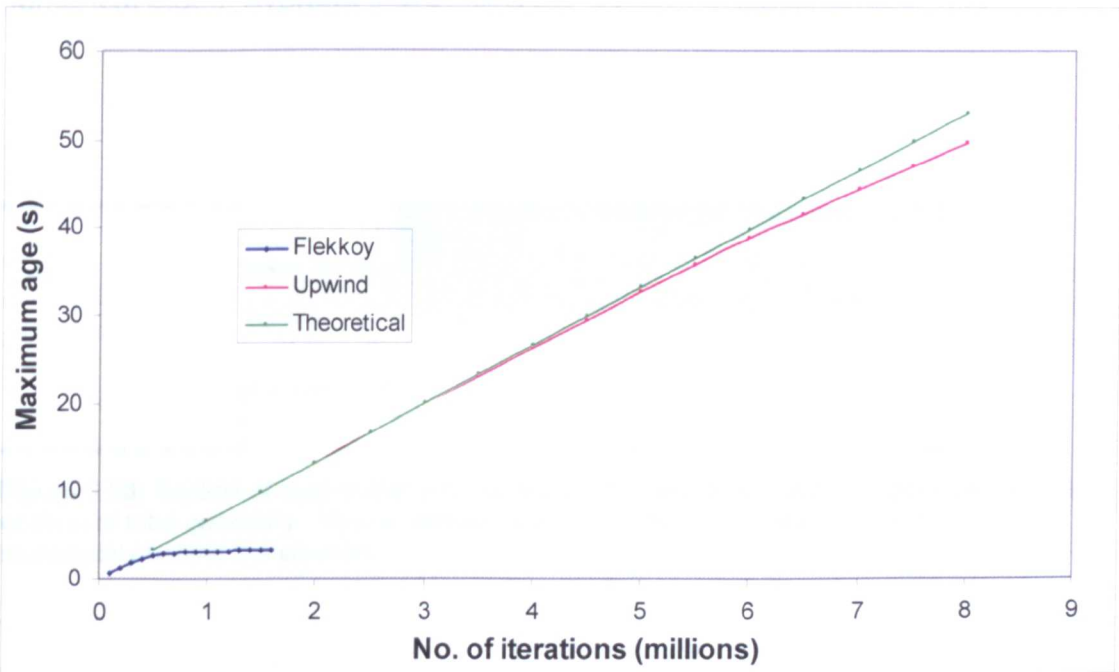

Figure 5.35: Convergence of age for Flekkoy model and upwind model results in fine grid plotted alongside theoretical age (assuming zero diffusion) for 3D Re=550 simulation.

The required clotting time is 42s. The results in figure 5.35 show that this is achievable with the upwind method of aging, but simulation of the full 600s experiment would require over 500 days on the SX-8 machine. The advantage of the upwind method is that an increased timestep can be used for the diffusion and clotting models. For the current simulation, the timestep could be increased up to 20, based on the limit given by Paolucci and Chenoweth [125]. This would increase the performance of the code, since changing the timestep from 1 to 5 resulted in an increase in the performance from 25MLUPS to 29MLUPS on the SX-8 machine. However, in order to perform this simulation in 1 week, a 70-fold increase in performance would be required, which is unlikely to be achieved. In terms of performance, the upwind model was not seen to be significantly different to the Flekkoy model.

5.6.8 Comparison with experiments

The milk clots were visualised by taking casts *in situ* [22]. Figure 5.36 shows a photograph of a section of a clot cast after a 600s experiment at a Reynolds number of 550. Photography was also used to analyse the *in vitro* results. A typical example of the deposited clot is shown in figure 5.37 alongside the numerical plot of average clot thickness.

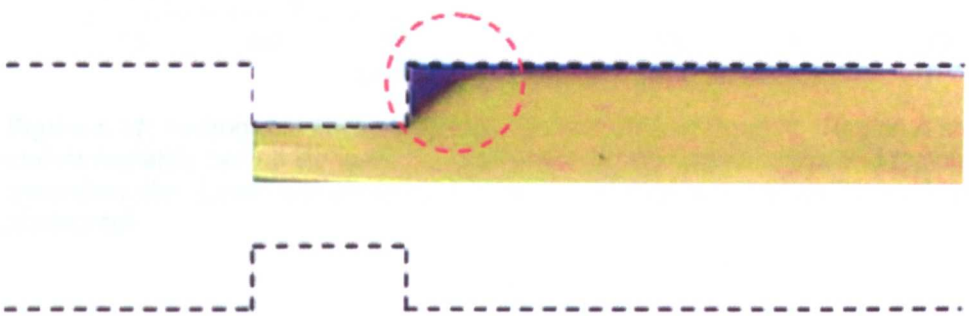

Figure 5.36: Section of cast of milk clot, removed from stenosis model. Dotted lines indicate location of tube geometry. Yellow defines fluid region, brown defines clot (circled), formed immediately behind the stenosis.

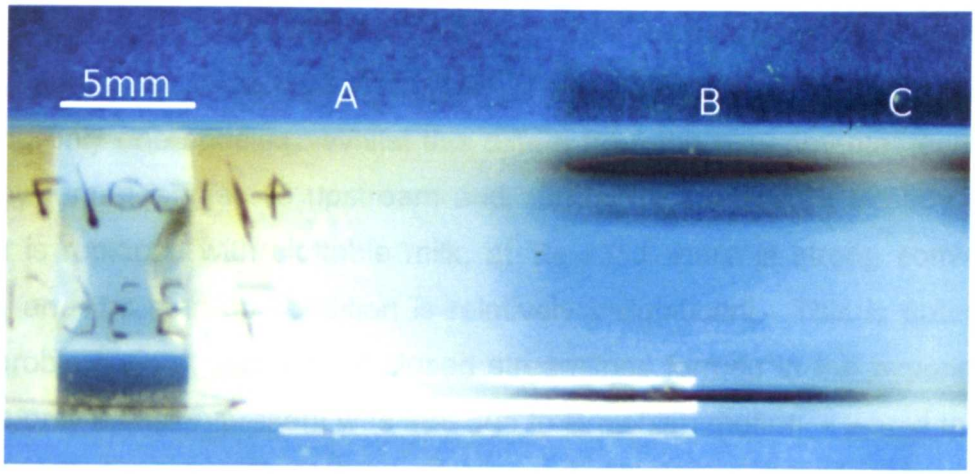

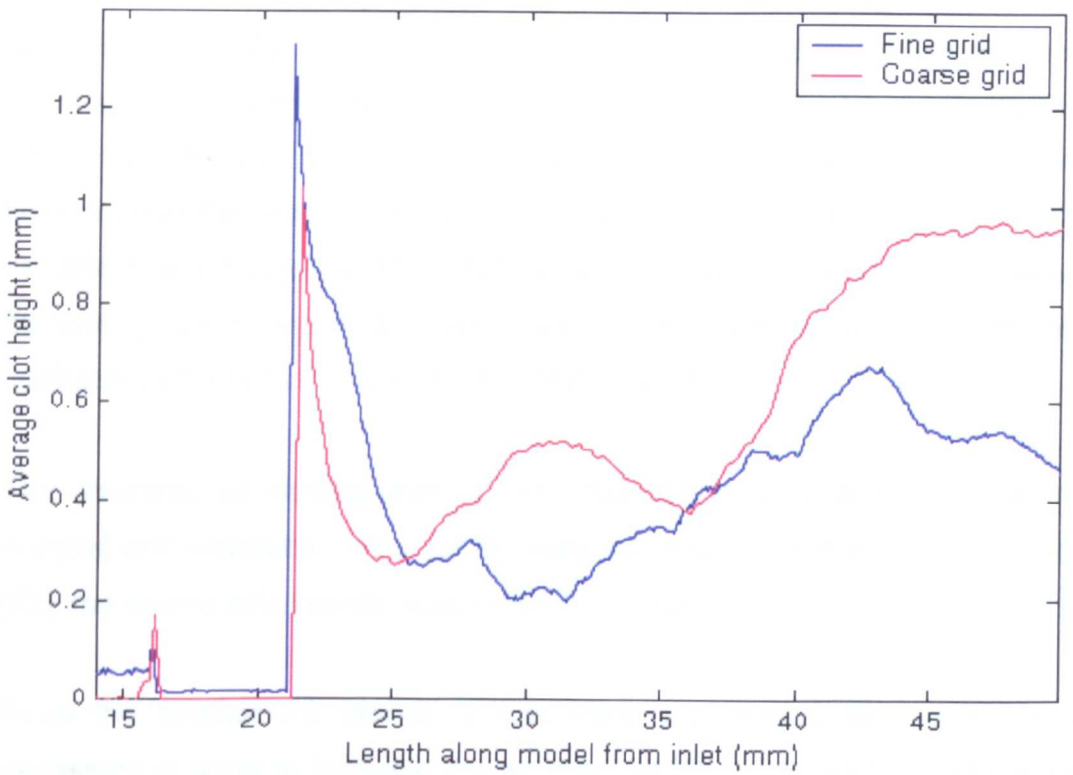

Figure 5.37: Photograph of experimental clot after 600s at Re=550. Region A shows primary clot immediately behind stenosis, B indicates the region spared of clot and region C shows the secondary clot. Lower plot shows numerical results obtained, rescaled in width to match photograph.

5.7 Discussion

The beginning of this chapter described the process of milk clotting and how it relates to that of blood clotting. The reduced complexity of the system is an advantage in terms of numerical modelling. The process reduces to a single reaction, which occurs at a given rate and hence in a given amount of time. For

this reason, a clotting model involving a residence time model was developed. When the fluid exceeds a threshold age it is permitted to clot, either by solidification or by increased viscosity. The simulation technique is efficient, involving only one species. Whilst this differs from the experimental technique whereby rennet is injected upstream and normal untreated milk already in the system is replaced with clottable milk, at $\mathrm{Re} = 550$ there is strong convective mixing, and the start-up condition is relatively insignificant. This is potentially more problematic at $\mathrm{Re} = 100$, if closed streamlines formed in the experiments and the only diffusion present was that due to Brownian motion, it would take an exceptionally long time for clottable fluid to enter the recirculation region. Here, fluid would become trapped, allowing it to reach the clotting time. However, disturbances in the flow patterns are present even at this Reynolds number because of the sensitivity of the experimental set-up to small vibrations [22]. These disturbances are sufficient to upset the streamlines and allow clottable fluid to enter the recirculation zone. Clearly such instabilities cannot easily be modelled and modelling both normal and clottable milk would increase the number of unknowns in the simulation. The experimental disturbances are captured by the diffusion present in the simulations.

The viscosity of clotting milk is time-dependent and dependent upon the enzyme concentration. As viscosity was not measured in Smith's experiments [22], the solidification model was selected for further work.

From the laminar 2D results, it was clear that further developments were necessary in order to increase the accuracy of the model and to provide results relevant to the *in vitro* experiments. The first development was the introduction of a proximity condition which acts to prevent the growth of isolated clots. However, this was shown to produce unrealistic results since a bridge formed very rapidly between the oldest regions of fluid immediately behind the stenosis and in the centre of the vortex. As it was likely that this type of structure would not be supported within the flow, a second condition relating to shear stress was introduced. Clots were only permitted to grow if the shear stress was below a threshold value. It was also demonstrated that the shear stress in the flow changes as the clot grows hence it is not easy to predict the threshold value of shear stress to use.

There is a difference between the shear stress that can break an existing clot and one that can prevent a clot from forming. The threshold shear stress values chosen were those which reproduced the results seen in the experiments. There is no published data on clot strength in its very early stages of development: such literature that does exist concentrates on the gel curing process over much longer timescales. The thresholds chosen are not inconsistent with the literature- i.e. they are lower than those associated with a curing gel [157, 171].

The aging model was found to be affected by the limits of the diffusion models resulting in reduced clotting times when compared with the experiments. However, the upwind aging model is capable of obtaining the required ages if the fine grid of dimensions $1214 \times 98 \times 98$ is used. The problem is a requirement for approximately 500 days of simulation time on the SX-8 which is simply not feasible. The reason this simulation proves so difficult is that the entire 600s is required in order to capture fully the dynamics of clot growth. With an explicit time-stepping scheme and a timestep of approximately $6.6 \times 10^{-6} s$, little else can be achieved using a direct simulation. Methods of increasing the timestep were considered, but this results in increases in the lattice velocity beyond the recommended limits. Grid size and simulation time were chosen based on the condition that the simulation time required was no longer than 1 week on the SX-6 machine.

As an alternative method for simulating the residence time of a fluid, particle tracking methods could be used such as those used by Jongen [148] or Kunov *et al.* [149]. These methods were not explored within this project.

The compromise chosen for the final simulation involved using the upwind method. This allows for a clotting time of 3s without negative values, but due to the accuracy of the scheme, the age distribution is only of first order accuracy. The significance of this simulation is that the clotting time is greater than the average transport time of fluid through the domain of 1.29s, which means that clotted fluid has resided in the model longer than the average time. The grid size was reduced and the lattice velocity increased. The grid was shown to affect the resulting flow field in that the recirculation zone was shortened, but

the overall flow features were qualitatively similar to those shown in Chapter 3. The threshold shear stress was the only parameter in the model that was not constrained in any way. The results reported in section 5.6 show that different clot deposition patterns can be obtained by varying this parameter and the results of figure 5.30 and 5.31 are qualitatively similar to the experimental results shown in figures 5.36 and 5.37. The key similarities are the primary region of deposition in the corner behind the stenosis and the secondary region of deposition further downstream. The thickness of the primary clot is seen to decrease with downstream distance in both the experimental and numerical results. Experimentally, these results were highly repeatable over the 15 experiments performed and Smith [22] reported that the average distance to the end of the first clot was 12.2 $\pm$ 1.5mm and the distance to the secondary band of clot was 28.3 $\pm$ 1.3mm. The numerical results obtained show that the position and size of the clear region depends upon the shear stress value. The results obtained using fine and coarse grids are qualitatively similar in that the primary features of initial clot deposition, cleared region and secondary clot deposit are present. However the overall shapes and sizes of the clots differ. This might be explained by the effect of the wall, since with the fine grid, it was necessary to use a rough wall to trigger the turbulence. This was not necessary with the coarse grid. This would then drastically affect the wall shear stress values which would hence affect the deposited clot. Alternatively, these results may well just indicate that grid convergence has not been obtained. Further large simulations are required in order to prove this.

The results of the clotting model show that, despite practical limitations on the direct simulation of an experiment of 600s duration, it is possible to reproduce the experiments, given appropriate choice of the clotting time and the threshold shear stress. This chapter demonstrates that it is relatively straightforward to implement a physics-based local clotting model so that the clot growth is intimately coupled with the local characteristics of the flow field.

Chapter Six: Development of the Framework

6.1 Theory of Thrombosis: Initiation

The ultimate response to vessel injury is to form a thrombus, plugging the vessel to prevent further blood loss and to regain haemostasis. This process must be rapid, localised and carefully controlled. The immediate response to injury is vasoconstriction. The vessel constricts to reduce blood loss before a more stable clot can be formed [7, 172]. Following constriction, platelets form a plug by adhering to the site of injury and attracting other platelets. This initial plug is subsequently stabilised by the production of fibrin via the coagulation cascade. Fibrin acts as a mesh to capture and stabilise platelets and other blood cells.

This complex process can be instigated by trauma as described above and can also be initiated in disease. As will be seen in Chapter 7 this is one focus of this project.

In order to elucidate the events and observations involved in thrombus formation, the topic has been split into sections describing the processes of initiation and clot deposition.

6.1.1 Virchow's triad

In 1856 Virchow defined what is now commonly known as Virchow's triad [173, 174]. This emphasises the importance of three entities determining blood clotting [175]. These are:

i) Properties of the blood
ii) Properties of material in contact with blood
iii) Properties of blood flow defined geometrically

These factors can act independently and simultaneously in order to dictate the state of blood regarding the likelihood of thrombosis. In simple terms, these factors represent changes in the blood, changes in the vessel wall and stasis. [176].

The first element of the triad; properties of the blood, relates to the level of activation of coagulation factors in the blood. These may be increased by a number of factors including; advancing age, surgery and/or trauma, the use of oral contraceptives or pregnancy [177]. Increased coagulability will not be discussed further in this project and for all the work described, 'normal' levels of coagulation factors are considered for the initial conditions.

The second element relates predominantly to the vessel wall. Coagulation can be initiated by foreign materials in a similar manner, but this will not be the focus of the current project. The vessel wall endothelium is a protective barrier which, when intact, does not initiate or support platelet adhesion and coagulation [172, 178]. Thrombus formation on an intact endothelium has been demonstrated experimentally [179] but this work used a fibrinogen solution with addition of thrombin, hence fibrin clots (without platelets) developed. The inherent thromboresistance is, in part, due to several anti-platelet and anticoagulant substances produced by endothelial cells [172]. In the case of vessel injury, these are down-regulated leading to an imbalance in favour of procoagulant activity. The endothelium consists of a single layer of flattened cells lining the inner surface of all blood vessels in the body [180]. These cells dictate the balance between procoagulant and anticoagulant factors as well as those of pro- and anti-adhesion forces [181]. Depending upon its exact nature, damage to the endothelium may lead to the release of tissue factor and/or exposure of collagen in the underlying tissue (the subendothelium). This will be revisited in following sections since collagen and tissue factor are known to activate thrombotic processes. Figure 6.1 shows the vessel wall and the various layers described above.

There is some dispute as to whether the third element, stasis, can lead to the onset of thrombosis in the absence of either of the other two elements of the triad, or whether it merely acts as a site of optimal conditions promoting amplification and accumulation of clotting factors [176]. In 1962, Mustard *et al.* [182] claimed that the evidence supporting the theory of stasis was based on the agreement between areas of stagnation and areas of deposited thrombus. They also recognised that the flow of blood can act to replace activated clotting factors with inactive factors, thus impeding the process of thrombosis. This

notion was supported in later work by Wessler and Yin [183], who concluded that, if the vessel wall is normal, there must be an increase in the levels of activating factors for thrombosis to occur. Recirculation zones are commonly viewed as locations of favourable conditions allowing previously activated platelets and clotting factors to aggregate into thrombi [184-187]. Locations of deposition will be discussed in a subsequent section of this chapter.

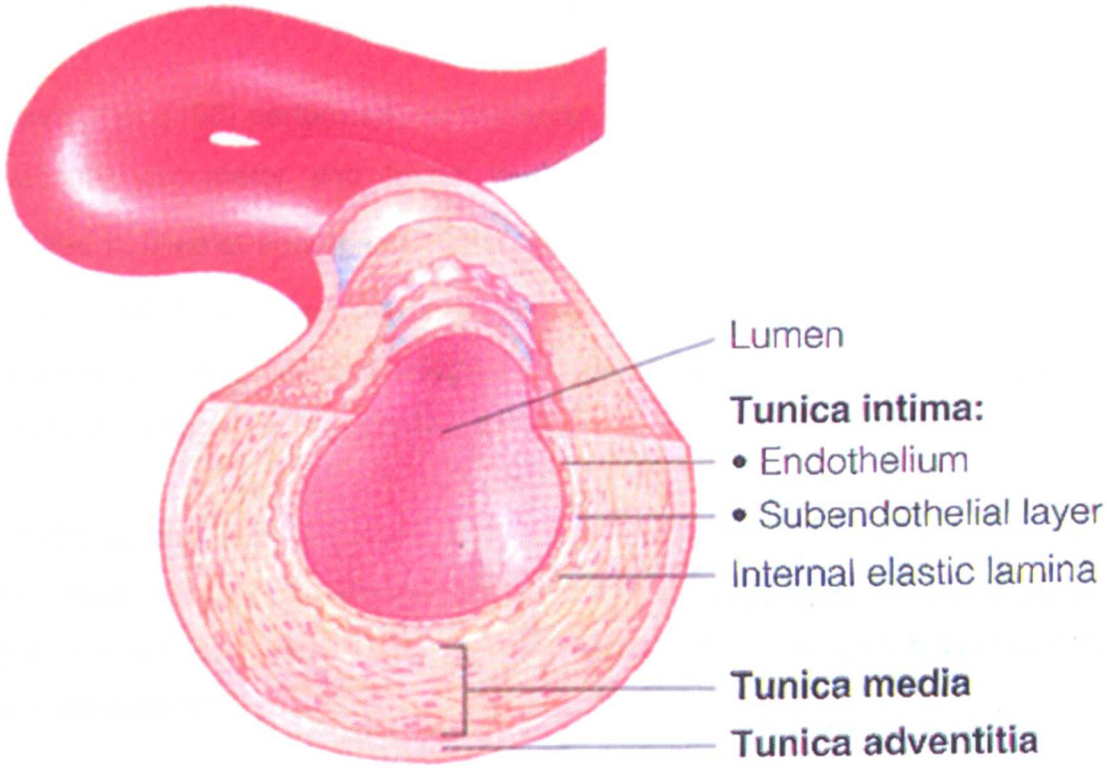

Figure 6.1: Cross section of an artery showing vessel structure [188].

6.1.2 Platelets

Platelets contribute less than 1% of the volume of whole blood [7], but there are between 180,000 and 350,000 platelets per cubic millimetre of blood [9]. Platelet adhesion and activation is one of the first responses to occur in the event of injury, acting rapidly to minimise blood loss. Platelets are activated by collagen [189] which is exposed following damage to the endothelium or exposure of the subendothelium, but are also activated by the final enzyme of the cascade, thrombin. Adenosine diphosphate (ADP) and thromboxane A_2 (TxA_2) are released by activated platelets [190, 191] and also cause platelet activation. This positive feedback mechanism is known as synergistic

activation. Platelet activation involves a change in the cell shape and the extension of projections called pseudopods which allow for the subsequent processes of adhesion and aggregation [178, 192].

It has been shown that platelets can become activated by high shear stresses and this is seen to be dependent upon the time of exposure. As shown in Chapter 5, the shear stress is a flow derived parameter which can be calculated within the code and thus is of particular interest in this project.

Brown *et al.* [193] performed experiments on platelet rich plasma (PRP) with a rotational viscometer and found that very low shear stresses $50 dyn/cm^2$ resulted in platelet aggregation, stresses of $100 dyn/cm^2$ caused cell lysis and stresses of $250 dyn/cm^2$ resulted in the fragmentation of platelets[1]. The relevance of these different effects must be considered. The threshold which results in aggregation is important, but this also depends upon exposure time.

In 1979, Karino and Goldsmith [194] presented the first evidence that platelets could aggregate in an annular vortex without the addition of any chemical agents. It was at this point that factors such as shear stress and residence time were considered.

Schmid-Schönbein *et al.* [187] conducted a set of experiments with erythrocytes and platelets and found evidence for direct activation of platelets in the shear stress range of $50-100 Nm^{-2}$ and indirect activation, via the release of ADP from erythrocytes at shear stresses of $200 Nm^{-2}$.

The idea of indirect activation was revisited in 1985 by Wurzinger *et al.* [184] in a study which also investigated the exposure time. The magnitude of the shear force was discovered to have a greater effect than the exposure time, both yielding an increased alteration of platelets with increasing magnitude. It was concluded that high shear forces in the order of $100 Nm^{-2}$ are capable of destroying platelets and red cells within milliseconds, although the issue as to

---

[1] $1 dyn/cm^2 = 0.1 Nm^{-2}$

whether shear stresses of this magnitude occur in the normal human circulation was raised. Calculations showed that a wall shear stress of $145Nm^{-2}$ could be reached in a 90% arterial stenosis for about 50ms, but under normal conditions, the peak shear stresses in the circulation fall in the range $5-20Nm^{-2}$.

In 1994, Hellums [195] corroborated the earlier work of others by producing a plot of shear stress versus exposure time for platelet granule release, an indicator of activation. It was concluded that such stress levels will only be reached in certain pathophysiological flows such as through atherosclerotic arteries or prosthetic valves.

Bluestein *et al.* [103] attempted to calculate numerically the shear history of platelets by integrating along a single streamline. Axisymmetric turbulent simulations of flow through a smooth stenosis were performed using FIDAP. The cumulative effect of shear stress and exposure time was obtained by summing the products of instantaneous values along the streamline. This showed a clear increase in the throat of the stenosis and platelets which had been exposed to elevated shear stress could be found in the vicinity of the recirculation zone. The idea of a shear layer between the central jet and the recirculation zone emerged. This implies that platelets within the recirculation zone can be activated by adjacent platelets in the jet before aggregating in a low shear region within the recirculation zone. These simulations were validated against experimental results of platelet deposition.

In 1997, Holme *et al.* [196] conducted experiments using human blood in a parallel plate perfusion chamber device in order to determine whether a high shear stress, at various exposure times, or a sudden increase in shear stress caused the greatest platelet activation. Experiments were performed at shear rates relevant to healthy and diseased arteries. This work indicated that a *change* in shear stress (induced by a stenosis) triggered platelet activation, again with the conclusion that activation did not occur at the physiological shear stresses present in the healthy arteries.

In 2002 Zhang *et al.* [197] used a cone-and-plate viscometer to mimic stenotic shear profiles and measured both platelet activation and aggregation. A higher

level of activation was observed for the stenotic shear profile compared to constant shear, although the level of activation was much lower than that observed following ADP-induced activation. The hypothesis given was that platelets can become mechanically crosslinked when briefly exposed to high shear and thus agglutinate in a reversible fashion that does not require activation. Zhang *et al.* [197] suggest that platelets can only be activated and irreversibly aggregate during exposure to high shear for an unrealistically long time. The importance of the low shear post-stenotic region allowing aggregation was identified and it was hypothesised that aggregation increases in this region due to an increased frequency of platelet-platelet collisions.

In subsequent work, Zhang *et al.* [198] carried out further work based on this hypothesis and showed that only platelets exposed to high shear ($10Nm^{-2}$) for more than 20s were activated and irreversibly aggregated. Again, they claimed that "*shear-induced platelet aggregation may actually be a process of shear-induced reversible platelet cross-linking involving minimal platelet activation.*" Platelets aggregated by short pulses of high shear then undergo rapid disaggregation and shear-aggregated-disaggregated platelets remain responsive to agonist stimulation. This would act to protect platelets from temporary exposure to very high shear stress due to changes in posture, muscle tone and exercise. However, as discussed in the conclusions drawn by Zhang *et al.* [198], the situation becomes more complex when whole blood is considered. Erythrocytes can promote cell-cell collisions, increase the probability of cross-linking and also release activating chemicals such as ADP.

It is important to understand that, *in vivo*, the biological events leading to platelet activation are very complex and that not all eventualities can be considered. In 2004, Yin *et al.* [199] computed the shear stress histories of platelets using a stochastic model that simulated the action of turbulence in order to obtain the platelet trajectories. Turbulent, 2D simulations were performed in FIDAP for flow through bileaflet and monoleaflet mechanical heart valves. The cumulative effect of shear stress and exposure time was computed by summation of the two products for platelets close to the valve leaflets. Whilst the focus of this article was a comparison of two types of heart valve and not on

accurately obtaining the shear history of the platelets, it does however describe methodology that can be used to calculate the shear histories.

In 1979, Ramstack *et al.* [200] demonstrated that experimental data from canine PRP could be fitted to an exponential equation of the form $s = 1 - \exp[-K\gamma t]$ where s is the degree of stimulation experienced by a platelet, K a decay constant for a particular platelet function, γ the local shearing strain-rate and t is the time of exposure to the shear for that platelet. This provides a simple relationship between the shear strain rate, exposure time and stimulation, which is related to activation.

A more detailed calculation of shear histories is presented in the review by Anand *et al.* [122]. An activation number, $A(t)$ is defined which "*quantifies the activation due to prolonged exposure to supra-threshold shear stresses*".

$$A(t) = A(0) + \frac{1}{A_0}\int_0 e^{k\left(\frac{|\tau_{rz}|}{\tau_{thr}}-1\right)} H\left(|\tau_{rz}| - \tau_{thr}\right)dt \qquad \textbf{6.1}$$

$$H\left(|\tau_{rz}| - \tau_{thr}\right) = \begin{cases} 1 : |\tau_{rz}| \geq \tau_{thr} \\ 0 : |\tau_{rz}| < \tau_{thr} \end{cases} \qquad \textbf{6.2}$$

The criterion for activation is that the activation parameter must lie in the range $A_{thr} < A(t) < A_{damage}$, thus it must be above a certain threshold to cause activation, but not so big that it lyses the platelets. If this condition is satisfied, the concentration of activated platelets is incremented by the concentration of normal (resting) platelets. The parameters for the activation criterion are $A_0 = 300s$, $k = 0.75$, $\tau_{thr} = 5Nm^{-2}$, $A_{thr} = 1$, $A_{damage} = 3$. These parameters were fitted to previously published data [193, 201, 202].

The activation parameter is claimed to be relevant for time-varying shear stresses, which incorporates the information from the literature presented previously. The model takes into account the fact that it takes a finite amount of time for a resting platelet to transform into the activated form. Platelets can by lysed within this period.

> "*The initiation criterion brings out the idea that platelet activation is initiated by exposure to shear stresses, and that coagulation will begin if the platelets are not lysed between the instant of activation and coagulation.*" [122]

The process of activation has been considered in this section. As for the processes of adhesion and aggregation, adhesion relates to the attachment of platelets to a surface (to the vessel wall, for example), whereas aggregation relates to the clumping of platelets to one another. The biochemical details of these two processes are highly complex and will not be discussed further. However, the trends of aggregation associated with features such as the flow field will be revisited in a section 6.2.1 since it is this process that is modelled within the lattice Boltzmann framework.

6.1.3 The coagulation cascade

Following initiation via one of the elements of Virchow's triad, the events in the coagulation cascade can propagate and the end result is the production of fibrin which stabilises the clot. This response occurs alongside that of platelet plug formation.

A representation of the coagulation cascade is shown in figure 6.2. As can be seen, the cascade has two principle branches known as the intrinsic and extrinsic pathways. The intrinsic pathway (labelled as the contact system) is triggered by collagen exposed in the subendothelium when the lining of the vessel is damaged. It can also be initiated by contact with foreign material. The extrinsic pathway (labelled as cellular injury) is initiated when a vessel ruptures causing the release of tissue factors. The two pathways converge to what is termed the common pathway, resulting in the production of thrombin. The individual elements of the cascade (coagulation factors) are plasma proteins and are numbered according to their sequence of discovery [172]. Some of the reactions in the cascade occur within the blood plasma, and some on the surface of activated platelets [203].

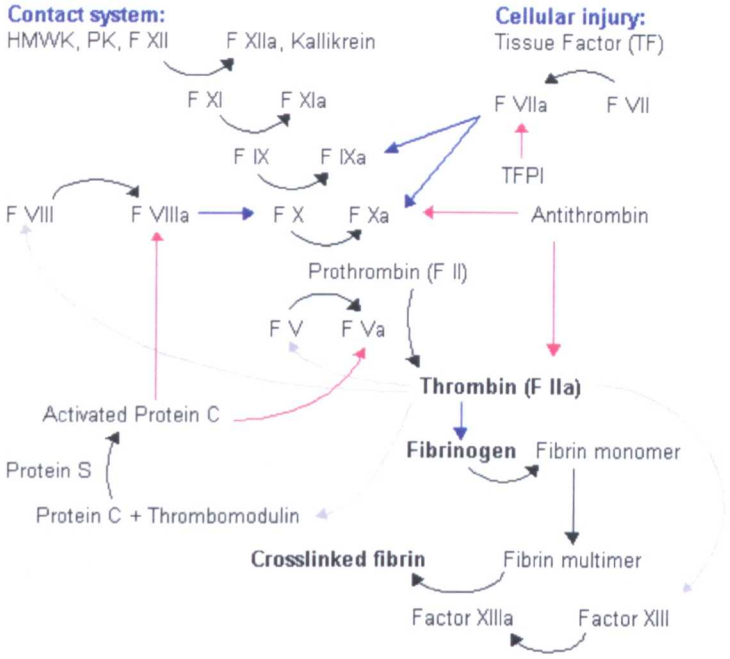

Figure 6.2: The coagulation cascade. Factors are labelled with an 'F' followed by the Roman numeral relating to the order of discovery [204].

The ultimate role of the cascade is to provide a rapid response to injury and this is obtained by the amplification of the coagulation factors as the cascade propagates. Thrombus formation is normally complete 3-6 minutes after vessel damage. The extrinsic pathway is more rapid since fewer reactions are involved and when severe tissue trauma occurs, clot formation can result within 15s [7].

There is a finely controlled balance of pro- and anti-coagulants in the blood and the main inhibitors that regulate the cascade are antithrombin, tissue factor pathway inhibitor, protein C and protein S [122, 205]. These are important in preventing widespread thrombosis from an isolated area of vascular damage [206]. In addition, once a thrombus has been deposited, it can subsequently be removed by factors released from the endothelium in a process known as fibrinolysis. The action of inhibitors and the process of fibrinolysis are not considered in this project.

6.2 Theory of Thrombosis: Thrombus Deposition

The previous section described the initiation of thrombosis with activation of the coagulation cascade and involvement of platelets. If the vessel wall is injured,

in the case of a cut for example, thrombus forms over the region of damage in order to prevent excess blood loss. However, this process is more complex in flowing blood. The local flow field dictates the deposition profile by not only transporting the activated factors and platelets away from the thrombus or to regions favouring thrombosis, but also by physically shaping any existing thrombus deposits. In the extreme, thrombosis can be inhibited by rapid flow [207]. It has also been demonstrated that fibrin polymerisation depends upon the shear rate [151]; at low shear rates there is a reduction in the molecule collision rate, therefore a decrease in clot formation and at high shear rates, fibrin breakage exposes more reaction sites, causing an increase in clot formation. The adhesion of platelets to the subendothelium will depend upon factors such as the reaction rate with the wall, which itself is dependent upon the wall shear stress [208], as well as the magnitude of the diffusion coefficient, particularly in regions where the convective transport is low [94]. However, the complex process of adhesion in the boundary layer will not be considered, instead correlations between macroscopic transport properties and regions of deposition will be exploited. This section presents some of the findings on this topic.

6.2.1 Effects of flow

In 1973, Baumgartner performed *in vivo* and *in vitro* experiments on rabbit aortas which had been denuded of endothelium [209]. It was discovered that, in both cases, when blood flow was unaltered, a tight, continuous layer of platelets, but no fibrin, were deposited whereas at a reduced flow, significantly fewer platelets were deposited along with fibrin. Baumgartner attributes this behaviour to the frequency and force with which platelets are pushed against a surface. Platelets can subsequently be removed from the surface if the shear force exceeds a critical value. Baumgartner claimed that the formation of fibrin requires stagnant blood to prevent the dilution of procoagulant factors. This agrees with the conclusion of Leonard [210] who recognised the significance of regions of recirculation in preventing the escape of reaction products leading to thrombogenesis.

Karino and Goldsmith [194] demonstrated that platelet aggregation in an annular vortex occurred because of a "*favourable combination of long residence times and frequent interparticle collisions*". This is supported by Schmid-Schönbein *et al.* [187] who proposed that deposition in a stenosis model first takes place at the reattachment point, where flow is directed towards the wall. Experimental results of Karino and Goldsmith [211] found an adhesion peak between the tubular expansion and the reattachment point. The explanation given for this was that, in a vortex with closed streamlines, the velocity is extremely low at the reattachment point and hence the frequency of collisions is small. Slightly upstream of this, the radial component of the velocity is higher, resulting in increased collisions with the wall. This theory was supported in a theoretical paper by Goldsmith and Turitto [94] and also by experimental results published by David *et al.* [208]. Recirculation zones are described by Schmid-Schönbein *et al.* [187] as "*sites of autocatalytic augmentation*" of previously activated enzymes and sites of high residence time offering ideal fluid dynamic conditions for aggregate growth [187].

Schmid-Schönbein *et al.* [187] outlined a model for thrombosis in stenoses that hypothesised platelet activation in the stenosis throat where shear stresses were high. These activated platelets then become trapped in the distal recirculation zone allowing for amplification and adhesion as described above. This model was supported experimentally by Schoephoerster *et al.* [212] where elevated levels of deposited platelets were found in areas of reattachment and recirculation and decreased levels were seen in areas of high shear.

In 1985, Wurzinger *et al.* [184] examined the effect of shear stress on platelet aggregation and found an optimum range of approximately 0.025–0.12Pa in PRP. This is in agreement with later work by Affeld and Gadischke [213]. These values are low compared to those required for platelet activation which are of the order of 100Pa. Again, the reattachment point was noted to be the primary adhesion point. Here the flow vectors were perpendicular to the wall and thus transported platelets to the wall.

It has been substantiated that thrombus deposition occurs in regions of flow recirculation where blood is retained significantly longer than average and

where the shear stresses are relatively low [101, 103, 104, 150, 179, 185]. However, a certain minimum shear rate is required to allow for increased platelet collision with the subendothelium and other platelets, thus there is a critical range of shear stresses which provides maximal thrombus deposition [184, 209, 213]. The location of deposition also depends upon the source and location of the activation. Colleagues, Markou *et al.* [214] and Wootton *et al.* [215], found peak platelet deposition in the throat of collagen-coated stenoses, where the shear stress is greatest. Similar results are found using stenoses with severely damaged vessel walls [216, 217]. Strony *et al.* also found peak depositions in the apex of the stenosis but attributed the activation to the sudden high shear stress in the entrance of the stenosis slightly upstream of the throat [218]. This only goes to portray the hugely complex process of thrombosis, with its dependence on a large number of experimental conditions. Great care must be taken in drawing conclusions from results in the literature.

6.2.2 Thrombus structure

There are a number of factors that dictate the structure and composition of a thrombus such as the flow conditions, the location of the thrombus and the cause of activation. The following presents a brief review outlining the main findings.

Stasis thrombi are composed mainly of red cells, trapped by a fibrin mesh, possibly without platelets, thus giving a red appearance [182]. This is related to discussion in the previous section describing sites of stasis as regions where the coagulation cascade can propagate producing thrombin, and ultimately, fibrin. Such thrombi are more commonly found in the veins rather than arteries, since venous flow is slower. These sluggish, sometimes undisturbed flow conditions also allow for more extensive thrombi to develop [182]. Stasis thrombi are very similar to clots formed in a test tube and the overall structure of the thrombus is likely to be homogeneous [219]. In contrast, white (platelet) thrombus is prevalent in arteries where the flow is rapid [220].

There are other differences between arterial and venous thrombi. French [219] describes how thrombus in a leg vein generally has a pale head, in the region of attachment to the vessel wall, formed by platelet aggregates, with a dark red tail. Thrombi found in arteries are however very pale in colour, with little extension along the vessel.

In terms of strength, thrombi formed in regions of slow flow, are not as dense as those formed in arteries which are harder and structured in a pattern indicative of the stresses applied during formation [210]. The fact that the concentrations of platelets and fibrin can dictate the final strength of a clot is important when features such as emboli are considered, as in the following section [122].

The paper by Baumgartner [209], discussed in the previous section, described thrombi produced *in vivo* and *in vitro*. The latter were shown to consist only of platelets, unlike the former which were always be associated with leukocytes.

6.2.3 Emboli

When considering the flow conditions favouring thrombus deposition there are two possible influences of shear stress. The first is whether the thrombus can deposit or not and the second relates to whether, once deposited, the thrombus will be removed (forming emboli). The first effect has been examined by Bluestein *et al.* [103].

> "*Although acting as a platelet activation agent, the high shear stress at the wall of the throat itself washes away the platelets, preventing their adhesion to the wall.*"

Emboli are important *in vivo* because of potentially fatal consequences associated with vessel obstruction. Emboli are produced when thrombus is dislodged from the wall and travels downstream in the flow field.

It is somewhat simplistic to think of a single shear stress value responsible for thrombus prevention or breakage because the strength of the thrombus will vary

with time [221]. However, at this stage, a single value will be used based on the literature. A more complex model for embolism was developed by Scott Wilson *et al.* [222] in 1986, which considered a theoretical distribution of thrombus size with embolisation occurring for thrombi attaining a critical size. Their results show that the embolisation process affects the fine detail of the thrombus but not the overall structure.

In 1989, Basmadjian produced a map relating to the likelihood of embolisation based on the height of the thrombus, shear stress and time of exposure [223]. Based on this work, a value of 60Pa was used by Goodman *et al.* in 2005 in their model of platelet deposition and embolisation [224].

In 1999, Riha *et al.* [225] presented a collection of data for the fracture stresses of thrombi formed from platelet rich plasma (PRP), platelet poor plasma (PPP) and whole blood of varying haematocrit. For a haematocrit of 40%, the fracture shear stress was reported to be 211 $\pm$ 43 Pa. This value was used in the model by Anand *et al.* [122]. Riha *et al.* commented on the fact that the maximum pathological shear stress in the circulation is approximately 40Pa [218, 226] and therefore inhomogeneity and fibrinolysis must act to decrease the strength of the thrombus.

6.3 Modelling Thrombosis

A variety of approaches have been taken in attempts to model the complex processes involved in thrombosis and a comprehensive review of progress is reported by Anand *et al.* [122]. A complete model involving all the biochemical interactions at play within a physiologically relevant geometry has yet to be developed. The focus tends to be on either one or two of the strands of Virchow's triad. If a set of equations describing all or some of the coagulation cascade is implemented, the flow field is, generally neglected or over-simplified [122, 203, 207, 227-230] and, in models where realistic flow fields are considered, the biochemistry of the system is often reduced to very simple models [150, 152]. Modelling the response of platelets alone has proved

popular [175, 208, 231-235] as experimental validation can be readily performed using platelet rich plasma.

In 1999, Sorensen *et al.* [236] described a model of platelet activation and deposition. This represents platelets and the final elements of the coagulation cascade as massless species transported by convection and diffusion. A set of 7 differential equations were used, adapted from the published literature, and platelet deposition was realised via a surface flux boundary condition with consideration of the local concentration of activated platelets. The simple 2D flow field was computed using the Navier-Stokes equations, but the effect of the growing thrombus on the flow was not considered. In a second publication by the same authors, validation was performed using collagen as the reactive wall and simple parallel-plate flow [237]. The authors reported good agreement with several sets of experiments.

In 2001, Wootton *et al.* [215] presented experimental and numerical results for platelet deposition on a collagen-coated stenosis. The computational model was based on earlier work by Turitto and Baumgartner [231] and used a species transport model for the platelets. In the near wall region, platelets were activated by collagen and free, unactivated platelets became attached and activated at a constant rate. The model considers physiological flow and shear dependent diffusivity but, again, does not consider the effect of the growing thrombus on the flow field. Comparison with experiments shows agreement in the upstream and throat regions of the stenosis, but downstream of the throat, the model under-predicts the amount of deposition. Due to the shear stress exposure measured, this work does not consider the possibility of shear stress activation with subsequent downstream aggregation. This phenomenon will be considered later in this chapter.

In 2004, Fogelson and Guy [238] presented a continuum model of platelet aggregation with extensive detail given to reactions occurring at the vessel wall. This very detailed model represents aggregation using elastic links. The stresses caused by the links are coupled to the fluid, resulting in associated stresses therein. This captures the effect of the growing thrombus on the flow field. Two different length-scales are considered; one relative to the diameter of

the vessel (order of mm) and one relative to the diameter of a platelet (order of μm). The Navier-Stokes equations are used to solve the flow field and shear dependent diffusivity is included. Platelet-wall interactions are modelled by considering a rate constant which dictates alterations in the concentrations of normal and activated platelets in contact with reactive sites at the vessel wall. When platelets are activated, they release an activating agent, adenosine diphosphate (ADP), which is also transported by advection and diffusion. Simulations were performed in 2D stenosed vessels with a diameter of approximately 1mm. The cap of the stenosis (plaque) was assumed to have ruptured, exposing platelet activation sites to the blood. A significant feature of this model is its capability of simulating embolus. The elastic links can rupture under certain conditions and the associated thrombus can break off and travel downstream.

In 2005, Bedekar *et al.* [239] further developed the work of Sorensen *et al.* [236]. Platelets are activated by a reactive surface and by contact with previously activated platelets and thrombin. Generation and inhibition of thrombin is also modelled. Rate constants and equations were obtained from the literature. The flow was solved using the Navier-Stokes equations and simulations were performed in both a cylindrical tube and an aneurysm. The geometry of the aneurysm was obtained from CT (computed tomography) data.

A similar model of thrombosis is reported by Goodman *et al.* [224] , but in this case, experimental validation is provided. This model considers platelet adhesion, with resulting effects on the flow field, together with an embolism model. Platelet activation is due to agonists in the bulk flow and again, the work of Sorensen *et al.* [236] was used as a basis for this. The effect of the growing thrombus on the flow field was modelled by increasing the viscosity by a factor of 1×10^{5} in clottable cells. These cells could then release agonists and thrombin (the final enzyme in the cascade), which could, in turn, activate other platelets in the vicinity. The experiments and computations were performed in stenosed vessels and, in most cases, the results were found to be in agreement.

In summary, a complete model of thrombosis has yet to be developed. Various aspects have been considered, such as reactions in the coagulation cascade, or the adhesion and aggregation of platelets in physiological geometries using the Navier-Stokes equations.

A small number of lattice Boltzmann thrombosis models have been reported. In 2004, Tamagawa and Matsuo [240] presented a model which tracks the motion of 200 particles in a backward facing step geometry. In this model, thrombosis is permitted if the shear rate and distance from the wall fall below a defined threshold. Investigations also considered the use of a distance dependent threshold shear rate. This latter scheme gave the best agreement with experimental data. Most recently, in 2005, Ouared and Chopard [61] described a lattice Boltzmann model based on shear stress. Clotting was permitted only in regions of low shear stress. Thrombus was simulated with suspensions using a model previously developed for sediment transport and deposition.

The results of the models developed in the course of the current project to track the age of the fluid using a passive scalar tracer were presented in Chapter 5. This simulated the final reaction in the cascade and the results were compared to those produced experimentally with enzyme-activated milk; a recognised blood-clotting analogue [79, 167, 168, 241]. The local rule allowing thrombus formation was that the age of the fluid must be above a certain threshold. Qualitative agreement was seen with experimental data obtained for a sharp-edged stenosis. This work considered 3D simulations with shear stress and proximity conditions, again with good agreement.

In the current chapter, the development of a lattice Boltzmann framework for modelling thrombosis is discussed. The framework incorporates a number of features of thrombus development, including the response of platelets and the coagulation cascade. This work describes the foundations on which more detailed models can subsequently be built and demonstrates the ease and suitability of the lattice Boltzmann method for modelling a complex system of reactions. Since the fluid simulated is blood, it must be emphasised that based on the vessel size it is modelled as a non-Newtonian fluid.

6.4 Lattice Boltzmann Modelling of Platelet Thrombus

A large amount of literature has been presented concerning the role of platelets in the process of thrombosis. The key features of interest in this project are activation: via prolonged exposure to high shear stress, by agonists such as ADP or thrombin or by contact with subendothelial collagen. If some features of, or indeed the entire, coagulation cascade is to be modelled, it is important to define the initiating event, since with a shear stress model alone, only platelet thrombi form, without generation of fibrin.

As for many of the models described in Section 6.3, massless species are used to represent normal and activated platelets and the proteins and enzymes of the coagulation cascade. This is justified since a platelet has a mass of $\approx 1\times10^{-14}kg$ [242] and a volume of $1\times10^{-17}m^3$ [9], giving a density of $\approx 1000kgm^{-3}$, comparable with that of blood $1060kgm^{-3}$, the carrier fluid. Platelets are discoid fragments with a diameter of $(2-4)\mu m$ [7], which is significantly smaller than a typical lattice size in the simulations $(\approx 1\times10^{-4}m)$.

The species are transported by convection and diffusion using the algorithm developed by Flekkoy [113]. The diffusion coefficient appropriate for platelets is $1.6\times10^{-13}m^2s^{-1}$ [122], but Chapter 4 highlights the difficulties encountered when attempting to use such values. For this reason, a higher, more stable value was used in order to prevent negative concentrations.

Two platelet clotting models have been developed within this project and are described below. The solidification process is as described for the milk clotting work of Chapter 5, but with a different set of local rules.

6.4.1 Platelet thrombus: shear stress activation

The first platelet clotting model considered in this work computes the shear history of platelets, with activation occurring once a certain threshold has been exceeded. A fluid node is transformed into a solid node if the concentration of

activated platelets attains a defined threshold and the shear stress is below threshold; thus only permitting clot formation in low shear regions. This model is only appropriate in geometries where the shear stress may rise above the normal wall value, such as in a stenosed artery, as described in section 6.1.2.

The model used for tracking the shear stress over time is based on work by Anand *et al.* [122] as described in section 6.1.2. An activation number, $A(t)$ is defined, which quantifies the activation due to prolonged exposure to shear stress. In this model, the shear stress must be above a threshold in order to contribute to the activation. The following equations define the activation number and condition for contribution.

$$A(t) = A(0) + \frac{1}{A_0}\int_0 e^{k\left(\frac{|\tau|}{\tau_{thr}}-1\right)} H\left(|\tau| - \tau_{thr}\right)dt \qquad \textbf{6.3}$$

$$H\left(|\tau| - \tau_{thr}\right) = \begin{cases} 1 : |\tau| \geq \tau_{thr} \\ 0 : |\tau| < \tau_{thr} \end{cases} \qquad \textbf{6.4}$$

In the original publication [122], the constants are defined as follows: $A_0 = 300s$, $k = 0.75$, $\tau_{thr} = 5Nm^{-2}$. If the value of $A(t)$ exceeds a threshold, activation can occur. Anand *et al.* [122] define this threshold to be unity.

Because of the explicit nature of the LB code, it would be somewhat difficult and computationally expensive to consider the activation time (1s) and for this reason, the model has been simplified so that only the instantaneous values are used in order to dictate the subsequent concentrations of normal and activated platelets.

The criterion for activation then becomes:

$$\text{If } A(t) > A_{thr}$$

$$\text{Then } [AP](t+1) = [AP](t) + [RP](t) \qquad \textbf{6.5}$$

This model is incorporated into the lattice Boltzmann framework by using a species with a very low diffusion coefficient to trace the values of $A(t)$. The concentration of this species is updated locally at every timestep depending on the shear stress and equations 6.3 and 6.5. This allows for the activation parameter to travel with the fluid and hence follow the platelets.

At each timestep, the activation threshold is computed and if this is above threshold, the concentration of activated platelets is incremented by the concentration of normal platelets at that grid point and added to any previous value (eqn. 6.5). The concentration of normal platelets is then set to zero at that particular grid point. This essentially activates all normal platelets at a grid point if the activation parameter is above threshold.

The synergistic activation of platelets is modelled using the equation taken from Kuharsky and Fogelson [203], shown below, which is also used by Anand *et al.* [122]. Other models were considered, but as these used an additional tracer to represent ADP this decreased the efficiency of the code [224, 232, 236, 243]. The equation of Kuharsky and Fogelson [203] directly increases the concentration of activated platelets, rather than modelling the transport of ADP and other agonists separately.

$$\frac{d[AP]}{dt} = k_{AP}^{AP}[AP][RP] \qquad \textbf{6.6}$$

$[AP]$ and $[RP]$ are the concentrations of activated and resting (normal) platelets respectively. The rate constant, k_{AP}^{AP} is given as $3\times10^{8} M^{-1}s^{-1}$. M here represents the molar concentration, which is the number of moles per litre. The molar mass of platelets is $1.28\times10^{12} g$ [224, 244], hence the rate constant is $2.3438\times10^{-4} m^{3}kg^{-1}s^{-1}$, which can easily be converted into lattice units as described in Chapter 2.

Clotting occurs if the concentration of activated platelets is above threshold. It is not, as yet, possible to model the motion of emboli in the existing LB code and so a criterion is used which allows thrombus to deposit only in regions of low

shear. This is analogous to the work performed on the milk clotting model described in Chapter 5. Figure 6.3 shows a flow chart of the operations performed in the source code.

6.4.2 Platelet clotting: collagen exposure

A second model assumes a small region of collagen exposure on the wall, which can activate platelets by direct contact. The collagen represents a 'damaged' region of the wall. The cause of injury is not considered at this stage. As described in Section 6.1, collagen initiates the intrinsic pathway of coagulation and can also activate platelets. At this stage only platelets are considered. A species is used as a marker for the location of collagen exposure which is prevented from transporting. The equation describing the activation process is adapted from Wootton *et al.* [215] and is shown below.

$$\frac{d[AP]}{dt} = k_t[RP] \qquad \textbf{6.7}$$

Wootton *et al.* [215] define the rate constant $k_t = 5 \times 10^{-3} cms^{-1}$. This is because the original representation is in terms of the rate of platelet accumulation per unit area. The appropriate value to use in units of s^{-1} is obtained by dividing through by the length scale. If collagen is present at a certain lattice point, the concentration of activated platelets is increased according to equation 6.7 and the concentration of normal platelets is reduced by an equal amount. Again, other models available were considered [236, 238], but that of Wootton *et al.* [215] was the simplest for implementation and computational reasons.

As described in the previous section, the synergistic activation of platelets is also modelled. Clotting occurs when the concentration of activated platelets is above threshold.

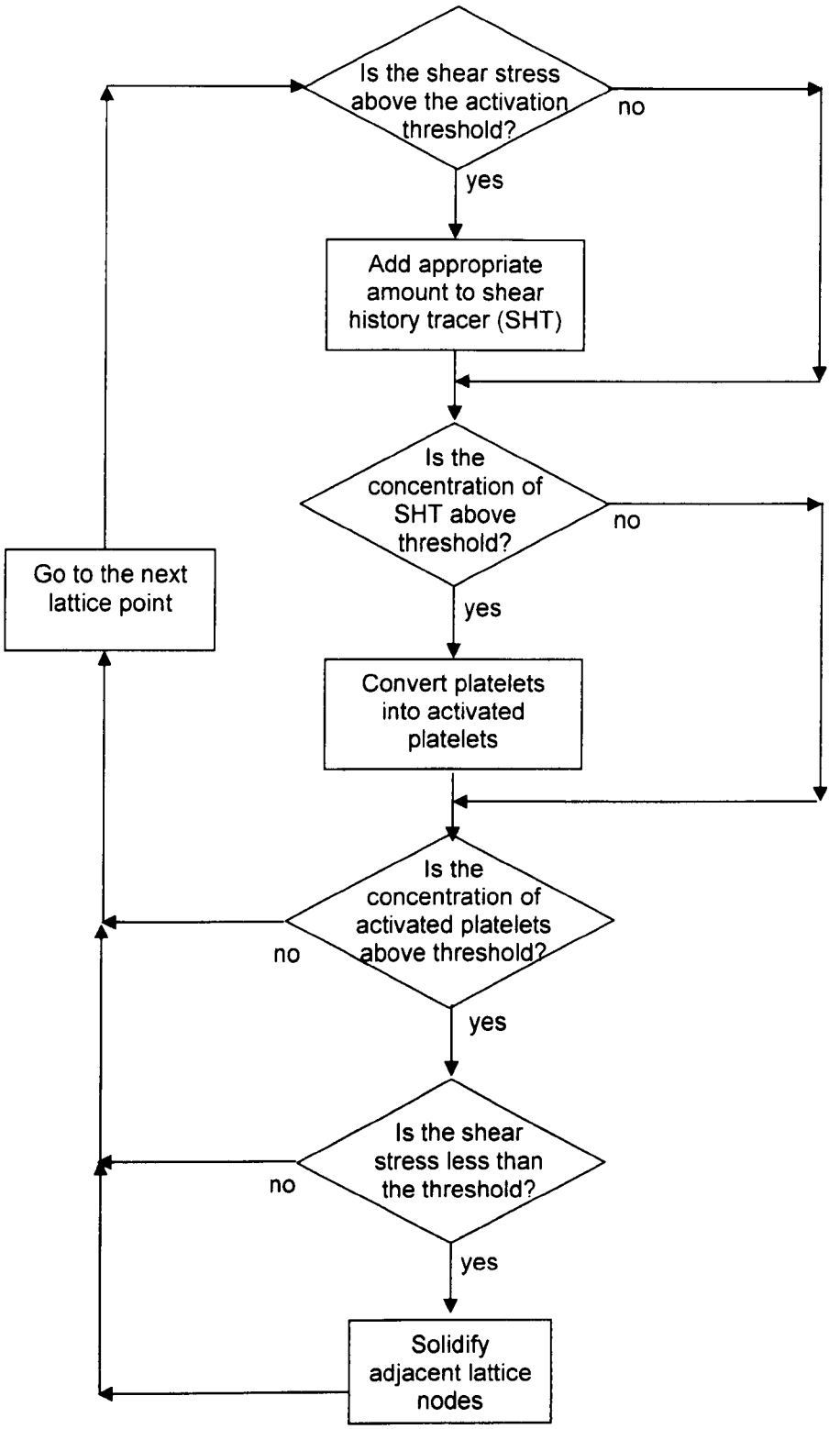

Figure 6.3: Flow chart illustrating the shear stress activation/aggregation model.

6.5 Lattice Boltzmann Modelling of the Coagulation Cascade

It is not practicable to model the entire coagulation cascade since it involves the activation and inactivation of a large number of proteins. As a first attempt to model the final reaction in the coagulation cascade, thrombin is released as a source from the damaged wall region. Thrombin, the final enzyme of the cascade reacts with fibrinogen, which is normally present in the blood, to produce fibrin. Thrombin can also activate platelets. This model neglects the previous reactions in the cascade, thus assuming that damage exposing collagen in the subendothelium results in the production of thrombin. Figure 6.4 shows a flow diagram of this model.

The associated *decrease* in the concentration of normal platelets is equal to the *increase* in the concentration of activated platelets. The associated *decrease* in the concentration of fibrinogen is equal to the *increase* in the concentration of fibrin. This depletion of fibrinogen was described and included in the model developed by Anand *et al.* [122], but was not considered by Zarnitsina *et al.* [229]. The following statement from Anand *et al.*, along with intuition, explains the decision.

"*The rate of depletion of a zymogen*[1] *is equal to the rate of its activation into the corresponding enzyme. The corresponding enzyme is generated from the zymogen and is depleted by inactivation due to inhibitors.*"

Since inactivation is not currently being modelled, the concentration of thrombin remains unaltered thus there is no concomitant decrease in thrombin when it participates in the activation of platelets or the conversion of fibrinogen to fibrin.

The equation used for modelling the conversion of fibrinogen into fibrin was taken from Zarnitsina *et al.* [229] and is shown below. This was considered more appropriate, based on computational efficiency, than alternative versions in the literature [122, 245].

---

[1] An enzyme in its inactive form.

$$\frac{d[Ia]}{dt} = k_1[IIa] \qquad \textbf{6.8}$$

$[Ia]$ and $[IIa]$ represent the concentrations of fibrin and thrombin respectively and the rate constant, $k_1 = 0.047s^{-1}$.

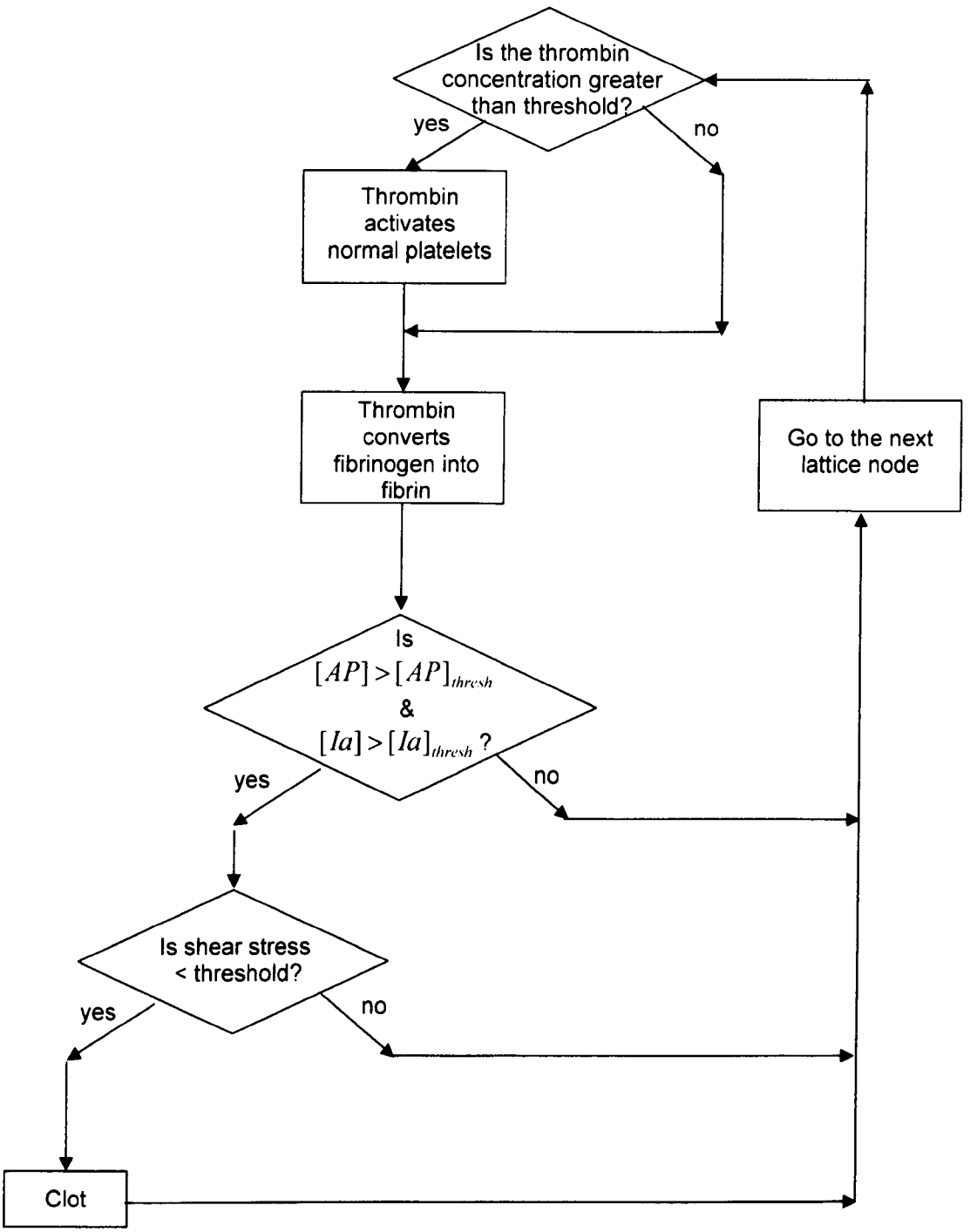

Figure 6.4: Flow chart of clotting model for thrombin release from damaged endothelium.

The equation representing the activation of platelets by thrombin is taken from Kuharsky and Fogelson [203] later used by Anand *et al.* [122]. This was chosen for its simplicity above other option available in the literature [224, 236, 246]

$$\frac{d[AP]}{dt} = k_{AP}^{IIa}[RP] \qquad \textbf{6.9}$$

The rate constant, k_{AP}^{IIa} used by both groups is $0.5s^{-1}$. The synergistic activation is considered in the same way as previously described

6.6 Results

The results to be presented are preliminary, simply demonstrating the functionality of the different models. The rate constants used are not as previously given, however ratios between rate constants have been maintained. This is not seen as a major issue at this stage because without validation, it is difficult to justify the conversion of lattice Boltzmann simulation parameters into flow parameters in real units. The later part of this section however does show comparisons with a previously published model by Wootton *et al.* [215] and the rate constants are in agreement.

6.6.1 Platelet clotting: shear stress activation

In order to verify that the model was behaving as required, some initial simulations were performed with the various strands of the model. In all cases, the initial and inlet concentrations of normal platelets is $1ML^{-3}$ and those of activated platelets is $0ML^{-3}$, where M represents the lattice unit of mass. The 2D stenosis model has been used, which has dimensions 532×82 with a Reynolds number of 100. The diffusion coefficient was $D = 1 \times 10^{-4} L^2 T^{-1}$. Although no comparisons are made with experiments at this point, in order to illustrate the magnitude of this diffusion coefficient, an approximate vessel must be considered. The obvious choice is the femoral artery, as used previously in this project, which has a diameter of 8mm. Using the dynamic viscosity and density of whole blood[1] [215] of $\mu = 3.5mPas$ and $\rho = 1060kgm^{-3}$ respectively,

[1] This is not necessarily appropriate in this case since only platelets are being considered.

the length and timescales are calculated to be $L = 1 \times 10^{-4} m$ and $T = 1.2943 \times 10^{-5} s$. This means that the diffusion coefficient above is approximately $7.726 \times 10^{-8} m^2 s^{-1}$, and hence the limiting value is too large by a factor of almost 1×10^6.

The converged flow field was obtained after 1×10^5 iterations, before implementing the shear stress model. Because the diffusion coefficient was not as low as required, in order to test this part of the model, the values used in the model proposed by Anand *et al.* could not be used. Arbitrary values were chosen for the constants in equation 6.3 to obtain results in a reasonable simulation time. The distribution of the tracer storing the shear history after a variety of iterations is shown in Figure 6.5. This shows that initially, the shear history tracer is only non-zero in the region near the stenosis. However, as the simulation progresses, platelets from this region make their way into the recirculation region, to finally reach the centre of the vortex and the corner immediately behind the stenosis.

The behaviour of the platelet activation part of the code was investigated before any clotting was allowed. The synergistic activation of platelets was not considered at this stage. If the concentration of the shear history tracer exceeds 5 units, activated platelets are released with a concentration of 1 unit. Figure 6.6 shows the distribution of activated platelets at subsequent times following the converged flow solution. This shows the behaviour expected. Platelets are primarily activated in the stenosis region and the activation is dependent upon both the shear stress and the duration of the applied shear stress. Activated platelets are then transported into the recirculation zone where, although they experience lower shear stress, longer residence times occur, thus allowing for further activation.

In order to examine the behaviour of the related clotting model following the activation of platelets, a variety of threshold concentrations of activated platelets were chosen along with different values of the shear threshold. Clotting is permitted if the concentration of activated platelets exceeds the threshold and the shear stress is sub-threshold. Two types of clot were produced and the converged clots took the form shown in figure 6.7.

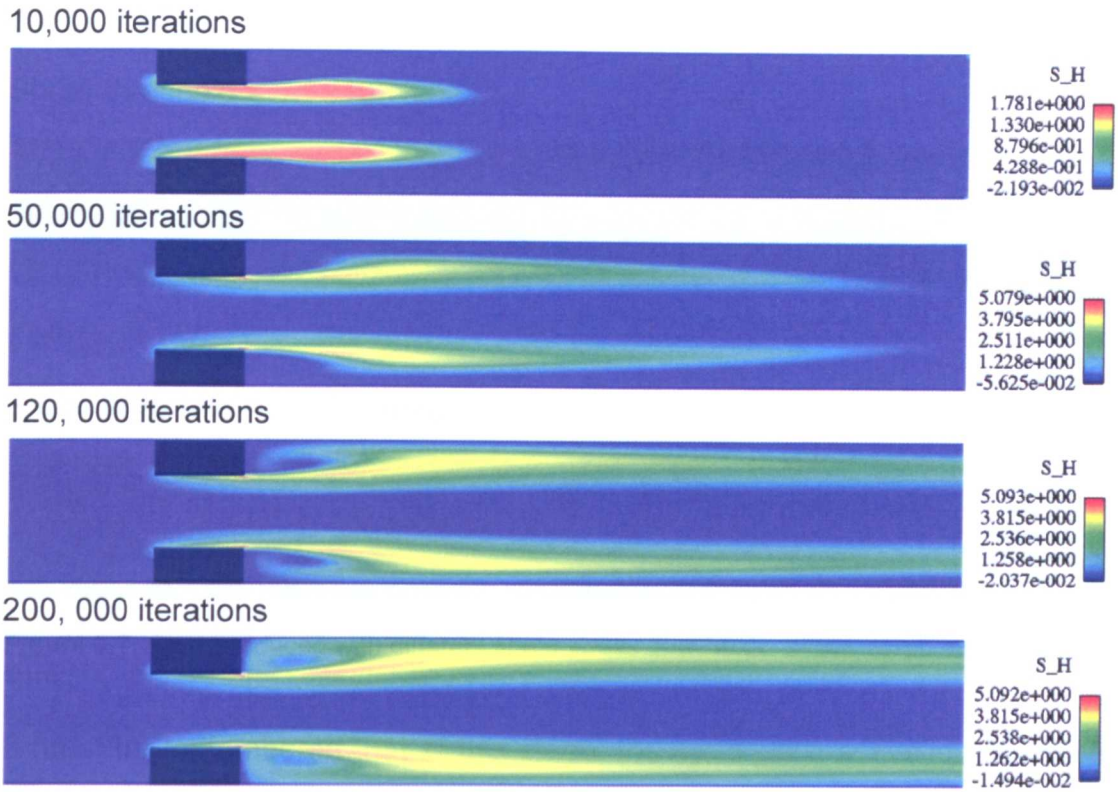

Figure 6.5: Distribution of shear history tracer with time.

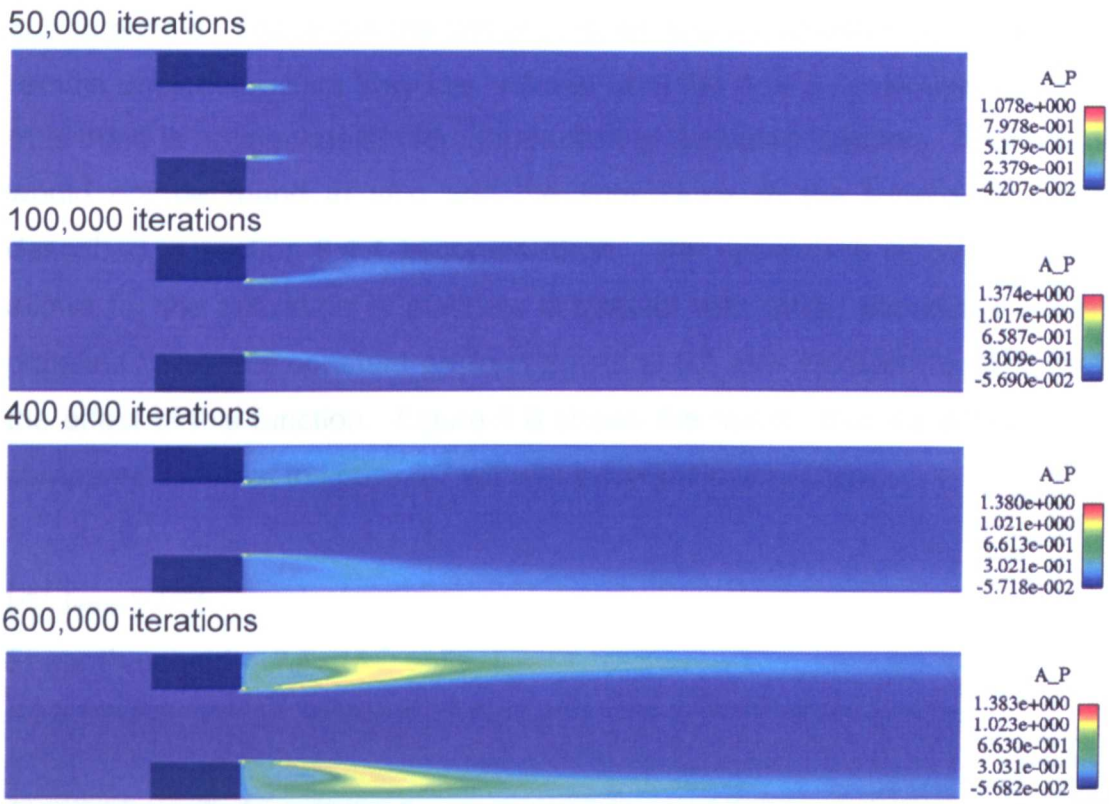

Figure 6.6: Distribution of activated platelets shown at various stages after the start of the model.

$[AP]_{thresh} = 1ML^{-3}$

Shear threshold = 7.5×10^{-6} units

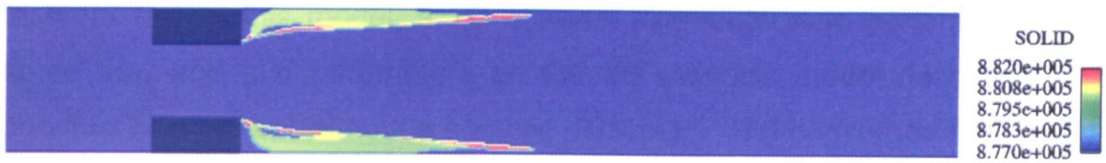

$[AP]_{thresh} = 1ML^{-3}$

Shear threshold = 3×10^{-6} units

Figure 6.7: Clots produced with different shear stress thresholds, above which clots do not form.

It must be remembered that at this stage, the synergistic activation of platelets has not been included. This is evident in the results shown in figure 6.7, since 'holes' void of clot are produced where the concentration of activated platelets is sub-threshold. These are the last regions to receive activated platelets and will remain unclotted, since they are isolated from the flow by surrounding clot and thus there is no mechanism for introduction of activated platelets. This situation would not be found *in vivo* and the importance of the synergistic function described in section 6.4.1 becomes clear. The synergistic activation function allows for the activation of platelets in contact with other, previously activated platelets. The rate constant given in equation 6.6 was selected to demonstrate the effect of this function. Figure 6.8 shows the result obtained and should be compared with that in figure 6.7 without synergistic activation.

$[AP]_{thresh} = 1ML^{-3}$

Shear threshold = 7.5×10^{-6} units

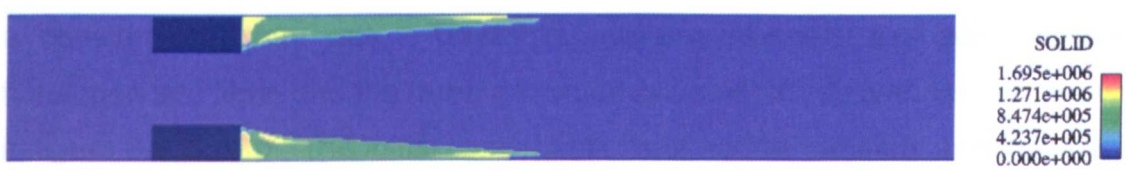

Figure 6.8: Clot produced with both shear stress and synergistic activation of platelets.

6.6.2 Platelet clotting: collagen exposure

In order to test this model, a 2D channel simulation was performed with the same flow and grid parameters as the 2D stenosis model described in the previous section, but without a stenotic occlusion. The converged flow field was obtained after 1×10^5 iterations, without the platelet model. A region of 50 lattice points located approximately halfway along the upper wall was defined as 'damaged' where collagen was exposed. Figure 6.9 shows the results of a clot produced after 1×10^5 iterations. The condition used to form the clot was that the concentration of activated platelets must be greater than that of normal platelets.

Figure 6.9: Clot produced at site of damaged wall. Arrow marks the region of damage, red defines newly formed clot.

Figure 6.9 shows that the model is behaving as expected, leading to clot deposition near the region of damage. This is an important observation regarding the *in vivo* response to wall damage. The increased width of clot is downstream of the damaged region due to transport of activated platelets by the flow.

6.6.3 Blood clotting: thrombin release

Once again, a 2D channel was used and a section of the upper wall of length 50 lattice units was marked as damaged, but in this case, thrombin was released at a constant, arbitrary rate. Thrombin activates platelets and also converts fibrinogen into fibrin and the threshold value of thrombin required for this, shown in figure 6.4 is zero. The initial concentrations of normal platelets and fibrinogen were $0.16ML^{-3}$ and $0.84ML^{-3}$ respectively. These were chosen such that the sum was 1 and the ratio was the average ratio taken from the literature [9, 122, 190, 224, 236, 244, 247-250]. These values were used as inlet boundary

conditions for the remainder of the simulation. The rate constants used maintained the same ratio and their magnitudes were those from the presented literature, with the channel chosen to have a width of 8mm. The grid and flow parameters were those described in section 6.6.2. The converged flow field was obtained after 1×10^{5} iterations, without the thrombus model. An additional 1×10^{5} iterations were performed with the thrombus model, wherein a source of thrombin with concentration of 1×10^{-3} was released. The limiting diffusion coefficient was $D=1\times10^{-4}L^{2}T^{-1}=7.726\times10^{-8}m^{2}s^{-1}$, which is several orders of magnitude too large, since Anand *et al.* give values for the elements of the cascade of approximately $D=1\times10^{-11}m^{2}s^{-1}$. Thresholds of activated platelets and fibrin required for clotting were $2\times10^{-2}ML^{-3}$ and $1\times10^{-3}ML^{-3}$ respectively. Figure 6.10 shows an image of the clot formed after 1×10^{5} iterations.

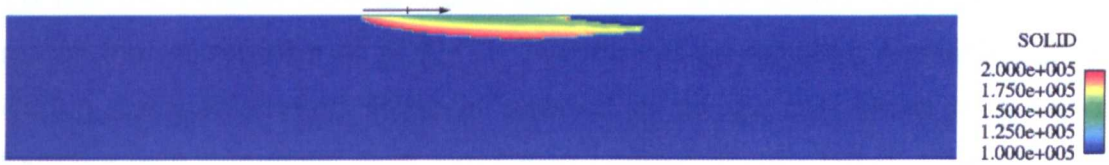

Figure 6.10: Thrombus deposition in 2D channel. Wall region of damage (thrombin release) is indicated by the arrow.

The limiting shear stress condition can be used to observe its effect on the resulting clot. Figure 6.11 shows a clot produced using the above parameters and a threshold shear stress of $3.5\times10^{-5}ML^{-1}T^{-2}$.

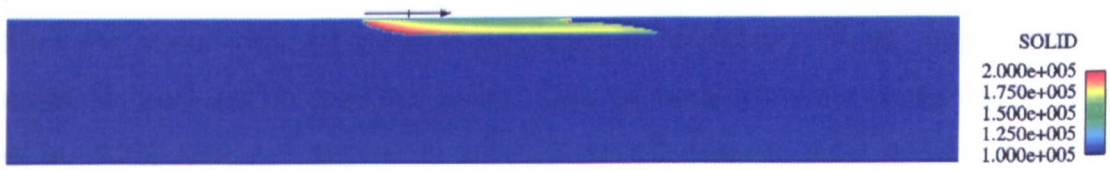

Figure 6.11: Thrombus deposition in 2D channel using shear stress condition. Wall region of damage (thrombin release) is indicated by the arrow.

When further iterations were performed it was found that, if a limiting shear stress is used, a bigger clot will grow. This can only mean that the activated platelets and thrombin are transported away from the original region of damage to a low shear region. The longer it takes for a clot to grow over the damaged area and block the source of thrombin, the greater the concentrations of activated species in the domain. The time it takes for a clot to grow is affected by the shear stress and the threshold concentrations used for clotting. A finite

amount of time is required for thrombin to act, during which the species are transported away from the original region of damage. The size of this clot is not reduced with the introduction of a shear stress condition. In this situation, clots are prevented from growing, but species are still being activated. These can finally form a clot when they reach a lower shear region further downstream. This explains why the clot is larger in length rather than thickness. It is interesting to note that this problem will increase with the introduction into the model of additional clotting factors from earlier stages of the cascade, since it will take longer for activated platelets and fibrin to form. Threshold values must be very small in order for clot to grow and isolate the damaged wall.

6.6.4 Comparison with published data

To test the platelet clotting model developed, a simulation was performed to match that of Wootton *et al.* [215]. Wootton *et al.* describe experimental work with a collagen coated stenosis inserted in an *ex vivo* shunt in a baboon together with numerical work simulating platelet accumulation. The numerical model is a species transport model that includes; convection, shear-enhanced diffusion, near-wall platelet concentration and a kinetic model of platelet activation and aggregation. The authors claim that the duration of shear stress exposure in a stenotic coronary or carotid artery is lower than that required for shear-induced activation *in vitro* and that the residence time for particles in the poststenotic region of these arteries is also short relative to the characteristic time for shear-induced platelet aggregation *in vitro*. These statements are apparently based on previous work. One of these previous works by Bluestein *et al.* [103] does not appear to support the absence of such activation and the minimum Reynolds number in this study was Re = 300, almost twice that used by Wootton *et al.* $(\mathrm{Re} = 160)$. As the Reynolds number will influence the shear history of platelets significantly, it is surprising that this conclusion was made without further justification. The work of Cao and Rittgers [251] was also cited, quotations from which are given below.

"*It is concluded that residence times exceed 1s for at least 13% (and up to 61%) of cells downstream of 75% and 95% asymmetric stenoses under ICA (internal carotid artery) and LAD (left anterior descending) flow conditions and,*

thus, these cases may be sufficient to allow platelet adherence and eventual thrombus formation once stimulated."

The work of Boreda *et al.* [252] is cited, which does support the assumptions of Wootton *et al.* [215].

Another paper quoted by Wootton *et al.* is that by Huang and Hellums [234]. In the introduction to this paper, a shear stress of 50 dyn/cm^2 is given as being capable of triggering platelet activation, causing the release of granule contents into the suspending medium, and eliciting platelet aggregation. In SI units, this is equivalent to $5Pa$. The peak shear rate recorded numerically by Wootton *et al.* is approximately $4\times10^3 s^{-1}$, which (using the blood viscosity of $3.5mPas$ given) equates to a shear stress of 14Pa. It is appreciated that the shear stress exposure over time is relevant, but no comparisons of these variables are made by Wootton *et al.* [215]. It appears that the focus of the work by Huang and Hellums is that of platelet aggregation, whereas Wootton *et al.* describe platelet activation when referencing this work. The following text from Wootton *et al.* is therefore confusing.

"*A stenosis also briefly exposes platelets to high shear stress, which has been shown to activate platelets in vitro. The duration of shear stress exposure in a stenotic coronary or carotid artery is lower than required for shear-induced activation in vitro (ref. Bluestein et al. and Boreda et al.). The residence time for particles in the poststenotic region of these arteries (ref. Cao and Rittgers) is also short relative to the characteristic time for shear-induced platelet aggregation in vitro (ref. Huang and Hellums). These studies suggest that the primary role of flow in thrombosis on a stenosis is to enhance platelet transport in regions of high shear.*"

In order to provide agreement with Wootton *et al.* [215], the previously developed shear stress activation model was not employed in this section but the model presented in section 6.4.2 which exposes collagen on the wall leading to platelet activation was used. The synergistic activation of platelets was also included. This was not considered by Wootton *et al.* [215], but these

authors did consider the thrombogenic nature of the deposited clot, which can activate further platelets.

The numerical model by Wootton *et al.* is based on previous work by Turitto and Baumgartner [231]. A surface reaction was considered as illustrated below:

$$\text{Free, unactivated platelets} \xrightarrow{k_t} \text{attached, activated platelets}$$

"*which lumps together both activation and the binding of platelet glycoproteins to adhesive proteins into one overall rate* k_t. *This model assumes that most activation takes place near the thrombus surface, where platelet activating species are likely to be most concentrated. The platelet flux,* j, *(rate of platelet accumulation per unit surface area) into the thrombus at axial location* x *was computed by:*

$$j(x) = k_t c_0(x) \qquad \textbf{6.10}$$

where c_0 *is the concentration of free platelets at the surface and* k_t *is the kinetic rate of aggregation of platelets to the thrombus.*"

Wootton *et al.* [215] use the rate constant $k_t = 5 \times 10^{-3} cms^{-1}$ to give the best match between experimental and computed values for the three stenoses investigated. The effect of the growing thrombus on the flow field was ignored and the extent of platelet accumulation was monitored by integrating the platelet flux over a specified region of interest. The geometry and collagen region are shown in the following diagram which is taken directly from Wootton *et al.* [215].

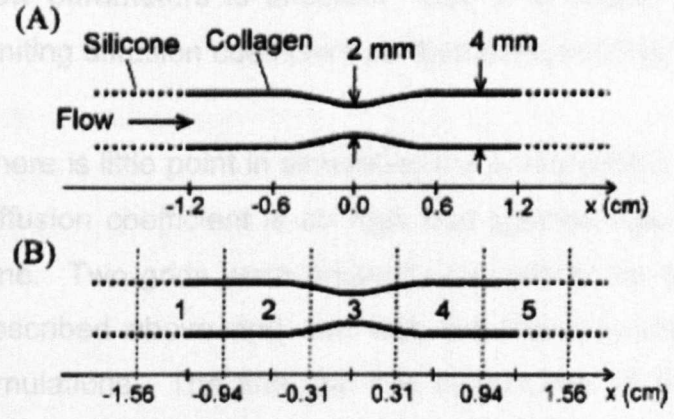

Figure 6.12: Geometry taken from Wootton *et al.* [215] showing 5 regions of interest.

Three stenoses were used; 50%, 75% and 90% (by area). For the purpose of comparison, only the 75% stenosis was considered in the LB simulation.

A sinusoidal stenosis was created using Matlab with a 1 diameter inlet and a 3 diameter outlet (measured beyond the region of collagen). Shear dependent diffusivity was not considered and the thermal diffusion coefficient should be $D = 1.6 \times 10^{-13} m^2 s^{-1}$, according to Wootton *et al.* [215]. This agrees with the value given by Anand *et al.* [122].

The entire duration of the simulation and experiment by Wootton *et al.* [215] is 100 minutes. The LB grid size was chosen so that the entire experiment was simulated within a week on the SX-8 machine. This results in a grid of dimensions $204 \times 22 \times 22$ and the length and time scales are therefore $L = 2 \times 10^{-4} m$ and $T = 3.2785 \times 10^{-5} s$ respectively. This grid is incredibly coarse and it was initially believed that the flow parameters would not be comparable. However, the recirculation length was 19.3mm when measured from the end of the stenosis. Wootton *et al.* [215] recorded a value of 19.6mm. The peak shear rate was calculated by importing the data into Matlab and extracting a single line profile from the back of the stenosis. A value of approximately $2610 s^{-1}$ was obtained. Wootton *et al.* [215] reported a value of approximately $4700 s^{-1}$. However, their simulation included mesh refinement at the walls with a resolution of $1-2 \mu m$. The LB grid used has a resolution of $200 \mu m$. Since the shear rate will increase towards the wall, this is in line with the underestimated value in the LB simulation. It is obvious that such a coarse grid is necessary in order to meet the target simulation time and in consequence the accuracy of the flow parameters is affected. Use of a coarse grid gives an increase in the limiting diffusion coefficient as discussed in Chapter 4.

There is little point in simulating the entire experiment time of 100 minutes if the diffusion coefficient is so high that species values converge much before this time. Two grids were originally considered for the simulation, the coarse grid described above and one with the finest diameter used for the milk clotting simulations. The fine grid has dimensions of $964 \times 98 \times 98$. The recirculation length measured for this grid was 19.6mm, again agreeing with Wootton *et al.*

[215]. However, using a week on the SX-8 machine, only 2s of *real* time can be simulated. This simulation was therefore abandoned.

Using the coarse grid, the rate constants were chosen to agree with Wootton *et al.* [215] for the activation of platelets by collagen and with Kuharsky and Fogelson [203] for the synergistic activation of platelets, as described in Section 6.4. The limiting diffusion coefficient was found to be $D = 3.3 \times 10^{-3} L^2 T^{-1} \approx 4 \times 10^{-6} m^2 s^{-1}$; therefore 25 million times too large.

No data has been found for the concentration of activated platelets required to cause clotting. This is probably because people tend to report the actual concentration values rather than using a solidification step. Goodman *et al.* [224] modelled platelet activation and used a condition that, if the volume of adherent platelets within a grid cell was greater than the grid cell volume, then that cell was designated as thrombus and the local viscosity increased 100,000 fold.

A series of clotting threshold values $[AP]_{thresh}$ were used and the results analysed every 2×10^4 iterations. This is equivalent to approximately 0.66s. Many of these simulations crashed due to total occlusion of the lumen. If the simulations did not crash, the converged clot deposition profile was a single layer on the post-stenotic region of collagen.

Wootton *et al.* [215] reported that, *in vitro,* occlusion occurred within the given experiment time (100 minutes) for the 75% and 90% stenoses. In the current simulations, in order to analyse the results prior to a crash, the simulation with the highest clotting threshold that crashed ($[AP]_{thresh} = 4 \times 10^{-3} ML^{-3}$) was rerun and results written more frequently. Figure 6.13 shows the results produced, analysed frequently prior to occlusion. Following this, the thrombus propagates further both upstream and downstream.

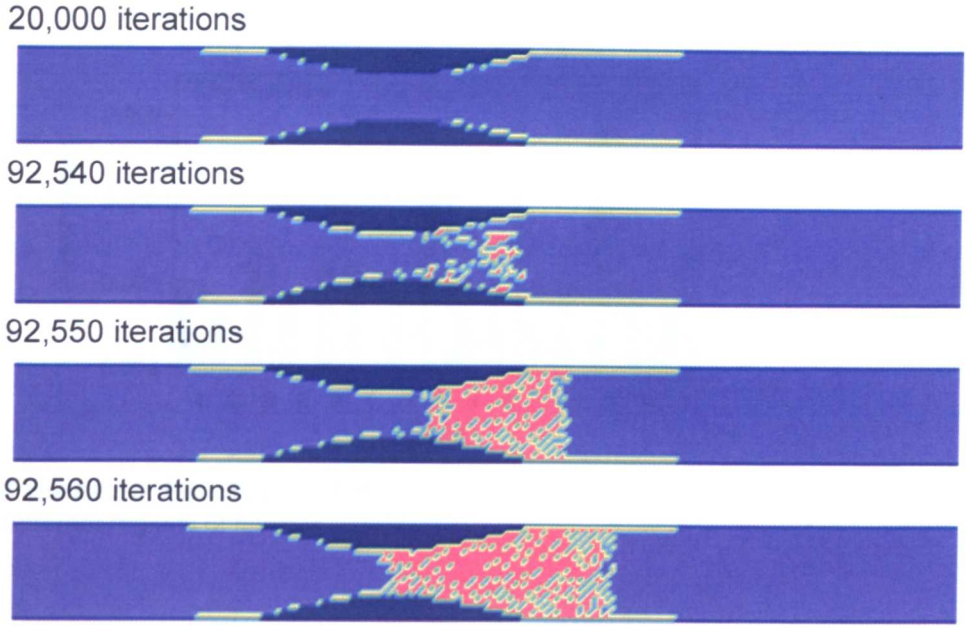

Figure 6.13: LB platelet clotting model with collagen and synergistic activation of platelets. Attempt to simulate the results of Wootton *et al.* [215].

Comparison with Wootton's results is not totally appropriate because different diffusion coefficients are used and the clotting takes place over very different timescales. The final image in figure 6.13 is after approximately 3s whereas figure 6.14 shows Wootton's results obtained after 15 minutes. Figure 6.15 shows their results obtained with this geometry after 5-60 minutes. The performance of this model was approximately $18.90 MLUPS$ therefore simulation of 3s took only 8 minutes of CPU time. Vessel occlusion has occurred more rapidly in the simulation due to the limiting diffusion coefficient in use which acts to disperse the activated platelets at a faster rate. The key comparisons that can be made here are that clot deposition is greatest in region 3 for both sets of results and occlusion occurs from within this region.

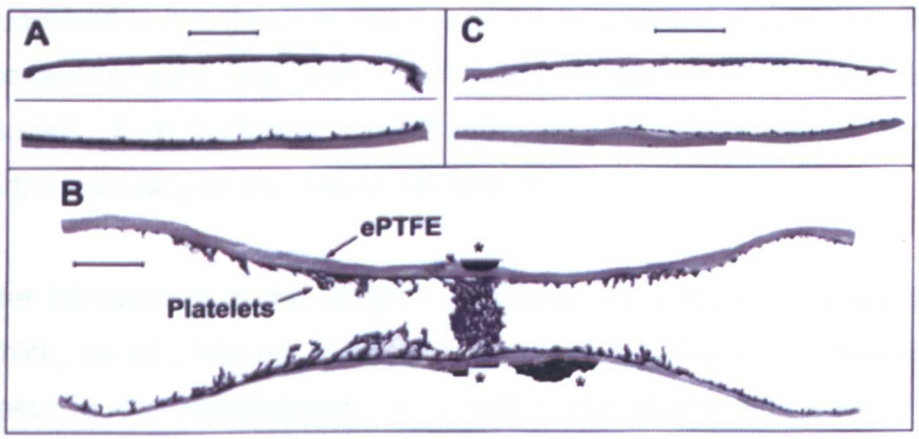

Figure 6.14: Results taken from Wootton *et al.* [215] after 15 min of blood flow. 'A' shows the inlet section, 'B' the throat section and 'C' the outlet section.

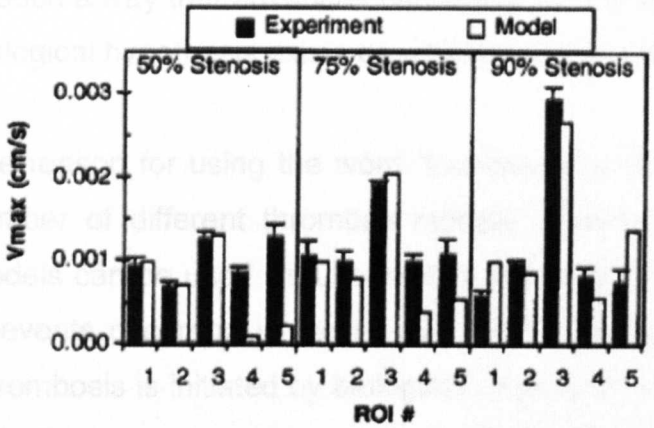

Figure 6.15: Results taken from Wootton *et al.* [215] showing average platelet accumulation in different regions of interest.

6.7 Discussion

This chapter focused on extracting the important data from the literature in order to increase the understanding of the processes involved in thrombosis, particularly with regards to possibilities for modelling. The primary aim in developing a model is that the flow solution can still be performed accurately in realistic geometries and either 2 or 3 dimensions. The thrombosis models developed are created alongside the LB flow solver and may be called depending upon the local rules specified. The use of passive scalar tracers was adopted; this was shown to be a popular choice in the literature. However, due to limitations of the existing diffusion model, as discussed in Chapter 4, the accuracy of the results is sacrificed. As a first attempt, this chapter demonstrates the possibilities that exist for modelling aspects of thrombosis using the work of previously published models. The advantage of the models described in this thesis is that the effect of thrombus accumulation is fed back to the surrounding flow field. This feature is not found in many of the existing models. If, in the future, the diffusion model can be improved, a direct increase in the accuracy of the results will be seen.

The introduction to this chapter described the complex process of thrombosis, which, as yet, has not been simulated in full. The aim of this chapter was to describe the development of a lattice Boltzmann framework for simulating thrombosis, along with some initial results. The framework has been developed

in such a way that advances can easily be implemented, providing that a sound biological hypothesis exists on which any assumptions can be based.

The reason for using the word 'framework' in this chapter is evident when the number of different thrombus models developed is considered. Any of the models can be used simultaneously, the only requirement being that sequence of events occurring in the *in vivo* or *in vitro* situation should be well defined. Thrombosis is initiated by biological phenomena such as prolonged exposure to high shear stresses and exposure of the subendothelium. The development of such models provides confidence in developing more detailed models in the future and this work can be used as a starting point.

The first model proposed simulates shear stress activation of platelets. The results show that elevated shear stress, found in the region of the stenotic occlusion activates platelets, which are then transported into a low shear stress region of recirculation where they can aggregate. This notion has been discussed previously [103, 187]. Figure 6.8 shows that, one of the last regions to clot is the corner, immediately downstream of the stenosis. This is because it takes a significant amount of time for activated platelets to develop in this region. However, the primary region of deposition is near the reattachment point, in agreement with the literature discussed. If the synergistic function is not used, this region never clots because it is blocked from the luminal flow by previously deposited clot. Results not presented show that this is the case regardless of the simulation parameters chosen.

The second model simulates platelet activation by contact with exposed collagen and other activated platelets. The clot covers the original region of damage, thus reducing the rate of deposition and hence limiting the final size of the thrombus. The maximum thickness of the thrombus is shifted downstream of the original area of collagen exposure, due to the influence of the flow field.

The third model includes the behaviour of both platelets and the final stage of the coagulation cascade. The use of a source term of thrombin at the wall is not entirely appropriate. When a vessel wall is damaged *in vivo*, the reactions in the cascade occur, whilst blood is flowing and before thrombin is produced.

This means that thrombin will be released downstream of the site of injury, depending on flow field and the timescale associated with propagation of the cascade. This requires either inclusion of the remaining reactions of the cascade, or the formulation of a sensible approximation. This issue will be addressed in the chapter which follows.

The models and results presented in this chapter show how the behaviour of platelets and the coagulation cascade can be simulated. It is acknowledged that there are many free parameters in the models and also that the results shown are specific to the parameters used. However, in future, when comparisons are made with experimental results, the parameters can be chosen appropriately, with an increase in the accuracy of the results.

The *in vivo* behaviour is highly complex and, by necessity, only some of this has been covered in the literature review. The phenomenon of inhibition must be considered in future. This will inactivate the clotting factors and platelets and control the resulting clot growth. The diffusivity of platelets is known to be dependent upon the motion of red cells, since these affect their motion [231] and can increase the diffusion coefficient by up to 4 orders of magnitude, depending upon the shear rate [253]. This still places the limiting diffusion coefficient at least 2 orders of magnitude above that of platelets. Red blood cells have not been considered in these models, but if they are required in future simulations this would necessitate consideration of the shear dependent release of ADP from red cells as well as from platelets.

Activation of platelets in these models has been assumed to be instantaneous, whereas Anand *et al.* defined a 1s delay for this process [122]. The models developed in this chapter do not consider the adhesion of platelets to the vessel wall and to each other. Instead, a more simplistic threshold concentration has been used.

In the shear stress model, the clot is able to form on a supposedly intact endothelium, but as discussed in the literature review, this is unlikely to occur *in vivo*. The purpose of these simulations was to demonstrate a feature that can be incorporated into a more detailed, more accurate model in future.

The issue of performance is not addressed in this chapter, but it is obvious that the more species that are used and the more complex the reactions, the less efficient the code becomes. This has been kept in mind whilst developing the models and, for this reason the simplest relationships available in the literature were always chosen.

In future, increased effort should be placed on validation. However, this is difficult given that so many of the individual biological phenomena described above have not been considered. The work of Wootton *et al.* [215] does however provide a useful starting point and the features of the models developed in this study, namely shear stress activation and synergistic activation could possibly be used to explain the discrepancies that Wootton *et al.* [215] see between their numerical and experimental results.

The main achievement of this chapter is providing a bridge between the complex biological behaviour described in the literature and the lattice Boltzmann model. This work is intended to be a starting point for the development of more accurate and efficient models to represent the process of thrombosis.

Chapter Seven: Deep Vein Thrombosis

7.1 Literature Review

Deep vein thrombosis (DVT) is the term used to describe a blood clot that forms in the deep veins, usually in the leg. The dangers associated with deep vein thrombosis are similar to those of arterial thrombosis; if the clot breaks away (embolises) and travels through the circulatory system, it can prove fatal if it restricts blood flow to a major organ. In the case of deep vein thrombosis, the clot may travel into the right side of the heart, then into the main branches of the arteries to the lung, where it can block the blood flow. This is called pulmonary embolism and is a common cause of sudden death [254].

The aetiology of DVT has been the subject of some considerable discussion and the exact mechanism has yet to be determined. The relationship between prolonged periods of inactivity and the incidence of pulmonary embolism was identified by Simpson during the Second World War [255]. Death statistics obtained over a two month period in 1939 were compared to those recorded for the same period in 1940. Results were categorised by cause of death and a striking, six-fold increase in death (from 4 to 24 cases), from pulmonary embolism was observed.

"*The increase from 4 to 24 cases is accounted for by the 21 cases of sudden death from this cause in persons in, or more usually, leaving the shelters after a night or a succession of nights in them. It was clear that it resulted in some way from this enforced confinement.*"

Simpson [255] describes the case of a 60 year old woman who sat in a deck chair continuously for 10 hours. Approximately 10 minutes after leaving the shelter to walk home, she collapsed in the street, dead. Many of the subjects were elderly and a little obese and showed varicosities of the leg veins, but all had spent a long period of rest "*in a deck chair or some similar seat, the front edge of which pressed into the legs as they lay over it, compressing the veins and causing obstruction, stasis, oedema, and thrombosis – probably in that order.*"

This publication emphasised the urgent need for bunks in shelters, particularly for elderly people. It is interesting to note Simpson's hypothesis as to the cause of DVT and also how, since 1940, emphasis has changed from a mechanically driven event to a more biochemical one.

In recent years, public awareness of deep vein thrombosis has grown due to its relationship with inadequate accommodation during long-haul flights and also as a serious complication following surgery [254]. DVT has been reported in the case of an IT worker after an 8 hour shift [256] and a 14 year old boy who spent 10 hours kneeling down playing computer games [257].

The potential involvement of the vessel endothelium was recognised as early as 1951, when McLachlin and Paterson [258] suggested that intimal damage may be caused by collapse of the vein due to pressure on the back of the calf while a patient is lying in bed.

"*This collapse prevents the endothelium from obtaining nourishment from the circulating blood stream.*"

Further investigations in 1960 by McLachlin *et al.* [259] demonstrated that stasis formed in the pockets of venous valves, directly linking the formation of thrombosis behind valve pockets with stasis. It was shown that such regions of stasis could be disturbed by contraction of the calf muscles.

In 1977, Malone [260] described an alternative interpretation of Virchow's triad; suggesting that, rather than a disparate set of competing alternatives, a single mechanism exists. He postulated that changes in blood flow cause change in the vessel which, in turn, causes change in the blood constituents. It had already been established that the arrangement of veins and muscles in the calf is such that contraction of the calf muscles will 'pump' the veins [261]. One particular hypothesis given by Malone for the aetiology of DVT [260] is that calf inactivity causes a loss of pulsatile flow, i.e. the venous return pulsates only when the calf muscles are contracting intermittently. This results in streamline and steady venous blood flow. He suggested that;

"A change from pulsatile flow to non pulsatile flow is a 'change of blood flow' within the context of Virchow's category, and could produce thrombogenic conditions in valve pockets." [260]

McLachlin and McLachlin [261] describe a preventative technique whereby electrodes could be used during surgery to stimulate the muscles of an anaesthetised patient. They claim that *"there is no doubt that blood can be kept moving in the legs in this physiological manner."*

Malone [260] suggests that calf muscle pump failure is likely to cause stasis (static, not just slow or inadequate flow) and proposes that the subsequent introduction of fresh blood is the significant event leading to thrombosis. The conclusion to this work is summarised by the following points:

- The cause of reduced venous blood flow is reduced arterial blood flow; this may be local or general, and be caused by physiological or pathological change.
- The irrigation of valve pockets in veins is likely to cease when peripheral muscles are pathologically inactive, or, are paralysed during anaesthesia.
- This may cause ischaemia of valve tissues.

Malone claims that it is certain that anoxia (complete deprivation of oxygen) or hypoxia (shortage of oxygen in the body) follows prolonged venous stasis, the endothelium is likely to suffer damage when starved of an essential metabolite and hence, endothelial degeneration could follow prolonged and severe venous hypoxaemia (shortage of oxygen in the blood). As will be seen later, in the absence of histological evidence of overt damage to the endothelium this claim proved to be controversial.

The formation of Malone's ultimate hypothesis comes by highlighting potential differences in the effect of hypoxia on platelets and on endothelial cells.

"The endothelium is fixed and dependent on a blood borne oxygen supply, whereas the circulating cells can obtain a direct oxygen supply from the lungs.

The vein endothelium may be oxygen starved, while the cells moving into and through the lining have been recently oxygenated; the difference between endothelial cells and circulating cells in a hypoxic segment is, therefore, that they have been exposed to hypoxaemia for different periods of time."

However, if circulation of these cells ceases, they must incur an oxygen debt, and "*each hypoxaemic pocket in veins may become a trap and a graveyard for platelets and leucocytes.*"

Malone also discusses the issue described in Chapter 6 concerning the physiological response to a damaged wall. He claims that it would be dangerous if blood continued to flow through a vessel which was effectively dead. Plasma would leak out through the vessel wall once the endothelial barrier was destroyed, ultimately bringing the circulation to a stop. He stated that;

"*The presence of 'dead material' in a vessel lining may therefore stimulate physiological clotting in order to maintain vascular integrity and retain circulating volume.*"

"*When a tiny, insignificant, patch of endothelium is killed inside a valve pocket, gross plasma loss is unlikely, and vascular integrity is not threatened! By impairing valve cusp movement, the events lead to more cell death and more clot formation, and then by a coup-de-grace of pathological physiology, the valve obstructs normal flow as it was designed to obstruct abnormal flow.*"

It therefore seems that the physiological response can easily get out of control and even small regions of damage can lead to large regions of clot growth, in an attempt to maintain the circulation. The point discussed in Chapter 6 concerned the response to a small region of damage in a channel. It would appear that attempts are made to repair the area of damage, although this must be limited based on the presence of flow in channels compared to valve regions.

In 1978, Malone and Morris investigated Malone's hypothesis experimentally [262]. Hypoxaemia or hypoxia was induced in rabbit veins by a number of different means. The veins were subsequently re-perfused with either normal or hypoxaemic blood. Excised human veins were also used to investigate the effects of stagnant hypoxia. These experiments were designed to answer the following questions:

- Does hypoxia damage the endothelial lining of a vein?
- Do platelets and leucocytes react with, and attach, to vein wall damaged by hypoxia, in the same way that they are known to attach to the wall when it is damaged by physical or chemical means?
- Is the reactivity of circulating cells dependent on their viability while the endothelial cells nearby are compromised or dead?

The conditions were such that stagnant flow was interrupted by normal flow, thus reproducing the situation arising when prolonged periods of inactivity are followed by activity.

Time of exposure to hypoxia or hypoxaemia was varied and the results confirmed that severe, prolonged, hypoxaemia causes endothelial damage. Platelets and leucocytes were seen to aggregate in hypoxic vessels caused by hypokinetic (defective muscular action) and anaemic methods (carbon monoxide administration[1]), but not by anoxic/arterial hypoxaemia (asphyxiation by excess nitrogen[2]). Thus if both circulating cells and endothelial cells are hypoxic, aggregation does not occur, whereas if only the endothelial cells are hypoxic and the circulating cells can re-oxygenate in the lungs, then aggregation will occur. There was histological evidence of gross endothelial damage in the veins with hypoxia and hypoxaemia. Malone and Morris discuss the concept of platelets and leucocytes being phagocytic, and thus, must be viable in order to attack the dying/dead endothelial cells. The phagocytic capability of platelets was reported by Movat *et al.* [263] and Mustard *et al.* [264] in 1965.

---

[1] This method suffocates the peripheral, fixed tissues whilst keeping the flowing blood oxygenated.
[2] This method reduces the oxygen supply to both the blood and the tissues.

Two important statements from Malone and Morris [262] are shown below.

"*One classical hypothesis explains thrombogenesis by postulating that platelets are primarily responsible for the lesion, and that the many leucocytes present in most experimental thrombi, and all natural thrombi, are secondary arrivals, caught up in a fibrin mesh, as commonly postulated. The experimental results reported ....lend no support to this hypothesis. Firstly, the leucocytes are seen to be attached directly to the vessel walls alongside the platelets; and secondly, the platelet: leucocyte ratio in the lesions examined was not significantly different from that in ordinary blood, about 50:1.*"

"*No fibrin mesh, no net like structure entrapping the leucocytes, was visualised in our histological preparations. The circumstances which produced these experimental lesions suggest that both platelets and leucocytes manifest their common phagocytic function which leads them to marginate together, and in approximately proportionate numbers relative to their numbers in fluid blood, on damaged vessel linings.*"

The first statement is significant because it suggests a role for leucocytes, not previously considered in this project. The second statement by Malone and Morris [262] is important because it suggests that, even though the subendothelium is exposed (whether or not this means that collagen is exposed), the coagulation cascade is not initiated.

Hume *et al.* [265] describe the importance of activation of both platelets and the coagulation cascade, but it is not clear from this article where or how the cascade is initiated. Sevitt [266] claims that most venous thrombi are primarily formed of erythrocytes trapped in a fibrin mesh, but also contain many platelets.

Further experimental evidence relating hypoxia to thrombosis was reported in 1981 by Hamer *et al.* [267]. This particular investigation examined the likelihood of hypoxia behind valves in non-pulsatile flow. Previous work by Malone and Morris [262] demonstrated that hypoxia can lead to endothelial damage, so the question remained as to whether a sufficient degree of hypoxia could ensue in conditions of non-pulsatile flow brought on by calf muscle pump

inactivity. Experiments performed on 8 dogs and 2 human subjects demonstrated a lower oxygen tension in valve pockets after a few minutes of non-pulsatile, steady flow than in valve pockets disturbed by pulsatile flow, or in the nearby vein lumen. The oxygen tension in the blood in the region near the cusp and in the 'parietalis' endothelium (the endothelium lining the valve on the pocket side, rather than the luminal aspect) immediately fell to very low values, suggesting that the cuspal endothelium receives little or no oxygen from the cusp tissue and is mainly dependent on the blood in the pocket for oxygen. When streamline flow was maintained for 2 hours, thrombus, consisting of platelets, fibrin and trapped blood cells formed on the parietalis surface. This observation clearly contradicts Malone and Morris' findings [262] which reported no sign of fibrin in the deposits. Hamer concludes that with steady flows, sufficient hypoxia results, causing endothelial damage, which in turn, as for other known forms of endothelial damage, can result in venous thrombosis.

In 1984, Okoye *et al.* conducted an experimental study on human subjects measuring luminal oxygen tension in the femoral vein, during and after application of graduated pressure stockings [268]. A significant reduction from the baseline value was reported 30s and 60s after application and also 2 min after removal of the stockings. The authors relate this to the "*washing out of stagnant hypoxic blood*". Hamer *et al.* [267] were cited by Okoye *et al.* [268] who claim their work is "*an indirect way of confirming the findings of Hamer et al.*". Thus this study supports the theory of hypoxia in venous valve pockets.

In 1984, Hamer and Malone [269] reported further experimental evidence of thrombosis caused by hypoxia. This was emphasised as being a more physiologically relevant explanation for the pathogenesis of deep vein thrombosis in apparently normal veins. Three groups of dogs were used, one exposed to a prolonged period of immobility, one with prolonged immobility interspersed with frequent periods of passive movement and one with prolonged immobility with infrequent bouts of active movement. Ten percent of dogs in the first group developed thrombi, 10% in the second group and 69% in the third group. The thrombi originated in the venous valve pockets, or from the confluence of tributary veins with the main femoral vein, and most consisted of platelets, red blood cells and fibrin.

"In our view, the strikingly higher incidence of thrombi in Group 3, compared with Groups 1 and 2, was related to the combination of endothelial hypoxia within valve pockets produced by prolonged stasis and the subsequent re-introduction of fresh blood into the valve pockets for short periods, the latter resulting from the short periods of active shivering of the animals' lower limbs."

The results from Group 1 show that, without the introduction of fresh blood, fewer thrombi are produced and those from Group 2 show that frequent passive movements "*washed out*" the valve pockets often enough to make hypoxic endothelial damage improbable.

They concluded that, "*....localised venous valve-pocket stasis alternating with infrequent, intermittent restoration of (valve-pocket) perfusion play a major part in spontaneous clinical thrombogenesis.*"

In 1984, Schaub *et al.* [270] reported the effects of stasis and occlusion in cats. Stasis was produced for 5 minutes, followed by 5 minutes of reflow. This was performed 3 times in succession and the deposition consisted mainly of leucocytes, with few erythrocytes or platelets. Fibrin was only observed after 24 or 72 hours of stasis. The timeframes used by Hamer and Malone [269] are total experiments of 6 hours, with periods of stasis forming over at least 20 minutes. This is likely to have a significant effect on the resulting thrombus, particularly in light of the fact that Malone and Morris [262] failed to observe any change in endothelium when perfusion was interrupted for periods of 20 or 75 minutes. Schaub *et al.* [270] suggest that leucocytes play a primary role in the initiation of deep vein thrombosis. The sequence of events reported is as follows:

- Polymorphonuclear neutrophils (PMNs) adhere to the venous surface
- PMNs release superoxides and proteases that can promote endothelial cell death and exposure of the basement membrane
- Loss of endothelium and exposure of basement membrane (vascular injury) are thrombogenic and both platelets and coagulation factors are activated

This sounds like a description of the series of events leading to endothelial damage immediately after stasis but probably occurs too early in the process to have been noted in Hamer and Malone's study [269]. Of significance, is the finding that hypoxia, as a consequence of stasis in conditions of steady flow, leads to endothelial damage (on a macroscopic level), which can subsequently activate platelets and the coagulation cascade.

Thomas reviewed the subject of venous thrombogenesis in 1985 [271].

"*Recent experimental data point to the conclusion that local venous stasis is a necessary but not a sufficient cause of thrombosis, that endothelial cell damage, either with or without superimposed stasis, represents a relatively weak thrombogenic stimulus in veins, and that the best additional candidate necessary to produce DVT is a hypercoagulable state, the nature of which has yet to be defined.*"

In discussing activated clotting factors, Thomas concludes by saying that "*it is the simultaneous combination of stasis and activated clotting factors that represents such a potent thrombogenic stimulus.*" This is in line with the existing knowledge regarding regions of stasis as sites for amplification of clotting factors.

Of greatest importance to the current topic in the discussion of Thomas [271] is vessel wall damage. Reference is made to a previous paper by the same author [272]. Jugular veins of rabbits were clamped to stop blood flow and stasis was maintained for periods of either 40 or 60 minutes. In some cases, blood flow was subsequently re-established for a further 30 minutes and this provided no evidence that anoxia impairs the natural 'thromboresistance' of the endothelium. Thomas references work presented by Malone and Morris in 1978 [262] in this context and states that some evidence of anoxic changes in the endothelium were observed, but "*no platelets were observed adhering to the exposed subendothelium even when flow had been restored after the period of stasis.*"

Thomas [271] also discusses publications apparently opposing this notion.

"Postmortem studies in humans failed to show any significant histological lesion in the vessel wall that could serve as a nidus for thrombus formation. However, it has been difficult to exclude the possibility that some subtle change in the vessel wall, perhaps resulting from anoxia, alters the normal non-thrombogenicity of the endothelium, so that platelets adhere and become the focus of an early thrombus."

There is clearly some confusion; the above quotation goes some way towards accepting the results of Malone and Morris [262], whilst the conclusions of Thomas' previous work in rabbits provided no support for the notion of endothelial damage due to hypoxia. One of the references cited by Thomas [271] is that of McLachlin and Paterson [258], which simply admits to not identifying any lesions in the vein wall at the site of thrombus formation, but attributes this to initiation by "*more general causes*". This is also true for the cited work from Sevitt [273]. The thrombi analysed post-mortem in this study came from 41 injured or burned subjects, most of whom were elderly and 23 of who had hip fractures, hence there were many reasons for coagulation factors to be higher than normal. Anticoagulants had been administered to 27 of these patients. With the exception of one patient, there was no evidence of intimal damage in the valve pocket. No significant differences were seen between the endothelia of the study group and a control group without thrombi. The authors concluded that valve-pocket thrombi form on intact endothelium, but admitted that subtle changes due to hypoxia or splits in the endothelial lining could not be excluded. This is inline with the disclaimer made by Thomas [271].

Thus involvement of hypoxic damage cannot be ruled out. Failure to identify endothelial damage post-mortem at sites of thrombosis does not indicate that hypoxic endothelial damage cannot instigate thrombogenesis. Clearly, if a person suffers a DVT, there are many potential causes. Hypoxic endothelial damage is not the only contributor. If the coagulation factors are higher than normal and can accumulate in a region of stasis, thrombosis will occur. It is appreciated that thrombi may form on intact endothelia, but, there must be contributions from the other strands of Virchow's triad for thrombogenesis to

occur, such as change in blood flow (stasis) or change in blood chemistry (clotting factors).

One important factor that could explain the different conclusions of Malone and Morris [262] and Thomas [272] is that of the location of the endothelium being described. Malone and Morris [262] describe the 'parietalis' [267], which is the endothelium lining the valve on the pocket side, rather than the luminal aspect. The valve itself is avascular [274], whereas the endothelium of the vein can receive nutrients from the underlying tissue of the vessel wall. Indeed, the parietalis is the region most likely to be affected by hypoxia [260, 262]. Thomas [272] concentrates on the endothelium of the vessel wall.

In 1985, Thomas *et al.* [275] mechanically crushed jugular veins of rabbits in order to produce wall damage. Following the 30 seconds of crushing, blood flow was restored for either 5 or 60 minutes. Stasis experiments were also performed whereby, following the above procedure, the veins were distended with blood and tied at both ends for 20 minutes. The vessels were analysed using scanning electron microscopy (SEM) and transmission electron microscopy (TEM). Even though the entire vein had been clamped, only small regions of damage were observed. No endothelium remained on the damaged region. For the first cohort, with a reperfusion time of 5 minutes, the subendothelium was predominantly covered with platelets and some erythrocytes were present, but no fibrin was observed. Images show regions of exposed collagen, which depending on the experimental conditions could cause platelet activation and fibrin formation. However, even in the stasis experiments, there was no evidence of fibrin formation and the blood within the segments remained fluid.

"*The absence of fibrin, even after 1h of restored blood flow, indicates that a more extensive injury is needed to produce fibrin in a low velocity blood flow system, perhaps because insufficient platelets were recruited at any one site to form a 'critical mass' for fibrin formation.*"

It is not straightforward to compare the degree of damage in different experiments. The experiments performed by Hamer and Malone [269] lasted 6

hours with periods of stasis up to 1 hour. Fibrin was observed in these experiments. In contrast, as discussed previously, Malone and Morris [262] produced hypoxia for periods up to several hours, yet no fibrin mesh was seen. Thomas *et al.* [275] suggest that the flow conditions can prevent the build-up of procoagulants.

In 1989, Breddin [176] reviewed the state of research into DVT and actively criticised generic experimental models for their dissimilarities with the *in vivo* situation. One particular point of focus was the influence of flow and the importance of maintaining flow, as is the case *in vivo*, was emphasised. This favours experiments such as those by Hamer and Malone [269] where living dogs were used, stasis occurring naturally in the valve pockets by inactivity and disturbed by leg movement, as opposed to those by Thomas *et al.* [275] in which rabbit jugular veins were ligated at both ends, thus preventing the flow.

Lawson *et al.* [276] demonstrated experimentally that hypoxia leads to tissue factor expression, resulting in fibrin deposition. Yan *et al.* [277, 278] subsequently described this work in more detail. The conclusion is that this pathway has been suggested for this alternative route to thrombin production. However, this is not relevant at this stage since the result is that hypoxia will eventually cause platelet activation and thrombin generation. Whether this is due to exposure of collagen or expression of tissue factor is irrelevant.

7.2 Adapting and Applying the Framework

In order to create a model of deep vein thrombosis using the framework developed in Chapter 6, the hypothesis developed by Malone [260], which was later supported experimentally [262, 267-269] will be used. A summary of this model has recently been given [279]. Malone's work has been reviewed by other authors, with some agreement, and some disagreement and the key issues have been discussed above. It is significant that in the work by Hamer and Malone [269], veins with valves are used and flow is maintained. The dogs are treated such that the response in humans is simulated as opposed to preventing flow in a vein, to observe the effect of stasis, as in the experiments of Thomas *et al.* [272, 275].

To summarise the hypothesis given by Malone [260]; when the calf muscles in the leg are inactive, blood flow in the deep veins becomes sluggish and laminar. The veins contain a number of bi-leaflet valves which prevent backflow. These tend to remain fixed, in a semi-open position during periods of inactivity, as shown in figure 7.1, leading to areas of stasis behind the leaflets.

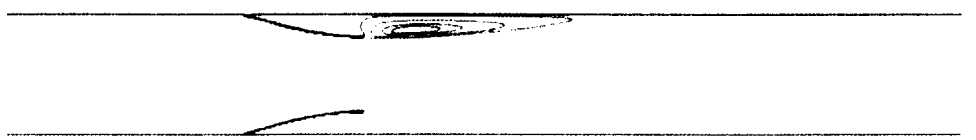

Figure 7.1: Representation of geometry of venous valves and recirculation zone at $\mathrm{Re} \approx 320$.

As oxygen is taken up and used by the tissues, there is a gradual deoxygenation of the blood in this region. Thus a prolonged period of stasis can damage the protective layer of the endothelium covering the valve leaflets and may lead to exposure of the underlying collagen. This process is not as severe for the endothelium on the vessel wall since it can obtain oxygen from the underlying tissues. When mobility is restored, oxygenated blood floods into the region behind the valve carrying healthy blood cells and platelets. On contact with the exposed collagen these will become activated and the coagulation cascade is initiated.

The model is therefore as follows:

- Initial uniform concentration of oxygen. This concentration is also used as an inlet boundary value.
- Oxygen is consumed by all endothelial cells on the valve leaflets and the walls.
- If the oxygen concentration drops below a threshold value on the valve leaflet, the corresponding lattice point will be defined as 'damaged', analogous to collagen exposure.
- The wall damage model created in Chapter 6 will be used hence platelets are activated by the exposed collagen and fibrinogen is converted into fibrin.
- Clotting occurs if a sufficient concentration of activated platelets and fibrin are present.

Regarding the geometry to be used, initially, a 2D simulation will be considered with an idealised valve configuration of sinusoidal form. Extensions to 3D are made using the geometry created in ANSYS in the course of another project[1].

7.2.1 Oxygen transport model

Oxygen is transported and consumed at the walls of the vessel and the valve according to the constant wall flux relationship proposed by Rappitsch and Perktold [280].

$$q_w = \alpha c_w \qquad \textbf{7.1}$$

c_w is the oxygen concentration at the wall and α is a constant, defined by the authors as $\alpha = 1.87 \times 10^{-3} cms^{-1}$. This is utilised in the model by formulating a first order reaction equation as shown in equation 7.2. The constant α must be divided through by the length scale of the lattice in use, in order to give an appropriate rate constant in units of s^{-1}. Equation 7.2 only applies to the lattice sites adjacent to the walls.

$$\frac{d[O_2]}{dt} = k_{O_2}[O_2] \qquad \textbf{7.2}$$

The initial and inlet concentration of oxygen is set to $1ML^{-3}$, since only relative values are required. The wall is a sink for oxygen and there is an implicit assumption that the distance to the wall from the nearest node is constant. The curved boundaries of the valve leaflets are not considered separately, and this will introduce some error.

Hamer and Malone [269] discovered that approximately 1 hour of stasis, followed by movement, caused a 7 fold increase in the incidence of thrombosis compared to a period of 20 minutes. Using the data presented by Hamer *et al.*

---

[1] This geometry was created by A.J. Narracott, University of Sheffield as part of a parallel DVT project.

[267], this would be likely to cause a drop to approximately 10% (of the luminal oxygen concentration) in the bottom of the valve pocket. For this reason, the threshold concentration required to cause collagen exposure was set to $0.1ML^{-3}$. When the concentration of oxygen falls below the threshold value of 0.1 on lattice nodes adjacent to the valve leaflets, the concentration of collagen was set to be non-zero. Collagen simply becomes exposed, not emitted and so this species was not permitted to convect or diffuse.

The depletion of oxygen was tested using the 2D stenosis model at a Reynolds number of 100, since the flow and diffusion characteristics have been previously investigated. Figure 7.2 shows the distribution of oxygen which was depleted following convergence of the flow field.

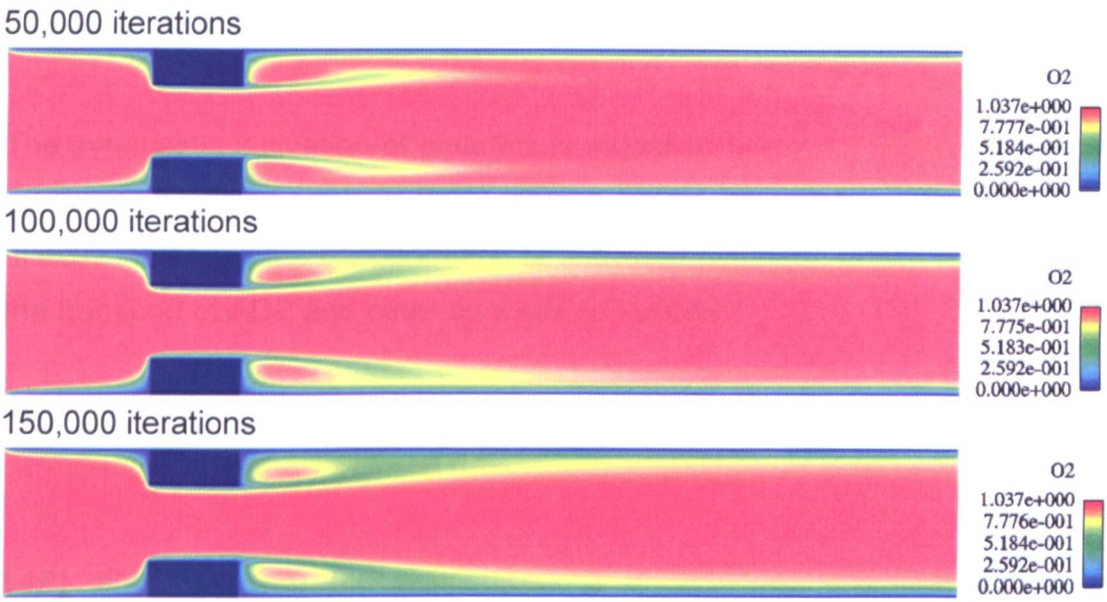

Figure 7.2: Distribution of oxygen in stenosis model following depletion at the wall in 2D Reynolds number 100 stenosis simulation.

Figure 7.2 shows that the oxygen concentration decreases near the wall, but is maintained in the centre of the vortex, where the only method of transport is diffusion. It is expected that this value will decrease further with time because of the finite amount of diffusion.

The next stage of the model assumes that the subject has moved, causing sufficient mixing to replace the deoxygenated blood with blood of a normal oxygen concentration.

7.2.2 Thrombosis model

The equation describing the activation of platelets in contact with collagen is adapted from the work of Wootton *et al.* [215] and shown below, as in Chapter 6.

$$\frac{d[AP]}{dt} = k_{coll}[RP] \qquad \textbf{7.3}$$

Wootton *et al.* [215] define the rate constant $k_t = 5 \times 10^{-3} cms^{-1}$, which must be divided through by the length scale in order to satisfy equation 7.3. If collagen is present at a certain lattice point, the concentration of activated platelets is increased according to equation 7.3 and the concentration of normal platelets is reduced by the same amount.

The synergistic activation of platelets is modelled using the equation published by Kuharsky and Fogelson [203], shown below, as used in Chapter 6. This directly increases the concentration of activated platelets, rather than modelling the transport of ADP and other agonists separately.

$$\frac{d[AP]}{dt} = k_{AP}^{AP}[AP][RP] \qquad \textbf{7.4}$$

$[AP]$ and $[RP]$ are the concentrations of activated and resting (normal) platelets respectively. The rate constant, k_{AP}^{AP} is given as $3 \times 10^{8} M^{-1} s^{-1}$. Here M represents the molar concentration, which is defined as the number of moles per litre of platelets. A mole of platelets has a mass of $1.28 \times 10^{12} g$, estimated from data in the literature [224, 244] hence the rate constant is $2.3438 \times 10^{-4} m^{3} kg^{-1} s^{-1}$, which can easily be converted into lattice units as described in Chapter 2.

Collagen also initiates the coagulation cascade. The first event is the conversion of factor XII into its active form, XIIa. A source term, with arbitrary concentration, of factor XIIa is released from the lattice points where collagen

has been exposed. The reactions in the cascade propagate and the final enzyme produced is thrombin. Instead of modelling all the reactions of the cascade, a simple first order reaction equation is used, which converts factor XIIa into thrombin with a rate constant of the order of that for the slowest reaction in the cascade [229]. The resulting equation is shown below.

$$\frac{d[IIa]}{dt} = k_{xiia}[XIIa] \qquad \textbf{7.5}$$

The rate constant, k_{xiia} used is $1\times10^{-5}\,\mathrm{min}^{-1}$ and $[IIa]$ and $[XIIa]$ represent the concentrations of thrombin and factor XIIa respectively. The initial and inlet conditions for these two species are concentrations of zero.

The equation representing the activation of platelets by thrombin is taken from the work of Kuharsky and Fogelson [203], later used by Anand *et al.* [122].

$$\frac{d[AP]}{dt} = k_{AP}^{IIa}[RP] \qquad \textbf{7.6}$$

The rate constant, k_{AP}^{IIa} used by both groups is $0.5s^{-1}$.

The equation used for modelling the conversion of fibrinogen into fibrin was taken from the work of Zarnitsina *et al.* [229] and is shown below.

$$\frac{d[Ia]}{dt} = k_1[IIa] \qquad \textbf{7.7}$$

$[Ia]$ and $[IIa]$ represent the concentrations of fibrin and thrombin respectively and the rate constant, $k_1 = 0.047s^{-1}$.

In this model, thrombus is defined as an agglomerate of activated platelets and fibrin. Clotting is permitted if the concentrations of these species are above threshold. Appropriate data could not be found for these values and so arbitrary values are chosen based on the concentration distributions obtained in the simulation.

7.3 2D Results

The results to be presented are preliminary, simply demonstrating the functionality of the model. At this stage, no attempt has been made to compare these to experiments from the literature.

The valve leaflets in the simulation form an approximate maximal 35% occlusion, based on the work of Lurie *et al.* [281]. The average Reynolds number is approximately 320, calculated using the average velocity in, and diameter of the human common femoral vein. The geometric parameters are taken from data published by Ashby *et al.* [282]. Discretisation was performed with 82 lattice points across the width of the parent vessel and 640 point were used along the simulation length. The length and timescales are $L = 9.625 \times 10^{-5} m$ and $T = 1.200 \times 10^{-5} s$ respectively. The converged flow field was obtained by performing 1×10^5 iterations without the clotting model. The limiting diffusion coefficient is $5 \times 10^{-5} L^2 T^{-1} = 3.861 \times 10^{-8} m^2 s^{-1}$, which is used for all species. The appropriate diffusion coefficient to use for the transport of oxygen is $D = 1.6 \times 10^{-9} m^2 s^{-1}$ [280]. A further 14×10^6 iterations were then performed with the first stage of the model. In real time, this is equivalent to approximately 170s and takes almost 20 hours of CPU time on the SX-8 vector machine. This removes oxygen from the walls, as described previously, and exposes collagen if the oxygen concentration falls below a value of 0.1. Figure 7.3 shows the distribution of oxygen after 14×10^6 iterations and figure 7.4 shows the region of collagen exposure.

Figure 7.3: Oxygen distribution following 14×10^6 iterations.

A further 14×10^6 iterations were then performed for the second stage of the model. The oxygen and collagen routines were not activated in this stage because it is assumed that the subject has moved their lower limbs sufficiently to reintroduce oxygenated blood into the valve pocket. This assumption is

crucial for clotting to start. The second stage of the model causes the activation of platelets and factor XII, causing a source of factor XIIa, ultimately resulting in the generation of fibrin as previously described. Figure 7.5 shows the distribution of activated platelets and figure 7.6 shows the distribution of fibrin after the second stage of the model.

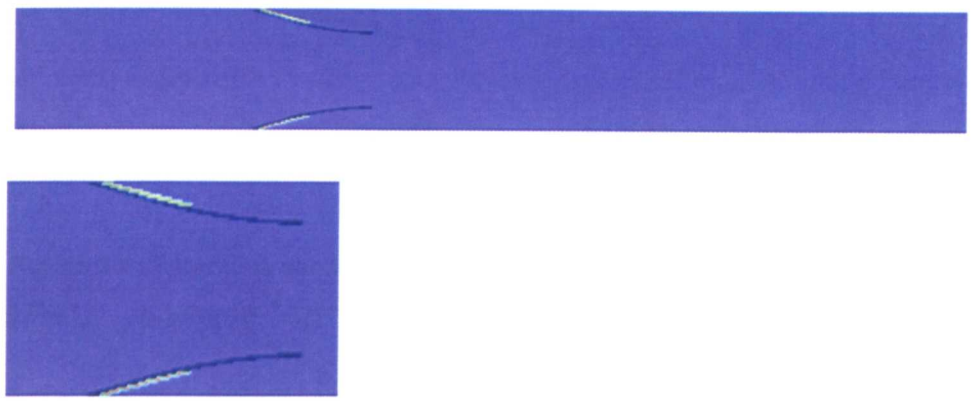

Figure 7.4: Valve with collagen exposed (pale region) after 14×10^6 iterations. Collagen is exposed on approximately half of the length of each valve leaflet. Lower image shows enlargement of valve region.

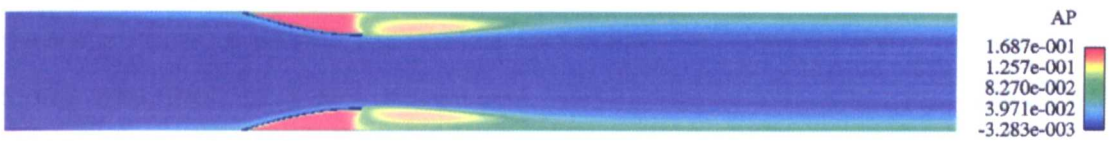

Figure 7.5: Distribution of activated platelets after 14×10^6 iterations in second stage of model.

Figure 7.6: Distribution of fibrin after 14×10^6 iterations in second stage of model.

Clotting was permitted if the concentrations of activated platelets and fibrin were above threshold. Two sets of values were used to demonstrate the onset and development of clotting; $[AP]_{thresh} = 0.1632ML^{-3}$, $[Fib]_{thresh} = 3.0 \times 10^{-4} ML^{-3}$ and $[AP]_{thresh} = 0.1642ML^{-3}$, $[Fib]_{thresh} = 1.7 \times 10^{-3} ML^{-3}$. The resulting clots are shown in figures 7.7 and 7.8 respectively.

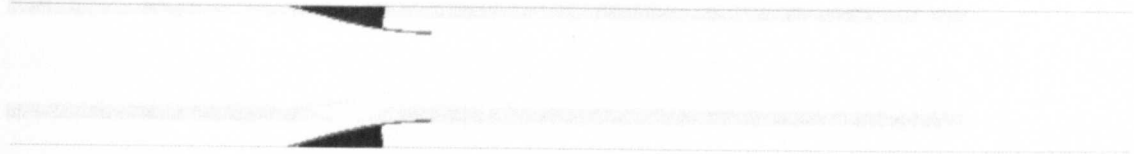

Figure 7.7: Thrombus deposition after 14×10^6 iterations with $[AP]_{thresh} = 0.1632 ML^{-3}$ and $[Fib]_{thresh} = 3.0 \times 10^{-4} ML^{-3}$.

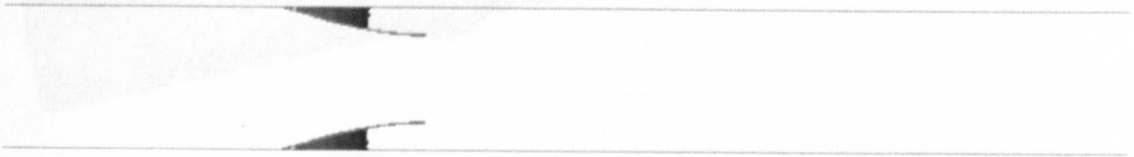

Figure 7.8: Thrombus deposition after 14×10^6 iterations with $[AP]_{thresh} = 0.1642 ML^{-3}$ and $[Fib]_{thresh} = 1.7 \times 10^{-3} ML^{-3}$.

7.4 3D Results

The geometry for the 3D simulations was originally created in ANSYS and then discretised into a voxel mesh[1]. The dimensions of the grid were $723 \times 91 \times 91$. A sinus was then included to provide further agreement with the physiological geometry [274]. The sinus was axisymmetric, of peak height 10 lattice points beyond the wall and with a length equal to that of the valve leaflet and the peak area occlusion created by the valves was 35% as in the 2D simulations. Figure 7.9 shows different views of the 3D geometry.

The Reynolds number was again 320 and this was obtained using a relaxation coefficient of $\omega = 1.97$ and an average velocity of $u_{av} = 1.1844 \times 10^{-2} LT^{-1}$. The grid had a parent luminal diameter of 69 lattice points, which represents 7.7mm [282]. The average real velocity measured in the common femoral vein is $27.6 cms^{-1}$ hence the length and timescales are $L = 1.1159 \times 10^{-4} m$ and $T = 9.5780 \times 10^{-6} s$.

The converged flow field was obtained after 1×10^6 iterations and the resulting distribution of velocity can be seen in figure 7.10.

[1] This task was performed by A.J. Narracott, University of Sheffield.

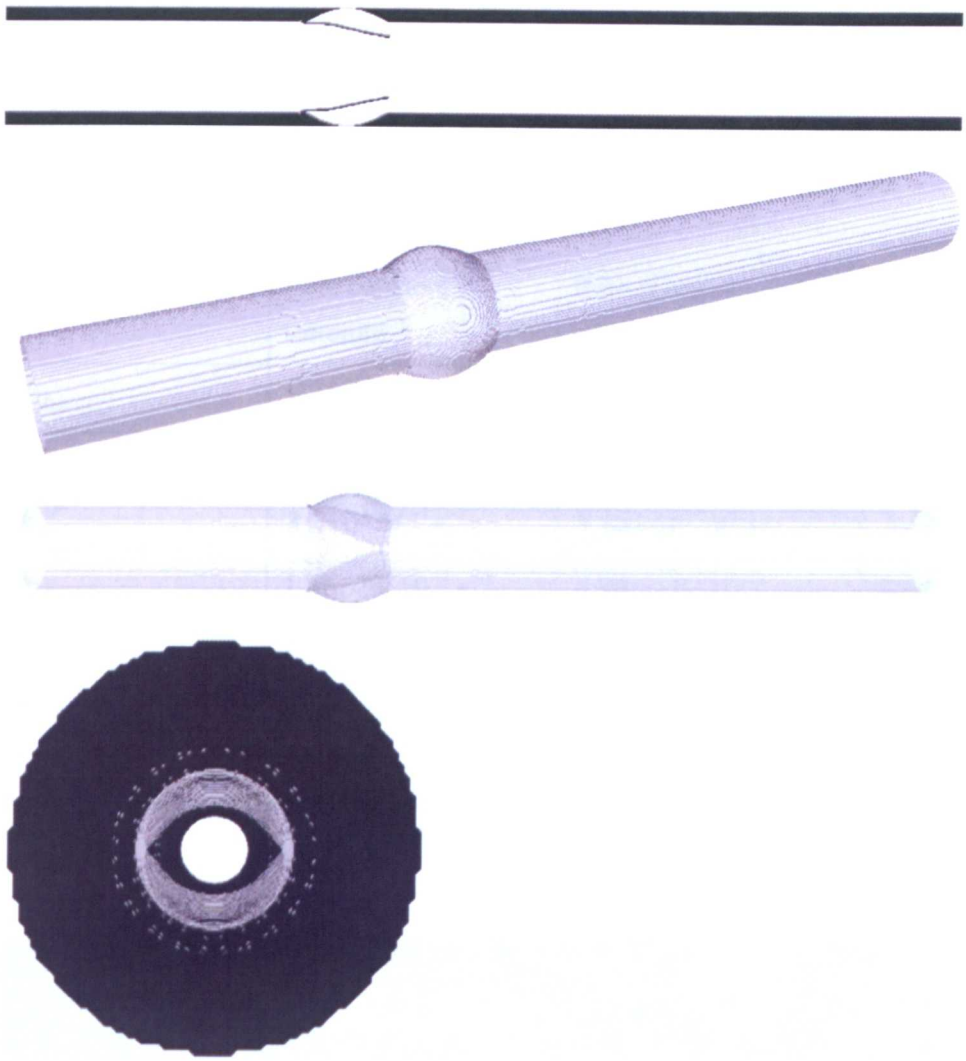

Figure 7.9: Geometry of 3D valve with sinus. Top to bottom: central cross sectional slice through geometry, isosurface, isosurface showing valves, perpendicular view down lumen showing reduction created by valves.

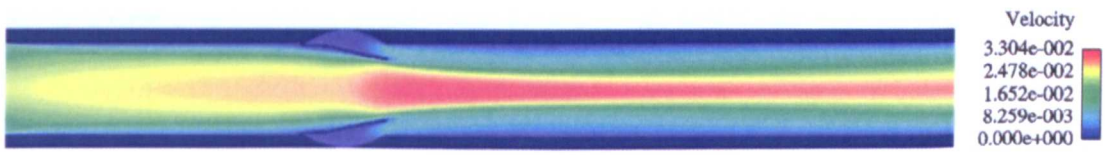

Figure 7.10: Distribution of velocity in central slice of geometry for 3D valve configuration.

The limiting diffusion coefficient is $5\times10^{-4}\,L^2T^{-1}$ which is equivalent to a real value of $D=6.5\times10^{-7}\,m^2s^{-1}$. The appropriate diffusion coefficient to use for the transport of oxygen is $D=1.6\times10^{-9}\,m^2s^{-1}$ [280]. Given the performance of the code (approximately $22MLUPS$), it would take approximately 3.5 years on the SX-8 to simulate the real time of 1 hour required for the initial stage of oxygen depletion and collagen exposure [269]. For this reason the rate constant of oxygen depletion was altered from that given previously. Due to the increased diffusion present and computational restrictions, in order to observe results in a

reasonable computational time, the rate constants for the cascade reactions had to be altered from those described previously. However, their ratios were maintained. The values used are shown in table 7.1 and values have been divided through for this specific length scale where appropriate.

	Rate constant in literature	Rate constant used in LB units	Equivalent rate constant in real units
k_{O_2}	$0.1676s^{-1}$	$4\times10^{-5}T^{-1}$	$4.18s^{-1}$
k_{coll}	$0.4481s^{-1}$	$1.07\times10^{-4}T^{-1}$	$11.17s^{-1}$
k_{AP}^{AP}	$3\times10^{8}M^{-1}s^{-1}$	$3.12\times10^{-6}L^{3}M^{-1}T^{-1}$	$7.47\times10^{9}M^{-1}s^{-1}$
k_{xiia}	$1.6667\times10^{-7}s^{-1}$	$3.98\times10^{-11}T^{-1}$	$4.16\times10^{-6}s^{-1}$
k_{AP}^{IIa}	$0.5s^{-1}$	$1.19\times10^{-4}T^{-1}$	$12.42s^{-1}$
k_1	$0.047s^{-1}$	$1.12\times10^{-5}T^{-1}$	$1.17s^{-1}$

Table 7.1: Rate constants taken from literature shown alongside those used in the 3D simulation.

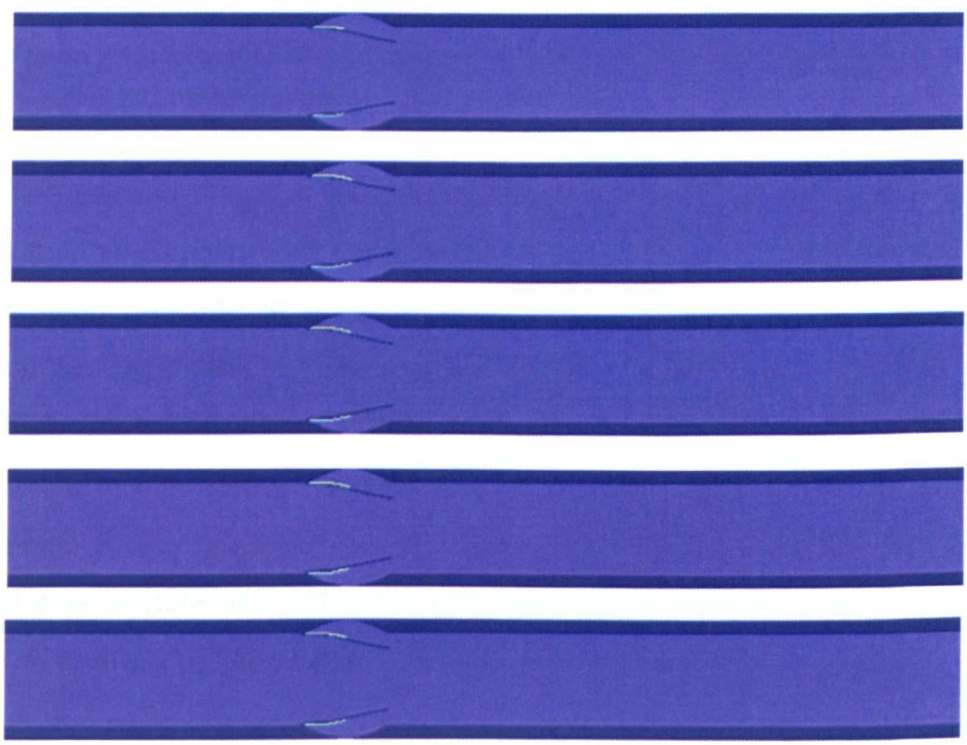

Figure 7.11: Central slice of 3D model showing regions of collagen deposition on valve leaflets after successive periods of 2×10^{5} iterations.

Based on the results of the oxygen depletion simulations, it was necessary to increase the oxygen threshold concentration to 40% of its original value. The

first stage of the model was simulated, thus collagen was exposed if the oxygen concentration fell below this threshold value. Figures 7.11 and 7.12 show the regions of collagen deposition after intervals of 2×10^5 iterations.

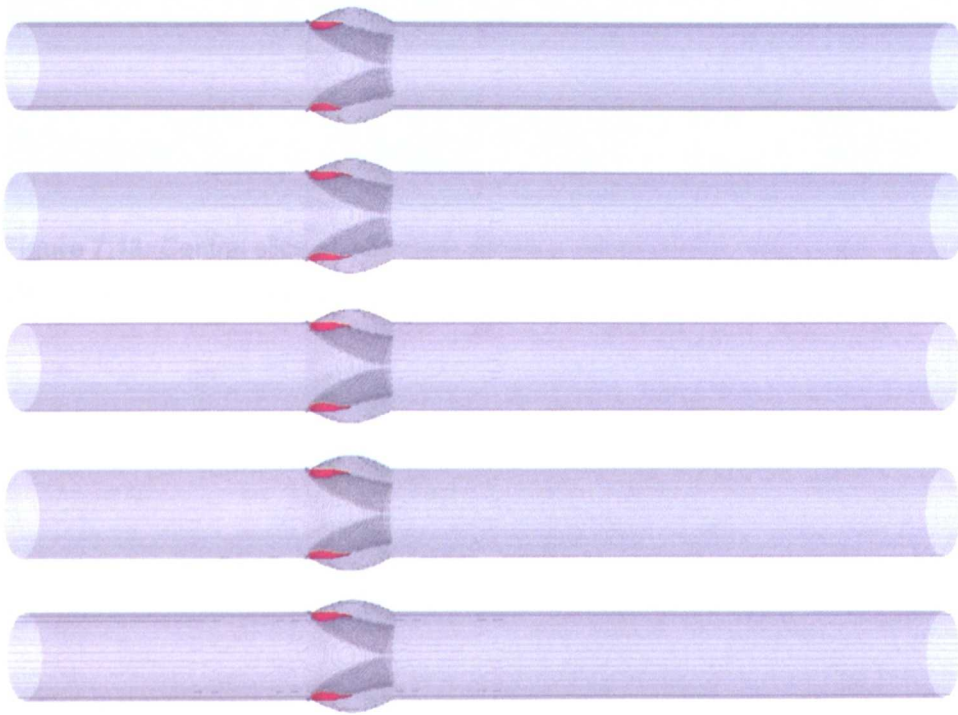

Figure 7.12: Isosurface of geometry showing regions of collagen deposition on valve leaflets in red after successive periods of 2×10^5 iterations.

The second stage of the model involved simulating a further 1×10^6 iterations with the oxygen and collagen routines inactive. The collagen activates the clotting cascade in order to produce a source of factor $XIIa$ and activates contacting platelets. The concentration distributions of activated platelets and fibrin produced were used in order to choose the appropriate thresholds to be used for the clotting. Values of $[AP]_{thresh} = 0.17ML^{-3}$ and $[Fib]_{thresh} = 5\times10^{-5}\,ML^{-3}$ units were chosen and the clots produced can be seen in figures 7.13 and 7.14. It was established that there was no change in the number of clotted nodes in the final 2×10^5 iterations.

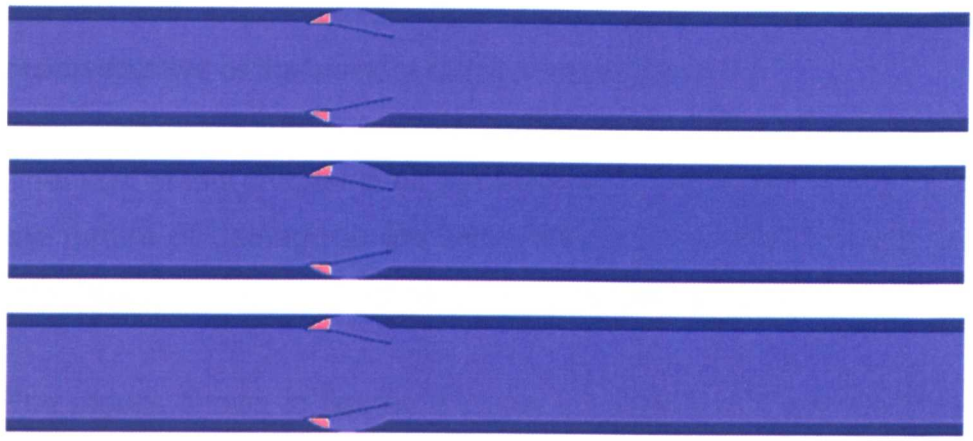

Figure 7.13: Central slice of 3D model showing clot deposited behind the valve leaflets. Top to bottom shows results following 6×10^5, 8×10^5 and 1×10^6 iterations.

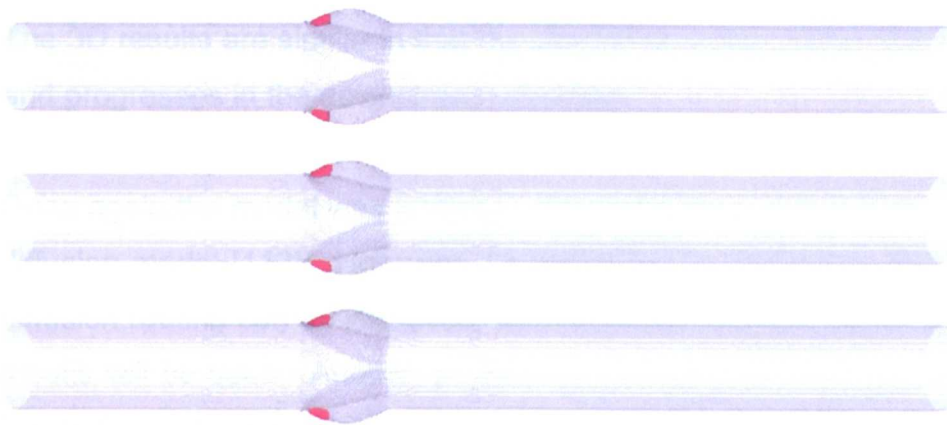

Figure 7.14: Clot deposition behind valve leaflets in 3D DVT model following periods of 6×10^5, 8×10^5 and 1×10^6 iterations.

7.5 Discussion

The aim of this chapter was to demonstrate a clinical application of the lattice Boltzmann framework for thrombosis simulation. The literature was reviewed in order to obtain an understanding of deep vein thrombosis and a supported hypothesis developed by Malone [260] was used. This required an extension to the framework to simulate oxygen depletion from both the walls of the vessel and the valves. The basis of this model is that hypoxia leads to endothelial damage of the valve leaflets, since they are avascular and hence depend on the blood for their oxygen. A further extension on the work presented in Chapter 6 was performed to account for the delay in the production of thrombin from a damaged endothelial surface. This was accounted for by considering a further species representing factor XIIa (first active factor of the cascade), which

transformed into thrombin (last active factor of the cascade) at a rate representative of the slowest reaction in the cascade.

The work of this chapter is an advancement of that described in Chapter 6 since the nature of damage to the endothelium is modelled as well as subsequent processes involved in coagulation and platelet aggregation.

The results shown in figures 7.7 and 7.8 appear to be very similar. However, the rate of growth was very different, the first being considerably quicker due to the lower thresholds required for thrombosis.

The 3D results are similar in that the clot forms in the corner of the valve pocket and progresses in the downstream direction.

Once again the model was limited by the instabilities of the Flekkoy convection-diffusion model [113]. However, as concluded in Chapter 6, if the convection-diffusion routine can be improved, an immediate increase in the accuracy of the results will be seen. Another problem is met when performing 3D simulations. Calculations showed that it would take approximately 3.5 years to simulate the initial 1 hour required for oxygen depletion. However, subsequent work by Malone, presented on the Traveller's Thrombosis website [283] speaks of periods of 2 hours for the time required for "*the first layer of venous valve pockets (attached to valve cusps) to die and thus to initiate a thrombotic sequence.*" The clot may then build up over a period of 9-24 hours. The cyclic behaviour involving periods of hypoxia followed by periods of re-perfusion [279, 283] required to form a single layer of clot has not been modelled, instead, just one cycle is considered in order to grow the associated clot. Clearly such a simulation time is out of reach for an explicit solver with a timestep of the order of microseconds. It is likely that the performance of the code could be improved if more time was available, but this is not expected to reduce the simulation time below the order of years. Chapter 5 described the difficulties met in trying to perform a simulation of the experimental milk clotting time of 600s.

The discussion section of Chapter 6 also applies to this section, particularly the number of biological processes that are not considered. The remaining parts of

the coagulation cascade would also need to be considered, along with inhibitors of the cascade which act to prevent the formation of thrombin.

Validation is also required before further developments can be made. However, there is little point in validating a model where many problems exist. This would remain a task for future work if the issues relating to diffusion and simulation time can be resolved.

Chapter Eight: Discussion and Conclusions

This thesis describes the development, implementation and validation of a number of clotting models, of varying degrees of complexity in, or coupled with, a Lattice Boltzmann flow solver. Experimental data on milk clotting is used as an initial validation set for a system in which the (bio)chemical processes are simpler. More complex models are developed to represent blood clotting (thrombosis), validated against experiments reported in the literature, and exercised to demonstrate the potential for simulation of clinically-important clotting phenomena including in the context of a simple model of deep vein thrombosis. The constraints of an explicit scheme such as that represented by the lattice Boltzmann approach are such that a number of compromises have to be made to enable the representation of relatively long time series events (order several minutes and upwards) in the vasculature. These constraints are defined, developed and explored in this thesis, and the final solutions presented are the best that can be obtained under them. Further improvements might be made by incremental developments of the core solver, but the greatest potential for overcoming the constraints must lie in the development of appropriate multi-scale and scale separation models.

It has been shown to be relatively simple, in a lattice Boltzmann solver, to define local rules for the creation and consumption of chemical species and threshold-induced clotting. The geometry can be changed during the simulation in order to feedback the effect of the growing clot on the flow field, which might promote or prevent further clot growth.

This thesis presents a critical appraisal of the LB technique and an account of the constraints on the implementation and application of a series of clotting models. These are summarised briefly below.

8.1 Flow Simulation

The results of simulations of the flow field through an idealised stenotic occlusion are presented in Chapter 3. A full grid convergence study was performed at a Reynolds number of 100, with the conclusion that the grid to be used occupied close to maximal memory on the SX-6 machine. Excellent

agreement was seen between the positions of reattachment in the numerical and experimental results provided by Smith [22]. Results were compared to simulations performed with the conventional Navier-Stokes solver CFX, also by Smith. The mean reported recirculation lengths for the CFX and LB solutions were 27.3mm and 29.0mm respectively. The experimental range recorded for this measurement was 25-30mm. Both simulations fall within this range.

A grid convergence study was not performed for the higher Reynolds number of 550, but the mesh used was the densest that could be supported within memory constraints. Qualitative agreement was seen between the experimental and numerical results in terms of the flow field. It is interesting to note that Smith [22], despite making numerous attempts to perturb the starting condition, the flow profile and the geometry, could produce only steady flow results in simulations at a Reynolds number of 550 using CFX, in contrast to the disturbed flow observed experimentally. Following further study by the CFX developers (Ian Jones, ANSYS-CFX, private communication) it is now believed that the steady flow solution might be theoretically correct at Re 550, but that the flow is in a critical regime and very sensitive to small fluctuations that would have been inevitable in the experimental set-up. This is perhaps indicated also by the measures that had to be taken (described in Chapter 3) to provoke the disturbed flow in the lattice Boltzmann solutions. Nevertheless, the qualitatively acceptable comparisons between measured and computed flow reported in Chapter 3 provide a good basis for the exercise of the clotting models. For a more comprehensive comparison of the results between the LB simulation and the experiments at this Reynolds number, an analysis of average parameters using turbulence modelling is required. The techniques and equipment available in the work by Smith [22] did not allow for such investigations: furthermore this is not the primary focus of this thesis, and is regarded as beyond the scope of the current work.

8.2 Milk Clotting Model

Chapter 5 describes the milk clotting model used in this project, which is based on a residence-time approach. Advances were made to incorporate a proximity

condition and a threshold shear stress rule. In reality, the viscosity of the milk would change with time, but no experimental data for this relationship was available. As discussed in this chapter, the strength of a milk clot is dependent upon a number of factors such as temperature, pH, age and enzyme concentration. The use of a single threshold value may be considered too simplistic, but due to the absence of further experimental data, such an extension could not be made. The experimental duration was 600s which represents an enormous challenge to an explicit solver like the lattice Boltzmann method. This is further exacerbated by the need for a fine grid in order to capture the detailed flow field. The full simulation of the experiment using the finest grid is estimated to need over 4 months of CPU time on the SX-8, providing a Mach number of 0.3 is used. Compromises were made in order for the simulation time to be completed in 1 week on the SX-6. Smith [22] could not obtain repeatable results for a shorter experimental duration and so no experimental data was available for shorter experimental times. Another major issue was that of diffusion. Chapter 4 outlined the limits on the diffusion models used and the more specific results presented in Chapter 5 show that, with the coarse grid, the maximum age in the model is limited to 3s due the presence of excessive diffusion. This situation is improved when the finest grid is used and the appropriate value can be set. Nevertheless, despite the necessary compromises, using the coarse grid and the shear stress condition, qualitative agreement with experiment was obtained. The striking feature of the experiments was a region where no clot was formed. This was seen in the numerical results and the size of this void was found to be dependent upon the threshold shear stress value used. The characteristic features of the clot deposition in the experiments can be reproduced numerically, by tuning of the shear stress threshold parameter, but since there is no data to confirm that the numerical value chosen has real physical significance, the association between experimental and numerical models is open to criticism. Nevertheless, the goal of gaining an understanding of underlying issues which can be to be used to inform the development of more detailed blood clotting models has certainly been achieved.

8.3 Lattice Boltzmann Framework for Thrombosis

Chapter 6 provides a detailed account of current understanding gained during this project of the underlying mechanisms leading to thrombosis. Platelet activation can be simulated by prolonged exposure to high shear stresses using the current framework. Activation of the clotting factors as well as platelets can be obtained by defining a region of exposed collagen, representing an area of damage, at the wall. All representations of clotting factors and platelets follow previous work in the literature and the most efficient equations have been used in order to reduce the complexity of the model. Due to its obvious complexity, no attempt has been made to model the coagulation cascade in its entirety, and in the first instance, the cascade is represented by a source of thrombin at a damaged wall, thus representing only the final reaction in the cascade. In later work, the first active element of the cascade is emitted. This is then converted into thrombin with a rate of reaction equivalent to the slowest reaction in the cascade. This allows the active factors to be transported away from the area of damage before thrombin is produced. This model was demonstrated in Chapter 7 considering the example of deep vein thrombosis, which was based on the theory of hypoxic endothelial damage of the valve leaflets, as described by Malone [260]. The decrease in oxygen causes damage to the vessel wall, resulting in the exposure of subendothelial collagen which causes the activation of platelets and factors in the clotting cascade. The framework can be applied to any pathological condition relating to thrombosis providing there is a sound hypothesis of the biological processes involved. The causes of platelet and clotting factor activation should be well defined.

An important consideration in the development of numerical models is validation. However, there are a number of problems with the existing models that must be addressed before a full programme of validation can be undertaken. The most important issue once again, relates to diffusion. The limiting diffusion coefficient that can be obtained with current methods is still several orders of magnitude greater than the values reported for the elements of blood. This does not affect the development of the models but limits the applicability of the results. It is believed that if a more appropriate diffusion model is incorporated, the accuracy of the results will directly increase.

Simulations can then be performed with validation against either existing literature or future experiments. The issue remains however, that due to the explicit time stepping method of the lattice Boltzmann scheme, it is extremely difficult to obtain simulations of lengthy experiments with a sufficiently accurate grid in three dimensions.

8.4 Future Work

It is clear that many simplifications have been made in the models developed in this project which must be addressed in the future.

First, the flow is steady. This was appropriate for the milk clotting work since the experiments undertaken by Smith [22] were conducted using steady flow in order to study the relationship between fixed, predictable recirculation zones and the resulting clot deposition. In the case of the DVT simulations, it is also appropriate to use steady flow, since sufficient damping of the pulsatile waveform has occurred by the time the blood reaches the venous circulation and, in the simulation, the subject is immobile, with the valve leaflets remaining in a fixed position. In the case of arterial flow, this is not the case. Should arterial flow be modelled in future, inclusion of time-dependent boundary conditions is essential. Pulsatility will affect features such as the recirculation zones and, by inference, clot deposition: Cao and Rittgers [251] demonstrate that, in pulsatile conditions, >99% of particles are washed out of recirculation zones formed downstream of a 75% or 95% stenosis within 10s and in consequence do not remain for the minimum time required for platelet adhesion. The streamlines in vortices are often not closed, thus particles can enter, remain for one or two orbits and then leave to rejoin the mainstream [94].

Flow throughout this study was assumed to be Newtonian; a common assumption for large vessels with high shear rates [15, 16]. However, in recirculation regions, the flow could have a sufficiently low shear rate to require non-Newtonian effects to be considered. A non-Newtonian option should be available.

The elasticity of vessel walls might also need consideration in order to improve the accuracy of the blood clotting models. Vessel compliance will affect the velocity distribution and hence the resulting shear stress field. However, Goldsmith and Turitto [94] have shown that appreciable levels of radial dilation are only found in the aorta and pulmonary arteries. Another issue is that, when stenoses are considered, the flow is disturbed more by the presence of the restriction than by the time-dependent movement of the vessel wall [102]. The elasticity is also considered to be of secondary importance when geometry is obtained from patient data due to the inaccuracy of locating the vessel wall [90].

Slack and Turitto [284] provide a guide to many common assumptions used in modelling blood flow. These are in agreement with the conclusions drawn above.

Future work should first concentrate on addressing the problem present in all the models, the diffusion routine. A number of alternative routines were considered in this project, but were not found to be advantageous for the current work. Stabilising schemes are required to remove the instabilities associated with large Peclet numbers. Examples of these are the fluctuation splitting scheme used by Sorensen *et al.* [236] or the streamline upwind/Petrov-Galerkin stabilising technique used by Rappitsch and Perktold [280]. Such methods apparently allow for the use of the lower diffusion coefficients required for the blood elements. Further work should initially concentrate on understanding and implementing such improved diffusion models. Introducing a shear dependent diffusivity would increase the required diffusion coefficient by several orders of magnitude due to the presence of red blood cells [231, 253], hence the limit will not be as severe.

The models can be extended to incorporate more detail of the coagulation cascade, particularly the action of inhibitors, which will limit the resulting clot growth. The shear stress condition used in the milk clotting work can also be implemented for these models in an attempt to capture the process of embolism.

Once this important step is introduced, validation may be feasible if experimental data can be obtained for short experiment times. Validation must not only consider the location and size of thrombotic deposition, but also the clot structure as defined by the relative distributions of platelets and fibrin.

It is clear from the simulations presented in this project, particularly those of the milk clotting experiment reported in Chapter 5, that it is difficult to explicitly simulate lengthy experiments with a sufficiently large grid. It is assumed that the flow field will be changing on a much faster timescale than that in which the clot grows. In the blood clotting models, a difference in the diffusive and reactive timescales will also be present, depending upon the diffusion coefficients and the reaction rates. For this reason, multi-scale techniques should be investigated. The options include adopting a scheme such as that of Alemani *et al.* [285] which specifically defines a time-splitting approach for the lattice Boltzmann BGK method, or attempting to model the clotting processes using a multiscale framework such as that under development in the European project 'COAST' [6].

In conclusion, issues associated with thrombosis modelling, and in particular the application of the lattice Boltzmann method in this context, have been described. The results of this project are limited by a number of effects but, once these are appropriately addressed, and validation has been performed, the models developed can be used to predict the location and form of clot deposition in any pathological environment.

Chapter Nine: Appendix

9.1 Obtaining Principle Shear Stresses via Solution of Cubic Equation

Calculation of the principle stresses requires solution of the following cubic equation:

$$S^3 - (\sigma_x + \sigma_y + \sigma_z)S^2 + (\sigma_x\sigma_y + \sigma_y\sigma_z + \sigma_x\sigma_z - \tau_{yz}^2 - \tau_{xz}^2 - \tau_{xy}^2)S - (\sigma_x\sigma_y\sigma_z + 2\tau_{yz}\tau_{xz}\tau_{xy} - \sigma_x\tau_{yz}^2 - \sigma_y\tau_{xz}^2 - \sigma_z\tau_{xy}^2) = 0 \qquad \textbf{9.1}$$

where the three *S* solutions are the principal stresses.

To solve this equation and obtain the three principal stresses, the methods proposed by Eric Weisstein [166] have been used.

The solutions of the general cubic equation $z^3 + a_2z^2 + a_1z + a_0 = 0$ are given by:

$$z_1 = -\frac{1}{3}a_2 + (S+T)$$

$$z_2 = -\frac{1}{3}a_2 - \frac{1}{2}(S+T) + \frac{1}{2}i\sqrt{3}(S-T) \qquad \textbf{9.2}$$

$$z_3 = -\frac{1}{3}a_2 - \frac{1}{2}(S+T) - \frac{1}{2}i\sqrt{3}(S-T)$$

where *S* and *T* are given by:

$$S = \sqrt[3]{R+\sqrt{D}}\,; \qquad T = \sqrt[3]{R-\sqrt{D}} \qquad \textbf{9.3}$$

and *R* and *D* are given by:

$$R = \frac{9a_2a_1 - 27a_0 - 2a_2^3}{54}; \qquad Q = \frac{3a_1 - a_2^2}{9}; \qquad D = Q^3 + R^2 \qquad \textbf{9.4}$$

The calculations presented provide a general solution to the cubic equation given in 9.1. However, performing this procedure every iteration is computationally expensive because of the relations presented in 9.3. *D* is negative if the solutions are real and unequal but it is not possible in Fortran to

raise a complex number to a non-integer power. For this reason, the values $R+\sqrt{D}$ and $R-\sqrt{D}$ must be converted into the trigonometric notation for representing complex numbers by calculating the argument and magnitude of each complex value. De Moivre's theorem can then be used to calculate the values of *S* and *T*, which requires additional consideration of the complex numbers and their positions within an argand diagram.

To simplify the approach, a solution can be found if all the roots are assumed to be real. The roots of 9.1 are defined as [166]:

$$z_1 = 2\sqrt{-Q}\cos\left(\frac{\theta}{3}\right) - \frac{a_2}{3}$$

$$z_2 = 2\sqrt{-Q}\cos\left(\frac{\theta+2\pi}{3}\right) - \frac{a_2}{3} \qquad \textbf{9.5}$$

$$z_2 = 2\sqrt{-Q}\cos\left(\frac{\theta+4\pi}{3}\right) - \frac{a_2}{3}$$

where $\theta = \cos^{-1}\left(\frac{R}{\sqrt{-Q^3}}\right)$ and *R* and *Q* as previously defined in **9.4**.

9.2 Publications

1. Harrison, S.E., Smith, S.M., Bernsdorf, J., Hose, D.R. and Lawford, P.V. (2007) Application and Validation of the Lattice Boltzmann Method for Modelling Flow-Related Clotting. Accepted for publication in Journal of Biomechanics.

2. Harrison, S.E., Bernsdorf, J., Hose, D.R. and Lawford, P.V. (2006) A Lattice Boltzmann Framework for Simulation of Thrombogenesis. Passed first review for Progress in Computational Fluid Dynamics.

3. Harrison, S.E., Bernsdorf, J., Hose, D.R. and Lawford, P.V. (2006) Development of a Lattice Boltzmann Framework for the Numerical Simulation of Thrombosis. Passed first review for International Journal of Modern Physics C.

4. Bernsdorf, J., Harrison, S.E., Smith, S.M., Lawford, P.V. and Hose, D.R., (2006) Numerical simulation of clotting processes: A lattice Boltzmann application in medical physics. Mathematics and Computers in Simulation, 72, (2-6), 89-92.

5. Bernsdorf, J., Harrison, S.E., Smith, S.M., Lawford, P.V. and Hose, D.R., (2006) Concurrent numerical simulation of flow and blood clotting using the lattice Boltzmann technique. International Journal of Bioinformatics Research and Applications, 2, (4), 371-380.

6. Bernsdorf, J., Harrison, S.E., Smith, S.M., Lawford, P.V. and Hose, D.R., (2006) Applying the lattice Boltzmann technique to biofluids: a novel approach to simulate blood coagulation. Accepted for publication in Computers and Mathematics with Applications.

Application and Validation of the Lattice Boltzmann Method for Modelling Flow-Related Clotting

S.E. Harrison[1], S.M. Smith[1], J. Bernsdorf[2], D.R. Hose[1], P.V. Lawford[1]

[1] Academic Unit of Medical Physics, University of Sheffield, UK.

[2] C&C Research Laboratories, NEC Europe Ltd., Germany.

Corresponding author:

S.E. Harrison,
University of Sheffield,
Department of Medical Physics & Clinical Engineering,
Royal Hallamshire Hospital,
I Floor,
Glossop Road,
Sheffield.
S10 2JF.
UK.
Email: s.harrison@sheffield.ac.uk
Telephone: +44 114 2712180
Fax: +44 114 2713403

Keywords: Milk clotting, lattice Boltzmann, stenosis.

Word count: 2890.
Revision 2, manuscript number: BM-D-06-00494.

This work is being submitted as an original article.

Abstract

The purpose of this paper is to present a simple clotting model, based on residence time and shear stress distribution, that can simulate the deposition over time of enzyme-activated milk in an *in vitro* system. Results for the model are compared with experiments exhibiting clot deposition in the region of a sharp-edged stenosis. The milk experiments have been shown to be a valuable analogue for the experimental representation of flow-induced blood clotting, particularly in the context of separation of hydrodynamic from biochemical factors. The facility to predict the flow-induced clotting of the blood analogue, in which the chemistry reduces to what is effectively a zero*th* order reaction, gives confidence in this physics-based approach to simulation of the final part of the coagulation cascade. This type of study is a necessary precursor to the development of a complex, multi-factorial, biochemical model of the process of thrombosis. In addition to the clotting simulations, comparisons are reported between the computed flow patterns prior to clot deposition and flow visualisation studies. Excellent agreement of hydrodynamic parameters are reported for a Reynolds number of 100, and qualitative agreement is seen for the complex, disturbed flow occurring at a physiologically relevant Reynolds number of 550. The explicit, time-stepping lattice Boltzmann approach may have particular merit for the transitional flow at this higher Reynolds number.

Introduction

Cardiovascular disease is responsible for an estimated 17 million deaths worldwide per year (WHO, 2006). Atherosclerosis is a disease leading to the formation of plaques, which may cause localised narrowing of the vessel, creating regions of stagnation and recirculation downstream of the obstruction, or even occlusion. Flow stasis is one of the elements of Virchow's triad of factors indicating propensity to thrombosis. Plaque rupture may result in emboli, possibly leading to myocardial infarction, pulmonary embolism or ischaemic stroke.

Following blood activation, the coagulation pathway is highly complex, involving a cascade of reactions. Attempts have been made to model the relevant molecular pathways (for a review see Anand et al., 2003), but these fail to consider realistic flow fields and their interaction with growing thrombi. Residence time models have been used to predict the location of thrombosis in physiologically representative geometries (Friedrich and Reininger, 1995; Narracott et al., 2005; Smith, 2005). These studies use the Navier-Stokes equations to predict the flow fields and implement a time varying viscosity model, as devised by Tippe and Müller-Mohnssen (1993).

The similarities between milk clotting and the final stages of blood coagulation were first noted in 1975 (Jollès, 1975). The final stage of the coagulation cascade involves thrombin-mediated enzymatic conversion of fibrinogen to insoluble fibrin monomers, which polymerise, forming a fibrin scaffold. Likewise, addition of the enzyme chymosin (rennet) to milk converts the substrate κ-casein into insoluble para-κ-casein which aggregates, forming a milk clot. The time delay between enzyme addition and the onset of clot formation is known as the clotting time (Dalgleish, 1982; Payens et al., 1977; Payens, 1977).

Experimental evaluation of enzymatically activated 'hypercoagulable' milk as a blood analogue was first reported in 1981 (Lewis and Macleod, 1981) and subsequently by others (Christy and Macleod, 1989; Keggen et al., 1996). The technique has proved a useful tool in the investigation of clot formation in the vicinity of prosthetic heart valves (Keggen et al., 1996; Martin and Christy, 2004). Advantages of the milk analogue are cost, availability, safety, simplicity and repeatability compared with blood experiments. It also has merit in the development and validation of computational clotting models because the chemistry is simpler and it is easier to identify and separate flow-related effects.

Experimental investigations in this study used hypercoagulable milk and a sharp-edged stenosis (75% by area) with an orifice of diameter 4mm and length 5mm in an 8mm diameter vessel. The diameter of the parent vessel is representative of the human femoral artery. Details of the experimental

apparatus are reported by Smith (2005), whose results are used to validate the computational models developed in this study. This provides an intermediary step in the development of a computational model of blood coagulation within physiologically relevant geometries.

This paper describes a computational model encompassing the aspects of flow simulation and fluid solidification, based on a residence time approach. This includes the fundamental influence of the changing geometry of a developing clot on the flow field, defining final clot morphology. Clot deposition is governed by shear stresses in the fluid.

The clotting models developed in this study use the lattice Boltzmann (LB) method, which can efficiently solve the flow field in complex and changing geometries. An extension of the passive-scalar diffusion model, to estimate residence time of a fluid, will also be described along with the clotting model. Flow fields and clot deposition simulations are compared to flow visualisation and experimental milk clots, respectively.

Methods

Lattice Boltzmann Method

The lattice Boltzmann method evolved from the lattice gas method, (Frisch et al., 1986; Wolfram, 1986), which is a simplified particle method (representing the dynamics of fluid particles on a lattice). The evolution of the lattice involves both a streaming and collision process at each discrete time step. The particles are propagated to the neighbouring lattice sites, dependent on their discrete velocities. The collision process changes the particle velocity whilst locally conserving both mass and momentum.

Disadvantages of this method were soon recognised; statistical noise, lack of Galilean invariance, high viscosity (therefore upper bound on Reynolds numbers) and an unphysical equation of state (Dahlburg et al., 1987; Benzi et al., 1992; Succi, 2001). Consequently, the lattice Boltzmann method emerged

(McNamara and Zanetti, 1988; Higuera et al., 1989; Higuera and Jiménez, 1989) which circumvents these issues if an appropriate collision operator is defined (Qian et al., 1992). Rather than tracking the motion of individual particles, this method examines the evolution of particle distributions as governed by the lattice Boltzmann equation (Eq. 1).

$$f_i(\vec{x} + \Delta t\vec{c}_i, t + \Delta t) = f_i(\vec{x}, t) + \Omega \qquad \mathbf{1}$$

f_i is the *distribution* of particles travelling with a discrete velocity $\vec{c}_i$ and Ω is the collision operator, where i represents the number of discrete velocities. In this paper, the collision operator is represented by a Bhatnagar Gross Krook (BGK) operator (Qian et al., 1992) as in equation 2.

$$\Omega_i = \omega(f_i^{eq}(\vec{x}, t) - f_i(\vec{x}, t)) \qquad \mathbf{2}$$

ω is the relaxation parameter and f_i^{eq} is the equilibrium distribution function which can be calculated from the macroscopic values of density, ρ and velocity, $\vec{u}$ as given in equation 3.

$$f_i^{eq}(\rho, \vec{u}) = t_p \rho\left(1 + \frac{\vec{c}_i \cdot \vec{u}}{c_s^2} + \frac{(\vec{c}_i \cdot \vec{u})^2}{2c_s^4} - \frac{\vec{u} \cdot \vec{u}}{2c_s^2}\right) \qquad \mathbf{3}$$

The speed of sound, c_s and the shear viscosity, ν are given by equations 4 and 5 respectively (Qian et al., 1992) and the distributions are weighted according to the lattice in use (represented by t_p, where p is the square modulus of the particle velocity).

$$c_s = \frac{1}{\sqrt{3}} \qquad \mathbf{4}$$

$$\nu = \frac{1}{6}\left(\frac{2}{\omega} - 1\right) \qquad \mathbf{5}$$

The evolution of the distributions is modelled using the lattice Boltzmann equation (Eq. 1), the BGK collision operator (Eq. 2) and the local macroscopic density and velocity values as given by equations 6 and 7.

$$\rho(\vec{x},t) = \sum_i f_i(\vec{x},t) \qquad \textbf{6}$$

$$\vec{u}(\vec{x},t) = \frac{\sum_i f_i(\vec{x},t)\vec{c}_i}{\rho(\vec{x},t)} \qquad \textbf{7}$$

The scheme is of second order accuracy (Qian et al., 1992).

The lattice Boltzmann equation has been shown to satisfy the incompressible Navier-Stokes equations under conditions of low Mach and Knudsen numbers. Further details of the lattice Boltzmann method and its relative merits can be found in the literature (Benzi et al., 1992; Chen and Doolen, 1998; Lallemand and Luo, 2000; Succi, 2001). Within this work, it is the preferred method since the growing clot can be simulated based on local rules and the effect of the clot on the flow field is therefore captured.

Wall Boundary Conditions

The LB method offers efficient and computationally cheap handling of regular Cartesian meshes. With an optimised implementation, tens of millions of grid points can be handled on a PC (Wellein et al., 2006). This allows use of the 'marker and cell' approach for geometry representation and sufficient accuracy (of the geometry and flow solution) can be obtained by marking lattice nodes as either occupied or free.

A 'bounce back' wall boundary condition is applied to the occupied lattice nodes. This reflects incoming density distributions, hence cancelling momentum creating a 'no-slip' wall boundary. Geometry remodelling during simulation is achieved by occupying free lattice nodes, or vice-versa, without the need for remeshing, unlike N-S based solvers.

The code utilised for this work is optimised for vector machines, such as the NEC SX series.

Flow in a Stenosed Vessel

The simulated geometry is an 8mm tube, with a 5mm long, 75% (by area) stenosis forming a square-edged occlusion, with its upstream face 2 diameters downstream of the inlet (see fig. 1). The boundary conditions for all simulations were a steady parabolic velocity profile at the inlet and constant pressure at the outlet. Residuals in the average velocity, originating from the transient calculation of the developing flow field from rest, were of order $1x10^{-3}$ relative to the mean value and the compressibility error was less than 1%.

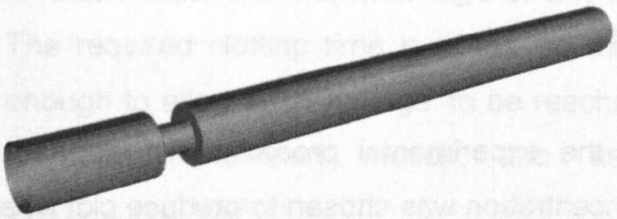

Figure 1: Idealised 75% stenosis geometry. Flow is directed from left to right.

Two Reynolds numbers were considered, based on the average velocity and diameter of the human femoral artery. The first, $\mathrm{Re} = 100$, lies in the laminar region and produces an axisymmetric toroidal vortex downstream of the stenosis. The second, $\mathrm{Re} = 550$, is physiologically similar to that in the femoral artery (Smith, 2005).

A grid convergence study was performed at $\mathrm{Re} = 100$, resulting in a grid size of $lx * ly * lz = 1214 * 98 * 98$, which was also used for the $\mathrm{Re} = 550$ flow simulations.

Experimental flow visualisation, reported later, indicated that the flow at $\mathrm{Re} = 550$ was significantly disturbed, with complex, time-dependent characteristics. This is challenging for the numerical flow solution, and the results are very sensitive to simulation parameters such as lattice velocity and viscosity. Flow instabilities similar to those observed experimentally were triggered by introducing random geometric irregularities of $\pm$1.5% on the radius

of the tube. Other methods of destabilising the flow were investigated, such as using asymmetric inlet velocity profiles, but the radius variation method was found to be most consistent in producing flow patterns similar to experimental observation. A sustained performance of almost 50 million lattice site updates per second (MLUPS), based on computations on the fluid nodes, was achieved for the flow solver on the SX8 machine.

For validation, an acrylic test section of identical geometry was constructed, with elongated inlet and outlet lengths. The flow was visualised by injecting dye immediately upstream of the stenosis. Dye became entrained in the near wall flow, demarcating the boundary between regions of recirculation and the central jet.

Milk Clotting Experiments

A detailed description of the experimental procedure is reported by Smith (2005). The enzymatic concentration was chosen to produce clot when the fluid reached an age (residence time) of 40.5s relative to that at the inlet to the computational domain. The total time of the experiment was 600s.

The Clotting Model

The simulation of flow and clotting at the physiological Reynolds number of 550 stretches current computational resource to the limit, despite the fact that the simulations were conducted using the highly optimised LB code on an SX8 vector supercomputer, which has a peak performance of 16 GFLOPS. The finest mesh analysed had a grid of $lx * ly * lz = 911 * 74 * 74$ and required 4 weeks of CPU time on the SX8. Results are compared between this grid and one of dimensions $lx * ly * lz = 456 * 38 * 38$.

Aging

Fluid residence time is a governing variable in the clotting model. All fluid within the domain is deemed clottable and detail of the enzymatic reaction between rennet and κ-casein is not considered. Fluid age is determined by adding a

constant concentration of a tracer species to every node in the model each timestep, hence the concentration of the species is proportional to the fluid age at that node. This differs from the experimental technique whereby rennet is injected upstream and normal untreated milk already in the system is replaced with clottable milk. However, the simulation technique is efficient, involving only one species. At $\mathrm{Re} = 550$ there is strong convective mixing, and the start-up condition is relatively insignificant.

The aging species is a passive scalar tracer, transported by convection and diffusion, using a first order upwind scheme for the convective term. The diffusion coefficient describes the rate of mixing between 'old' and 'young' fluid, and is an important parameter that must be chosen carefully. Excessive diffusion limits the maximum age of any fluid element in a recirculation zone. The required clotting time is 40.5s, so the diffusion coefficient should be low enough to allow such an 'age' to be reached. If the milk micelles are assumed to follow Brownian motion, the associated diffusion coefficient is $D = 1.14 \times 10^{-11} m^2 s^{-1}$.

Solidification

Any fluid nodes attaining the clotting time are transformed into solid nodes and no further mass transport is allowed. Within the LB model, a fluid node becomes an obstacle node and the solid surface boundary condition is applied. The flow field and age distribution adapt to the new geometry, whilst clotting on other fluid nodes may occur.

Two further constraints are implemented: for a fluid node to solidify, it must be, i) adjacent to a wall, the stenosis or a clot and ii) in a region where the shear stress is less than some predefined value. The first constraint prevents detached clots from growing in regions such as the centres of vortices, where they cannot adhere. If isolated clots developed in the *in vitro* experiment they would, in practice due to local velocity transients, be transported downstream and out of the system. The solidification model does not permit transport, but the proximity constraint prevents the formation of such clots. The shear stress constraint prevents the formation of clots that would not be supported in such a

flow field. In practice, there is likely to be a more complex relationship between a milk clot deposit and the shear stress, as suggested by Christy and Marosek (2000). The influence of the value chosen for the threshold shear stress on the predicted clot deposition patterns is reported below.

Results

Flow in a Stenosed Vessel

Figure 2 shows a snapshot of the flow-visualisation experiment at $\mathrm{Re} = 100$. The reattachment point is difficult to quantify precisely, due to the acute angle of impingement and dye mixing. The recirculation length was in the range 25-30mm when measured from the back face of the stenosis. Numerically, the recirculation length was measured as 29.0mm.

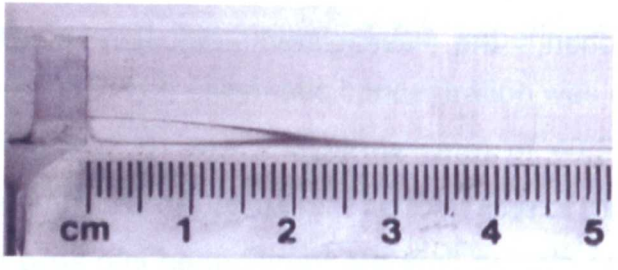

Figure 2: Flow visualisation results at Re =100. External tube wall can be seen.

At $\mathrm{Re} = 550$, complex temporally-disturbed experimental flow patterns were observed. There was no consistent periodicity in the flow patterns (no obvious vortex shedding), but the flow could not be categorically described as turbulent based on the limited experimental measures available. Good qualitative comparison of numerical and experimental results at $\mathrm{Re} = 550$ is illustrated in figures 3 and 4. The detailed flow structure at any instant in time was apparently random, but the overall characteristics were similar. The experimental results were captured from video of the flow visualisation study.

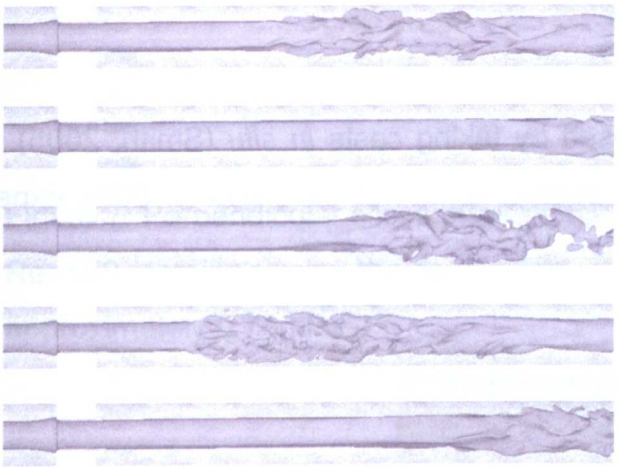

Figure 3: Lattice Boltzmann flow simulation results at Re=550. Isosurface of velocity shown inside core fluid domain. Arbitrary snapshots are shown to demonstrate the overall behaviour.

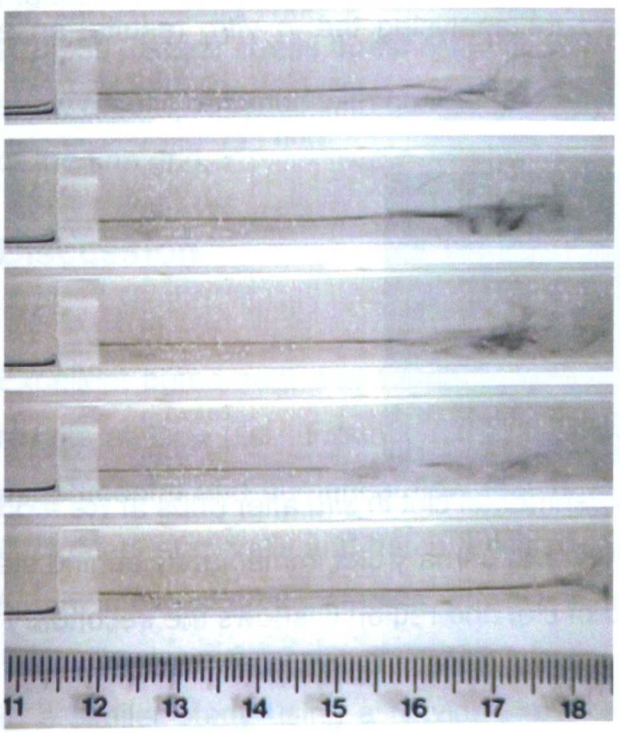

Figure 4: Flow visualisation results at Re = 550. External tube wall can be seen. Snapshots are shown to demonstrate the overall behaviour.

Milk Clotting Experiments

The milk clots were visualised by taking casts *in situ* (Smith, 2005). Figure 5 shows a photograph of a section of a clot cast after a 600s experiment at $\mathrm{Re} = 550$.

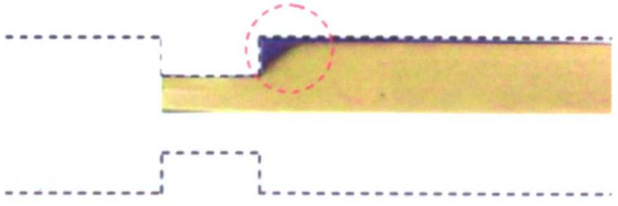

Figure 5: Section of cast of milk clot, extracted from stenosis model. Dotted lines indicate location of tube geometry. Yellow defines fluid region, brown defines clot (circled), formed immediately behind the stenosis.

Photography was also used for analysing the *in vitro* results, an example of which is shown in Figure 6.

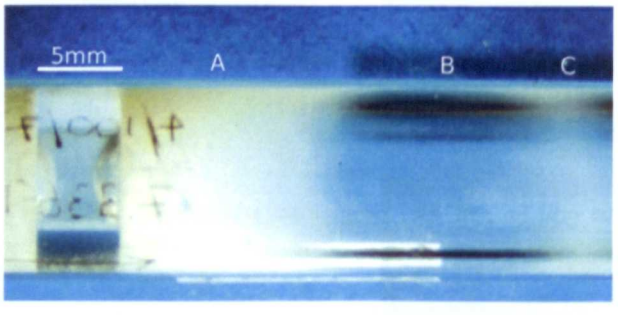

Figure 6: Photograph of experimental clot *in situ* after 600s at Re = 550. Flow is from left to right. Region A shows primary clot immediately behind stenosis, B indicates the region spared of clot and region C shows the secondary clot.

Clotting Model

The clotting time was chosen such that the same value could be obtained with both grids. The diffusion coefficient used was that appropriate to milk micelles, $D = 1.14 \times 10^{-11} m^2 s^{-1}$. Figures 7 and 8 show the results produced using different shear stress threshold values. Threshold values of approximately 0.75mPa and 1.5mPa were seen to give the best agreement with the experimental results.

Figure 7: Perpendicular slices through 3D domain showing simulated clot at Re=550, obtained using the coarse grid. Shear stress threshold is approximately 0.75mPa.

Figure 8: Perpendicular slices through 3D domain showing simulated clot at Re=550. Shear stress threshold is approximately 1.5mPa. Upper two images show results obtained with coarse grid and lower two images show the results of the fine grid.

Discussion

Excellent agreement was found between the numerical and experimental flow results at $\mathrm{Re} = 100$. Figures 3 and 4 show qualitative similarities between the experimental and numerical flow results at $\mathrm{Re} = 550$. The 'reattachment point' fluctuates temporally and has a range of 15-65mm in the simulations versus 30-55mm in experimental studies.

In a similar study using a Navier-Stokes solver, the transition from laminar to turbulent flow was reported at $\mathrm{Re} = 722$ (Sherwin and Blackburn, 2005). However, these authors used a smooth stenosis, which is likely to withstand higher Reynolds numbers before showing signs of turbulence (Cassanova and Giddens, 1978). It is therefore feasible to expect unsteady flow at $\mathrm{Re} = 550$ with a sharp-edged stenosis.

Figure 5 shows that experimentally, the clot forms in the corner behind the stenosis and the thickness decreases along the length of the tube. Numerically, similar results are produced (figs. 7 and 8).

Figure 6 shows two regions of clot separated by a cleared region. This was highly repeatable over the set of 15 experiments reported by Smith (2005). The average distance to the end of the first clot was 12.2 $\pm$ 1.5mm and the distance to the secondary band of clot was 28.3 $\pm$ 1.3mm. This striking feature is obtained numerically with both simulation grids; a band of cleared region develops, the length and position of which vary with the choice of the shear stress parameter. The position of the secondary clot may be related to the reattachment point, which fell in the range of 30-55mm for the experimental results shown.

The threshold shear stress values were chosen in order to reproduce the results seen in the experiments. There is no literature on the strength of the clot in the very early stages: such literature as does exist concentrates on the gel curing process over much longer timescales. It is noted that the thresholds chosen are not inconsistent with the literature- i.e. they are lower than those associated with a curing gel (Lucey, 2002; Mishra et al., 2005).

An excess amount of diffusion exists in the aging model, which, along with increased convective mixing, acts to limit the age values that can be obtained. The maximum age obtainable for the coarse grid was approximately 3s. The use of alternative diffusion models will be investigated in future work.

The results of the clotting model show that, despite practical limitations on the direct simulation of an experiment of 600s duration, it is possible to reproduce the experiments, given appropriate choice of the clotting time and the threshold shear stress. Qualitative agreement is seen between the experiments and simulations of complex flow in the transitional regime, but a more detailed quantitative comparison must be performed in future work. It is relatively straightforward to implement a physics-based local clotting model so that the clot growth is intimately coupled with the local characteristics of the flow field.

The lattice Boltzmann method has proven to be a suitable method for this problem due to the possibility of incorporating local rules into the model and the fact that the geometry can be changed during the simulation to represent the growth of the clot.

Future model developments will consider processes related to blood clotting such as the activation of platelets and clotting factors. This work is being used to build a lattice Boltzmann framework for the simulation of thrombosis caused by a variety of known physiological phenomena. This will contribute to an increased understanding of pathologies such as deep vein thrombosis. A complete model should also consider features such as pulsatile flow, distensible walls and patient specific geometries obtained from MR data.

Acknowledgements

S.E. Harrison is funded by NEC Europe Ltd. and the Engineering and Physical Sciences Research Council (EPSRC). S.M. Smith was funded by the EPSRC. The lattice Boltzmann flow solver into which the clotting routines were inserted was developed by the International Lattice Boltzmann Software Development Consortium.

References

Anand, M., Rajagopal, K., Rajagopal, K.R., 2003. A model incorporating some of the mechanical and biochemical factors underlying clot formation and dissolution in flowing blood. Journal of Theoretical Medicine 5, 183-218.

Benzi, R., Succi, S., Vergassola, M., 1992. The lattice Boltzmann equation: theory and applications. Physics Reports, 222, 145-197.

Cassanova, R. A., Giddens, D. P., 1978. Disorder distal to modeled stenoses in steady and pulsatile flow. Journal of Biomechanics 11, 441-453.

Chen, S., Doolen, G.D., 1998. Lattice Boltzmann method for fluid flows. Annual Review of Fluid Mechanics, 30, 329-364.

Christy, J.R., Macleod, N., 1989. The role of stasis in the clotting of blood and milk flows around solid objects. Cardiovascular Research 23, 949-959.

Christy, J.R.E., Marosek, K.W., 2000. Ultrasonic determination of clot deposition rates in a milk-based, in-vitro procedure for thrombogenicity assessment. The Journal of Heart Valve Disease 9, 379-388.

Dahlburg, J.P., Montgomery, D., Doolen, G.D., 1987. Noise and compressibility in lattice-gas fluids. Physical Review A, 36 2471-2474.

Dalgleish, D.G., 1982. The Enzymatic Coagulation of Milk. In: Fox, P.F. (Eds.), Developments in Dairy Chemistry, Volume 1. Elsevier Applied Science Publishers, London, pp. 157-187.

Friedrich, P., Reininger, A. J., 1995. Occlusive thrombus formation on indwelling catheters: in vitro investigation and computational analysis. Thrombosis and Haemostasis 73, 66-72.

Frisch, U., Hasslacher, B., Pomeau, Y., 1986. Lattice-gas automata for the Navier-Stokes equation. Physical Review Letters, 56, 1505-1508.

Higuera, F.J., Succi, S., Benzi, R., 1989. Lattice gas dynamics with enhanced collisions. Europhysics Letters, 9, 345-349.

Higuera, F.J., Jiménez, J., 1989. Boltzmann approach to lattice gas simulations. Europhysics Letters, 9, 663-668.

Jollès, P., 1975. Structural aspects of the milk clotting process. Comparative features with the blood clotting process. Molecular & Cellular Biochemistry 7, 73-85.

Keggen, L.A., Black, M.M., Lawford, P.V., Hose, D.R., Strachan, J.R., 1996. The use of enzyme activated milk for in vitro simulation of prosthetic valve thrombosis. Journal of Heart Valve Disease 5, 74-83.

Lallemand, P., Luo, L.-S., 2000. Theory of the lattice Boltzmann method: dispersion, dissipation, isotropy, Galilean invariance, and stability. Physical Review E, 61, 6546-6562.

Lewis, J.M.O., Macleod, N., 1981. Use of a coagulable fluid in vitro for the study and prediction of flow-induced thrombogenicity in cardiovascular prostheses. In Proceedings of the 2nd World Congress of Chemical Engineering, Montreal, 399-403.

Lucey, J.A., 2002. Formation and physical properties of milk protein gels. Journal of Dairy Science, 85, 281-294.

Martin, A.J., Christy, J.R.E., 2004. An in-vitro technique for assessment of thrombogenicity in mechanical prosthetic cardiac valves: evaluation with a range of valve types. The Journal of Heart Valve Disease, 13, 509-520.

McNamara, G.R., Zanetti, G., 1988. Use of the Boltzmann equation to simulate lattice-gas automata. Physical Review Letters, 61, 2332-2335.

Mishra, R., Govindasamy-Lucey, S., Lucey, J.A., 2005. Rheological properties of rennet-induced gels during the coagulation and cutting process: impact of processing conditions. Journal of Texture Studies, 36, 190-212.

Narracott, A., Smith, S., Lawford, P., Liu, H., Himeno, R., *Wilkinson, I., Griffiths,* P., Hose, R., 2005. Development and validation of models for the investigation of blood clotting in idealized stenoses and cerebral aneurysms. Journal of Artificial Organs 8, 56-62.

Payens, T.A.J., Wiersma, A.K., Brinkhuis, J., 1977. On enzymatic clotting processes I. Kinetics of enzyme-triggered coagulation reactions. Biophysical Chemistry 6, 253-261.

Payens, T.A.J., 1977. On enzymatic clotting processes II. The colloidal instability of chymosin-treated casein micelles. Biophysical Chemistry 6, 263-270.

Qian, Y.H., d'Humières, D., Lallemand, P., 1992. Lattice BGK models for Navier-Stokes equation. Europhysics Letters 17, 479-484.

Sherwin, S.J., Blackburn, H.M., 2005. Three-dimensional instabilities and transition of steady and pulsatile axisymmetric stenotic flows. Journal of Fluid Mechanics 533, 297-327.

Smith, S.M., 2005. Development of a technique for the prediction of clot localisation in vitro. PhD. thesis, Department of Medical Physics and Clinical Engineering, University of Sheffield, Sheffield.

Succi, S., 2001. The lattice Boltzmann equation for fluid dynamics and beyond. Oxford University Press, Oxford.

Tippe, A., Müller-Mohnssen, H., 1993. Shear dependence of the fibrin coagulation kinetics in vitro. Thrombosis Research 72, 379-388.

Wellein, G., Zeiser, T., Hager, G., Donath, S., 2006. On the single processor performance of simple lattice Boltzmann kernels. Computers and Fluids 35, 910-919.

Wolfram, S., 1986. Cellular automaton fluids 1: basic theory. Journal of Statistical Physics, 45, 471-526.

World Health Organisation (2006): Cardiovascular Disease. The Atlas of Heart Disease and Stroke.
http://www.who.int/cardiovascular_diseases/resources/atlas/en/index.html

A Lattice Boltzmann Framework for Simulation of Thrombogenesis

S.E. Harrison [a], J. Bernsdorf [b], D.R. Hose [a], P. Lawford [a]

[a] *Medical Physics and Clinical Engineering, University of Sheffield, Royal Hallamshire Hospital, Glossop Road, Sheffield. S10 2JF. UK.*
{s.harrison, d.r.hose, p.lawford}@sheffield.ac.uk

[b] *C&C Research Laboratories, NEC Europe Ltd., Rathausallee 10, D-53757 Sankt Augustin, Germany.*
j.bernsdorf@ccrl-nece.de

Abstract

A lattice Boltzmann framework has been developed which models the formation of thrombus following physical damage to platelets and activation of the coagulation cascade via one or more of the strands of Virchow's triad. The model includes concurrent simulation of flow, activation of blood and modification of the flow geometry following clot deposition.

Previous attempts have been made to simulate thrombus growth with the lattice Boltzmann method, but these earlier, simple models failed to consider the complex physical and biochemical interactions known to occur *in vivo*, some of which are included within our extended model. These are: i) platelet activation due to prolonged high shear stress exposure, ii) release of clotting factors following vessel wall damage.

An extended local clotting rule has been developed which takes into account the vicinity of the growing clot and local flow factors such as shear stress. This paper will focus on the implementation of these local rules, as an extension to the standard flow solver, for modelling the activation and clotting processes.

Key words: Blood clotting, lattice Boltzmann
PACS: 47.11.j, 02.60.x, 47.63.b

1 Introduction

Understanding thrombogenesis is crucial; the onset and development of thrombus formation will determine the likelihood of embolism, which itself can result

in heart attacks, strokes and pulmonary embolism. It is predicted that by the year 2020 heart disease and stroke will become the leading cause of death worldwide with over 20 million fatalities each year [1]. Thrombogenesis involves the activation and interaction of many chemical species, triggered by a variety of instigators. There are two main processes involved: the activation and aggregation of platelets and the activation of the coagulation cascade which ultimately results in fibrin formation. In the event of injury to a blood vessel, the first response is the activation of platelets. Activated platelets adhere to one another and to the site of injury, forming a loose plug to prevent excessive blood loss. Subsequently, fibrin is produced which acts as a mesh, capturing other blood cells and activated platelets and strengthening the original plug. The exact nature of the thrombus formed is dictated by the flow environment, and can result in the formation of either a white (platelet rich) or red (trapped red blood cell rich) thrombus.

In the present work, a lattice Boltzmann framework for modelling thrombosis is developed. This incorporates a number of features of thrombus development, such as the response of platelets and the coagulation cascade. This preliminary paper describes the foundations on which more detailed models can be built and demonstrates the ease and suitability of the lattice Boltzmann method for modelling a complex system of reactions.

2 Literature Review

In 1856, Virchow defined a triad of factors contributing to the initiation of thrombosis. The simplified entities of this triad are stasis, changes in the vessel wall and changes in the blood [2]. A variety of approaches have been taken in attempts to model these complex processes and a comprehensive review of progress is reported by Anand et al. [3]. A complete model involving the biochemical interactions at play within a physiologically relevant geometry has yet to be developed. The focus tends to be on either one or two of the strands of Virchow's triad. If a set of equations describing all or some of the coagulation cascade is implemented, the flow field is, generally, either neglected or over-simplified [3–9] and in models where realistic flow fields are considered, the biochemistry of the system is often reduced to very simple models [10,11]. Modelling the response of platelets alone has proved popular [12–19] and experimental validation can be readily performed using platelet rich plasma.

In 1999, Sorensen et al. [20] presented a model of platelet activation and deposition. This represents platelets and the final elements of the coagulation cascade as massless species transported by convection and diffusion. A set of 7 differential equations were used, adapted from the published literature, and

platelet deposition was realised via a surface flux boundary condition with consideration of the local concentration of activated platelets. The simple 2D flow field was computed using the Navier-Stokes equations, but the effect of the growing thrombus on the flow was not considered. In a second publication by the same authors, validations were performed using collagen as the reactive wall and simple parallel-plate flow [21]. The authors reported good agreement with several sets of experiments.

In 2001, Wootton et al. [22] presented experimental and numerical results for platelet deposition on a collagen-coated stenosis. The computational model was based on earlier work by Turrito and Baumgartner [12] and used a species transport model for the platelets. In the near wall region, platelets were activated by collagen and free, unactivated platelets became attached and activated at a constant rate. The model considers physiological flow and shear dependent diffusivity but, again, does not consider the effect of the growing thrombus on the flow field. Comparison with experiments shows agreement in the upstream and throat regions of the stenosis, but downstream of the throat, the model under-predicts the amount of deposition. Due to the shear stress exposure measured, this work does not consider the possibility of shear stress activation *with subsequent* downstream aggregation. This will be considered later in the present paper.

In 2004, Fogelson and Guy [23] presented a continuum model of platelet aggregation with extensive detail given to reactions occurring at the vessel wall. This very detailed model represents aggregation using elastic links. The stresses caused by the links are coupled to the fluid, resulting in associated stresses therein. This captures the effect of the growing thrombus on the flow field. Two different length-scales are considered; one relative to the diameter of the vessel (order of mm) and one relative to the diameter of a platelet (order of μm). The Navier-Stokes equations are used for solving the flow field and shear dependent diffusivity is included. Platelet-wall interactions are modelled by considering a rate constant which dictates alterations in the concentrations of normal and activated platelets in contact with reactive sites at the vessel wall. When platelets are activated, they release an activating agent, adenosine diphosphate (ADP), which is transported by advection and diffusion. Simulations were performed in 2D stenosed vessels with a diameter of approximately 1mm. The cap of the stenosis (plaque) was assumed to have ruptured, exposing platelet activation sites to the blood. A significant feature of this model is the ability to simulate embolus. The elastic links can break under certain conditions and the associated clot can break off and travel downstream.

In 2005, Bedekar et al. [24] further developed the work of Sorensen et al. [20]. Platelets are activated by a reactive surface and by contact with previously activated platelets and thrombin. The generation and inhibition of thrombin is also modelled. All rate constants and equations are taken from the literature.

The flow was solved using the Navier-Stokes equations and simulations were performed in both a cylindrical tube and in an aneurysm, the geometry of which was obtained from computed tomography data.

A similar model of thrombosis is reported by Goodman et al. [25], but in this case, experimental validation is provided. This model considers platelet adhesion, with resulting effects on the flow field, together with an embolism model. Platelet activation is due to agonists in the bulk flow and again, the work of Sorensen et al. [20] was used. The effect of the growing thrombus on the flow field was modelled by increasing the viscosity by a factor of 1×10^5 in clottable cells. These cells could then emit agonists and thrombin (final enzyme in the cascade), which could, in turn, activate other platelets in the vicinity. The experiments and computations were performed in stenosed vessels and, in most cases, the results were found to be in agreement.

In summary, a complete model of thrombosis has yet to be developed. Various aspects have been considered, such as reactions in the coagulation cascade, or the adhesion and aggregation of platelets in physiological geometries using the Navier-Stokes equations.

In recent years, a small number of lattice Boltzmann thrombosis models have been reported. In 2004, Tamagawa and Matsuo [26] presented a model which tracked the motion of 200 particles in a backward facing step geometry. In this model, thrombosis is permitted if the shear rate and distance from the wall fall below defined thresholds. Investigations also considered the use of a distance dependent threshold shear rate. This latter scheme gave the best agreement with experimental data.

In 2005, Ouared and Chopard [27] described a lattice Boltzmann model based on shear stress. Clotting was permitted only in regions of low shear stress. The principle of this is in line with common theories describing embolism, and prior activation of the coagulation cascade and platelets is assumed. Thrombus was simulated with suspensions using a model previously developed for sediment transport and deposition.

In 2006, Bernsdorf et al. [28] presented a simple lattice Boltzmann model that tracked the age of fluid, relative to that at the inlet, using a passive scalar tracer with a uniform source term. This simulates the final reaction in the cascade and the results were compared to those produced experimentally with enzyme activated milk; a recognised blood-clotting analogue. The local rule allowing thrombus formation was that the age of the fluid must be above a certain threshold. Qualitative agreement was seen with experimental data obtained by passing activated milk through a sharp-edged stenosis. This work has since been developed to consider 3D simulations with shear stress and proximity conditions [29], again with good agreement.

3 Methods

3.1 Sparse Lattice Boltzmann Implementation

For all simulations reported in this paper, a sparse lattice Boltzmann implementation is used [30] on an NEC SX8 vector machine. This method obtains increased efficiency by solving the lattice Boltzmann equations only on the fluid nodes. The effect of this is not seen here because mainly 2D channel flow is considered. The memory requirement for such an implementation scales with the number of fluid nodes as opposed to the size of the bounding box, hence this method is particularly suited to complex, physiological geometries. Further details can be found in the article by Bernsdorf et al. [28].

3.2 Developing the Framework

The literature review of this paper briefly describes the current progress in thrombosis modelling. The events in the coagulation cascade interconnect with the activation of platelets in such a way as to produce a stable clot.

The coagulation cascade is initiated by either tissue factor or collagen; a structural protein in the vessel wall. If external injury occurs, such as a wound or incision, tissue factor from the damaged tissues is released into the blood stream. A similar response may occur if the vessel wall becomes damaged. Removal of the lining of the blood vessel may expose collagen. This is not transported, but activates blood in contact. Collagen can also activate platelets, which are then attracted both to one another and to the vessel wall, forming an aggregate. In normal conditions, there is a balance between procoagulants and anticoagulants in the blood and unless this balance is disrupted, coagulation is not likely to occur.

Another feature of platelets is that they can be activated by exposure to high shear stress [31–34]. High shear stress has a cumulative effect and, if the total damage to a platelet exceeds a threshold value, activation will occur. If the shear stress is high, thrombus can be dislodged (embolise) or even prevented from developing [35–37].

When platelets are activated, they release adenosine diphosphate (ADP), which acts as a platelet agonist [3,23,25], the resulting positive feedback gives a rapid increase in the concentration of activated platelets known as synergistic activation.

Models representing some of these mechanisms have been introduced into the

lattice Boltzmann code as add-ons to the standard flow solver. As with previous work in the literature, massless species are used to represent normal and activated platelets and the proteins and enzymes of the coagulation cascade. This is justified since a platelet has a mass [38] of $\approx 1 \times 10^{-14} kg$ and a volume [39] of $\approx 1 \times 10^{-17} m^3$, giving a density of $\approx 1000 kgm^{-3}$, comparable with that of blood ($1060 kgm^{-3}$), the carrier fluid. Platelets are discoid fragments with a diameter [40] of $(2-4)\mu m$, which is significantly smaller than a typical lattice size in our simulations ($\approx 1 \times 10^{-4} m$). All species are transported by convection and diffusion using the algorithm developed by Flekkoy [41]. This considers distributions of concentration in order to solve the convection-diffusion equation, analogous to the lattice Boltzmann method.

Clotting is realised using a solid surface boundary condition [28] for fluid nodes satisfying local rules specific to the model in use. A proximity condition prevents isolated clots from growing in regions where they are not attached to either the vessel wall or an existing clot. This is based on the assumption that *in vivo*, any isolated clots would be transported by the flow. This effect cannot yet be simulated in the model.

The framework developed in this work can be used alongside any initiating factor, providing that data exists on the mechanism causing the activation of platelets and the coagulation cascade. The following sections describe the three basic models generated to date.

3.3 Platelet Clotting: Shear Stress Activation

The first platelet clotting model considered in this work computes the shear history of platelets, with activation occurring beyond a certain threshold. A fluid node is transformed into a solid node if the concentration of activated platelets attains a defined threshold and the shear stress is below threshold. This model is only appropriate in geometries where the shear stress may rise above the normal wall value, such as in a stenosed artery [42].

The model used for tracking the shear stress over time is based on the work by Anand et al. [3]. An activation number, $A(t)$ is defined, which quantifies the activation due to prolonged exposure to shear stress. In this model, the shear stress, must be above a threshold in order to contribute to the activation. The following equations define the activation number and condition for contribution.

$$A(t) = A(0) + \frac{1}{A_0} \int_0^t e^{k\left(\frac{|\tau|}{\tau_{thr}} - 1\right)} H\left(|\tau| - \tau_{thr}\right) dt \tag{1}$$

$$H\left(|\tau| - \tau_{thr}\right) = \begin{cases} 1 & : \quad |\tau| \geq \tau_{thr} \\ 0 & : \quad |\tau| < \tau_{thr} \end{cases} \tag{2}$$

In the original publication [3], the constants are defined as follows: $A_0 = 300s$, $k = 0.75$, $\tau_{thr} = 5Nm^{-2}$. If the value of $A(t)$ exceeds a threshold, activation can occur. Anand et al. [3] define this threshold to be equal to unity.

This model is incorporated into the lattice Boltzmann framework by using a species with a very low diffusion coefficient to trace the values of $A(t)$. The concentration of this species is updated locally at every timestep depending on the shear stress and equations (1) and (2). This allows for the activation parameter to travel with the fluid and hence follow the platelets.

At each timestep, the activation number is computed and if it is above threshold, equation 3 is implemented to alter the concentration of activated platelets. The concentration of normal platelets is therefore set to zero at that particular grid point. This essentially activates all normal platelets at a grid point if the activation parameter is above threshold. If the activation number is below threshold, the thresholds of normal and activated platelets remain unaltered.

$$\frac{d\left[AP\right]_{x,t}}{dt} = \left[RP\right]_{x,t} \tag{3}$$

The synergistic activation of platelets is modelled using the equation taken from Kuharsky and Fogelson [7], shown below. This directly increases the concentration of activated platelets, rather than modelling the transport of ADP and other agonists separately.

$$\frac{d\left[AP\right]_{x,t}}{dt} = k_{AP}^{AP}\left[AP\right]_{x,t}\left[RP\right]_{x,t} \tag{4}$$

$[AP]_{x,t}$ and $[RP]_{x,t}$ are the concentrations of activated and resting (normal) platelets respectively. The rate constant, k_{AP}^{AP} is given as $3 \times 10^8 M^{-1}s^{-1}$.

3.4 Platelet Clotting: Collagen Exposure

A second model assumes a small region of collagen exposure on the wall, which can activate platelets in direct contact. The collagen represents a 'damaged' region of the wall, although the underlying cause of this damage is not considered. A species is used as a marker for the location of exposed collagen but is

prevented from transporting. The equation describing the activation process is adapted from Wootton et al. [22] and is shown below.

$$\frac{d\left[AP\right]_{x,t}}{dt} = k_t \left[RP\right]_{x,t} \tag{5}$$

Wootton et al. [22] consider the rate of platelet accumulation per unit area and the rate constant is given as $k_t = 5 \times 10^{-3} cms^{-1}$. In order to satisfy the units of equation (5), this rate constant must be divided through by the length scale of the chosen lattice to give a value in units of inverse seconds. If collagen is present at a certain lattice point, the concentration of activated platelets is increased according to equation (5) and the concentration of normal platelets is reduced by an equal amount.

As described previously, the synergistic activation of platelets is also considered and clotting occurs when the concentration of activated platelets is above threshold.

3.5 Blood Clotting: Thrombin Release

As a first attempt to model the final reaction in the coagulation cascade, thrombin was released as a source from the damaged wall region. Thrombin is the final enzyme in the coagulation cascade and reacts with fibrinogen, normally present in the blood, to produce fibrin. Thrombin can also activate platelets.

The equation used for modelling the conversion of fibrinogen into fibrin was taken from Zarnitsina et al. [6] and is shown below.

$$\frac{d\left[Ia\right]_{x,t}}{dt} = k_1 \left[IIa\right]_{x,t} \tag{6}$$

$[Ia]$ and $[IIa]$ represent the concentrations of fibrin and thrombin respectively and the rate constant, $k_1 = 0.047 s^{-1}$.

The equation representing the activation of platelets by thrombin is taken from Kuharsky and Fogelson [7], later used by Anand et al. [3].

$$\frac{d\left[AP\right]_{x,t}}{dt} = k_{AP}^{IIa} \left[RP\right]_{x,t} \tag{7}$$

The rate constant, k_{AP}^{IIa} used by both groups is $0.5 s^{-1}$.

The synergistic activation is considered in the same way as previously described.

4 Results

The results presented are preliminary, but demonstrate the functionality of the different models. At this stage, no attempt has been made to compare the output of the models with experimental results in the literature. For this reason, the rate constants used are not as previously given, however, ratios between rate constants have been maintained. This is not seen as a major issue at this stage as, without validation, it is difficult to justify the conversion of lattice Boltzmann simulation parameters into flow parameters in real units.

4.1 Platelet Clotting: Shear Stress Activation

In order to test this particular model, a 2D sharp-edged 50% stenosis model is used, as illustrated in figure 1.

Fig. 1. Geometry of 2D 50% sharp edged stenosis. Flow is directed from left to right. Upper vortex is shown.

The grid dimensions used for the simulation were $lx^*ly = 532^*82$. A Reynolds number of 100 was used, which produced symmetrical laminar flow with 2 vortices downstream of the constriction. The average velocity in the inlet region was equal to approximately 5.34×10^{-3} and the lattice kinematic viscosity was equal to approximately 4.27×10^{-3} (both measured in lattice units). The converged flow field was obtained (1×10^5 iterations) before the platelet clotting model was initiated. The threshold values were chosen based on the concentrations observed as the simulation progressed. The diffusion coefficient used was equal to $D = 1 \times 10^{-4}$ (lattice units), the minimum that could be obtained due to instabilities in the diffusion routine. The initial concentration of normal platelets was equal to 1 (lattice units) throughout the domain and the remaining species had initial concentrations of zero. These values were used as inlet boundary conditions for the remainder of the simulation. The clot was permitted to grow if the concentration of activated platelets, $[AP]_{thresh}$ was equal to 1 (lattice units) and the shear stress was below the threshold value of 7.5×10^{-6} (lattice units). These parameters were chosen simply to illustrate the model capabilities and to produce some initial results. Figure 2 shows a

greyscale image of the clot formed after a further 2.2×10^6 iterations, wherein darker regions indicate newly deposited clot. This model achieved approximately 13 million lattice site updates per second (MLUPS) on an NEC SX8 vector machine.

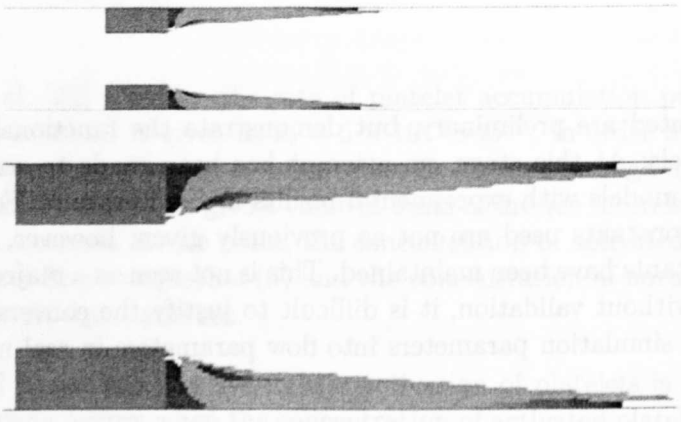

Fig. 2. Thrombus deposition immediately downstream of stenosis. The darker areas are newly formed clot. Lower image shows enlargement of clot region.

4.2 Platelet Clotting: Collagen Exposure

For this model, a 2D channel was used. A section of the upper wall of length 50 lattice units was marked as damaged, where collagen was exposed. The grid dimensions were $lx^*ly = 532^*82$ and the Reynolds number was equal to 100. The lattice velocity and viscosity are equal to those given in section 4.1. The converged flow field was obtained after 1×10^5 iterations, without the platelet model, then a further 1×10^5 iterations were performed with the platelet model. The threshold of activated platelets required to produce a clot was equal to 1, which again, was chosen to allow for the effects of the model to be observed. The initial and inlet boundary conditions were as described for the previous model. This model achieved approximately 18 MLUPS on an NEC SX8 vector machine.

Figure 3 shows a greyscale image of the clot formed after 1×10^5 iterations, wherein darker regions indicate newly deposited clot.

4.3 Blood Clotting: Thrombin Release

As before, a 2D channel was used and a section of the upper wall of length 50 lattice units was marked as damaged, but in this case thrombin was released from the site of injury at a constant, arbitrary rate. Thrombin activates

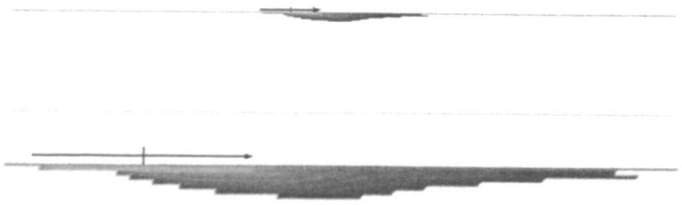

Fig. 3. Thrombus deposition in 2D channel. The region of wall damage (collagen exposure) is indicated by the arrow. The darker areas are newly formed clot. Lower image shows enlargement of clot region.

platelets and also converts fibrinogen into fibrin. The initial concentrations of normal platelets and fibrinogen were 0.16 (lattice units) and 0.84 (lattice units) respectively. These were chosen such that the sum was equal to 1 and the ratio was equal to the average taken from the literature [3,20,25,39,43–48]. These values were used as inlet boundary conditions for the remainder of the simulation. The grid dimensions were $lx^*ly = 532^*82$ and the Reynolds number was equal to 100. The converged flow field was obtained after 1×10^5 iterations, without the thrombus model, then a further 1×10^5 iterations were performed with the thrombus model. The threshold levels of activated platelets and fibrin required for clotting were 2×10^{-2} and 1×10^{-3} (lattice units) respectively, simply chosen to allow for the effects of the model to be observed. This model achieved approximately 15 MLUPS on an NEC SX8 vector machine.

Figure 4 shows a greyscale image of the clot formed after 1×10^5 iterations.

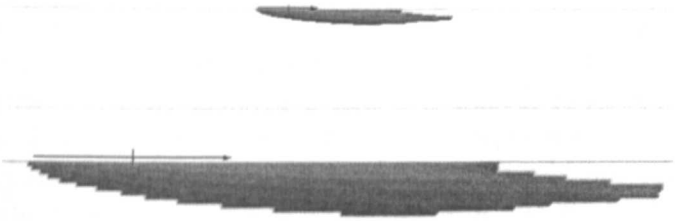

Fig. 4. Thrombus deposition in 2D channel. Region of wall damage (thrombin release) is indicated by the arrow. The darker areas are newly formed clot. Lower image shows enlargement of clot region.

5 Discussion

The introductory section of this paper describes the complex process of thrombosis, which, as yet, has not been simulated in full. The development of a lattice Boltzmann framework for simulating thrombosis has been described in this paper, along with some initial results. The framework has been developed in such a way that further features of the clotting process can easily be implemented, providing that sound biological hypotheses exist.

To date, three aspects of this complex process have been simulated. The first model simulates shear stress activation of platelets. The results show that the raised shear stress, found in the region of the stenotic occlusion activates the platelets, which are then transported into a low shear stress region of recirculation where they can aggregate. This notion has been postulated previously [33,36]. When platelets are activated, they must convect and diffuse into the recirculation region downstream of the stenosis. Figure 2 shows that the clot primarily forms along the wall and the last region to clot is that immediately behind the stenosis. This is because it takes significantly longer for activated platelets to reach this area. If the synergistic function is not used, blood in this region will never clot because it is shielded from the bulk luminal flow by previously deposited clot.

The second model simulates platelet activation by contact with exposed collagen and with other activated platelets. Figure 3 shows that the clot completely covers the region of damage of the wall, thus reducing the rate of deposition and final possible size of the thrombus. The maximum width of the thrombus is shifted downstream of the original area of collagen exposure, due to the flow field.

The third model includes the behaviour of platelets and the final part of the coagulation cascade. The use of a source term of thrombin at the wall might be considered to be an oversimplification of the biochemical processes involved. If a vessel wall is damaged, the preceding sequence of reactions in the cascade will occur whilst the blood is flowing, before thrombin is produced. This means that the initial release of thrombin will occur downstream of the damaged area, and the distribution of thrombin is thus dependent on the velocity and the rate at which the cascade propagates. A more accurate model of this system would require consideration of coagulation cascade reactions leading to thrombin production, or the formulation of a sensible approximation to this. This issue will be addressed in future work.

The models and results presented in this study show how the behaviour of platelets and the coagulation cascade can be simulated. It is appreciated that many free parameters have been used in the execution of the models and that the results shown are specific to the parameters used. The values of the clotting thresholds were chosen simply to allow for the effects of the model to be observed. Further experimental data is required for these values. In future, when comparisons are made with experimental results, the rate constants can be chosen to agree with those in the literature and their sensitivity investigated.

Improvements to the model are required, firstly to address the issue of the diffusion model, which currently places a lower bound on the diffusion coefficient that can be used.

The action of inhibitors has not been included at this stage. This may have a significant effect on the resulting deposition patterns and will be incorporated into more detailed models in future.

6 Conclusion

A lattice Boltzmann framework has been developed for simulation of thrombosis. This paper presents initial results. The complex process of coagulation has been simplified based on data obtained from the literature for platelet aggregation, including shear stress and synergistic activation of platelets. A model which includes the final reaction of the coagulation cascade and the response of platelets is also described. The results presented in this paper are preliminary and the models require further refinement and input data, but they demonstrate the functionality of the models and the ease at which such processes can be simulated. All models developed in this study are based on local rules and can be used in isolation or simultaneously. The geometry of the domain can be altered during simulation to mimic the formation of thrombus, which feeds back as a physical obstacle to the flow field. An advantage of the lattice Boltzmann method is the efficient manner in which this can be performed.

Future work will concentrate on validating the models and extending the coagulation cascade reactions, to include additional pro and anti coagulant reactions, in order to provide a more accurate representation of the *in vivo* system.

7 Acknowledgements

The lattice Boltzmann flow solver into which the clotting routines were inserted was developed by the International Lattice Boltzmann Software Development Consortium.

S.E. Harrison is funded by NEC Europe Ltd. and the Engineering and Physical Sciences Research Council.

References

[1] World Health Organisation: WHO publishes definitive atlas on global heart disease and stroke epidemic.

http://www.who.int/mediacentre/news/releases/2004/pr68/en/index.html (2004)

[2] Breddin, H.K., Thrombosis and Virchow's triad: what is established. Semin. Thromb. Hemost. 15, 237-239 (1989).

[3] Anand, M., Rajagopal, K. and Rajagopal, K.R., A model incorporating some of the mechanical and biochemical factors underlying clot formation and dissolution in flowing blood. J. Theor. Med. 5, 183-218 (2003).

[4] Baldwin, S.A. and Basmadjian, D., A mathematical model of thrombin production in blood coagulation, Part I: The sparsely covered membrane case. Ann. Biomed. Eng. 22, 357-370 (1994).

[5] Jones, K.C. and Mann, K.G., A model for the tissue factor pathway to thrombin. II. A mathematical simulation. J. Biol. Chem. 269, 23367-23373 (1994).

[6] Zarnitsina, V.I., Pokhilko, A.V. and Ataullakhanov, F.I., A mathematical model for the spatio-temporal dynamics of intrinsic pathway of blood coagulation. I. The model description. Thromb. Res. 84, 225-236 (1996).

[7] Kuharsky, A.L. and Fogelson, A.L., Surface-mediated control of blood coagulation: the role of binding site densities and platelet deposition. Biophys. J. 80, 1050-1074 (2001).

[8] Ataullakhanov, F.I., Zarnitsina, V.I., Pokhilko, A.V., Lobanov, A.I. and Morozova, O.L., Spatio-temporal dynamics of blood coagulation and pattern formation. A theoretical approach. Int. J. Bifurcat. Chaos. 12, 1985-2002 (2002).

[9] Ermakova, E.A., Panteleev, M.A. and Shnol, E.E., Blood coagulation and propagation of autowaves in flow. Pathophysiol. Haemost. Thromb. 34, 135-42 (2005).

[10] Narracott, A., Smith, S., Lawford, P., Liu, H., Himeno, R., Wilkinson, I., Griffiths, P. and Hose, R., Development and validation of models for the investigation of blood clotting in idealized stenoses and cerebral aneurysms. J. Artif. Organs. 8, 56-62 (2005).

[11] Friedrich, P. and Reininger, A.J., Occlusive thrombus formation on indwelling catheters: In vitro investigation and computational analysis. Thromb. Haemostasis, 73, 66-72 (1995).

[12] Turitto, V.T. and Baumgartner, H.R., Platelet deposition on subendothelium exposed to flowing blood: mathematical analysis of physical parameters. T. Am. Soc. Art. Int. Org. 21, 593-601 (1975).

[13] Fogelson, A.L., A mathematical model and numerical method for studying platelet adhesion and aggregation during blood clotting. J. Comput. Phys. 56, 111-134 (1984).

[14] Fogelson, A.L., Continuum models of platelet aggregation: formulation and mechanical properties. SIAM J. Appl. Math. 52, 1089-1110 (1992).

[15] Huang, P.Y. and Hellums, J.D., Aggregation and disaggregation kinetics of human blood platelets: Part I. Development and validation of a population balance method. Biophys. J. 65, 334-343 (1993).

[16] Huang, P.Y. and Hellums, J.D., Aggregation and disaggregation kinetics of human blood platelets: Part II. Shear-induced platelet aggregation. Biophys. J. 65, 344-353 (1993).

[17] Wang, N.-T. and Fogelson, A.L., Computational methods for continuum models of platelet aggregation. J. Comp. Phys. 151, 649-675 (1999).

[18] David, T., Thomas, S. and Walker, P.G., Platelet deposition in stagnation point flow: an analytical and computational simulation. Med. Eng. Phys. 23, 299-312 (2001).

[19] Affeld, K., Goubergrits, L., Kertzscher, U., Gadischke, J. and Reininger, A., Mathematical model of platelet deposition under flow conditions. Int. J. Artif. Organs. 27, 699-708 (2004).

[20] Sorensen, E.N., Burgreen, G.W., Wagner, W.R. and Antaki, J.F., Computational simulation of platelet deposition and activation: I. model development and properties. Ann. Biomed. Eng. 27, 436-448 (1999).

[21] Sorensen, E.N., Burgreen, G.W., Wagner, W.R. and Antaki, J.F., Computational simulation of platelet deposition and activation: II. results for poiseuille flow over collagen. Ann. Biomed. Eng. 27, 449-458 (1999).

[22] Wootton, D.M., Markou, C.P., Hanson, S.R. and Ku, D.N., A mechanistic model of acute platelet accumulation in thrombogenic stenoses. Ann. Biomed. Eng. 29, 321-329 (2001).

[23] Fogelson, A.L. and Guy, R.D., Platelet-wall interactions in continuum models of platelet thrombosis: formulation and numerical solution. Math. Med. Biol. 21, 293-334 (2004).

[24] Bedekar, A.S., Pant, K., Ventikos, Y. and Sundaram, S., A computational model combining vascular biology and haemodynamics for thrombosis prediction in anatomically accurate cerebral aneurysms. Food Bioprod. Process. 83, 118-126 (2005).

[25] Goodman, P.D., Barlow, E.T., Crapo, P.M., Mohammad, S.F. and Solen, K.A., Computational model of device-induced thrombosis and thromboembolism. Ann. Biomed. Eng. 33, 780-797 (2005).

[26] Tamagawa, M. and Matsuo, S., Predictions of thrombus formation using lattice Boltzmann method (modeling of adhesion force for particles to wall). JSME Int. J. C.-Mech. Sy. 47, 1027-1034 (2004).

[27] Ouared, R. and Chopard, B., Lattice Boltzmann simulations of blood flow: non-Newtonian rheology and clotting processes. J. Stat. Phys. 121, 209-221 (2005).

[28] Bernsdorf, J., Harrison, S.E., Smith, S.M., Lawford, P.V. and Hose, D.R., Numerical simulation of clotting processes: A lattice Boltzmann application in medical physics. Math. Comput. Simulat. 72, 89-92 (2006).

[29] Harrison, S.E., Smith, S.M., Bernsdorf, J., Hose, D.R. and Lawford, P.V., Application and validation of the lattice Boltzmann method for modelling flow-related clotting. Submitted to Journal of Biomechanics, (2006).

[30] Schulz, M., Krafczyk, M., Tölke, J. and Rank, E., Parallelization strategies and efficiency of CFD computations in complex geometries using lattice-Boltzmann methods on high-performance computers. In: M. Breuer, F. Durst, and C. Zenger (Eds). Proceedings of the 3rd International FORTWIHR Conference on High-Performance Scientific and Engineering Computing., Erlangen. p.115-122 (2002).

[31] Zhang, J.N., Bergeron, A.L., Yu, Q., Sun, C., McIntire, L.V., Lopez, J.A. and Dong, J.F., Platelet aggregation and activation under complex patterns of shear stress. Thromb. Haemostasis. 88, 817-821 (2002).

[32] Brown, C.H., 3rd, Leverett, L.B., Lewis, C.W., Alfrey, C.P., Jr. and Hellums, J.D., Morphological, biochemical, and functional changes in human platelets subjected to shear stress. J. Lab. Clin. Med. 86, 462-471 (1975).

[33] Schmid-Schönbein, H., Born, G.V.R., Richardson, P.D., Cusack, N., Rieger, H., Forst, R., Rohling-Winkel, I., Blasberg, P. and Wehmeyer, A., Rheology of thrombotic processes in flow: the interaction of erythrocytes and thrombocytes subjected to high flow forces. Biorheology. 18, 415-444 (1981).

[34] Hellums, J.D., 1993 Whitaker lecture: Biorheology in thrombosis research. Ann. Biomed. Eng. 22, 445-455 (1994).

[35] Basmadjian, D., Embolization: critical thrombus height, shear rates, and pulsatility. Patency of blood vessels. J. Biomed. Mater. Res. 23, 1315-1326 (1989).

[36] Bluestein, D., Niu, L., Schoephoerster, R.T. and Dewanjee, M.K., Fluid mechanics of arterial stenosis: relationship to the development of mural thrombus. Ann. Biomed. Eng. 25, 344-356 (1997).

[37] Riha, P., Wang, X., Liao, R. and Stoltz, J.F., Elasticity and fracture strain of whole blood clots. Clin. Hemorheol. Microcirc. 21, 45-49 (1999).

[38] Morgenstern, E., Human platelet morphology/ultrastructure. In: F.v. Bruchhausen and U. Walter (eds) Platelets and Their Factors. Berlin, Springer. p. 27-60 (1997).

[39] Weiss, H.J., Platelets: pathophysiology and antiplatelet drug therapy. Alan R. Liss, Inc., New York (1982).

[40] Marieb, E.N., Human Anatomy and Physiology. 4th edition. California, Benjamin/Cummings Publishing Company (1998).

[41] Flekkoy, E.G., Lattice Bhatnagar-Gross-Krook models for miscible fluids. Phys. Rev. E. 47, 4247-4257 (1993).

[42] Wurzinger, L.J., Blasberg, P. and Schmid-Schönbein, H., Towards a concept of thrombosis in accelerated flow: rheology, fluid dynamics, and biochemistry. Biorheology. 22, 437-449 (1985).

[43] Duckert, F., Blood coagulation and fibrinolysis, in Geigy Scientific Tables: Physical Chemistry, Composition of Blood, Hematology, Somatometric Data, C. Lentner, Editor. Ciba-Geigy. 222-235 (1984).

[44] Kuter, D.J., Hemorrhagic Disorders II. Platelets, in Hematology, W.S. Beck, Editor. 1991, The MIT Press.

[45] Kuter, D.J. and Rosenberg, R.D., Hemorrhagic Disorders III. Disorders of Hemostasis, in Hematology, W.S. Beck, Editor. p. 543-575 The MIT Press, Cambridge, MA (1991).

[46] Mann, K.G., Gaffney, D. and Bovill, E.G., Molecular biology, biochemistry, and lifespan of plasma coagulation factors, in Williams Hematology, E. Beutler, et al., Editors. McGraw-Hill, Inc (1995).

[47] Giacomini, A., Legovini, P., Antico, F., Gessoni, G., Valverse, S., Salvadego, M.M. and F.Manoni, Evaluation of platelet analysis on the ADVIA 120 hematology system. Lab. Hematology. 7, 180-185 (2001).

[48] Furie, B. and Furie, B.C., Molecular Basis of Blood Coagulation, in Hematology, Basic Principles and Practice, R. Hoffman, et al., Editors. 2005, Philadelphia, Pa.:Churchill Livingstone, (2005).

International Journal of Modern Physics C

Development of a Lattice Boltzmann Framework for Numerical Simulation of Thrombosis

S.E. HARRISON[1], J. BERNSDORF[2], D.R. HOSE[1], P.V. LAWFORD[1]

[1] *Medical Physics and Clinical Engineering, University of Sheffield, Royal Hallamshire Hospital, Glossop Road, Sheffield. S10 2JF. UK.*
{s.harrison, p.lawford, d.r.hose}@sheffield.ac.uk

[2] *C&C Research Laboratories, NEC Europe Ltd., Rathausallee 10, D-53757 Sankt Augustin, Germany*
j.bernsdorf@ccrl-nece.de

Received Day Month Year
Revised Day Month Year

The interacting factors relating to thrombogenesis were defined by Virchow in 1856 to be abnormalities of; blood chemistry, the vessel wall and haemodynamics. Together, these factors are known as Virchow's triad. Many attempts have been made to simulate numerically certain aspects of the complex phenomena of thrombosis, but a comprehensive model, which includes the biochemical and physical aspects of Virchow's triad, and is capable of predicting thrombus development within physiological geometries has not yet been developed. Such a model would consider the role of platelets and the coagulation cascade along with the properties of the flow in the chosen vessel.

A lattice Boltzmann thrombosis framework has been developed, on top of an existing flow solver, to model the formation of thrombi resulting from platelet activation and initiation of the coagulation cascade by one or more of the strands of Virchow's triad. Both processes then act in parallel, to restore homeostasis as the deposited thrombus disturbs the flow. Results are presented in a model of deep vein thrombosis (DVT), resulting from hypoxia and associated endothelial damage.

Keywords: Blood clotting; lattice Boltzmann; deep vein thrombosis

PACS Nos.: 11.25.Hf, 123.1K

1. Introduction

Thrombogenesis is a complex phenomenon involving the activation and interaction of many chemical species, triggered by one or more instigators. Two key processes are involved; the activation and aggregation of platelets and the activation of the coagulation cascade which ultimately results in fibrin formation. Activated platelets adhere to one another and to the site of injury, forming a loose plug whilst fibrin forms a mesh, capturing activated platelets and other blood cells thus strengthening the plug.

In 1856, Virchow defined a triad of factors contributing to the initiation of thrombosis. The simplified entities of the triad are stasis, changes in the vessel wall and changes in the blood [1]. A variety of approaches have been taken to model these processes and a comprehensive review of progress is reported by Anand et al [2]. A complete model involving the biochemical interactions within a physiologically relevant geometry has not yet been developed. The focus tends to be on one or, at most, two strands of Virchow's triad. If a set of equations describing the coagulation cascade is implemented, the flow field is, often neglected or oversimplified [2,3,4,5,6,7] and, where realistic flow fields are considered, the biochemistry of the system is often reduced to a very simple model [8,9]. However, some significant work has been performed in this field, simulating more physiological geometries with detailed platelet clotting models, some of which consider parts of the coagulation cascade [10,11,12,13,14]. The flow fields within these studies are modelled using the traditional Navier-Stokes equations.

There is a developing interest in using lattice Boltzmann techniques in this context. In 2004, Tamagawa and Matsuo [15] presented a model which tracked the motion of particles in a geometry with a backward facing step. Thrombosis is permitted if the shear rate and distance from the wall are sub-threshold. This study also used a distance dependent threshold shear rate which resulted in the best agreement with experimental data taken from the literature. Ouared and Chopard (2005) [16] described a lattice Boltzmann model based on shear stress, clotting is permitted in regions of low shear stress. Recently, Bernsdorf et al (2006) [17,18,19] presented a simple lattice Boltzmann model that tracks fluid age using a passive scalar tracer with a uniform source term. This simulates the final reaction in the cascade and 2D results are compared to those produced experimentally with hypercoagulable milk; a recognised blood analogue. The local rule allowing thrombus formation is that the age of the fluid must be above threshold. Qualitative agreement was observed, despite the fact that the threshold for the model was arbitrarily chosen. This work has since been improved with the use of appropriate thresholds in 3D simulations with shear stress and proximity conditions [20], providing further agreement with the experimental results.

The present paper describes the development of a lattice Boltzmann framework for modelling thrombosis. This incorporates many features of the biological system, including the response of platelets and the coagulation cascade. The framework provides a foundation for more detailed models and demonstrates the ease and suitability of the lattice Boltzmann method for modelling such a complex system of reactions. The framework has been applied in the context of a clinically relevant condition, deep vein thrombosis (DVT), and some initial results are presented.

2. Methods

2.1. *Developing the framework*

For all simulations reported in this paper, a sparse lattice Boltzmann implementation is used [21]. Efficiency is increased by solving the lattice Boltzmann equations only on the fluid nodes.

The coagulation cascade can be initiated by tissue factor or by collagen. If an injury occurs, tissue factor is released into the bloodstream. Damage to the lining of the vessel exposes collagen (a structural protein present in the vessel wall), which on contact, activates blood. Collagen also activates blood platelets, which are attracted to one another and to the vessel wall, forming an aggregate. Under normal conditions, there is a very stable balance between pro- and anti-coagulants in the blood and unless this equilibrium is disturbed, thrombosis will not occur.

Activated platelets release adenosine diphosphate (ADP). ADP is a platelet agonist [2,12,14] which stimulates a positive feedback reaction and rapidly increases the concentration of activated platelets. This process is known as synergistic activation.

Some of the mechanisms described above have been introduced into the lattice Boltzmann code as add-ons to the standard flow solver. The carrier fluid is blood, which has a density of $1060kgm^{-3}$ and a viscosity of $3.5mPas$. Massless species are used to represent normal and activated platelets and elements of the coagulation cascade and are transported by convection and diffusion using the algorithm developed by Flekkoy [25]. This is justified by the fact that platelets are discoid fragments with a density [22,23] of approximately $1000kgm^{-3}$ and a diameter [24] of $(2-4)\mu m$, hence their motion is not likely to affect either the shear or momentum of the carrier fluid. Clotting is realised using a solid surface boundary condition [17] for fluid nodes that satisfy local rules specific to the model in use. A proximity condition is used to prevent isolated clots from growing in regions where they are not attached to either the vessel wall or to existing clot.

2.2. *Example application: deep vein thrombosis*

Deep vein thrombosis (DVT) is a potentially life-threatening condition associated with periods of prolonged inactivity. *Thrombus forms in* the deep veins of the leg and may detach and travel to the lungs. The exact mechanism *is not known, but* key work by Malone [26] presents a convincing hypothesis, together with subsequent validation [27,28,29,30], which is used as a basis for our model. When the calf muscles in the leg are inactive, blood flow in the deep veins becomes sluggish and laminar. The veins contain a number of bi-leaflet valves which prevent backflow. These tend to remain in a fixed, semi-open position during periods of inactivity (see figure 1) leading to areas of stasis behind the leaflets. As oxygen is taken up and used by the tissues, there is a gradual deoxygenation of the blood in this region. Thus a prolonged period of stasis can damage the protective layer of cells (endothelium) covering the valve leaflets and may lead to exposure of the underlying collagen.

This process is not as severe for the normal vessel endothelium since it can obtain oxygen from the underlying tissues. When mobility is restored, oxygenated blood floods into the region behind the valve carrying healthy blood cells and platelets. On contact with the exposed collagen these will become activated and the coagulation cascade will be initiated.

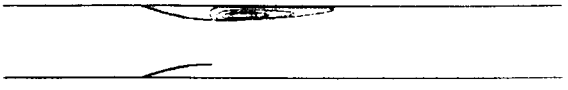

Fig. 1. Representation of geometry of venous valves and recirculation zone at $Re \approx 320$.

This sequence of events has been modelled within the lattice Boltzmann framework for thrombosis. The geometry used is two-dimensional with a 7.7mm wide parent vessel, representative of the human common femoral vein. We therefore assume that blood behaves as a Newtonian fluid. Discretisation was performed with 80 lattice points across this width, and a total bounding grid of 640*82 lattice points was used. The valve leaflets in the simulation present an approximate maximal 35% occlusion to the flow, a configuration based on experimental data from Lurie et al [32]. The average Reynolds number is approximately 320, calculated using the average velocity and diameter of the parent vessel. The geometric parameters are taken from Ashby et al [33].

As a first approach, oxygen is transported and consumed at the walls according to the constant wall flux relationship proposed by Rappitsch and Perktold [31].

$$q_w = \alpha c_w \tag{1}$$

c_w is the oxygen concentration at the wall and α is a constant, defined by the authors as $\alpha = 1.87 \times 10^{-3} cms^{-1}$. The initial and inlet concentration of oxygen is set to 1 (lattice units), since only relative values are required. Hamer and Malone [30] discovered that approximately 1 hour of stasis, followed by movement, caused a 7-fold increase in the incidence of thrombosis compared to a period of 20 minutes. From data presented by Hamer et al [28], this would be likely to cause a drop in the oxygen content in the bottom of the valve pocket to approximately 10% of the luminal value. For this reason, the threshold concentration required to cause collagen exposure was set to 0.1. When the concentration of oxygen falls below the threshold value of 0.1, on lattice nodes next to the valve leaflets, the concentration of collagen is set to be non-zero. Collagen simply becomes exposed, not released and so this species was not permitted to convect or diffuse. The next stage of the model assumes that the subject has moved, causing sufficient mixing, in order to replace the deoxygenated blood with blood of a normal oxygen concentration. The equation (2) describing the activation of platelets in contact with collagen is adapted from

the work of Wootton et al [11].

$$\frac{d[AP]}{dt} = k_t [RP] \tag{2}$$

Wootton et al [11] consider the rate of platelet accumulation per unit area and the rate constant is given as $k_t = 5 \times 10^{-3} cms^{-1}$. In order to satisfy the units of equation (2), this rate constant must be divided by the length scale of the chosen lattice to give a value in units of inverse seconds. If collagen is present at a certain lattice point, the concentration of activated platelets is increased according to equation (2) and the concentration of normal platelets is reduced by the same amount. The synergistic activation of platelets is modelled using equation (3) published by Kuharsky and Fogelson [5]. This directly increases the concentration of activated platelets, rather than modelling the transport of ADP and other agonists separately.

$$\frac{d[AP]}{dt} = k_{AP}^{AP} [AP] [RP] \tag{3}$$

$[AP]$ and $[RP]$ are the concentrations of activated and resting (normal) platelets respectively. The rate constant, k_{AP}^{AP} is given as $3 \times 10^8 M^{-1} s^{-1}$.

Collagen initiates the coagulation cascade, the first event being the conversion of factor XII into its active form, $XIIa$. A source term, with arbitrary concentration of factor $XIIa$ is released from the lattice points where collagen is exposed. The reactions in the cascade propagate and the final enzyme to be produced is thrombin. Instead of modelling all these reactions, a simple first order reaction equation (4) is used, which converts factor $XIIa$ into thrombin with a rate constant of the order of that of the slowest reaction in the cascade [4], which can also activate platelets.

$$\frac{d[IIa]}{dt} = k_{XIIa} [XIIa] \tag{4}$$

The rate constant, k_{XIIa} used is $1 \times 10^{-5} min^{-1}$ and $[IIa]$ and $[XIIa]$ represent the concentrations of thrombin and factor $XIIa$ respectively. The initial and inlet conditions for these species are concentrations of zero.

The equation representing the activation of platelets by thrombin is taken from Kuharsky and Fogelson [5], later used by Anand et al [2].

$$\frac{d[AP]}{dt} = k_{AP}^{IIa} [RP] \tag{5}$$

The rate constant, k_{AP}^{IIa} used by both groups is equal to $0.5 s^{-1}$.

The equation used for modelling the conversion of fibrinogen into fibrin (6) was taken from Zarnitsina et al [4].

$$\frac{d[Ia]}{dt} = k_1 [IIa] \tag{6}$$

$[Ia]$ and $[IIa]$ represent the concentrations of fibrin and thrombin respectively and the rate constant, $k_1 = 0.047 s^{-1}$.

Thrombus is defined as an agglomerate of activated platelets and fibrin. Clotting is permitted if the concentrations of these species are above threshold. Appropriate

data cannot be found in the literature and so arbitrary values are chosen based on the concentration distributions obtained in the simulation.

3. Results

The converged flow field was obtained after 1×10^5 iterations without the clotting model. Following this, a further 14×10^6 iterations were performed with the first stage of the model. This is equivalent to approximately 170s and takes almost 20 hours of CPU time on an NEC SX8 vector machine. This removes oxygen from the walls and exposes collagen if the oxygen concentration falls below a value of 0.1. Figure 2 shows the distribution of oxygen after 14×10^6 iterations and figure 3 shows the region of collagen exposure.

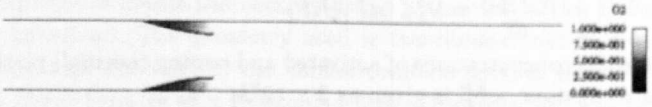

Fig. 2. Oxygen distribution following 14×10^6 iterations.

A further 14×10^6 iterations were performed for the second stage of the model where it is assumed that the subject has mobilised the leg and oxygenated blood has been reintroduced into the valve pocket. This assumption is crucial for clotting to start. The second stage of the model causes the activation of platelets and factor XII, causing a source of factor $XIIa$, ultimately resulting in the generation of fibrin. Figure 4 shows the distribution of activated platelets and figure 5 shows the distribution of fibrin after the second stage of the model.

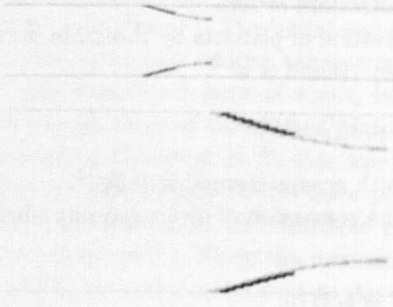

Fig. 3. Valve with collagen exposed (dark region) after 14×10^6 iterations in first stage of the model. Collagen is exposed on approximately half of the length of each valve leaflet. Lower image shows enlarged valve region.

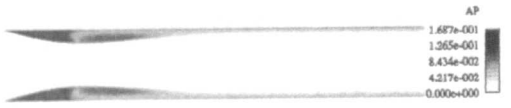

Fig. 4. Distribution of activated platelets after 14×10^6 iterations in second stage of the model.

Fig. 5. Distribution of fibrin after 14×10^6 iterations in second stage of the model.

Clotting was permitted if the concentrations of activated platelets and fibrin were above threshold. A single set of values were used to demonstrate the onset and development of clotting; $[AP]_{thresh} = 0.1632$, $[Fib]_{thresh} = 3.0 \times 10^{-4}$. The resulting clot is shown in figure 6.

Fig. 6. Thrombus deposition after 14×10^6 iterations.

4. Discussion

The aim of this paper is to describe the development of a lattice Boltzmann framework for simulating thrombosis and present preliminary results of a model of deep vein thrombosis. Damage to the endothelium is modelled, which simulates the initial stage of immobility. The result of this is captured in the second stage of the model, where the clotting cascade is initiated and platelets are activated. Platelets are also activated synergistically by other activated platelets and by thrombin, the final enzyme produced in the cascade.

The constant wall flux relationship used in the model might only be accurate when the wall is parallel to the grid. Further refinement might be justifiable if the appropriate constants can be obtained with suitable accuracy.

The diffusion coefficients used were not as in the literature because of instabilities in the diffusion model. This issue will be addressed in future work. The lowest diffusion coefficient obtainable was equivalent to approximately $4 \times 10^{-8} m^2 s^{-1}$, which is at least three orders of magnitude bigger than those required [2]. This affects the timescales over which the species are transported and thrombus forms, which in reality will be longer than 170s [30]. The rate constants, however, were all taken

from the literature which ensures that the reactions occur at the correct relative speed. The action of inhibitors has not been included and this is likely to have a significant effect on the resulting deposition.

5. Conclusion

A lattice Boltzmann framework has been developed for simulation of thrombosis and initial results in a model of deep vein thrombosis are presented. The complex process of coagulation has been simplified using existing literature on aggregation models. The cellular automata like algorithm of the lattice Boltzmann method was particularly suited to the models developed in this study which are based on local rules. The geometry of the domain is altered during simulation to mimic the formation of thrombi, which feedback as physical obstacles to the flow field. This can be performed in an efficient manner with the lattice Boltzmann method. Future work will concentrate on validating the models and extending the coagulation cascade reactions to include additional pro- and anti-coagulant reactions, in 3D geometries, in order to provide a more accurate representation of the *in vivo* system.

Acknowledgments

The lattice Boltzmann flow solver into which the clotting routines were inserted was developed by the International Lattice Boltzmann Software Development Consortium. S.E. Harrison is funded by NEC Europe Ltd. and the Engineering and Physical Sciences Research Council.

References

1. H.K. Breddin, *Semin. Thromb. Hemost.* **15**, 237 (1989).
2. M. Anand, K. Rajagopal and K.R. Rajagopal, *J. Theor. Med.* **5**, 183 (2003).
3. K.C. Jones and K.G. Mann, *J. Biol. Chem.* **269**, 23367 (1994).
4. V.I. Zarnitsina, A.V. Pokhilko and F.I. Ataullakhanov, *Thromb. Res.* **84**, 225 (1996).
5. A.L. Kuharsky and A.L. Fogelson, *Biophys. J.* **80**, 1050 (2001).
6. F.I. Ataullakhanov, V.I. Zarnitsina, A.V. Pokhilko, A.I. Lobanov and O.L. Morozova, *Int. J. Bifurcat. Chaos.* **12**, 1985 (2002).
7. E.A. Ermakova, M.A. Panteleev and E.E. Shnol, *Pathophysiol. Haemost. Thromb.* **34**, 135 (2005).
8. A. Narracott, S. Smith, P. Lawford, H. Liu, R. Himeno, I. Wilkinson, P. Griffiths and R. Hose, *J. Artif. Organs.* **8**, 56 (2005).
9. P. Friedrich and A.J. Reininger, *Thromb. Haemostasis.* **73**, 66 (1995).
10. E.N. Sorensen, G.W. Burgreen, W.R. Wagner and J.F. Antaki, *Ann. Biomed. Eng* **27**, 436 (1999).
11. D.M. Wootton, C.P. Markou, S.R. Hanson and D.N. Ku, *Ann. Biomed. Eng.* **29**, 321 (2001).
12. A.L. Fogelson and R.D. Guy, *Math. Med. Biol.* **21**, 293 (2004).
13. A.S. Bedekar, K. Pant, Y. Ventikos and S. Sundaram, *Food Bioprod. Process.* **83**, 118 (2005).
14. P.D. Goodman, E.T. Barlow, P.M. Crapo, S.F. Mohammad and K.A. Solen, *Ann. Biomed. Eng.* **33**, 780 (2005).

15. M. Tamagawa and S. Matsuo, *JSME Int. J. C.-Mech. Sy.* **47**, 1027 (2004).
16. R. Ouared and B. Chopard, *J. Stat. Phys.* **121**, 209 (2005).
17. J. Bernsdorf, S.E. Harrison, S.M. Smith, P.V. Lawford and D.R. Hose, *Math. Comput. Simulat.* **72**, 89 (2006).
18. J. Bernsdorf, S.E. Harrison, S.M. Smith, P.V. Lawford and D.R. Hose, *Int. J. Bioinformat. Res. Appl.* **2**, 371 (2006).
19. J. Bernsdorf, S.E. Harrison, S.M. Smith, P.V. Lawford and D.R. Hose, *Comput. Math. Appl.* In press (2006)
20. S.E. Harrison, S.M. Smith, J. Bernsdorf, D.R.Hose and P.V. Lawford, Submitted to *J. Biomech.* (2006).
21. M. Schulz,M. Krafczyk, J. Tölke and E. Rank, Proceedings of the 3rd International FORTWIHR Conference on High-Performance Scientific and Engineering Computing., Erlangen, p.115-122 (2002).
22. H.J. Weiss, Platelets: Pathophysiology and Antiplatelet Drug Therapy. (New York, Alan R. Liss, Inc 1982).
23. E. Morgenstern. Human platelet morphology/ultrastructure. In: F.v. Bruchhausen and U. Walter (eds) Platelets and Their Factors. (Berlin, Springer. p. 27-60, 1997).
24. E.N. Marieb, Human Anatomy and Physiology. 4th edition. (California, Benjamin/Cummings Publishing Company, 1998).
25. E.G. Flekkoy, *Phys. Rev. E* **47**, 4247 (1993).
26. P.C. Malone, *Med. Hypotheses.* **3**, 189 (1977).
27. P.C. Malone and C.J. Morris, *J. Pathol.* **125**, 119 (1978).
28. J.D. Hamer, P.C. Malone and I.A. Silver, *Brit. J. Surg.* **68**, 166 (1981).
29. G.C. Okoye, J.H. Evans, J. Beattie, G.D.O. Lowe, A.R. Lorimer and C.D. Forbes, *Thromb. Haemostasis* **51**, 103 (1984).
30. J.D. Hamer and P.C. Malone, *Ann. Roy. Coll. Surg.* **66**, 416 (1984).
31. G. Rappitsch and K. Perktold, *J. Biomech.* **29**, 207 (1996).
32. F. Lurie, R.L. Kistner, B. Eklof and D. Kessler, *J. Vasc. Surg.* **38**, 955 (2003).
33. E.C. Ashby, N.S. Ashford and M.J. Campbell, *Lancet.* **345**, 419 (1995).

Available online at www.sciencedirect.com
ScienceDirect
Mathematics and Computers in Simulation 72 (2006) 89–92
MATHEMATICS AND COMPUTERS IN SIMULATION
www.elsevier.com/locate/matcom

Numerical simulation of clotting processes: A lattice Boltzmann application in medical physics

J. Bernsdorf[a,*], S.E. Harrison[b], S.M. Smith[b], P.V. Lawford[b], D.R. Hose[b]

[a] *C&C Research Laboratories, NEC Europe Ltd., Rathausallee 10, D-53757 Sankt Augustin, Germany*
[b] *Medical Physics and Clinical Engineering, University of Sheffield, Royal Hallamshire Hospital, Glossop Road, Sheffield S10 2JF, UK*

Available online 3 July 2006

Abstract

In this paper, the concurrent numerical simulation of clotting and unsteady flow within a stenosed artery is described. The simplified blood clotting process is based on a residence time model, using a lattice Boltzmann flow solver with passive scalar advective–diffusive transport. Simulation results of a stenosed model artery are presented together with experimental blood analogue results. Aspects of an efficient unstructured implementation are briefly reviewed.

Keywords: Lattice Boltzmann; Blood flow; Blood clotting

1. Introduction

The formation of deposits (atherosclerotic plaques) within arteries, commonly leading to vessel stenosis, are features of cardiovascular disease. It is likely that regions of stagnant or recirculating flow will develop downstream of a stenosis and if blood remains in such a region for a prolonged period of time, thrombosis may occur.

To simulate the clotting process numerically, we extended the lattice Boltzmann method in two ways: an advection–diffusion scheme for a passive scalar [3] was applied in order to estimate the residence time of the fluid (blood), and a solidification procedure depending on the 'age' of the fluid was introduced. In order to perform simulations with sufficient resolution, it is necessary to avoid allocating memory for the large solid fraction surrounding the flow channels. Therefore, we implemented an unstructured lattice Boltzmann scheme allocating memory only for unoccupied lattice nodes (see Section 3).

2. Aging and clotting model

Thrombosis can be initiated by shear rates of sufficient magnitude to cause cell lysis and release clotting factors. Following activation, the route to coagulation involves a unique cascade of reactions. Several attempts have been made to model the relevant molecular pathways [10,8,1] but these fail to consider realistic flow fields and their development with the growth of the thrombus.

* Corresponding author.
E-mail addresses: j.bernsdorf@ccrl-nece.de (J. Bernsdorf), s.harrison@sheffield.ac.uk (S.E. Harrison), stephen.smith@sheffield.ac.uk (S.M. Smith), p.lawford@sheffield.ac.uk (P.V. Lawford), d.r.hose@sheffield.ac.uk (D.R. Hose).

0378-4754/$32.00
doi:10.1016/j.matcom.2006.05.008

In our simulations, we assume that previously activated fluid enters the flow domain at the inlet. The complex process of blood coagulation is replaced by the adjustable parameter 'residence time': if the activated fluid is 'old enough', it solidifies. Therefore, the first extension of the standard flow solver is a method to determine the 'age' of the fluid.

A passive scalar is used as a tracer to estimate the residence time of activated fluid in our model. This tracer is transported by advection–diffusion and a small, constant quantity is injected at every lattice node each time step. The local concentration of the tracer is therefore proportional to the average 'age' of the fluid which can be used as a threshold parameter within the clotting model.

For the carrier fluid and the tracer, separate particle density distribution functions with different relaxation times (relating to the kinematic viscosity or molecular diffusion coefficient) are used, based on the algorithm of Flekkøy [3]. All density distribution functions are coupled via the flow velocity which is determined from the carrier fluid. Feedback of species distributions on the flow field is neglected so only passive scalar transport is considered.

In this approach, we assume that the fluid is able to clot after a certain elapsed period post-activation. The local age of the fluid is determined by the concentration of the passive scalar tracer, as described above. When the local concentration of the tracer (computed at each timestep) reaches a given threshold, solidification takes place—a fluid node becomes an obstacle node and the solid surface boundary condition is applied. In the case of an unstructured implementation as described in Section 3, the adjacency list must be updated.

During subsequent iterations, the flow field and age distribution adapt to the new geometry, while further clotting on adjacent fluid nodes can occur. This allows for the concurrent simulation of solidification and flow, which is believed to be essential for capturing the complex flow-related clot morphology.

The additional cost of the subroutine for identifying new solid nodes by the age threshold and updating the adjacency list is below 5% of the overall cost of one iteration.

3. Unstructured lattice Boltzmann implementation

A major concern when performing accurate 3D simulations within large datasets (e.g. when using patient geometries) is the efficiency of the implementation regarding CPU time and memory consumption. In the following section, we briefly review some features of such an implementation (which was first adapted for the LB scheme by Schulz et al. [6]), before providing an extension to model clotting. For simplicity, implementations were performed using a D3Q19 BGK scheme [5] with a bounce back wall boundary condition.

Patient MR data can be used to obtain voxel meshes of realistic computational domains. This is a well-established procedure and enables lattice Boltzmann flow simulations to be applied within anatomical geometries [4]. The geometric information is provided as Cartesian coordinates of occupied lattice nodes within a given bounding box. To fulfil the requirement of allocating memory only for the fluid nodes' distributions, a pre-processing step is introduced.

Each fluid node is tagged with a marker (the node number), and for each of the 18 adjacent directions the destination node number for the shift operation is stored in an adjacency list (see Fig. 1).

The numbering of the fluid nodes can be obtained arbitrarily, or with a hardware dependent optimised ordering scheme, e.g. by applying space filling curves ensuring efficient cache usage [2]. The order of storing the density distribution and adjacency list in the computer's memory has a significant (hardware dependent) impact on performance [9].

The memory requirement for such an unstructured flow solver scales with the number of fluid nodes and not with the size of the bounding box as is the case with a full matrix implementation.

The advection step requires a look-up in the adjacency list to identify its next neighbouring nodes, thus replacing the simple index algebra of a full matrix code where the next neighbours are $x \pm 1$, $y \pm 1$, $z \pm 1$.

For the model used in this paper, the additional cost of the indirect address look-up was found to be below 10% (on an NEC SX 6i vector computer with 8 GFLOPS peak performance) when compared to a full matrix implementation. Therefore, the break-even point is reached when as little as 10% of the overall geometry is occupied. The sustained performance was measured to be (geometry independent) >25 MLUPS (million lattice site updates per second) at >4.5 GFLOPS for a variety of sample geometries.

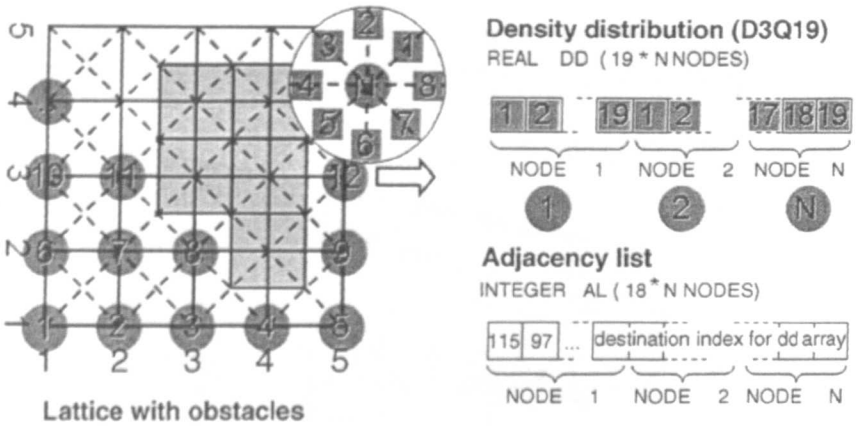

Fig. 1. 2D lattice with occupied nodes (left) and numbered fluid nodes, stored as a 1D vector with adjacency list (right).

4. Simulation results

The threshold concentration of the 'age' tracer required to initiate solidification was chosen to be small enough to allow clotting within a reasonable simulation time and large enough to avoid solidification of many lattice nodes within a few iterations.

For the 2D clotting simulation a lattice size of $lx \times ly = 532 \times 82$ nodes was used and an initial 200,000 iterations were performed to establish time-dependent flow at $Re = 550$. Following this, the tracer was injected at a constant rate. A further 300,000 iterations were performed to allow a clot to grow.

As can be seen in Fig. 2, clot growth initiates in the recirculation region downstream of the stenosis. The size of the clot increases gradually with time, whilst the flow field adapts to the new geometry. Of particular interest is the downstream migration of the recirculation region.

Our latest 3D results suggest that the final asymmetric shape of the clot might be an artefact caused by simulating turbulent flow in only two dimensions. For laminar flow, 3D results were produced which appeared to be qualitatively similar to experimental milk clotting results (see Fig. 3).

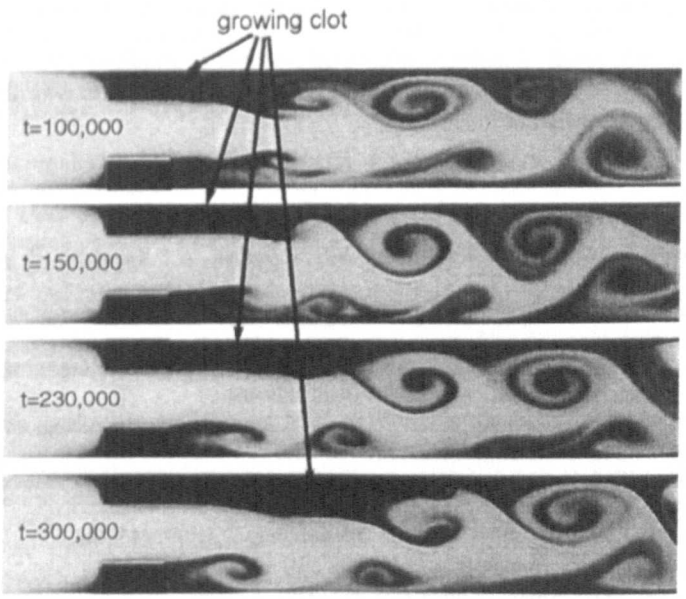

Fig. 2. Growing clot (black) downstream of a 2D stenosis at different time steps t. The age of the fluid is shown in greyscale, darker regions indicating older fluid.

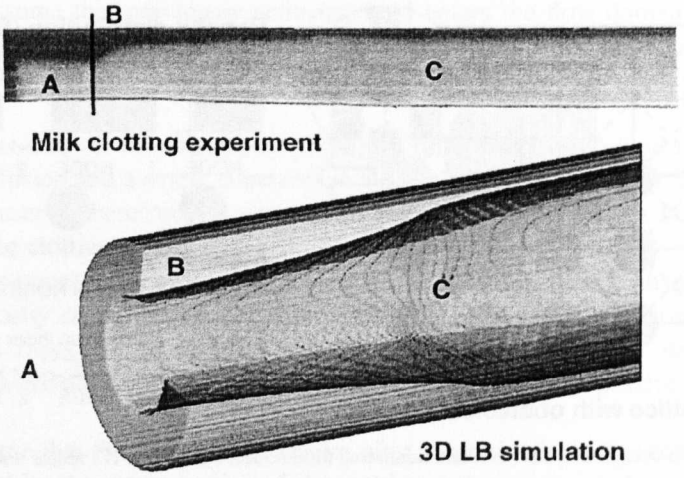

Fig. 3. Comparison of a $Re = 100$ milk clotting experiment (above) with 3D LB simulation (below). Region A indicates the stenosis bore, B the clot and C the void flow region.

Comparitive in vitro experimental data was obtained from a body of work carried out as part of another study using enzyme activated milk as a blood analogue. Enzyme activated milk has been used to simulate the latter stages of blood clotting. Full details can be found in Ref. [7].

Three-dimensional clotting simulations with turbulent flow will be performed in the future, allowing for a more accurate comparison with the experimental results.

5. Conclusion

In this paper, we have presented a novel approach for simulating clotting with the lattice Boltzmann technique. A passive scalar was used to trace the age of activated fluid. Two-dimensional concurrent flow and solidification simulation results were presented for $Re = 550$. Three-dimensional $Re = 100$ laminar results show good qualitative agreement with milk clotting experiments.

Further extensions towards a realistic blood clotting model, which are currently under development, will include pulsatile flow boundary conditions and more sophisticated clotting models derived from the theory of thrombogenesis.

Acknowledgments

The lattice Boltzmann flow solver into which the clotting routines were inserted was developed by the International Lattice Boltzmann Software Development Consortium.

References

[1] F.I. Ataullakhanov, Y.V. Krasotkina, V.I. Sarbash, R.I. Volkova, E.I. Sinauridse, A.Y. Kondratovich, Int. J. Bifurcation Chaos 12 (2002) 1969–1983.
[2] S. Donath, T. Zeiser, G. Hager, J. Habich, G. Wellein, Proc. ASIM (2005) 728–735.
[3] E.G. Flekkøy, Phys. Rev. E 47 (6) (1993) 4247–4257.
[4] A.G. Hoekstra, in: K.J. Bethe (Ed.), Computational Fluid and Solid Mechanics, Elsevier Science Ltd., 2005, pp. 672–675.
[5] Y.H. Qian, D. d'Humières, P. Lallemand, Europhys. Lett. 17 (6) (1992) 479–484.
[6] M. Schulz, M. Krafczyk, J. Tölke, E. Rank, in: M. Breuer, F. Durst, C. Zenger (Eds.), Proceedings of the 3rd International FORTWIHR Conference on HPSEC, March 12–14, 2001, Erlangen, 2002, pp. 115–122.
[7] S.M. Smith, Development of a technique for the prediction of clot localisation in vitro, Ph.D. Thesis, Medical Physics and Clinical Engineering, University of Sheffield, UK, 2005.
[8] E.N. Sorensen, G.W. Burgreen, W.R. Wagner, J.F. Antaki, Ann. Biomed. Eng. 27 (1999) 436–448.
[9] G. Wellein, T. Zeiser, S. Donath, G. Hager, Comput. Fluids 35 (2006) 910–919.
[10] V.I. Zarnitsina, A.V. Pokhilko, F.I. Ataullakhanov, Thromb. Res. 84 (1996) 225–236.

Concurrent numerical simulation of flow and blood clotting using the lattice Boltzmann technique

Jörg Bernsdorf*

C&C Research Laboratories, NEC Europe Ltd.,
Rathausallee 10, D-53757 Sankt Augustin, Germany
Fax: ++49-2241-9252-99 E-mail: j.bernsdorf@ccrl-nece.de
*Corresponding author

Sarah E. Harrison, Stephen M. Smith,
Patricia V. Lawford and D. Rodney Hose

Academic Unit of Medical Physics,
University of Sheffield, Royal Hallamshire Hospital,
Glossop Road, Sheffield, S10 2JF, UK
E-mail: s.harrison@sheffield.ac.uk
E-mail: stephen.smith@sheffield.ac.uk
E-mail: p.lawford@sheffield.ac.uk
E-mail: d.r.hose@sheffield.ac.uk

Abstract: In this paper, we describe a novel approach for a concurrent numerical simulation of the unsteady flow within an idealised stenosed artery and a simplified blood clotting process based on a residence time model. The applied numerical scheme is the lattice Boltzmann technique, which proved to be highly efficient particularly for transient flows and complex or varying geometries.

Keywords: blood clotting; stenosis; lattice Boltzmann.

Reference to this paper should be made as follows: Bernsdorf, J., Harrison, S.E., Smith, S.M., Lawford, P.V. and Hose, D.R. (xxxx) 'Concurrent numerical simulation of flow and blood clotting using the lattice Boltzmann technique', *Int. J. Bioinformatics Research and Applications*, Vol. x, No. x, pp.xxx–xxx.

Biographical notes: Jörg Bernsdorf is a Principal Researcher at the C&C Research Laboratories, NEC Europe Ltd. in St. Augustin, Germany, active in the areas of High Performance Computing (HPC) and computational fluid dynamics, particularly Lattice Boltzmann (LB) methods. He graduated in 1994 with a Diploma Degree in Physics from the University of Oldenburg. Between 1994 and 1999, he worked as a Research Scientist at the Institute of Fluid Mechanics (LSTM, University Erlangen-Nuremberg) with Professor F. Durst on complex geometry flow simulation and joined NEC in 1999. His current research involves the application of HPC/LB methods in medical physics.

Sarah E. Harrison graduated in 2003 with an MPhys(Hons.) in Physics with Medical Physics from the University of Sheffield. She is currently completing a PhD investigating cardiovascular applications of the lattice Boltzmann method, working under the supervision of D.R. Hose and P.V. Lawford and in

collaboration with J. Bernsdorf. Her studies are funded by NEC Europe Ltd. and the Engineering and Physical Sciences Research Council.

Stephen M. Smith studied Physics with Medical Physics at the University of Sheffield, graduating with a BSc(Hons.) in 1999. Following this, he completed the IPEM Basic Training for Clinical Scientists scheme and associated MSc in Medical Physics and Clinical Engineering, within Central Sheffield University Hospitals (now STH). In 2001 he began a PhD with P.V. Lawford and D.R. Hose investigating blood analogue deposition around sharp edged stenoses, with extension to computational analysis of the flow and deposits. This was awarded in 2005. Currently, He is working with Professor R.B. Panerai at the University of Leicester, investigating autonomic maintenance of blood pressure.

Patricia V. Lawford is a Senior Lecturer in Medical Physics at the University of Sheffield, located in the Royal Hallamshire Hospital. Following a First Degree in Human Anatomy and Cell Biology, she completed a doctorate in Biomedical Research in the field of Orthopaedics. She has been responsible for the UK Centre for Heart Valve evaluation, based in Sheffield and has worked as a Consultant to medical device manufacturers. Her current research interests are centred on the cardiovascular mechanics and cardiovascular implant devices.

D. Rodney Hose is a Senior Lecturer in Medical Physics at the University of Sheffield, located in the Royal Hallamshire Hospital. The early part of his career was spent in the aerospace industry, prior to completion of a doctorate in applied mechanics at the University of Manchester Institute of Science and Technology. His current research interests are centred on biomedical applications of numerical simulation, particularly in the context of the cardiovascular system.

1 Introduction

Cardiovascular disease annually claims the lives of approximately 17 million people worldwide (World Health Organisation: Cardiovascular Disease, 2005). Atherosclerosis is one particular disease which causes the formation of deposits (plaque) on the inner lining of an artery. Plaque rupture may result in emboli, which in turn may lead to myocardial infarction and ischaemic stroke. A secondary concern is that of flow disturbances associated with disease related narrowing of the vessel lumen (vessel stenosis, see Figure 1).

It is likely that areas of stagnant or recirculating flow will develop downstream of a stenosed artery and if activated blood remains in such a region for a prolonged period of time, thrombosis may occur.

Coagulation can be initiated by shear rates of sufficient magnitude to cause cell lysis and release clotting factors (Badimon and Badimon, 1989; Markou et al., 1993; Tippe and Muller-Mohnssen, 1993; Affeld and Gadischke, 1994; Affeld et al., 1995). Following activation, the route to coagulation involves a unique cascade of reactions. Several attempts have been made to model the relevant molecular pathways (Zarnitsina et al., 1996; Sorensen et al., 1999; Ataullakhanov et al., 2002a, 2002b) but these fail to consider realistic flow fields and their development with the growth of the thrombus. A comprehensive understanding of thrombosis requires full consideration of the 3 entities of Virchow's triad; blood chemistry, vessel wall properties and fluid mechanics.

Figure 1 Angiographic image of a stenosed coronary artery. Diameter of parent vessel is approximately 3 mm

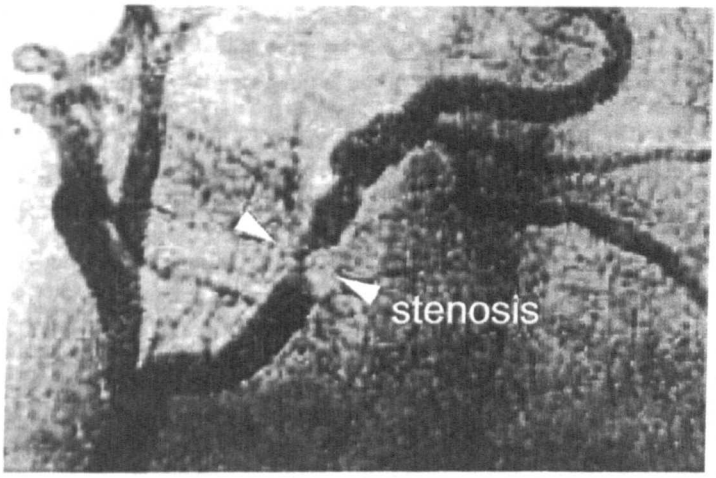

Source: Image courtesy of Dr. Julian Gunn

In this paper, we will not deal with the complex pathway to coagulation but describe a model, which covers the aspects of transient flow simulation and clotting of activated blood based on a simple residence time model. This approach is of course a very crude approximation of the highly complex biochemical processes, but it includes the interaction of a time–dependent flow-field with the varying geometry of a growing clot, which has a major influence on the final shape of the clot itself.

In Section 2, we will briefly describe the lattice Boltzmann flow simulation technique. An extension of the passive-scalar diffusion model to estimate the residence time of a fluid will be described in Section 3, followed by a residence-time based clotting model in Section 4. Section 5 will present first simulation results in comparison to experiments with milk clotting.

2 The lattice Boltzmann technique

The Lattice Boltzmann Method (LBM) is based on the numerical simulation of a time-, space- and velocity-discrete Boltzmann-type equation. The propagation and interaction of the particles of an 'artificial computer fluid' are calculated in terms of the time evolution of a density distribution function, representing an ensemble average of the particle distribution. The flow velocity and the fluid density are derived from the moments of the (time- and space-discrete) density distribution function, while the pressure is linked to the density by the (model specific) speed of sound. It can be shown theoretically (Frisch et al., 1987) and by a detailed quantitative evaluation of simulation results (see, e.g., Bernsdorf et al., 1998), that these flow quantities fulfill the time dependent incompressible Navier-Stokes equations under certain conditions.

2.1 Flow simulation

For simplicity, an equidistant orthogonal lattice is chosen for common LBM computations. On every lattice node $\vec{r}_*$, a set of i real numbers, the particle density distributions N_i, is stored. The updating of the lattice essentially consists of two steps:

- a streaming process, where the particle densities are shifted in discrete time steps t_* through the lattice along the connection lines in direction $\vec{c}_i$ to their next neighbouring nodes $\vec{r}_* + \vec{c}_i$
- a relaxation step, where the new local particle distributions are computed by evaluation of an equivalent to the Boltzmann collision integrals (Δ_i^{Boltz}).

For every time step, all quantities appearing in the Navier-Stokes equations (velocity, density, pressure gradient and viscosity) can be computed locally in terms of moments of the density distribution and (for the viscosity) the relaxation parameter ω.

For the present computations, the 3D nineteen-speed (D3Q19) LBM with single time Bhatnagar-Gross-Krook (BGK) relaxation collision operator Δ_i^{Boltz} proposed by Qian et al. (1992) is used:

$$N_i(t_* + 1, \vec{r}_* + \vec{c}_i) = N_i(t_*, \vec{r}_*) + \Delta_i^{\text{Boltz}}$$
$$\Delta_i^{\text{Boltz}} = \omega(N_i^{eq} - N_i)$$

with a local equilibrium distribution function N_i^{eq}:

$$N_i^{eq} = t_p \varrho \left\{ 1 + \frac{c_{i\alpha} u_\alpha}{c_s^2} + \frac{u_\alpha u_\beta}{2c_s^2} \left(\frac{c_{i\alpha} c_{i\beta}}{c_s^2} - \delta_{\alpha\beta} \right) \right\}.$$

This local equilibrium distribution function N_i^{eq} must be computed every time step for every node from the components of the local flow velocity u_α and u_β, the fluid density ϱ, a lattice geometry weighting factor t_p and the speed of sound c_s, which we choose in order to recover the incompressible time-dependent Navier-Stokes equations:

$$\partial_t \varrho + \partial_\alpha (\varrho u_\alpha) = 0$$
$$\partial_t (\varrho u_\alpha) + \partial_\alpha (\varrho u_\alpha u_\beta) = -\partial_\alpha p + \mu \partial_\beta (\partial_\beta u_\alpha + \partial_\alpha u_\beta).$$

The present LB method is of second-order accuracy in space and time.

2.2 Wall boundary conditions

A special feature of the LBM is the efficient and cheap handling of equidistant Cartesian meshes. In combination with a highly optimised implementation, tens of millions of grid points can be handled on large PCs or workstations. This allows one to use the 'marker and cell' approach for representing the geometry with sufficient accuracy by marking single lattice nodes as being occupied or free.

On occupied lattice nodes a so called "bounce back wall boundary condition" is applied, which simply shifts back the density distributions which have been propagated to

the occupied lattice nodes. The inversion of momentum of the shifted distributions leads to the physical zero velocity wall boundary condition.

Arbitrary complex geometries can be approximated by clusters of occupied lattice nodes, similar to a three-dimensional pixel image: the so called "voxel geometry". Geometry can either be generated analytically for generic shapes like tubes or a package of spheres or gained from medical imaging techniques such as MRI (Rothman, 1988; Bernsdorf et al., 1999).

Changing the geometry during run-time can be achieved by occupying previously free lattice nodes or vice versa without the necessity of remeshing. An appropriate local rule must be defined which decides at each iteration if a free lattice node turns into a solid or remains unoccupied. Further details of how we exploit this for the clotting simulation will be given in a later section.

An important feature of the lattice Boltzmann voxel approach is the fact that the performance is almost independent of the complexity of the geometry involved. The code we used for the simulations presented in this paper is highly optimised for vector – parallel machines such as the NEC SX series, a sustained performance of 25 million lattice site updates per second is achieved on 1 processor of an NEC SX6.

3 Aging model

Assuming that clotting occurs after a certain elapsed period since the 'activation' of blood, the residence time of the activated fluid is the most important variable for the clotting process because it indicates the likelihood of clot formation.

A passive scalar is used as a tracer to estimate the residence time of activated fluid in our model. This tracer is transported by advection-diffusion and a small, constant quantity is injected at every lattice node each time step. The local concentration of the tracer is therefore proportional to the average 'age' of the fluid (blood) which can be used as a threshold parameter within the clotting model.

The diffusion coefficient relates to the amount of mixing between different regions of a fluid and is an important parameter that must be chosen carefully. Recirculation zones with closed streamlines may be produced, for example, immediately downstream of the stenosis and the only mechanism of transport between these regions and the remaining flow is diffusion.

For the carrier fluid and the tracer, separate particle density distribution functions with different relaxation times (relating to the kinematic viscosity or molecular diffusion coefficient) are used, based on the algorithm of Flekkøy (1993). All density distribution functions are coupled via the flow velocity which is determined from the carrier fluid. Feedback of the species distributions on the flow field is neglected so only passive scalar transport is considered.

4 Clotting model

In this approach we assume that a fluid (blood) is able to clot after a certain elapsed period post activation. The local age of the fluid is determined by the concentration of the passive scalar tracer, as described in the previous section.

When the local concentration of the tracer (which is computed at each timestep) reaches a certain threshold, solidification takes place. Within the lattice Boltzmann framework this means a fluid node becomes an obstacle node and the solid surface boundary condition is applied. During subsequent iterations the flow field and age distribution adapt to the new geometry, while further clotting on adjacent fluid nodes may occur.

This allows for the concurrent simulation of solidification and flow, which is believed to be essential for capturing the complex flow related clot morphology.

5 Simulation results

With our lattice Boltzmann implementation all simulations presented in this paper were carried out on the single CPU NEC SX6i vector computer with a peak performance of 8 GFLOPS. Our code always achieved a sustained performance of more than 50% of the peak performance with about 25 million lattice site updates per second for the flow simulation alone. Although these figures indicate a very good vectorisation, the simulation of 320,000 iterations (2.75 s real time) of the turbulent Re = 550 3D flow, presented in Section 1, required 40 CPU hours.

Since the aging and clotting models require additional computational effort, the preliminary clotting simulations presented in Chapter 2 are restricted to two dimensions.

5.1 Flow through an idealised stenosis

Prior to simulations using the aging and clotting models, we required verification that the lattice Boltzmann flow solver accurately computes flow through an idealised stenosis. The stenosis is 5 mm long forming a square edged occlusion of 75% by area, 2 diameters downstream of the inlet (see Figure 2).

Figure 2 Idealised 75% stenosis geometry

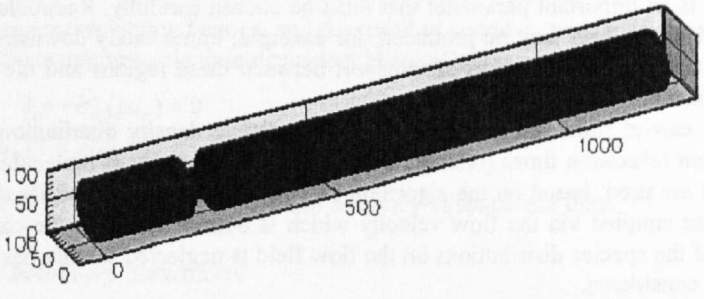

Throughout these simulations we applied a steady parabolic velocity profile at the inlet and constant pressure at the outlet. The non-Newtonian behaviour of blood was ignored.

A simulation of laminar flow with a Reynolds number of Re = 100 was performed which gave a recirculation length of 29 mm.

For the purpose of validation, a perspex test section was constructed of identical geometry. Flow visualisation was carried out at Re = 100 by the injection of a dye stream immediately upstream of the stenosis. This dye became entrained near the wall within the

stenosis, therefore demarcating the boundary layer between regions of recirculation and the central jet (Figure 3). These results show similar dimensions of the recirculation zone, although exact determination of the reattachment point is not possible.

Figure 3 Comparison of experimental (above) and numerical (below) results for flow through a 75% stenosis, Re = 100

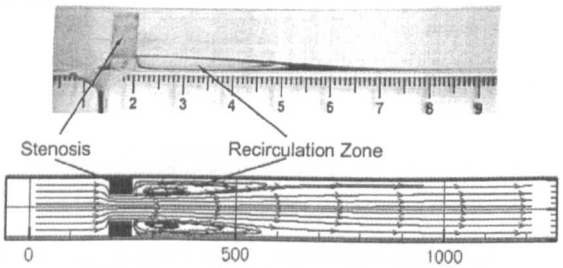

The next challenge was simulating turbulent flow at a Reynolds number of Re = 550, which is approximately the average Reynolds number within the femoral artery. Achieving turbulent flow at such low Reynolds numbers is not trivial since the flow will tend to damp back into the unsteady but laminar regime.

It transpired that the slightly rough walls (generated by randomly varying the radius ±1 lattice node) we used to model our arteries ($lx \times ly \times lz = 1214 \times 98 \times 98$) in the three-dimensional simulations were sufficient to induce and maintain turbulence. After a long transient initial period where complex vortices developed, laminar flow broke down and fully turbulent flow was observed (see Figure 4), remaining stable until the end of the simulation (320,000 iterations).

Figure 4 Snapshot of a velocity isosurface of fully developed turbulent flow through a 75% stenosis at Re = 550

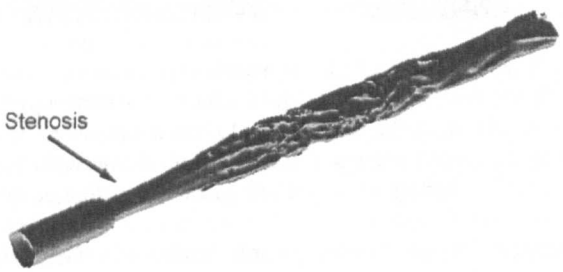

Qualitatively comparing the computational flow solutions to experimental results, good agreement can be observed between the size and speed of the flow features. A final statistical evaluation of the flow field will be carried out in the future to capture all turbulent parameters.

5.2 Clotting simulation

For the 2D clotting simulation a lattice size of $lx \times ly = 532 \times 82$ nodes was used and an initial 200,000 iterations were performed to establish time–dependent flow at Re = 550. Following this, the tracer was injected at a constant rate.

Defining a threshold for the tracer concentration, indicating the age of the fluid, allows us to implement the solidification process: all fluid lattice nodes where a concentration above this threshold is found are solidified and no further mass transport is allowed. The threshold concentration was chosen to be small enough to allow clotting within a reasonable simulation time and large enough to avoid solidification of many lattice nodes within a few iterations. Obstruction of the outlet due to clot growing from the walls must also be avoided.

A further 300,000 iterations (equivalent to 11.7 s in real time) were performed to allow a clot to grow (see Figure 5).

Figure 5 Growing clot (black) downstream of a 2D stenosis at different time steps t. The age of the fluid is shown in grey, darker regions indicating older fluid

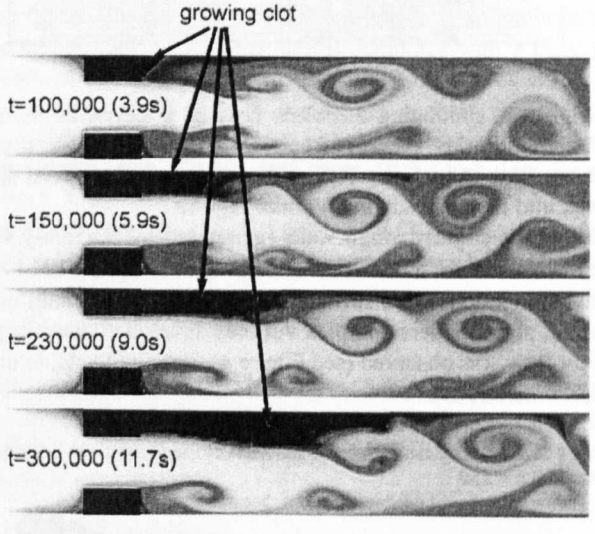

In this first approach we exploit the fact that a scale separation exists between the typical rate at which clot forms and the frequency with which flow patterns change. This means it is not necessary to adhere to the experimental time scales where a clot grows within several minutes. For the results presented here the typical timescale associated with clot growth is approximately 2 orders of magnitude greater than that associated with vortex shedding.

As can be seen in Figure 5, clot growth initiates in the recirculation domain downstream of the stenosis.

The size of the clot increases gradually with time, whilst the flow field adapts to the new geometry. Of particular interest is the downstream migration of the recirculation region. Due to vortex shedding, a secondary vortex is established leading to a second concentration maximum approximately 1 vortex diameter downstream of the clot (see Figure 6).

A secondary clot has been identified experimentally at this Reynolds number (Re = 550), though the relation between this and a secondary vortex must be investigated further.

Figure 6 Secondary milk clot (above) in the experiment and secondary peak in the tracer concentration (below: numerical simulation, darker regions indicating older fluid

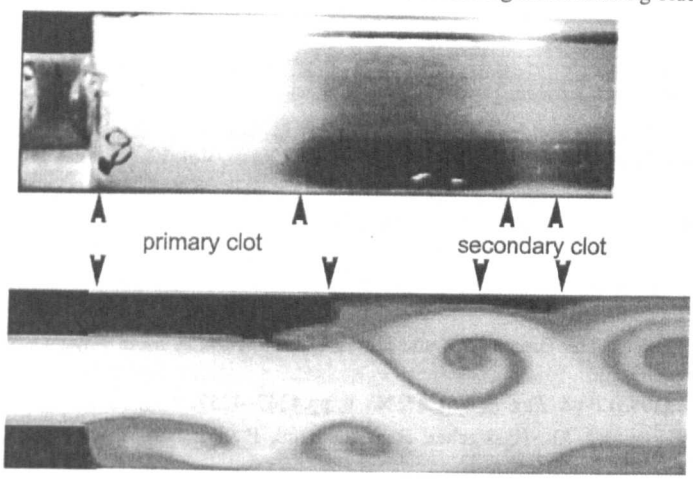

The final asymmetric shape of the clot reflects the effect of unsteady flow on the pattern formation procedure, showing some qualitative similarities with results of milk clotting experiments using comparable flows. Three-dimensional clotting simulations will be performed in future, allowing for a more accurate comparison with the experimental results.

6 Conclusion

In this paper we have presented a novel approach for simulating clotting using the lattice Boltzmann technique, with direct reference to the clotting of blood, by using a passive scalar as a tracer of the age of activated fluid.

Three-dimensional simulations of flow through an idealised stenosis show good agreement with experimental results, while preliminary two-dimensional clotting simulations produce clotting patterns comparable with milk clotting experiments.

This paper has been restricted to briefly introducing the methods and further details will be presented in a separate publication. Further simulations will include extension to three dimensions and consider more complex clotting algorithms. Taking account of the vicinity of a growing clot and flow parameters such as the wall shear stress might considerably affect the onset and development of clotting.

Of course, parabolic flow is not physiologically relevant and the use of pulsatile flow, with its inherent mixing effect, will be considered in future work. Finally, shedding of emboli from the clot, which is significant in vivo, as it leads to the lethal phenomena of myocardial infarction and ischaemic stroke, will be modelled in the future.

Acknowledgements

The Lattice Boltzmann flow solver into which the clotting routines were inserted was developed by the International Lattice Boltzmann Software Development Consortium.

References

Affeld, K. and Gadischke, J. (1994) *3rd International Symposium Reihe 17*, Biotechnik Nr.107, pp.35–40.

Affeld, K., Reininger, A.J., Gadischke, J., Grunert, K., Schmidt, S. and Thiele, F. (1995) *Artif. Organs.*, Vol. 19, pp.597–602.

Ataullakhanov, F.I., Krasotkina, Y.V., Sarbash, V.I., Volkova, R.I., Sinauridse, E.I. and Kondratovich, A.Y. (2002a) *Int. J. Bifurcation and Chaos*, Vol. 12, pp.1969–1983.

Ataullakhanov, F.I., Zarnitsina, V.I., Pokhilko, A.V., Lobanov, A.I. and Morozova, O.L. (2002b) *Int. J. Bifurcation and Chaos*, Vol. 12, pp.1985–2002.

Badimon, L. and Badimon, J.J. (1989) *J. Clin. Invest.*, Vol. 84, pp.1134–1144.

Bernsdorf, J., Günnewig, O., Hamm, W. and Münker, O. (1999) *GIT Labor-Fachzeitschrift 4/99*, Wekstoffe, pp.387–390.

Bernsdorf, J., Zeiser, Th., Brenner, G. and Durst, F. (1998) *Int. J. Mod. Phys. C*, Vol. 9, No. 8, pp.1129–1141.

Flekkøy, E.G. (1993) *Phys. Rev. E*, Vol. 47, No. 6, pp.4247–4257.

Frisch, U., d'Humières, D., Hasslacher, B., Lallemand, P., Pomeau, Y. and Rivet, J-P. (1987) *Complex Systems 1*, pp.649–707.

Markou, C.P., Hanson, S.R., Siegel, J.M. and Ku, D.N., (1993) *Adv. Bioeng.*, Vol. 26, pp.555–558.

Qian, Y.H., d'Humières, D. and Lallemand, P. (1992) *Europhys. Lett.*, Vol. 17, No. 6, pp.479–484.

Rothman, D.H. (1988) *Geophysics*, Vol. 53, pp.509–518.

Sorensen, E.N., Burgreen, G.W., Wagner, W.R. and Antaki, J.F. (1999) *Ann. Biomed. Eng.*, Vol. 27, pp.436–448, 449–458.

Tippe, A. and Muller-Mohnssen, H. (1993) *Thromb. Res.*, Vol. 72, pp.379–388.

World Health Organisation: Cardiovascular Disease (2005) http://www.who.int/cardiovascular_diseases/resources/atlas/en/.

Zarnitsina, V.I., Pokhilko, A.V. and Ataullakhanov, F.I. (1996) *Thromb. Res.*, Vol. 84, pp.225–236, 333–344.

Applying the lattice Boltzmann technique to biofluids: a novel approach to simulate blood coagulation

J.Bernsdorf [a] S.E.Harrison [b] S.M.Smith [b] P.V.Lawford [b]
D.R.Hose [b]

[a] *C&C Research Laboratories, NEC Europe Ltd., Rathausallee 10, D-53757 Sankt Augustin, Germany*
bernsdorf@ccrl-nece.de

[b] *Medical Physics and Clinical Engineering, University of Sheffield, Royal Hallamshire Hospital, Glossop Road, Sheffield, S10 2JF, UK*
{s.harrison, stephen.smith, p.lawford, d.r.hose}@sheffield.ac.uk

Abstract

In this paper we describe an extension of the lattice Boltzmann method to simulate blood clotting based on a simple residence time model. Simulation results of a stenosed model artery are presented together with experimental blood analogue results. Aspects of an efficient unstructured implementation are briefly reviewed.

Key words: Blood Clotting; Stenosis; Lattice Boltzmann

1 Introduction

Cardiovascular disease annually claims the lives of approximately 17 million people worldwide (1). Atherosclerosis is one particular disease which causes the formation of deposits (plaque) on the inner lining of an artery, commonly termed vessel stenosis (see Fig. 1). It is likely that areas of stagnant or recirculating flow will develop downstream of a stenosed artery and if activated blood remains in such a region for a prolonged period of time, thrombosis may occur.

In this paper we will not consider the complex pathway to coagulation, but describe a model which can simulate *both the transient flow* and the clotting of activated blood based on residence time. Although this is a *simplified approxi*mation of the highly complex biochemical processes, it includes the interaction

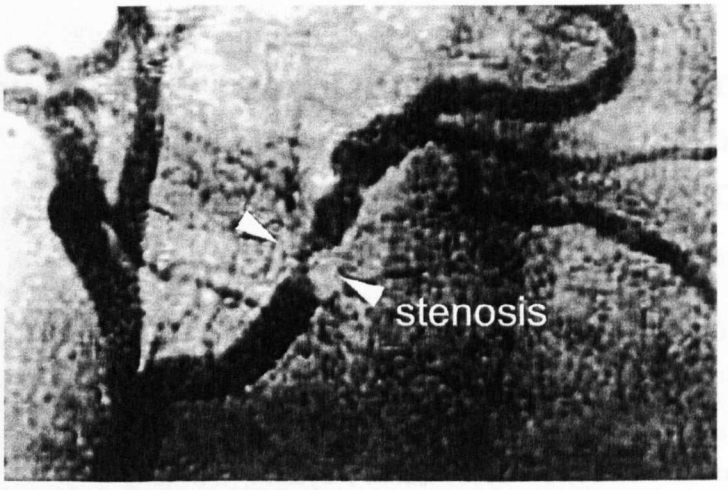

Fig. 1. Angiographic image of a stenosed coronary artery. Diameter of parent vessel is approximately 3mm (image courtesy of Dr. Julian Gunn).

of a time-dependent flow field with the varying geometry of a growing clot, which itself has a major influence on the final clot morphology.

Many blood–related features, such as flow pulsatility and vessel wall distensibility have not been considered, allowing for comparison with *in vitro* experiments using milk as a blood analogue (2).

In the following section we briefly review the unstructured implementation of the lattice Boltzmann algorithm, which prevents the allocation of memory for the solid fraction (occupied lattice nodes). This is particularly necessary for medical simulations, where the number of fluid nodes (void geometry) is often just a small percentage of the overall number of lattice nodes within the bounding box.

In section 3 we discuss adaptations of the lattice Boltzmann method for simulating blood coagulation within a stenosed artery. An unstructured lattice Boltzmann algorithm is used to compute the flow field, clotting is via addition of an 'age' scalar, itself subject to a passive scalar advection-diffusion scheme and solidification occurs based on a threshold age.

Preliminary 2D turbulent and 3D laminar clotting simulation results are presented along with milk clotting experiments (serving as a blood analogue) for comparison in section 4.

2 Efficiency aspects of the implementation

A major concern when performing accurate 3D simulations within large datasets (e.g. patient geometries) is the efficiency of the implementation with regards to CPU time and memory consumption.

The average Reynolds number in the femoral artery is approximately $Re = 550$, leading to unsteady complex flow patterns when obstructed. Therefore, the minimum diameter of the parent vessel must be discretised with 50–100 lattice units to resolve the whole range of vortices. The length of the domain is problem dependent, but to capture features such as recirculation domains at a sufficient distance upstream of the outlet, some 10 diameters of length may be required. This results in flow domains containing several million fluid lattice nodes.

The requirement for solving this problem within a reasonable time (order of days) is a code capable of doing several 10 million lattice site updates per second (MLUPS) in 3D.

This can only be achieved with:

(1) a lattice Boltzmann implementation which allocates memory only for the fluid nodes (unstructured implementation) and not for all the obstacle nodes (full matrix implementation) contained in the (often 10 times larger) bounding box (see Fig. 2)
(2) a highly efficient implementation of the advection-relaxation routine, which typically consumes a large proportion of the CPU time

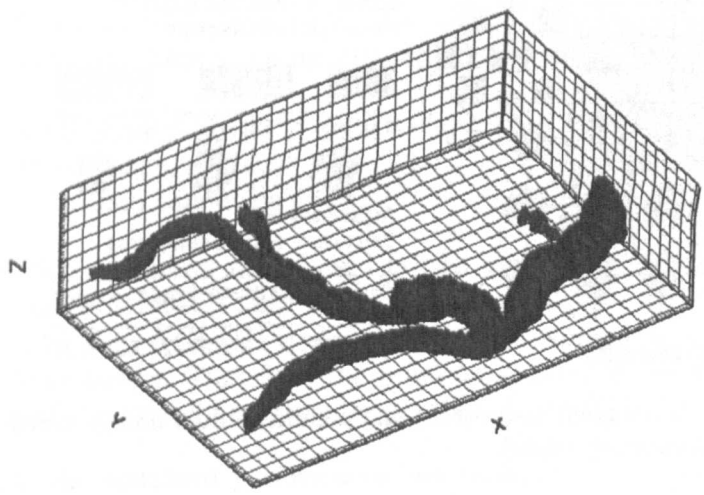

Fig. 2. MRA of the abdominal aorta and iliac bifurcation. Only 5 % of the lattice nodes within the 3.4 million node bounding box are fluid nodes.

In the following we briefly review some features of such an implementation (which was first adapted for the LB scheme by Schulz, Krafczyk et al. (3)), before we provide an extension to model clotting.

For simplicity, implementations are performed using a D3Q19 BGK scheme (4) with simple bounce back wall boundaries.

$$N_i(t_* + 1, \vec{r_*} + \vec{c_i}) = N_i(t_*, \vec{r_*}) + \triangle_i^{Boltz} \tag{1}$$

$$\triangle_i^{Boltz} = \omega \left(N_i^{eq} - N_i \right) \tag{2}$$

with a local equilibrium distribution function N_i^{eq}:

$$N_i^{eq} = t_p \, \varrho \left\{ 1 + \frac{c_{i\alpha} \, u_\alpha}{c_s^2} + \frac{u_\alpha \, u_\beta}{2 c_s^2} \left(\frac{c_{i\alpha} \, c_{i\beta}}{c_s^2} - \delta_{\alpha\beta} \right) \right\} \tag{3}$$

The geometry information is provided in terms of Cartesian coordinates of occupied lattice nodes within a given bounding box. To fulfil the first aforementioned requirement of allocating memory only for the fluid nodes' distributions, a pre-processing step is introduced.

Each fluid node is tagged with a marker (the node number), and for each of the 18 adjacent directions the destination node number for the shift operation is stored in an adjacency list (see Fig. 3).

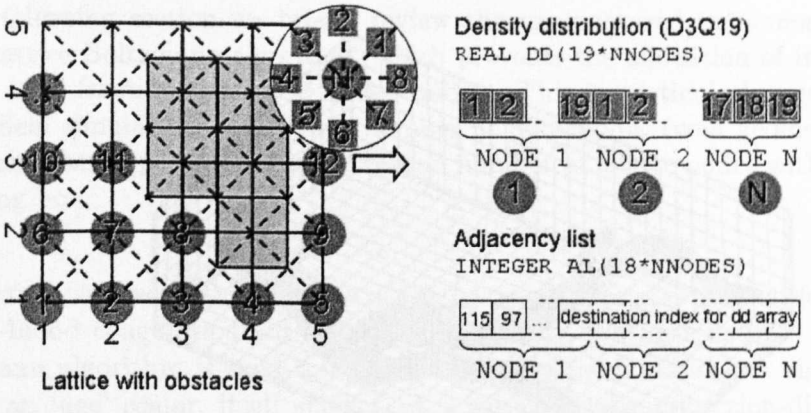

Fig. 3. 2D lattice with occupied nodes (left) and numbered fluid nodes, stored as a 1D vector with adjacency list (right).

The numbering of the fluid nodes can be obtained arbitrarily, or with a hardware dependent optimised ordering scheme, e.g. by applying space filling curves taking care of efficient cache usage (5).

The memory requirement for such an unstructured flow solver scales with the number of fluid nodes, not with the size of the bounding box as is the case with a full matrix implementation.

The advection-relaxation subroutine with one loop running over all fluid nodes (previously identified by the pre-processor) is by far the most time-consuming, so an efficient implementation of the equations (1) - (3) is mandatory.

The advection step requires a lookup in the adjacency list to identify its next neighbouring nodes, thus replacing the simple index algebra of a full matrix code where the next neighbours are just $x \pm 1, y \pm 1, z \pm 1$.

The order of storing the density distribution and adjacency list in the computer's memory has a significant (hardware dependent) impact on the performance (6). Depending on the implementation paradigm for the density distribution (double layer to avoid overwriting during propagation or clever shift strategy with a small ghost layer) and programming language, various combinations of types can be identified:

(1) **Collision optimised:** the density distribution is stored node by node in a 1D array, so the 19 densities required for the collision are adjacent in the memory.
(2) **Advection optimised:** the density distribution is stored direction-wise, starting with the zero-velocity distribution, direction 1, 2 etc. storing all cells involved in a certain shift operation close to each other in the memory.
(3) (1) or (2) with **integrated double layer**: instead of allocating a second 'double layer', the 'double cell' for each cell is stored next to the cell within the same array.
(4) (1), (2) or (3) with **mixed type:** the density distribution and adjacency list are stored within the same (REAL/INTEGER) mixed type array.

The decision for one or the other model is likely to be driven by the hardware, programming language, required performance and possible extensions, so a general rule of thumb cannot be given.

For the collision optimised model used in this paper, the additional cost of the indirect address lookup was found to be below 10 % (on an NEC SX6i vector computer with 8 GFLOPS peak performance) when compared to a full matrix implementation. Therefore, the break even point is reached when as little as 10% of the overall geometry is occupied.

Furthermore, the sustained performance was measured to be (geometry independent) $>$ 25 MLUPS at $>$ 4.5 GFLOPS for a variety of testcases with different size and geometry (such as packed beds of spheres, porous media and tube like structures with stenoses).

3 Coagulation model

Coagulation can be initiated by shear rates of sufficient magnitude to cause cell lysis and release clotting factors (7; 8; 9; 10; 11). Following activation, the route to coagulation involves a unique cascade of reactions. Several attempts have been made to model the relevant molecular pathways (12; 13; 14; 15; 16; 17) but these fail to consider realistic flow fields and their development with the growth of the thrombus.

In our simulations, we assume that all fluid in the domain can clot, providing it is old enough. The complex process of coagulation is replaced by the adjustable parameter 'age'. Fluid enters the domain with zero age and ages in proportion to the elapsed time. The age of any element of fluid at any subsequent time is equal to the residence time, which depends upon the flow conditions. If the fluid is old enough, it solidifies. The majority of fluid should be transported out of the domain without becoming old enough to clot. However, fluid that becomes trapped within recirculation zones is likely to reach the critical age, allowing it to clot. Therefore, the first extension of the standard flow solver is a method to determine the age of the fluid.

3.1 Aging model

Assuming that clotting occurs after a certain elapsed period since the 'activation' of blood, the residence time of the activated fluid is the most important variable for the clotting process because it indicates the likelihood of clot formation.

A passive scalar is used as a tracer to estimate the residence time of fluid in our model. Fluid enters the domain with a tracer concentration (age) of zero. A small, constant quantity is injected at every lattice node each time step and the tracer is transported by advection-diffusion. The local concentration of the tracer is therefore proportional to the average 'age' of the fluid which can be used as a threshold parameter within the clotting model.

The diffusion coefficient relates to the amount of mixing between different regions of the fluid and is an important parameter that must be chosen carefully. Recirculation zones with closed streamlines may be produced, for example, immediately downstream of the stenosis and the only mechanism of transport between these regions and the remaining flow is diffusion (see Fig. 4).

For the carrier fluid and the tracer, separate particle density distribution functions with different relaxation times (relating to the kinematic viscosity or molecular diffusion coefficient) are used, based on the algorithm of

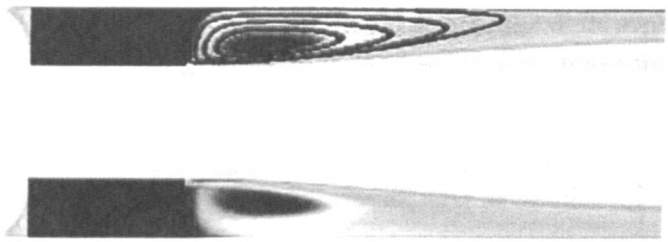

Fig. 4. Tracer species distribution ('age') of a fluid in a 2D laminar stenosis model. Streamlines are plotted in the upper recirculation zone.

Flekkøy (18). All density distribution functions are coupled via the flow velocity which is determined from the carrier fluid. Feedback of the species distributions on the flow field is neglected so only passive scalar transport is considered.

3.2 Clotting model

In this approach we assume that the fluid is able to clot after a certain elapsed period post activation. The local age of the fluid is determined by the concentration of the passive scalar tracer, as described in the previous section.

When the local concentration of the tracer (which is computed at each timestep) reaches a certain threshold, solidification takes place.

Within the lattice Boltzmann framework this means a fluid node becomes an obstacle node and the solid surface boundary condition is applied. In case of an unstructured implementation as described in section 2, an update of the adjacency list is required.

The flow field and age distribution adapt to the new geometry, while further clotting on adjacent fluid nodes can occur. This allows for the concurrent simulation of solidification and flow, which is believed to be essential for capturing the complex flow related clot morphology.

The additional cost of the subroutine for identifying new solid nodes by the age threshold and updating the adjacency list is below 5% of the overall cost of one iteration.

4 Simulation results

With our lattice Boltzmann implementation all simulations presented in this paper were carried out on the single CPU SX 6i vector computer which has

a peak performance of 8 GFLOPS. Our code always achieved a sustained performance of more than 50% of the peak performance with about 25 MLUPS for the flow simulation alone.

Parabolic velocity inlet and constant pressure outlet conditions were applied for all simulations presented in this paper.

4.1 Validation of the aging model

For the previously described aging model the most simple validation involves simulating the age distribution of a laminar fluid in a 2D channel. For this purpose a channel of $lx * ly = 200 * 42$ lattice nodes was created and allowed to develop a steady, laminar flow profile. At each subsequent iteration, a small amount of the previously described passive-scalar tracer was added to the local concentration at all lattice points, while the concentration at the inlet boundary was held to zero and constant at the outlet.

Flow velocity is maximum in the centre of the channel, falling parabolically to zero at the walls. Therefore, after a certain time has elapsed, the 'youngest' fluid will be found in the centre at the inlet and the 'oldest' fluid will be found near the outlet walls (see Fig. 5).

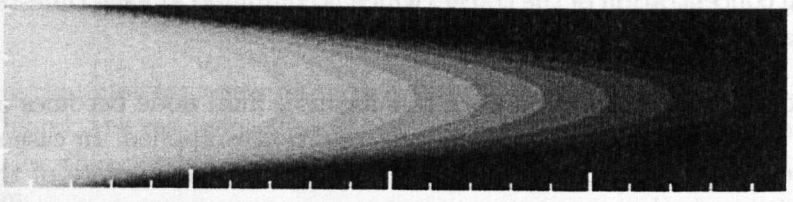

Fig. 5. Tracer concentration ('age') for parabolic channel flow.

The average age distribution can be calculated analytically for pure advection in a parabolic channel flow. A comparison of this result is in very good agreement with our numerical simulation when a very high Peclet number is applied (see Fig. 6). The Peclet number is determined using the channel width and average flow velocity.

In previous blood analogue clotting experiments, clot deposition was observed to be maximal in regions distal to the stenosis. One explanation for this is that the recirculation regions retain clottable fluid, allowing it to age and adhere.

Simulations of 2D laminar ($Re = 100$) and turbulent ($Re = 550$) channel flow containing a stenosis of 50% by diameter (equivalent to the 75% by area stenosis in 3D) clearly indicate that the regions with the highest concentration of the tracer, and hence the oldest fluid, are similar in location to the clot depositions produced experimentally.

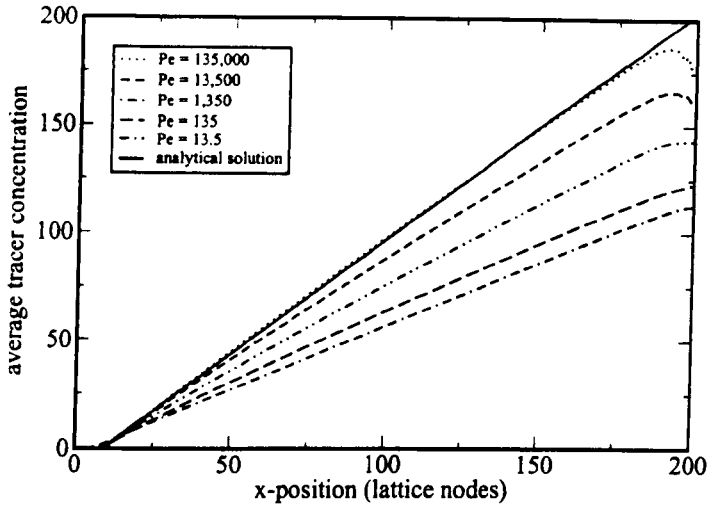

Fig. 6. Comparison of analytical and simulated age distribution for various Peclet numbers (laminar 2D channel flow).

4.2 Clotting simulation

A 2D stenosis simulation was performed to test the model with suitable parameters. A lattice size of $lx * ly = 532 * 82$ nodes was used and an initial 200,000 iterations were performed to establish time-dependent flow at $Re = 550$. Following this, the tracer was injected with a concentration of 0.002 each timestep, and the diffusion coefficient was $D = 0.000623$. This results in a Peclet number of ≈ 4000 (all quantities are dimensionless or measured in lattice units) based on the given channel width and average flow velocity.

Defining a threshold for the tracer concentration, indicating the age of the fluid, allows us to implement the solidification process: all fluid lattice nodes where a concentration above this threshold is found are solidified and no further mass transport is allowed. The threshold concentration was chosen to be 150 which was small enough to allow clotting within a reasonable simulation time and large enough to avoid solidification of many lattice nodes within a few iterations. Obstruction of the outlet due to clot growing from the walls must also be avoided.

A further 300,000 iterations were performed to allow a clot to grow (see Fig. 7).

In this first approach we exploit the fact that a scale separation exists between the typical rate at which clot forms and the frequency with which flow patterns change. This means it is not necessary to adhere to the experimental time scales where a clot grows within several minutes. For the results presented here the typical timescale associated with clot growth is approximately two orders of magnitude greater than that associated with vortex shedding.

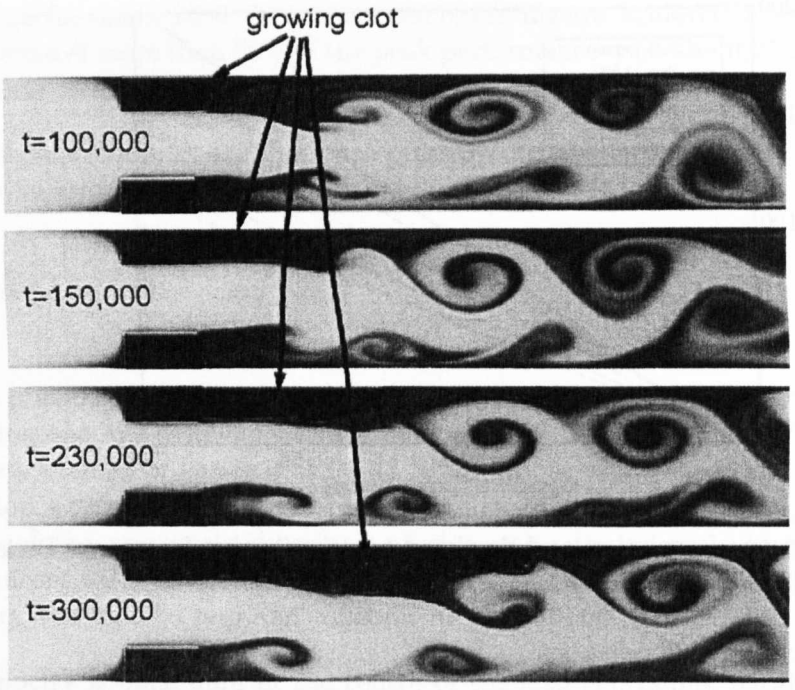

Fig. 7. Growing clot (black) downstream of a 2D stenosis at different time steps t. The age of the fluid is shown in grey, darker regions indicating older fluid.

As can be seen in Fig. 7, clot growth initiates in the recirculation domain downstream of the stenosis.

The size of the clot increases gradually with time, whilst the flow field adapts to the new geometry. Of particular interest is the downstream migration of the recirculation region.

The final asymmetric shape of the clot reflects the effect of unsteady flow on the pattern formation procedure, showing some qualitative similarities with results of milk clotting experiments using comparable flows. The model has been tested in 3D, with a simulation at the lower Reynolds number of $Re = 100$, where the flow is more predictable. A full parameter study is yet to be performed, but preliminary results show qualitative similarities with experimental milk clots (see Fig. 8). Three dimensional clotting simulations with turbulent flow will be performed in future, allowing for further comparison with the experimental results.

5 Conclusion

In this paper we have presented a novel approach for simulating clotting with the lattice Boltzmann technique, by using a passive scalar as a tracer of the

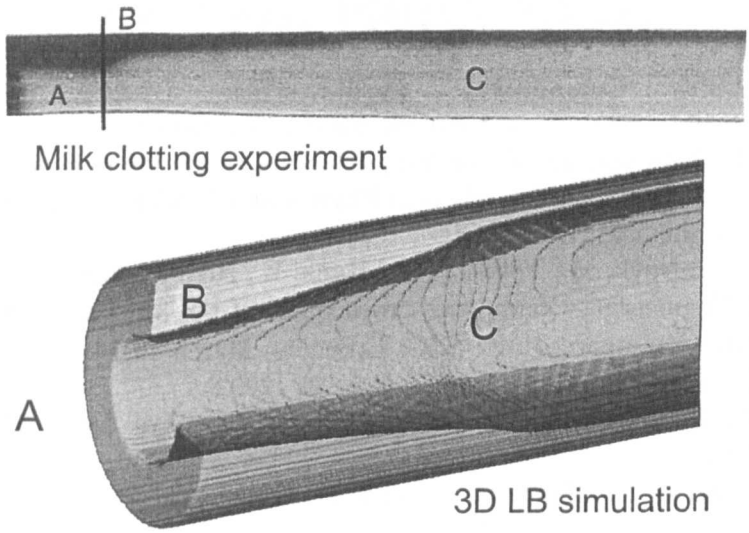

Fig. 8. Comparison of a $Re = 100$ milk clotting experiment (top) with 3D LB simulation (bottom). Region A indicates the stenosis bore, B the clot and C the void flow region.

age of activated fluid. A special focus was set on an efficient implementation aspects.

Two dimensional concurrent flow and solidification simulation results were presented for $Re = 550$, while three dimensional $Re = 100$ laminar results show good qualitative agreement with milk clotting experiments.

This paper has been restricted to briefly introducing the methods and further details will be presented in a separate publication. Future simulations will consider more complex clotting algorithms, taking account of the vicinity of a growing clot and flow parameters such as the wall shear stress, which might considerably affect the onset and development of clotting.

Acknowledgements

The lattice Boltzmann flow solver into which the clotting routines were inserted was developed by the International Lattice Boltzmann Software Development Consortium.

References

[1] World Health Organisation: Cardiovascular Disease (2005) http://www.who.int/cardiovascular_diseases/resources/atlas/en/

[2] Smith, S.M., Development of a technique for the prediction of clot localisation in vitro, Ph.D. Thesis, Medical Physics and Clinical Engineering, University of Sheffield, UK (2005).

[3] Schulz, M., Krafczyk, M., Tölke, J. and Rank, E., High-Performance Scientific and Engineering Computing,Proceedings of the 3rd International FORTWIHR Conference on HPSEC, Erlangen, March 12-14, 2001, Ed. Breuer, M., Durst, F. and C. Zenger: 115-122 (2002).

[4] Qian, Y.H., d'Humières D. and Lallemand P., Europhys. Lett., **17**(6): 479-484 (1992).

[5] Donath S., Zeiser T., Hager G., Habich J., Wellein G., Proceedings of ASIM 2005.

[6] Wellein G., Zeiser T., Donath S., and Hager G., accepted for publication in: Computer & Fluids (2005).

[7] Badimon L.and Badimon JJ., J. Clin. Invest. **84**: 1134-1144 (1989).

[8] Markou C.P., Hanson S.R., Siegel J.M., Ku D.N., Adv. Bioeng **26**: 555-558 (1993).

[9] Tippe A. and Muller-Mohnssen H., Thromb. Res. **72**: 379-388 (1993).

[10] Affeld K. and Gadischke J., 3rd International Symposium Reihe 17: Biotechnik **Nr.107**: 35-40 (1994).

[11] Affeld K., Reininger A.J., Gadischke J., Grunert K., Schmidt S. and Thiele F., Artif. Organs **19**: 597-602 (1995).

[12] Zarnitsina V.I., Pokhilko A.V. and Ataullakhanov F.I., Thromb. Res. **84**: 225-236 (1996).

[13] Zarnitsina V.I., Pokhilko A.V. and Ataullakhanov F.I., Thromb. Res. **84**: 333-344 (1996).

[14] Sorensen E.N., Burgreen G.W., Wagner W.R. and Antaki J.F., Ann. Biomed. Eng. **27**: 436-448 (1999).

[15] Sorensen E.N., Burgreen G.W., Wagner W.R. and Antaki J.F., Ann. Biomed. Eng. **27**: 449-458 (1999).

[16] Ataullakhanov F.I., Krasotkina Y.V., Sarbash V.I., Volkova R.I., Sinauridse E.I. and Kondratovich A.Y., Int. J. Bifurcation and Chaos **12**: 1969-1983 (2002).

[17] Ataullakhanov F.I., Zarnitsina V.I., Pokhilko A.V., Lobanov A.I. and Morozova O.L., Int. J. Bifurcation and Chaos **12**: 1985-2002 (2002).

[18] Flekkøy E.G., Phys. Rev. E **47**(6): 4247-4257 (1993).

Chapter Ten: References

1. Physiome Project. (2006) http://www.physiome.org

2. IUPS Physiome Project. (2006) http://www.physiome.org.nz/

3. Virtual Physiological Human. (2006) http://www.biomedtown.org/biomed_town/STEP/Reception/step-definitions/VirtualPhysiologicalHuman/

4. The Virtual Medical Man. (2006) http://www.telegraph.co.uk/connected/main.jhtml?xml=/connected/2006/10/31/ecman31.xml

5. Aneurist. (2006) http://www.aneurist.org/

6. Coast. (2006) www.complex-automata.org

7. Marieb, E.N. (1998) *Human Anatomy and Physiology*. 4th edition, Benjamin/Cummings Publishing Company, California.

8. Beck, W.S. (1991) Erythropoiesis and introduction to the anemias. *In*: W.S. Beck (eds) *Hematology*. 5th edition. Cambridge, MA, The MIT Press. p. 23-35.

9. Weiss, H.J. (1982) *Platelets: Pathophysiology and Antiplatelet Drug Therapy*. Alan R. Liss, Inc., New York.

10. British Heart Foundation. *2006 Coronary heart disease statistics.* http://www.bhf.org.uk/professionals/uploaded/BHF_FINAL_UK_FACTSHEET_02052006.pdf

11. Berger, S.A. and Jou, L.-D. (2000) Flows in stenotic vessels. *Annual Review of Fluid Mechanics*, 32, 347-382.

12. World Health Organisation, *What can I do to avoid a heart attack or a stroke?* (2006) http://www.who.int/features/qa/27/en/index.html

13. World Health Organisation: *WHO publishes definitive atlas on global heart disease and stroke epidemic.* (2004) http://www.who.int/mediacentre/news/releases/2004/pr68/en/index.html

14. Steinman, D.A. (2002) Image-based computational fluid dynamics modeling in realistic arterial geometries. *Annals of Biomedical Engineering*, 30, 483-497.

15. Ku, D.N. (1997) Blood flow in arteries. *Annual Review of Fluid Mechanics*, 29, 399-434.

16. Brown, B.H., Smallwood, R.H., Barber, D.C., Lawford, P.V. and Hose, D.R. (1999) *Medical Physics and Biomedical Engineering*. Institute of Physics Publishing, Bristol.

17. McNamara, G.R. and Zanetti, G. (1988) Use of the Boltzmann equation to simulate lattice-gas automata. *Physical Review Letters*, 61, 2332-2335.

18. Kaandorp, J.A., Lowe, C.P., Frenkel, D. and Sloot, P.M.A. (1996) Effect of nutrient diffusion and flow on coral morphology. *Physical Review Letters*, 77, 2328-2331.

19. Kaandorp, J.A. and Sloot, P.M.A. (2001) Morphological models of radiate accretive growth and the influence of hydrodynamics. *Journal of Theoretical Biology*, 209, 257-274.

20. Merks, R., Hoekstra, A., Kaandorp, J. and Sloot, P. (2003) Models of coral growth: spontaneous branching, compactification and the Laplacian growth assumption. *Journal of Theoretical Biology*, 224, 153-166.

21. Masselot, A. and Chopard, B. (1998) A lattice Boltzmann model for particle transport and deposition. *Europhysics Letters*, 42, 259-264.

22. Smith, S.M. (2005) *Development of a technique for the prediction of clot localisation in vitro*. PhD thesis, University of Sheffield, Sheffield.

23. Frisch, U., Hasslacher, B. and Pomeau, Y. (1986) Lattice-gas automata for the Navier-Stokes equation. *Physical Review Letters*, 56, 1505-1508.

24. Wolfram, S. (1986) Cellular automaton fluids 1: basic theory. *Journal of Statistical Physics*, 45, 471-526.

25. *Lattice Boltzmann Method,* SCS Lattice Boltzmann Research group, University of Amsterdam. http://www.science.uva.nl/research/scs/projects/lbm_web/lbm.html

26. Dahlburg, J.P., Montgomery, D. and Doolen, G.D. (1987) Noise and compressibility in lattice-gas fluids. *Physical Review A*, 36, 2471-2474.

27. Benzi, R., Succi, S. and Vergassola, M. (1992) The lattice Boltzmann equation: theory and applications. *Physics Reports*, 222, 145-197.

28. Succi, S. (2001) *The lattice Boltzmann equation for fluid dynamics and beyond*. Oxford University Press, Oxford, UK.

29. Lallemand, P. and Luo, L.-S. (2000) Theory of the lattice Boltzmann method: dispersion, dissipation, isotropy, Galilean invariance, and stability. *Physical Review E*, 61, 6546-6562.

30. Higuera, F.J., Succi, S. and Benzi, R. (1989) Lattice gas dynamics with enhanced collisions. *Europhysics Letters*, 9, 345-349.

31. Higuera, F.J. and Jiménez, J. (1989) Boltzmann approach to lattice gas simulations. *Europhysics Letters*, 9, 663-668.

32. Qian, Y.H., d'Humières, D. and Lallemand, P. (1992) Lattice BGK models for Navier-Stokes equation. *Europhysics Letters*, 17, 479-484.

33. Luo, L.-S. *Theory of the lattice Boltzmann equation.* Lecture notes: Workshop (IV) on Soft Matters (Complex Fluids) - Low Dimensional Liquids and Approaches of Numerical Simulation to Liquid Dynamics, China Centre of Advanced Science and Technology, Beijing, China. (2000) http://research.nianet.org/~luo/Reprints-luo/2000/LectureNotes.pdf

34. Chen, S. and Doolen, G.D. (1998) Lattice Boltzmann method for fluid flows. *Annual Review of Fluid Mechanics*, 30, 329-364.

35. He, X. and Luo, L.-S. (1997) *A priori* derivation of the lattice Boltzmann equation. *Physical Review E*, 55, R6333-R6336.

36. He, X. and Luo, L.-S. (1997) Theory of the lattice Boltzmann method: from the Boltzmann equation to the lattice Boltzmann equation. *Physical Review E*, 56, 6811-6817.

37. Nourgaliev, R.R., Dinh, T.N., Theofanous, T.G. and Joseph, D. (2003) The lattice Boltzmann equation method: theoretical interpretation, numerics and implications. *International Journal of Multiphase Flow*, 29, 117-169.

38. Frisch, U. (1991) Relation between the lattice Boltzmann equation and the Navier-Stokes equations. *Physica D*, 47, 231-232.

39. Chen, H., Chen, S. and Matthaeus, W.H. (1992) Recovery of the Navier-Stokes equations using a lattice-gas Boltzmann method. *Physical Review A*, 45, R5339-R5342.

40. Reider, M.B. and Sterling, J.D. (1995) Accuracy of discrete-velocity BGK models for the simulation of the incompressible Navier-Stokes equations. *Computers and Fluids*, 24, 459-467.

41. Frisch, U., d'Humières, D., Hasslacher, B., Lallemand, P., Pomeau, Y. and Rivet, J.-P. (1987) Lattice gas hydrodynamics in two and three dimensions. *Complex Systems*, 1, 649-707.

42. He, X. and Luo, L.-S. (1997) Lattice Boltzmann model for the incompressible Navier-Stokes equation. *Journal of Statistical Physics*, 88, 927-944.

43. Succi, S. (1997) Lattice Boltzmann equation: failure or success. *Physica A*, 240, 221-228.

44. Ladd, A.J.C. (1994) Numerical simulations of particulate suspensions via a discretized Boltzmann equation. Part 1. Theoretical foundation. *Journal of Fluid Mechanics*, 271, 285-309.

45. Ladd, A.J.C. (1994) Numerical simulations of particulate suspensions via a discretized Boltzmann equation. Part 2. Numerical results. *Journal of Fluid Mechanics*, 271, 311-339.

46. Breuer, M., Bernsdorf, J., Zeiser, T. and Durst, F. (2000) Accurate computations of the laminar flow past a square cylinder based on two different methods: lattice Boltzmann and finite-volume. *International Journal of Heat and Fluid Flow*, 21, 186-196.

47. Al-Jahmany, Y.Y., Brenner, G. and Brunn, P.O. (2004) Comparative study of lattice-Boltzmann and finite volume methods for the simulation of laminar flow through a 4:1 planar contraction. *International Journal for Numerical Methods in Fluids*, 46, 903-920.

48. Noble, D.R., Georgiadis, J.G. and Buckius, R.O. (1996) Comparison of accuracy and performance for lattice Boltzmann and finite difference simulations of steady viscous flow. *International Journal for Numerical Methods in Fluids*, 23, 1-18.

49. Bernsdorf, J., Durst, F. and Schäfer, M. (1999) Comparison of cellular automata and finite volume techniques for simulation of incompressible flows in complex geometries. *International Journal for Numerical Methods in Fluids*, 29, 251-264.

50. Kandhai, D., Vidal, D.J.-E., Hoekstra, A.G., Hoefsloot, H., Iedema, P. and Sloot, P.M.A. (1999) Lattice-Boltzmann and finite element simulations of fluid flow in a SMRX static mixer reactor. *International Journal for Numerical Methods in Fluids*, 31, 1019-1033.

51. Lockard, D.P., Luo, L.-S., Milder, S.D. and Singer, B.A. (2002) Evaluation of PowerFLOW for aerodynamic applications. *Journal of Statistical Physics*, 107, 423-478.

52. Geller, S., Krafczyk, M., Tölke, J., Turek, S. and Hron, J. (2006) Benchmark computations based on lattice-Boltzmann, finite element and finite volume methods for laminar flows. *Computers and Fluids*, 35, 888-897.

53. Artoli, A.M. (2003) *Mesoscopic Computational Haemodynamics*. PhD thesis, University of Amsterdam, Amsterdam.

54. Artoli, A.M., Kandhai, D., Hoefsloot, H.C.J., Hoekstra, A.G. and Sloot, P.M.A. (2004) Lattice BGK simulations of flow in a symmetric bifurcation. *Future Generation Computer Systems*, 20, 909-916.

55. Artoli, A.M., Hoekstra, A.G. and Sloot, P.M.A. (2006) Mesoscopic simulations of systolic flow in the human abdominal aorta. *Journal of Biomechanics*, 39, 873-884.

56. Belleman, R.G. and Sloot, P.M.A. (2001) *Simulated vascular reconstruction in a virtual operating theatre.* In: (Eds). *Computer Assisted Radiology and Surgery conference (CARS)*, Berlin, Germany.

57. Abrahamyan, L., Schaap, J.A., Hoekstra, A.G., Shamonin, D., Box, F.M.A., van der Geest, R.J., Reiber, J.H.C. and Sloot, P.M.A. (2005) A problem solving environment for image-based computational hemodynamics. *Lecture Notes in Computer Science*, 3514, 287-294.

58. Hirabayashi, M., Ohta, M., Rüfenacht, D.A. and Chopard, B. (2003) Characterization of flow reduction properties in an aneurysm due to a stent. *Physical Review E*, 68, 021918.

59. Hirabayashi, M., Ohta, M., Rüfenacht, D.A. and Chopard, B. (2003) *Lattice Boltzmann analysis of the flow reduction mechanism in stented cerebral aneurysms for the endovascular treatment.* In: P.M.A. Sloot (Eds). *International Conference on Computational Science*, Saint Petersburg. p.1044-1053.

60. Hirabayashi, M., Ohta, M., Rüfenacht, D.A. and Chopard, B. (2004) A lattice Boltzmann study of blood flow in stented aneurism. *Future Generation Computer Systems*, 20, 925-934.

61. Ouared, R. and Chopard, B. (2005) Lattice Boltzmann simulations of blood flow: non-Newtonian rheology and clotting processes. *Journal of Statistical Physics*, 121, 209-221.

62. Chopard, B., Ouared, R. and Rüfenacht, D.A. (2006) A lattice Boltzmann simulation of clotting in stented aneurysms and comparison with velocity or shear rate reductions. *Mathematics and Computers in Simulation*, 72, 108-112.

63. Dupin, M.M., Halliday, I. and Care, C.M. (2003) Multi-component lattice Boltzmann equation for mesoscale blood flow. *Journal of Physics A: Mathematical and General*, 36, 8517-8534.

64. Dupin, M.M., Halliday, I. and Care, C.M. (2006) A multi-component lattice Boltzmann scheme: towards the mesoscale simulation of blood flow. *Medical Engineering & Physics*, 28, 13-18.

65. Materials Modelling Group (2006). *Multi component fluid flow.* Sheffield Hallam University. http://www.shu.ac.uk/research/meri/mmg/research/fluid-flow.html

66. Krafczyk, M., Cerrolaza, M., Schulz, M. and Rank, E. (1998) Analysis of 3D transient blood flow passing through an artificial aortic valve by Lattice-Boltzmann methods. *Journal of Biomechanics*, 31, 453-462.

67. Krafczyk, M., Tölke, J., Rank, E. and Schulz, M. (2001) Two-dimensional simulation of fluid-structure interaction using lattice Boltzmann methods. *Computers and Structures*, 79, 2031-2037.

68. Fang, H., Wang, Z., Lin, Z. and Liu, M. (2002) Lattice Boltzmann method for simulating the viscous flow in large distensible blood vessels. *Physical Review E*, 65, 051925.

69. Li, H., Fang, H., Lin, Z., Xu, S. and Chen, S. (2004) Lattice Boltzmann simulation of particle suspensions in a two-dimensional symmetric stenotic artery. *Physical Review E*, 69, 031919.

70. Boyd, J., Buick, J.M., Cosgrove, J.A. and Stansell, P. (2004) Application of the lattice Boltzmann method to arterial flow simulation: investigation of boundary conditions for complex arterial geometries. *Australasian Physical and Engineering Sciences in Medicine*, 27, 207-212.

71. Boyd, J., Buick, J., Cosgrove, J.A. and Stansell, P. (2005) Application of the lattice Boltzmann model to simulated stenosis growth in a two-dimensional carotid artery. *Physics in Medicine and Biology*, 50, 4783-4796.

72. Migliorini, C., Qian, Y., Chen, H., Brown, E.B., Jain, R.K. and Munn, L.L. (2002) Red blood cells augment leukocyte rolling in a virtual blood vessel. *Biophysical Journal*, 83, 1834-1841.

73. Sun, C., Migliorini, C. and Munn, L.L. (2003) Red blood cells initiate leukocyte rolling in postcapillary expansions: a lattice Boltzmann analysis. *Biophysical Journal*, 85, 208-222.

74. Sun, C. and Munn, L.L. (2006) Influence of erythrocyte aggregation on leukocyte margination in postcapillary expansions: a lattice Boltzmann analysis. *Physica A*, 362, 191-196.

75. Beronov, K.N. and Durst, F. (2005) Numerische Simulation pulsierender Strömungen in Blutgefäßen des Gehirns mit Aneurysmen mittels Lattice-Boltzmann-Verfahren. *Zeitschrift für Medizinische Physik*, 15, 257-264.

76. Chen, C., Chen, H., Freed, D., Shock, R., Staroselsky, I., Zhang, R., Coşkun, A.Ü., Stone, P.H. and Feldman, C.L. (2006) Simulation of blood flow using extended Boltzmann kinetic approach. *Physica A*, 362, 174-181.

77. Winterer, V.-H. *Direct simulation of turbulent flow using digital lattice Boltzmann automata.* Rechenzentrum Universität Freiburg. (2006) http://omnibus.uni-freiburg.de/~vowi/BFG-Talk/geier/bfg/dlb1.html

78. Schulz, M., Krafczyk, M., Tölke, J. and Rank, E. (2002) *Parallelization strategies and efficiency of CFD computations in complex geometries using lattice-Boltzmann methods on high-performance computers.* In: M. Breuer, F. Durst, and C. Zenger (Eds). *Proceedings of the 3rd International FORTWIHR Conference on High-Performance Scientific and Engineering Computing.*, Erlangen. p.115-122.

79. Bernsdorf, J., Harrison, S.E., Smith, S.M., Lawford, P.V. and Hose, D.R. (2006) Numerical simulation of clotting processes: A lattice Boltzmann application in medical physics. *Mathematics and Computers in Simulation*, 72, 89-92.

80. NEC. *HPCE, SX Series*. (2006). http://www.hpce.nec.com/47.0.html

81. Ziegler, D.P. (1993) Boundary conditions for lattice Boltzmann simulations. *Journal of Statistical Physics*, 71, 1171-1177.

82. He, X., Zou, Q., Luo, L.-S. and Dembo, M. (1997) Analytical solutions of simple flows and analysis of nonslip boundary conditions for the lattice Boltzmann BGK model. *Journal of Statistical Physics*, 87, 115-136.

83. Kandhai, D., Koponen, A., Hoekstra, A., Kataja, M., Timonen, J. and Sloot, P.M.A. (1999) Implementation aspects of 3D lattice-BGK: boundaries, accuracy, and a new fast relaxation method. *Journal of Computational Physics*, 150, 482-501.

84. Noble, D.R., Chen, S., Georgiadis, J.G. and Buckius, R.O. (1995) A consistent hydrodynamic boundary condition for the lattice Boltzmann method. *Physics of Fluids*, 7, 203-209.

85. Chen, S., Martínez, D. and Mei, R. (1996) On boundary conditions in lattice Boltzmann methods. *Physics of Fluids*, 8, 2527-2536.

86. Zou, Q. and He, X. (1997) On pressure and velocity boundary conditions for the lattice Boltzmann BGK model. *Physics of Fluids*, 9, 1591-1598.

87. Inamuro, T., Yoshino, M. and Ogino, F. (1995) A non-slip boundary condition for lattice Boltzmann simulations. *Physics of Fluids*, 7, 2928-2930.

88. Ginzburg, I. and d'Humières, D. (2003) Multireflection boundary conditions for lattice Boltzmann models. *Physical Review E*, 68, 066614.

89. White, F.M. (2003) *Fluid Mechanics*. 5th edition, McGraw-Hill, London, UK.

90. Hoekstra, A.G. (2005) Image-based computational hemodynamics with the lattice Boltzmann method. *In*: K.J. Bathe (eds) *Computational Fluid and Solid Mechanics 2005*. Elsevier Science Ltd. p. 672-675.

91. Artoli, A.M., Abrahamyan, L. and Hoekstra, A.G. (2004) Accuracy versus performance in lattice Boltzmann simulations of systolic flows. *Lecture Notes in Computer Science*, 3039, 548-555.

92. Artoli, A.M., Hoekstra, A.G. and Sloot, P.M.A. (2006) Optimizing lattice Boltzmann simulations for unsteady flows. *Computers and Fluids*, 35, 227-240.

93. Abrahamyan, L., Hoekstra, A.G. and Sloot, P.M.A. (2006) Simulating time harmonic flows with the lattice Boltzmann method. *Submitted to International Journal of Modern Physics C*.

94. Goldsmith, H.L. and Turitto, V.T. (1986) Rheological aspects of thrombosis and haemostasis: basic principles and applications. *Thrombosis and Haemostasis*, 55, 415-435.

95. Zarins, C.K., Giddens, D.P., Bharadvaj, B.K., Sottiurai, V.S., Mabon, R.F. and Glagov, S. (1983) Carotid bifurcation atherosclerosis. Quantitative correlation of plaque localization with flow velocity profiles and wall shear stress. *Circulation Research*, 53, 502-514.

96. Ku, D.N., Giddens, D.P., Zarins, C.K. and Glagov, S. (1985) Pulsatile flow and atherosclerosis in the human carotid bifurcation. *Arteriosclerosis*, 5, 293-302.

97. Cassanova, R.A. and Giddens, D.P. (1978) Disorder distal to modeled stenoses in steady and pulsatile flow. *Journal of Biomechanics*, 11, 441-453.

98. Ahmed, S.A. and Giddens, D.P. (1983) Velocity measurements in steady flow through axisymmetric stenoses at moderate Reynolds numbers. *Journal of Biomechanics*, 16, 505-516.

99. Beratlis, N., Balaras, E., Parvinian, B. and Kiger, K. (2005) A numerical and experimental investigation of transitional pulsatile flow in a stenosed channel. *Journal of Biomechanical Engineering*, 127, 1147-1157.

100. Azuma, T. and Fukushima, T. (1976) Flow patterns in stenotic blood vessel models. *Biorheology*, 13, 337-355.

101. Hyun, S., Kleinstreuer, C. and Archie, J.P. (2000) Hemodynamics analyses of arterial expansions with implications to thrombosis and restenosis. *Medical Engineering & Physics*, 22, 13-27.

102. Young, D.F. (1979) Fluid mechanics of arterial stenoses. *Journal of Biomechanical Engineering*, 101, 157-175.

103. Bluestein, D., Niu, L., Schoephoerster, R.T. and Dewanjee, M.K. (1997) Fluid mechanics of arterial stenosis: relationship to the development of mural thrombus. *Annals of Biomedical Engineering*, 25, 344-356.

104. Bluestein, D., Gutierrez, C., Londono, M. and Schoephoerster, R.T. (1999) Vortex shedding in steady flow through a model of an arterial stenosis and its relevance to mural platelet deposition. *Annals of Biomedical Engineering*, 27, 763-773.

105. Lee, K.W. and Xu, X.Y. (2002) Modelling of flow and wall behaviour in a mildly stenosed tube. *Medical Engineering & Physics*, 24, 575-586.

106. Sherwin, S.J. and Blackburn, H.M. (2005) Three-dimensional instabilities and transition of steady and pulsatile axisymmetric stenotic flows. *Journal of Fluid Mechanics*, 533, 297-327.

107. Yao, H., Ang, K.C., Yeo, J.H. and Sim, E.K.W. (2000) Computational modelling of blood flow through curved stenosed arteries. *Journal of Medical Engineering and Technology*, 24, 163-168.

108. Stroud, J.S., Berger, S.A. and Saloner, D. (2000) Influence of stenosis morphology on flow through severely stenotic vessels: implications for plaque rupture. *Journal of Biomechanics*, 33, 443-455.

109. Ferguson, G.G., Eliasziw, M., Barr, H.W.K., Clagett, G.P., Barnes, R.W., Wallace, M.C., Taylor, D.W., Haynes, R.B., Finan, J.W., Hachinski, V.C. and Barnett, H.J.M. (1999) The North American Symptomatic Carotid Endarterectomy Trial: surgical results in 1415 patients. *Stroke*, 30, 1751-1758.

110. Barnett, H.J.M., Taylor, D.W., Eliasziw, M., Fox, A.J., Ferguson, G.G., Haynes, R.B., Rankin, R.N., Clagett, G.P., Hachinski, V.C., Sackett, D.L., Thorpe, K.E. and Meldrum, H.E. (1998) Benefit of carotid endarterectomy in patients with symptomatic moderate or severe stenosis. *New England Journal of Medicine*, 339, 1415-1425.

111. Chua, L.P., Yu, S.C.M. and Xue, Q. (2001) Scaling laws for wall shear stress through stenoses under steady and pulsatile flow conditions. *Proceedings of the Institution of Mechanical Engineers, Part H: Journal of Engineering in Medicine*, 215, 503-514.

112. Thornburg, H.J., Ghia, U., Osswald, G.A. and Ghia, K.N. (1992) Efficient computation of unsteady vortical flow using flow-adaptive time dependent grids. *Fluid Dynamics Research*, 10, 371-397.

113. Flekkoy, E.G. (1993) Lattice Bhatnagar-Gross-Krook models for miscible fluids. *Physical Review E*, 47, 4247-4257.

114. Flekkoy, E.G., Oxaal, U., Feder, J. and Jossang, T. (1995) Hydrodynamic dispersion at stagnation points: simulations and experiments. *Physical Review E*, 52, 4952-4962.

115. Cali, A., Succi, S., Cancelliere, A., Benzi, R. and Gramignani, M. (1992) Diffusion and hydrodynamic dispersion with the lattice Boltzmann method. *Physical Review. A*, 45, (8), 5771-5774.

116. Weimar, J.R. and Boon, J.P. (1996) Nonlinear reactions advected by a flow. *Physica A*, 224, 207-215.

117. van der Sman, R.G.M. and Ernst, M.H. (2000) Convection-diffusion lattice Boltzmann scheme for irregular lattices. *Journal of Computational Physics*, 160, 766-782.

118. Merks, R.M.H., Hoekstra, A.G. and Sloot, P.M.A. (2002) The moment propagation method for advection-diffusion in the lattice Boltzmann method: validation and Peclet number limits. *Journal of Computational Physics*, 183, 563-576.

119. Ginzburg, I. (2005) Equilibrium-type and link-type lattice Boltzmann models for generic advection and anisotropic-dispersion equation. *Advanced in Water Resources*, 28, 1171-1195.

120. Ginzburg, I. (2005) Generic boundary conditions for lattice Boltzmann models and their application to advection and anisotropic dispersion equations. *Advanced in Water Resources*, 28, 1196-1216.

121. Stockman, H.W., Glass, R.J., Cooper, C. and Rajaram, H. (1998) Accuracy and computational efficiency in 3D dispersion via lattice-Boltzmann: models for dispersion in rough fractures and double-diffusive fingering. *International Journal of Modern Physics C*, 9, 1545-1557.

122. Anand, M., Rajagopal, K. and Rajagopal, K.R. (2003) A model incorporating some of the mechanical and biochemical factors underlying clot formation and dissolution in flowing blood. *Journal of Theoretical Medicine*, 5, 183-218.

123. Jacques, S.L. and Prahl, S.A. Time-resolved diffusion theory. (1998) *Oregon Medical Laser Centre.* http://omlc.ogi.edu/classroom/ece532/class5/trdt.html

124. Isenberg, J. and Davis, G.d.V. (1975) Finite difference methods in heat and mass transfer. *In*: C. Gutfinger (eds) *Topics in Transport Phenomena*. Washington, Hemisphere Publishing Corporation. p. 457-553.

125. Paolucci, S. and Chenoweth, D.R. (1982) Stability of the explicit finite differenced transport equation. *Journal of Computational Physics*, 47, 489-496.

126. Patankar, S.V. (1980) *Numerical Heat Transfer and Fluid Flow.* Hemisphere Publishing Corporation, London.

127. Brooks, A.N. and Hughes, T.J.R. (1982) Streamline upwind/Petrov-Galerkin formulations for convection dominated flows with particular emphasis on the incompressible Navier-Stokes equations. *Computer Methods in Applied Mechanics and Engineering*, 32, 199-259.

128. Anderson, J.D. (1995) *Computational Fluid Dynamics*. McGraw-Hill, Singapore.

129. Raithby, G.D. (1976) A critical evaluation of upstream differencing applied to problems involving fluid flow. *Computer Methods in Applied Mechanics and Engineering*, 9, 75-103.

130. Raithby, G.D. (1976) Skew upstream differencing schemes for problems involving fluid flow. *Computer Methods in Applied Mechanics and Engineering*, 9, 153-164.

131. de Vahl Davis, G. and Mallinson, G.D. (1972) *False diffusion in numerical fluid mechanics.* Report number 1972/FMT/1. School of Mechanical and Industrial Engineering, University of New South Wales.

132. Rakotomalala, N., Salin, D. and Watzky, P. (1997) Miscible displacement between two parallel plates: BGK lattice gas simulations. *Journal of Fluid Mechanics*, 338, 277-297.

133. Jollès, P. (1975) Structural aspects of the milk clotting process. Comparative features with the blood clotting process. *Molecular & Cellular Biochemistry*, 7, (2), 73-85.

134. Lewis, J.M.O. and Macleod, N. (1981) *Use of a coagulable fluid in vitro for the study and prediction of flow-induced thrombogenicity in cardiovascular prostheses.* In: (Eds). *Proc II World Congress of Chemical Engineering*, Montreal. p.399-403.

135. Christy, J.R.E. and Macleod, N. (1989) The role of stasis in the clotting of blood and milk flows around solid objects. *Cardiovascular Research*, 23, 949-59.

136. Keggen, L.A., Black, M.M., Lawford, P.V., Hose, D.R. and Strachan, J.R. (1996) The use of enzyme activated milk for in vitro simulation of prosthetic valve thrombosis. *The Journal of Heart Valve Disease*, 5, 74-83.

137. Dalgleish, D.G. (1982) The Enzymatic Coagulation of Milk. *In*: P.F. Fox (eds) *Developments in Dairy Chemistry, Volume 1, The Development Series*. London, Elsevier Applied Science Publishers. p. 157-187.

138. Goff, H.D. Dairy chemistry and physics. University of Guelph, Canada. http://www.foodsci.uoguelph.ca/dairyedu/chem.html

139. Payens, T.A.J. (1977) On enzymatic clotting processes II. The colloidal instability of chymosin-treated casein micelles. *Biophysical Chemistry*, 6, 263-270.

140. de Kruif, C.G., Jeurnink, T.J.M. and Zoon, P. (1992) The viscosity of milk during the initial stages of renneting. *Netherlands Milk and Dairy Journal*, 46, 123-137.

141. Payens, T.A.J., Wiersma, A.K. and Brinkhuis, J. (1977) On enzymatic clotting processes I. Kinetics of enzyme-triggered coagulation reactions. *Biophysical Chemistry*, 6, 253-261.

142. Scott Blair, G.W. and Oosthuizen, J.C. (1961) A viscometric study of the breakdown of casein in milk by rennin and rennet. *Journal of Dairy Research*, 28, 165-173.

143. Keggen, L.A. (1996) *Simulation techniques to study the potential for flow related thrombus deposition on prosthetic heart valves.* PhD thesis, University of Sheffield, Sheffield, UK.

144. Danckwerts, P.V. (1953) Continuous flow systems. Distribution of residence times. *Chemical Engineering Science*, 2, 1-13.

145. Spalding, S.B. (1958) A note on mean residence-times in steady flows of arbitrary complexity. *Chemical Engineering Science*, 9, 74-77.

146. Danckwerts, P.V. (1958) Local residence-times in continuous-flow systems. *Chemical Engineering Science*, 9, 78-79.

147. Józsa, J. and Krámer, T. (2000) *Modelling residence time as advection-diffusion with zero-order reaction kinetics.* In: (Eds). *Proceedings of the Hydroinformatics 2000 Conference*, Cedar Rapids, Iowa.

148. Jongen, T. (2004) Extension of the age-of-fluid method to unsteady and closed-flow systems. *American Institute of Chemical Engineers Journal*, 50, 2020-2037.

149. Kunov, M.J., Steinman, D.A. and Ethier, C.R. (1996) Particle volumetric residence time calculations in arterial geometries. *Journal of Biomedical Engineering*, 118, 158-164.

150. Friedrich, P. and Reininger, A.J. (1995) Occlusive thrombus formation on indwelling catheters: in vitro investigation and computational analysis. *Thrombosis and Haemostasis*, 73, 66-72.

151. Tippe, A. and Müller-Mohnssen, H. (1993) Shear dependence of the fibrin coagulation kinetics in vitro. *Thrombosis Research*, 72, 379-388.

152. Narracott, A., Smith, S., Lawford, P., Liu, H., Himeno, R., Wilkinson, I., Griffiths, P. and Hose, R. (2005) Development and validation of models for the investigation of blood clotting in idealized stenoses and cerebral aneurysms. *Journal of Artificial Organs*, 8, 56-62.

153. Parmentier, E.M., Morton, W.A. and Petschek, H.E. (1977) Platelet aggregate formation in a region of separated blood flow. *The Physics of Fluids*, 20, 2012-2021.

154. Christy, J.R.E. and Marosek, K.W. (2000) Ultrasonic determination of clot deposition rates in a milk-based, in-vitro procedure for thrombogenicity assessment. *The Journal of Heart Valve Disease*, 9, 379-388.

155. Esteves, C.L.C., Lucey, J.A., Wang, T. and Pires, E.M.V. (2003) Effect of pH on the gelation properties of skim milk gels made from plant coagulants and chymosin. *Journal of Dairy Science*, 86, 2558-2567.

156. Carlson, A., Hill, C.G. and Olson, N.F. (1987) The kinetics of milk coagulation: IV. The kinetics of the gel-firming process. *Biotechnology and Bioengineering*, 29, 612-624.

157. Mishra, R., Govindasamy-Lucey, S. and Lucey, J.A. (2005) Rheological properties of rennet-induced gels during the coagulation and cutting

process: impact of processing conditions. *Journal of Texture Studies*, 36, 190-212.

158. Tuszynski, W.B. (1971) A kinetic model of the clotting of casein by rennet. *Journal of Dairy Research*, 38, 115-125.

159. Scott Blair, G.W. (1971) A simple model to describe the kinetics of the coagulation of casein (milk) and fibrin (blood). *Rheologica Acta*, 10, 316-318.

160. Douillard, R. (1973) Rheological analysis of curd formation. *Journal of Texture Studies*, 4, 158-165.

161. Lucey, J.A., Tamehana, M., Singh, H. and Munro, P.A. (2000) Rheological properties of milk gels formed by a combination of rennet and glucono-delta-lactone. *Journal of Dairy Research*, 67, 415-427.

162. Halliday, I., Hammond, L.A. and Care, C.M. (2002) Enhanced closure scheme for lattice Boltzmann equation hydrodynamics. *Journal of Physics A: Mathematical and General*, 35, L157-L166.

163. Artoli, A.M., Hoekstra, A.G. and Sloot, P.M.A. (2002) 3D pulsatile flow with the lattice Boltzmann BGK method. *International Journal of Modern Physics C*, 13, 1119-1134.

164. Yu, H., Girimaji, S.S. and Luo, L.-S. (2005) DNS and LES of decaying isotropic turbulence with and without frame rotation using lattice Boltzmann method. *Journal of Computational Physics*, 209, 599-616.

165. Timoshenko, S.P. and Goodier, J.N. (1970) *Theory of Elasticity*. McGraw-Hill, London, UK.

166. Weisstein, E.W. "Cubic Formula." From *MathWorld*--A Wolfram Web Resource. http://mathworld.wolfram.com/CubicFormula.html

167. Bernsdorf, J., Harrison, S.E., Smith, S.M., Lawford, P.V. and Hose, D.R. (2006) Concurrent numerical simulation of flow and blood clotting using the lattice Boltzmann technique. *Accepted for publication in International Journal of Bioinformatics Research and Applications*.

168. Bernsdorf, J., Harrison, S.E., Smith, S.M., Lawford, P.V. and Hose, D.R. (2006) Applying the lattice Boltzmann technique to biofluids: a novel approach to simulate blood coagulation. *Accepted for publication in Computers and Mathematics with Applications*.

169. Weisstein, E.W. "Brownian Motion" From *MathWorld*--A Wolfram Web Resource. http://scienceworld.wolfram.com/physics/BrownianMotion.html

170. Fox, P.F. (1989) The milk protein system. *In*: P.F. Fox (eds) *Developments in Dairy Chemistry*. Essex, UK, Elsevier Science Publishers Ltd. p. 1-54.

171. Lucey, J.A. (2002) Formation and physical properties of milk protein gels. *Journal of Dairy Science*, 85, 281-294.

172. Saito, H. (1996) Normal hemostatic mechanisms. *In*: O.D. Ratnoff and C.D. Forbes (eds) *Disorders of Hemostasis*. London, W.B. Saunders Company. p. 23-52.

173. Virchow, R. (1856) Über den Faserstoff: Phlogose und Thrombose im Gefäßsystem. (eds) *Gesammelte Abhandlungen zur wissenschaftlichen Medicin*. Frankfurt am Main, Meidinger & Sohn Corp. p. 458.

174. Virchow, R.L.K. (1998) *Thrombosis and Emboli; translated by A.C. Matzdorff and W.R. Bell.* Science History Publications, Canton, Massachusetts.

175. Affeld, K., Goubergrits, L., Kertzscher, U., Gadischke, J. and Reininger, A. (2004) Mathematical model of platelet deposition under flow conditions. *The International Journal of Artificial Organs*, 27, 699-708.

176. Breddin, H.K. (1989) Thrombosis and Virchow's triad: what is established. *Seminars in thrombosis and hemostasis*, 15, 237-239.

177. Bulger, C.M., Jacobs, C. and Patel, N.H. (2004) Epidemiology of acute deep vein thrombosis. *Techniques in Vascular and Interventional Radiology*, 7, 50-54.

178. Leopold, J.A. and Loscalzo, J. (2000) Platelets and fibrinolysis. *In*: M.C. Berndt (eds) *Platelets, Thrombosis and the Vessel Wall*. Amsterdam, Harwood academic publishers. p. 21-39.

179. Reininger, A.J., Heinzmann, U., Reininger, C.B., Friedrich, P. and Wurzinger, L.J. (1994) Flow mediated fibrin thrombus formation in an endothelium-lined model of arterial branching. *Thrombosis Research*, 74, 629-641.

180. French, J.E. (1966) Atherosclerosis in relation to the structure and function of the arterial intima, with special reference to the endothelium. *International Review of Experimental Pathology*, 5, 253-353.

181. Gross, P.L. and Aird, W.C. (2000) The endothelium and thrombosis. *Seminars in thrombosis and hemostasis*, 26, 463-478.

182. Mustard, J.F., Murphy, E.A., Rowsell, H.C. and Downie, H.G. (1962) Factors influencing thrombus formation in vivo. *American Journal of Medicine*, 33, 621-647.

183. Wessler, S. and Yin, E.T. (1969) On the mechanism of thrombosis. *Progress in Hematology*, 6, 201-32.

184. Wurzinger, L.J., Blasberg, P. and Schmid-Schönbein, H. (1985) Towards a concept of thrombosis in accelerated flow: rheology, fluid dynamics, and biochemistry. *Biorheology*, 22, 437-449.

185. Reininger, A.J., Reininger, C.B., Heinzmann, U. and Wurzinger, L.J. (1995) Residence time in niches of stagnant flow determines fibrin clot formation in an arterial branching model - detailed flow analysis and experimental results. *Thrombosis and Haemostasis*, 74, 916-922.

186. Einav, S. and Bluestein, D. (2004) Dynamics of blood flow and platelet transport in pathological vessels. *Annals of the New York Academy of Sciences*, 1015, 351-366.

187. Schmid-Schönbein, H., Born, G.V.R., Richardson, P.D., Cusack, N., Rieger, H., Forst, R., Rohling-Winkel, I., Blasberg, P. and Wehmeyer, A. (1981) Rheology of thrombotic processes in flow: the interaction of erythrocytes and thrombocytes subjected to high flow forces. *Biorheology*, 18, 415-444.

188. Marieb, E.N. (1995) *Human Anatomy and Physiology.* 3rd edition, Benjamin/Cummings Publishing Company,

189. Ruf, A., Frojmovic, M.M. and Patscheke, H. (1997) Platelet aggregation. *In*: F.v. Bruchhausen and U. Walter (eds) *Platelets and their Factors.* London, Springer. p. 83-98.

190. Kuter, D.J. (1991) Hemorrhagic disorders II. Platelets. *In*: W.S. Beck (eds) *Hematology.* 5th edition. London, The MIT Press. p. 543-575.

191. Brass, L.F. (2005) The molecular basis of platelet activation. *In*: R. Hoffman, et al. (eds) *Hematology. Basic Principles and Practice.* 4th edition. Philadelphia, Churchill Livingstone. p. 1899-1914.

192. McNicol, A., Israels, S.J. and Gerrard, J.M. (1993) Platelets. *In*: L. Poller (eds) *Recent Advances in Blood Coagulation, No. 6.* Edinburgh, Churchill Livingstone. p. 17-49.

193. Brown, C.H., Leverett, L.B., Lewis, C.W., Alfrey, C.P. and Hellums, J.D. (1975) Morphological, biochemical, and functional changes in human platelets subjected to shear stress. *The Journal of Laboratory and Clinical Medicine*, 86, 462-471.

194. Karino, T. and Goldsmith, H.L. (1979) Aggregation of human platelets in an annular vortex distal to a tubular expansion. *Microvascular Research*, 17, 217-237.

195. Hellums, J.D. (1994) 1993 Whitaker lecture: biorheology in thrombosis research. *Annals of Biomedical Engineering*, 22, 445-455.

196. Holme, P.A., Orvim, U., Hamers, M.J., Solum, N.O., Brosstad, F.R., Barstad, R.M. and Sakariassen, K.S. (1997) Shear-induced platelet activation and platelet microparticle formation at blood flow conditions as in arteries with a severe stenosis. *Arteriosclerosis Thrombosis and Vascular Biology*, 17, 646-653.

197. Zhang, J.-N., Bergeron, A.L., Yu, Q., Sun, C., McIntire, L.V., Lopez, J.A. and Dong, J.-F. (2002) Platelet aggregation and activation under complex patterns of shear stress. *Thrombosis and Haemostasis*, 88, 817-821.

198. Zhang, J.-N., Bergeron, A.L., Yu, Q., Sun, C., McBride, L., Bray, P.F. and Dong, J.-F. (2003) Duration of exposure to high fluid shear stress is critical in shear-induced platelet activation-aggregation. *Thrombosis and Haemostasis*, 90, 672-678.

199. Yin, W., Alemu, Y., Affeld, K., Jesty, J. and Bluestein, D. (2004) Flow-induced platelet activation in bileaflet and monoleaflet mechanical heart valves. *Annals of Biomedical Engineering*, 32, 1058-1066.

200. Ramstack, J.M., Zuckerman, L. and Mockros, L.F. (1979) Shear-induced activation of platelets. *Journal of Biomechanics*, 12, 113-125.

201. Wurzinger, L.J., Opitz, R., Wolf, M. and Schmid-Schönbein, H. (1985) "Shear induced platelet activation" - a critical reappraisal. *Biorheology*, 22, 399-413.

202. Brown, C.H., Lemuth, R.F., Hellums, J.D., Leverett, L.B. and Alfrey, C.P. (1975) Response of human platelets to shear stress. *Transactions: American Society for Artificial Internal Organs*, 21, 35-39.

203. Kuharsky, A.L. and Fogelson, A.L. (2001) Surface-mediated control of blood coagulation: the role of binding site densities and platelet deposition. *Biophysical Journal*, 80, 1050-1074.

204. Wikipedia Coagulation. (2006) http://en.wikipedia.org/wiki/Coagulation

205. Crowther, M.A. and Ginsberg, J.S. (2005) Venous thromboembolism. *In*: R. Hoffman, et al. (eds) *Hematology. Basic Principles and Practice.* Philadelphia, Churchill Livingstone. p. 2225-2239.

206. Rosenberg, R.D. (1991) Hemorrhagic disorders I. Protein interactions in the clotting mechanism. *In*: W.S. Beck (eds) *Hematology*. 5th edition. Cambridge, MA, The MIT Press. p. 507-542.

207. Ermakova, E.A., Panteleev, M.A. and Shnol, E.E. (2005) Blood coagulation and propagation of autowaves in flow. *Pathophysiology of Haemostasis and Thrombosis*, 34, 135-142.

208. David, T., Thomas, S. and Walker, P.G. (2001) Platelet deposition in stagnation point flow: an analytical and computational simulation. *Medical Engineering & Physics*, 23, 299-312.

209. Baumgartner, H.R. (1973) The role of blood flow in platelet adhesion, fibrin deposition, and formation of mural thrombi. *Microvascular Research*, 5, 167-179.

210. Leonard, E.F. (1972) The role of flow in thrombogenesis. *Bulletin of the New York Academy of Medicine*, 48, 273-280.

211. Karino, T. and Goldsmith, H.L. (1979) Adhesion of human platelets to collagen on the walls distal to a tubular expansion. *Microvascular Research*, 17, 238-262.

212. Schoephoerster, R.T., Oynes, F., Nunez, G., Kapadvanjwala, M. and Dewanjee, M.K. (1993) Effects of local geometry and fluid dynamics on regional platelet deposition on artificial surfaces. *Arteriosclerosis and Thrombosis*, 13, 1806-1813.

213. Affeld, K. and Gadischke, J. (1994) *Shear rate and thrombin transport.* In: D. Liepsch (Eds). *Biofluid Mechanics: Proceedings of the 3rd International Symposium.*, Munich, Germany. p.35-40.

214. Markou, C.P., Hanson, S.R., Siegel, J.M. and Ku, D.N. (1993) The role of high wall shear rate on thrombus formation in stenoses. *Advances in Bioengineering; American Society of Mechanical Engineers, Bioengineering Division (Publication) BED*, 26, 555-558.

215. Wootton, D.M., Markou, C.P., Hanson, S.R. and Ku, D.N. (2001) A mechanistic model of acute platelet accumulation in thrombogenic stenoses. *Annals of Biomedical Engineering*, 29, 321-329.

216. Badimon, L. and Badimon, J.J. (1989) Mechanisms of arterial thrombosis in nonparallel streamlines: platelet thrombi grow on the apex of stenotic severely injured vessel wall. Experimental study in the pig model. *The Journal of Clinical Investigation*, 84, 1134-1144.

217. Lassila, R., Badimon, J.J., Vallabhajosula, S. and Badimon, L. (1990) Dynamic monitoring of platelet deposition on severely damaged vessel wall in flowing blood. Effects of different stenoses on thrombus growth. *Arteriosclerosis*, 10, 306-315.

218. Strony, J., Beaudoin, A., Brands, D. and Adelman, B. (1993) Analysis of shear stress and hemodynamic factors in a model of coronary artery stenosis and thrombosis. *The American Journal of Physiology*, 265, H1787-H1796.

219. French, J.E. (1965) The structure of natural and experimental thrombi. *Annals of the Royal College of Surgeons of England*, 36, 191-200.

220. Salzman, E.W. (1972) The events that lead to thrombosis. *Bulletin of the New York Academy of Medicine*, 48, 225-234.

221. Scott Blair, G.W. and Burnett, J. (1963) An equation to describe the rate of setting of blood and milk. *Biorheology*, 1, 183-191.

222. Scott Wilson, R., Marmur, A. and Cooper, S.L. (1986) A model of deposition and embolization of proteins and platelets on biomaterial surfaces. *Annals of Biomedical Engineering*, 14, 383-400.

223. Basmadjian, D. (1989) Embolization: critical thrombus height, shear rates, and pulsatility. Patency of blood vessels. *Journal of Biomedical Materials Research*, 23, 1315-1326.

224. Goodman, P.D., Barlow, E.T., Crapo, P.M., Mohammad, S.F. and Solen, K.A. (2005) Computational model of device-induced thrombosis and thromboembolism. *Annals of Biomedical Engineering*, 33, 780-797.

225. Riha, P., Wang, X., Liao, R. and Stoltz, J.F. (1999) Elasticity and fracture strain of whole blood clots. *Clinical Hemorheology and Microcirculation*, 21, 45-49.

226. Kroll, M.H., Hellums, J.D., McIntire, L.V., Schafer, A.I. and Moake, J.L. (1996) Platelets and shear stress. *Blood*, 88, 1525-1541.

227. Baldwin, S.A. and Basmadjian, D. (1994) A mathematical model of thrombin production in blood coagulation, Part I: The sparsely covered membrane case. *Annals of Biomedical Engineering*, 22, 357-370.

228. Jones, K.C. and Mann, K.G. (1994) A model for the tissue factor pathway to thrombin. II. A mathematical simulation. *The Journal of Biological Chemistry*, 269, 23367-23373.

229. Zarnitsina, V.I., Pokhilko, A.V. and Ataullakhanov, F.I. (1996) A mathematical model for the spatio-temporal dynamics of intrinsic pathway of blood coagulation. I. The model description. *Thrombosis Research*, 84, 225-236.

230. Ataullakhanov, F.I., Zarnitsina, V.I., Pokhilko, A.V., Lobanov, A.I. and Morozova, O.L. (2002) Spatio-temporal dynamics of blood coagulation and pattern formation. A theoretical approach. *International Journal of Bifurcation and Chaos*, 12, 1985-2002.

231. Turitto, V.T. and Baumgartner, H.R. (1975) Platelet deposition on subendothelium exposed to flowing blood: mathematical analysis of physical parameters. *Transactions: American Society for Artificial Internal Organs*, 21, 593-601.

232. Fogelson, A.L. (1984) A mathematical model and numerical method for studying platelet adhesion and aggregation during blood clotting. *Journal of Computational Physics*, 56, 111-134.

233. Huang, P.Y. and Hellums, J.D. (1993) Aggregation and disaggregation kinetics of human blood platelets: Part I. Development and validation of a population balance method. *Biophysical Journal*, 65, 334-343.

234. Huang, P.Y. and Hellums, J.D. (1993) Aggregation and disaggregation kinetics of human blood platelets: Part II. Shear-induced platelet aggregation. *Biophysical Journal*, 65, 344-353.

235. Wang, N.-T. and Fogelson, A.L. (1999) Computational methods for continuum models of platelet aggregation. *Journal of Computational Physics*, 151, 649-675.

236. Sorensen, E.N., Burgreen, G.W., Wagner, W.R. and Antaki, J.F. (1999) Computational simulation of platelet deposition and activation: I. Model development and properties. *Annals of Biomedical Engineering*, 27, 436-448.

237. Sorensen, E.N., Burgreen, G.W., Wagner, W.R. and Antaki, J.F. (1999) Computational simulation of platelet deposition and activation: II. Results for Poiseuille flow over collagen. *Annals of Biomedical Engineering*, 27, 449-458.

238. Fogelson, A.L. and Guy, R.D. (2004) Platelet-wall interactions in continuum models of platelet thrombosis: formulation and numerical solution. *Mathematical Medicine and Biology*, 21, 293-334.

239. Bedekar, A.S., Pant, K., Ventikos, Y. and Sundaram, S. (2005) A computational model combining vascular biology and haemodynamics for thrombosis prediction in anatomically accurate cerebral aneurysms. *Food and Bioproducts Processing*, 83, 118-126.

240. Tamagawa, M. and Matsuo, S. (2004) Predictions of thrombus formation using lattice Boltzmann method (modeling of adhesion force for particles to wall). *JSME International Journal Series C*, 47, 1027-1034.

241. Harrison, S.E., Smith, S.M., Bernsdorf, J., Hose, D.R. and Lawford, P.V. (2006) Application and validation of the lattice Boltzmann method for modelling flow-related clotting. *Accepted for publication in Journal of Biomechanics.*

242. Morgenstern, E. (1997) Human platelet morphology/ultrastructure. *In*: F.v. Bruchhausen and U. Walter (eds) *Platelets and Their Factors*. Berlin, Springer. p. 27-60.

243. Fogelson, A.L. (1992) Continuum models of platelet aggregation: formulation and mechanical properties. *SIAM Journal of Applied Mathematics*, 52, 1089-1110.

244. Giacomini, A., Legovini, P., Antico, F., Gessoni, G., Valverde, S., Salvadego, M.M. and Manoni, F. (2001) Evaluation of platelet analysis on the ADVIA 120 hematology system. *Laboratory Hematology*, 7, 180-185.

245. Tsiang, M., Paborsky, L.R., Li, W.X., Jain, A.K., Mao, C.T., Dunn, K.E., Lee, D.W., Matsumura, S.Y., Matteucci, M.D., Coutre, S.E., Leung, L.L. and Gibbs, C.S. (1996) Protein engineering thrombin for optimal specificity and potency of anticoagulant activity *in vivo*. *Biochemistry*, 35, 16449-16457.

246. Xu, C.Q., Zeng, Y.J. and Gregersen, H. (2002) Dynamic model of the role of platelets in the blood coagulation system. *Medical Engineering & Physics*, 24, 587-593.

247. Duckert, F. (1984) Blood coagulation and fibrinolysis. *In*: C. Lentner (eds) *Geigy Scientific Tables: Physical Chemistry, Composition of Blood, Hematology, Somatometric Data*. Ciba-Geigy. p. 222-235.

248. Kuter, D.J. and Rosenberg, R.D. (1991) Hemorrhagic Disorders III. Disorders of Hemostasis. *In*: W.S. Beck (eds) *Hematology*. 5th. Cambridge, MA, The MIT Press. p. 577-598.

249. Mann, K.G., Gaffney, D. and Bovill, E.G. (1995) Molecular biology, biochemistry, and lifespan of plasma coagulation factors. *In*: E. Beutler, et al. (eds) *Williams Hematology*. 5th edition. New York, McGraw-Hill, Inc. p. 1206-1226.

250. Furie, B. and Furie, B.C. (2005) Molecular basis of blood coagulation. *In*: R. Hoffman, et al. (eds) *Hematology, Basic Principles and Practice*. 4th edition. Philadelphia, Churchill Livingstone. p. 1931-1953.

251. Cao, J. and Rittgers, S.E. (1998) Particle motion within *in vitro* models of stenosed internal carotid and left anterior descending coronary arteries. *Annals of Biomedical Engineering*, 26, 190-199.

252. Boreda, R., Fatemi, R.S. and Rittgers, S.E. (1995) Potential for platelet stimulation in critically stenosed carotid and coronary arteries. *Journal of Vascular Investigation*, 1, 26-37.

253. Wootton, D.M. and Ku, D.N. (1999) Fluid mechanics of vascular systems, diseases, and thrombosis. *Annual Review of Biomedical Engineering*, 1, 299-329.

254. NHS Direct Health Encyclopaedia: Deep Vein Thrombosis. (2006) http://www.nhsdirect.nhs.uk/articles/article.aspx?articleId=122

255. Simpson, K. (1940) Shelter deaths from pulmonary embolism. *The Lancet*, 236, 744.

256. BBC News: *Worker gets DVT sitting at desk.* (2006) http://news.bbc.co.uk/1/hi/england/bristol/4753833.stm

257. BBC News: *Computer game teenager gets DVT.* (2004) http://news.bbc.co.uk/1/hi/health/3441237.stm

258. McLachlin, J. and Paterson, J.C. (1951) Some basic observations on venous thrombosis and pulmonary embolism. *Surgery, Gynecology and Obstetrics*, 93, 1-8.

259. McLachlin, A.D., McLachlin, J.A., Jory, T.A. and Rawling, E.G. (1960) Venous stasis in the lower extremities. *Annals of Surgery*, 152, 678-685.

260. Malone, P.C. (1977) A hypothesis concerning the aetiology of venous thrombosis. *Medical Hypotheses*, 3, 189-201.

261. McLachlin, J. and McLachlin, A.D. (1958) The peripheral venous heart. *AMA Archives of Surgery*, 77, 568-575.

262. Malone, P.C. and Morris, C.J. (1978) The sequestration and margination of platelets and leucocytes in veins during conditions of hypokinetic and anaemic hypoxia: potential significance in clinical postoperative venous thrombosis. *Journal of Pathology*, 125, 119-129.

263. Movat, H.Z., Weiser, W.J., Glynn, M.F. and Mustard, J.F. (1965) Platelet phagocytosis and aggregation. *The Journal of Cell Biology*, 27, 531-543.

264. Mustard, J.F., Movat, H.Z. and Glynn, M.F. (1965) Platelet phagocytosis. *Thrombosis et diathesis haemorrhagica supplement*, 17, 271-274.

265. Hume, M., Sevitt, S. and Thomas, D.P. (1970) *Venous Thrombosis and Pulmonary Embolism*. Harvard University Press, London.

266. Sevitt, S. (1978) Pathology and pathogenesis of deep vein thrombi. *In*: J.J. Bergan and J.S.T. Yao (eds) *Venous Problems*. Chicago, Year Book Medical Publishers, Inc. p. 257-279.

267. Hamer, J.D., Malone, P.C. and Silver, I.A. (1981) The PO_2 in venous valve pockets: its possible bearing on thrombogenesis. *The British Journal of Surgery*, 68, 166-170.

268. Okoye, G.C., Evans, J.H., Beattie, J., Lowe, G.D.O., Lorimer, A.R. and Forbes, C.D. (1984) Response of femoral venous oxygen tension to graduated pressure stockings - possible relationship to deep vein thrombosis. *Thrombosis and Haemostasis*, 51, 103-104.

269. Hamer, J.D. and Malone, P.C. (1984) Experimental deep venous thrombogenesis by a non-invasive method. *Annals of the Royal College of Surgeons of England*, 66, 416-419.

270. Schaub, R.G., Simmons, C.A., Koets, M.H., Romano, P.J. and Stewart, G.J. (1984) Early events in the formation of a venous thrombus following local trauma and stasis. *Laboratory Investigation*, 51, 218-224.

271. Thomas, D.P. (1985) Venous thrombogenesis. *Annual Review of Medicine*, 36, 39-50.

272. Thomas, D.P., Merton, R.E. and Hockley, D.J. (1983) The effect of stasis on the venous endothelium: an ultrastructural study. *British Journal of Haematology*, 55, 113-122.

273. Sevitt, S. (1974) The structure and growth of valve-pocket thrombi in femoral veins. *Journal of Clinical Pathology*, 27, 517-528.

274. Saphir, O. and Lev, M. (1952) Venous valvulitis. *AMA Archives of Pathology*, 53, 456-469.

275. Thomas, D.P., Merton, R.E., Wood, R.D. and Hockley, D.J. (1985) The relationship between vessel wall injury and venous thrombosis: an experimental study. *British Journal of Haematology*, 59, 449-457.

276. Lawson, C.A., Yan, S.D., Yan, S.F., Liao, H., Zhou, Y.S., Sobel, J., Kisiel, W. and Stern, D.M. (1997) Monocytes and tissue factor promote thrombosis in a murine model of oxygen deprivation. *The Journal of Clinical Investigation*, 99, 1729-1738.

277. Yan, S.-F., Mackman, N., Kisiel, W., Stern, D.M. and Pinsky, D.J. (1999) Hypoxia/hypoxemia-induced activation of the procoagulant pathways and the pathogenesis of ischemia-associated thrombosis. *Arteriosclerosis, Thrombosis and Vascular Biology*, 19, 2029-2035.

278. Yan, S.-F., Pinsky, D.J. and Stern, D.M. (2000) A pathway leading to hypoxia-induced vascular fibrin deposition. *Seminars in thrombosis and hemostasis*, 26, 479-483.

279. Malone, P.C. and Agutter, P.S. (2006) The aetiology of deep venous thrombosis. *Quarterly Journal of Medicine*, 99, 581-593.

280. Rappitsch, G. and Perktold, K. (1996) Computer simulation of convective diffusion processes in large arteries. *Journal of Biomechanics*, 29, 207-215.

281. Lurie, F., Kistner, R.L., Eklof, B. and Kessler, D. (2003) Mechanism of venous valve closure and role of the valve in circulation: a new concept. *Journal of Vascular Surgery*, 38, 955-961.

282. Ashby, E.C., Ashford, N.S. and Campbell, M.J. (1995) Posture, blood velocity in common femoral vein, and prophylaxis of venous thromboembolism. *The Lancet*, 345, 419-421.

283. Malone, P.C. Deep Venous Thrombosis - DVT. (2002) http://www.travellersthrombosis.co.uk/

284. Slack, S.M. and Turitto, V.T. (1993) Fluid dynamic and hemorheologic considerations. *Cardiovascular Pathology*, 2, 11S-21S.

285. Alemani, D., Chopard, B., Galceran, J. and Buffle, J. (2005) LBGK method coupled to time splitting technique for solving reaction-diffusion processes in complex systems. *Physical Chemistry Chemical Physics*, 7, 3331-3341.